DISSERTATION

STUDIES OF U^{6+} WITH THE RESIS METHOD: DIFFICULTIES AND FUTURE DIRECTIONS

Submitted by

Christopher Scott Smith

Department of Physics

In partial fulfillment of the requirements

For the Degree of Doctor of Philosophy

Colorado State University

Fort Collins, Colorado

Summer 2015

Doctoral Committee:

Advisor: Stephen R. Lundeen

Randy A. Bartels
Jacob L. Roberts
Mingzhong Wu

ABSTRACT

STUDIES OF U^{6+} WITH THE RESIS METHOD: DIFFICULTIES AND FUTURE DIRECTIONS

This dissertation analyzes the details of previous resonant excitation Stark ionization spectroscopy (RESIS) measurements carried out on U^{5+} Rydberg states, aiming to determine properties of the ground state of U^{6+}. These measurements were unsuccessful for apparently two reasons, a large background, and unexpectedly small signal sizes.

It has been concluded that the background is a result of a prodigious amount of metastable states within the initial U^{6+} ion beam. Detailed simulations of the metastable population within the beamline showed the metastable hypothesis is plausible. Some reduction of the background within the RESIS technique was achieved with a redesign of the detection region in the apparatus.

Detailed simulations of the RESIS signal size showed that the experimental resolved signals of the U^{5+} Rydberg states were no more than ¼ the size expected from just ground state signal ions. A satisfactory explanation was proposed that metastable Rydberg ions bound to the lowest metastable level ($J = 1$) are forbidden to autoionize and can contribute to the measured signal. These metastable states compose 75% of the measured signal, diluting the ground state signal and preventing identification of the resolved signals.

A possible future approach to the U^{5+} Rydberg state experiment is proposed that probes the Rydberg electron energies with a 1.5 μm laser, and looks like it could successfully measure the properties of the U^{6+} ion.

ACKNOWLEDGEMENTS

I would like to thank my adviser Steve Lundeen for all his help throughout my graduate experience. There couldn't have been a more accessible adviser who was always willing to share his expertise on any topic and give guidance through the entire education experience. Steve always made the research fun and exciting, even when I was frustrated or overwhelmed.

I would also like to thank all the staff and faculty at the J. R. MacDonald Laboratory at KSU, who helped make the experiments run as smoothly as possible, and were always able to fix things as quickly as possible. In addition to being a friend in our time as KSU, Charles Fehrenbach always worked to give us the best beams possible, and had innumerable clever ideas on how to improve the process.

The friendship of my fellow graduate students in our group, Julie Keele and Shannon Woods, was invaluable throughout, whether it was helping collecting data late into the night, teaching me how to run the beamline, explaining theoretical ideas to me, or just joking around.

I would also like to thank my parents for their support and love throughout graduate school. They always made it possible for me to continue my education, and encouraged me every step of the way. They have supported me throughout my life and have shown me that both hard work and spending time with those I care about are important. Both my brother and my sister also helped by pushing me to greater achievements.

Lastly, I'd like to thank my fiancée Marjorie Hamburger. Her love and support have both kept me sane throughout a challenging process as well as inspired me to try and be a better person. I thank her for dealing with the difficulties that come with dating a graduate student.

TABLE OF CONTENTS

LIST OF TABLES

LIST OF FIGURES

Chapter 1: Introduction

1.1 Introduction

The chemistry of the actinide ions is important in many areas of national importance, such as the production and disposal of nuclear fuel, the stability of nuclear weapons, and the clean up of nuclear materials. The U^{6+} and Th^{4+} ions are the most common oxidation states of those two elements, and therefore are typical ions of the actinide chemistry at large. Yet no measurements of any properties of these ions had been made prior to the current project in the Lundeen group. Furthermore, theoretical predictions of their properties from first principles are extremely difficult due to their large number of electrons and highly relativistic nature, and therefore suspect in the absence of experimental tests. For this reason, experimental measurements of the U^{6+} and Th^{4+} ions are important for two reasons, to provide chemistry models experimental values to use in their modeling, and to provide a check on the complicated theoretically modeling that is done to predict the properties of these and similarly complex ions. The resonant excitation Stark ionization spectroscopy (RESIS) technique has the unique ability to measure properties of ions (such as permanent moments and polarizabilities) that would help increase the understanding of the actinide ions at large.

This dissertation explores recent studies of the radon-like ions of thorium and uranium using the RESIS technique, and aims to explain why the thorium experiments were successful and the uranium ones were not. In order to explore these surprisingly different outcomes, it will require careful analysis of factors that can be ignored in a successful experiment, such as the expected signal sizes, and the dominant sources of background.

This chapter describes the characteristics of high-*L* Rydberg levels that are measured with the RESIS technique, and shows how this spectroscopy provides measurements of positive ion properties. The basic experimental method of the RESIS technique will also be discussed, as well as an overview of the results of the uranium and thorium experiments, with an emphasis on the problems experienced in uranium studies.

1.2 High-*L* Rydberg States

The RESIS technique revolves around high-*L* Rydberg states, which are a positive ion core with a weakly bound electron (known as the Rydberg electron) attached in a state of large orbital angular momentum ($L \geq 6$). Figure 1.1 shows a diagram of what this state looks like. They can either be Rydberg atoms if the total charge of the system is zero, or Rydberg ions if the positive ion core has charge greater than one.

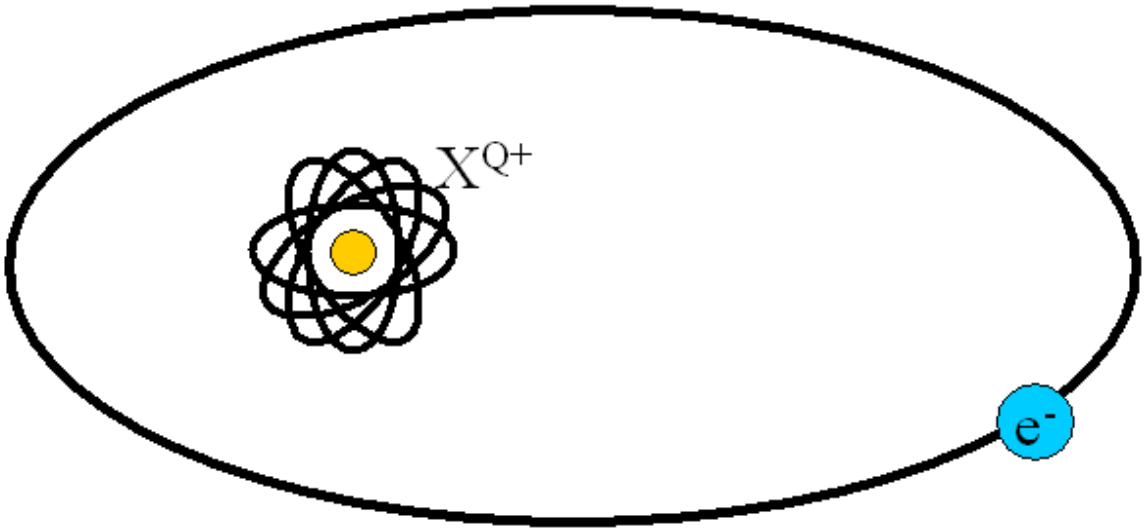

Figure 1.1: Schematic of a Rydberg atom or ion. X is an arbitrary element with a positive charge of Q.

This system is very close to hydrogenic when the electron has a large enough orbital angular momentum (i.e. the electron is far away from the ion core). The Rydberg electron can be

labeled in the same way as the hydrogen electron with the quantum numbers *n*, *L*, and *m*. Its binding the energy is close to the well-known hydrogenic energy given in atomic units (1 a.u. = 2 Ryd = 27.2114 eV) as:

$$E_{hyd} = -\frac{1}{2}\frac{Q^2}{n^2}$$

where Q is the charge of the ion core. Note that this energy is independent of the angular momentum quantum number, *L*. In reality there are long-range interactions between the Rydberg electron and the positively charged ion core other than the dominant Coulomb interaction that break the hydrogenic degeneracy with *L*. This perturbs energies away from hydrogenic by an amount that decreases with *L*. The magnitude of these long-range interactions depends on the properties of the ion core, which fall into two categories: permanent moments and polarizabilities. The two most dominant properties in the energy of the system are the quadrupole moment, and the scalar dipole polarizability. For this dissertation all ions discussed will have a core angular momentum of zero ($J = 0$) making the quadrupole moment zero. The dominant property of the ion core is then the scalar dipole polarizability. The connection between the magnitude of the perturbation and the core properties has been studied in depth for many years, and has been extended to very high orders [1]. For this dissertation, the leading term is sufficient, and is given as:

$$E_{perturbation} = -\frac{1}{2}\alpha_D \langle n, L | r^{-4} | n, L \rangle$$

where $\alpha_{D,0}$ is the scalar dipole moment. This shows that the perturbation energy is easily relate-able to the dipole polarizability. This means that if the energy levels of a Rydberg system with a core ion of interest are spectroscopically measured, then the core's properties can then be determined. In this way the Rydberg electrons can be viewed as a probe to study the ion core.

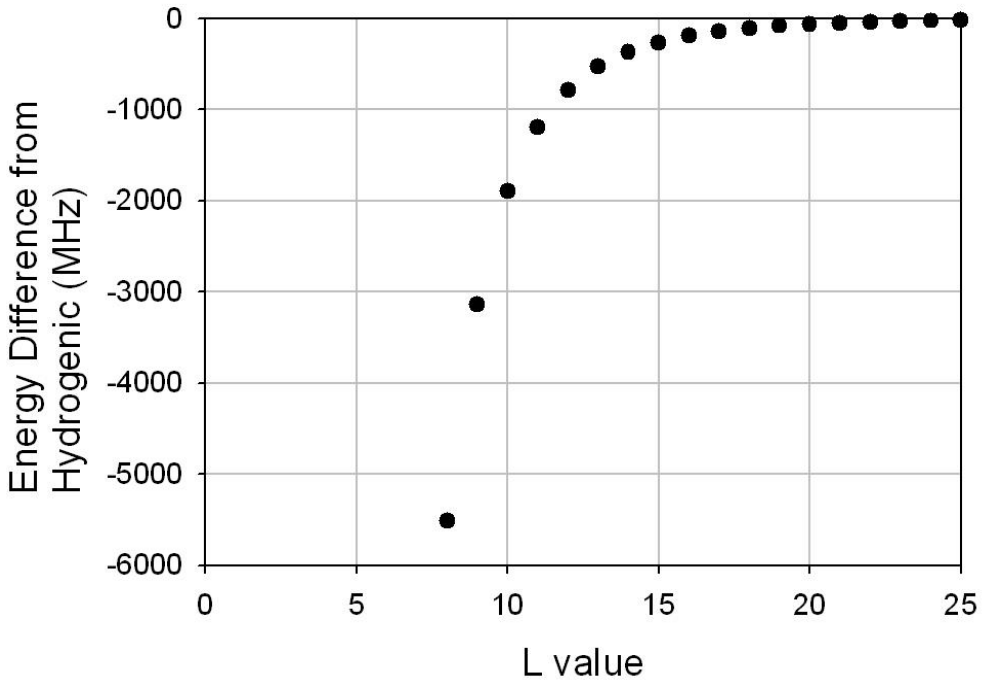

Figure 1.2: Energy perturbation away from hydrogenic for $n = 53$ U^{6+} as a function of the L value.

Figure 1.2 shows the larger perturbation away from hydrogenic for the lower L values. The highest L values aren't shown, but the trend would continue where they are essentially hydrogenic. The lowest L levels become more dependent on the higher order terms and therefore become more complicated theoretically. For this reason they aren't shown in figure 1.2. Since the highest-L values are only separated by tens of MHz, they become very hard to resolve spectroscopically. Experimentally, this leaves L values that are about $L = 10$ that are perturbed from hydrogenic far enough to be resolvable from the high-L states, but have high enough L values to still be relatively simple theoretically.

1.3 RESIS Experimental Technique

The RESIS technique was originally designed for studying neutral Rydberg states and their singly charged ion cores. For instance, Ni^+ was one of the most recent ions studied. Ni^+ will be used as an example to give a brief overview of the RESIS technique (more detail will be given in chapter 2) [2]. First a beam of the ion of interest is created from an ion source. The beam passes through focusing, then collides with a Rydberg target to create neutral Rydberg states. The Rydberg target is a thermal beam of Rubidium that has an electron excited by lasers to a high-energy state. Most of the ion beam doesn't capture an electron (~99%), but the ones that do are of interest.

The beam then passes through an electric field region called the pre-ionizer to Stark ionize Rydberg ions in high-*n* states and block passage of any remaining Ni^+ ions. Following this, the beam passes through the Laser Interaction Region (LIR) where a CO_2 laser excites a transition of choice to an *n* state that was cleared out within the pre-ionizer. This means the only Rydberg atoms with that *n* value are those excited in the LIR. The CO_2 laser is used due to its flexibility in choosing laser lines, and since it has energies close to the excitation of convenient hydrogenic transitions (~1000 cm^{-1}). The transition is chosen to have energy close to laser lines that are available, a typical transition might be $n = 10$ to 30 or $n = 9$ to 19. The CO_2 laser reflects off a rotate-able mirror to allow for Doppler tuning. The Doppler tuning allows probing of energies close to the nominal hydrogenic transition to determine the energies of the resolved lower-*L* states. In this way the energy levels of the Rydberg atom can be determined. This means the beam needs a velocity that is high enough that the Rydberg states don't decay before detection can occur, and also such that sufficient Doppler tuning can occur ($v/c \sim .001$). Since excitation only occurs from a single initial *n* value, there are still a lot of Rydberg states present

that weren't excited. The CO_2 laser is chopped so that excitation can be monitored with a lock-in amplifier. Figure 1.3 shows a schematic demonstrating the relative populations of the n = 10 state and n = 30 state for the Ni^+ RESIS technique. This shows the capture into all n states (but less capture into high-n states), ionization of high-n states in a pre-ionizing region, excitation within the LIR, and detection of Rydberg states that have been excited.

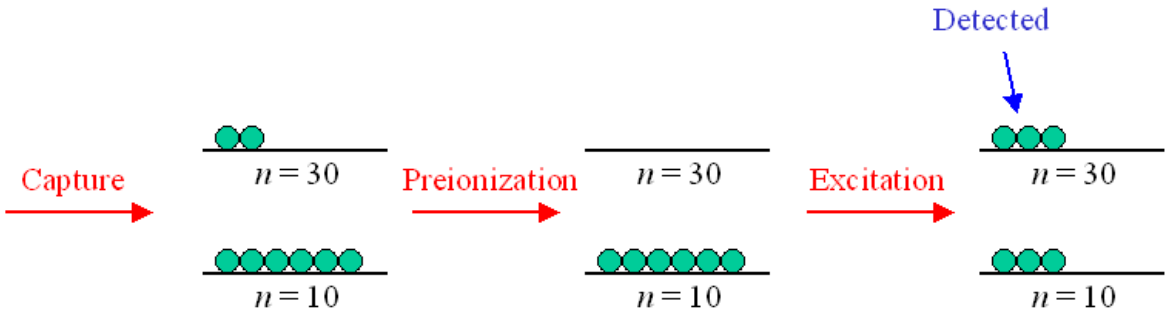

Figure 1.3: Schematic of the relative populations of the n = 10 and 30 states of nickel at key points in the beamline. After charge capture, both states will be populated, but less capture into the higher-n state. The preionizer Stark ionizes all atoms in the $n \geq 30$ state. Excitation in the LIR then equalizes the population in the two n states. The states that were excited are detected by Stark ionization in the detector.

After excitation, the beam passes into the detector region, a schematic of which is shown in figure 1.4. The detector contains an electric field whose size is chosen to be large enough to Stark ionize all L states within the upper-n state of the chosen transition. Since the beam passed through the pre-ionizer region that ionized high-n Rydberg states, the only states that should be ionizable within the detector are those that are excited within the CO_2 laser. This ionization separates the signal ions in charge from other charge capture atoms that are present within the detector, such as atoms that captured from the Rydberg target into an n that is not of interest. The detector is also designed such that ionization happens at a negative potential, usually ~4 to 8 kV. This can be seen in figure 1.2, where the Rydberg states first pass through a ramp down region that puts them at potential, without experiencing a field large enough to Stark ionize them.

Only after this are they placed in a region whose field is large enough to Stark ionize the signal ions. This means that any ion that is Stark ionized within the detector has its energy changed by ~4 to 8 keV. We refer to this as "energy tagging". In this way, the signal ions are separated in energy from other ions that may be present. The apertures in the Stark ionizer are 6.4 mm (1/4"). This means that within a length of ~6.4 mm the field changes to its full magnitude. For this reason, most of the Stark ionization occurs in about 6.4 mm. After ionization, the beam is deflected vertically which separates beams based on their charge and energy. This provides physical separation of the signal beam from the other beams that were previously on the same trajectory. The signal beam is then detected using a channel electron multiplier.

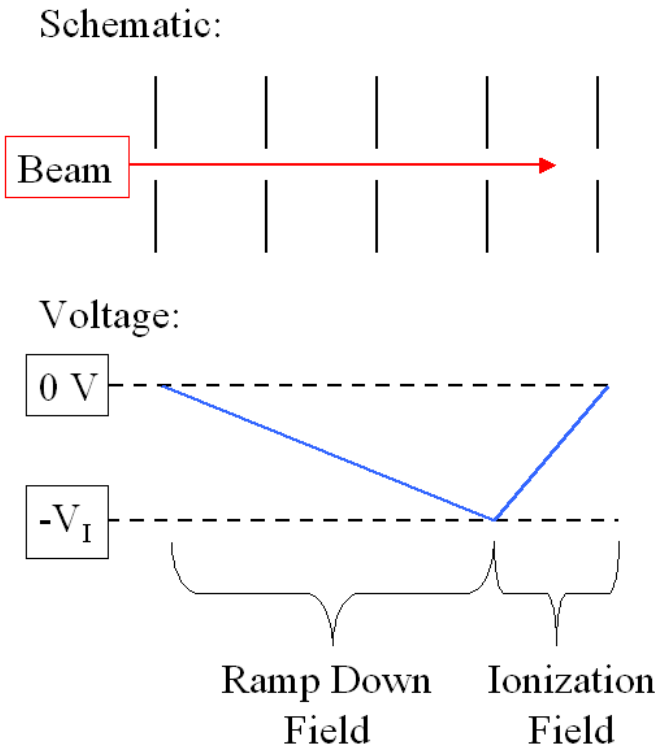

Figure 1.4: Schematic of the Stark ionization region used in the RESIS technique. Shown below is the voltage scheme used. The ramp down field is not large enough to Stark ionize the signal Rydberg ions, but the ionization field is. The signal ions therefore ionize at the potential $-V_S$.

This technique has been used successfully in a range of experiments with neutral Rydberg atoms to measure the properties of the core ions of Ni^+, Ba^+, Mg^+, and Ar^+[2- 5]. The question became whether the technique could be expanded to Rydberg ions. This would be systems where the positive ion core is multiply ionized. These systems are still hydrogenic, but their higher charge means that most Rydberg electrons are more tightly bound. It is not obvious whether the CO_2 laser will be able to excite a transition whose upper state can be ionized in the detector. However, by using transitions with much higher-*n* values, transitions can be found that are compatible with the CO_2 laser's frequency and are bound weakly enough to be Stark ionized in the detector. Typical transitions might be $n = 37$ to 73 for charge 4+ ions, and $n = 53$ to 93 for charge 6+ ions.

The CO_2 laser was not the only part of the beamline that needed new consideration when transitioning from Rydberg atoms to Rydberg ions, the charge capture from the Rydberg target also changes. The same target that was used for Rydberg atoms can be used for the Rydberg ions since the binding energy of capture is approximately independent of the core ion charge. If the charge of the capturing ion goes up and the binding energy of capture remains approximately the same, then the *n* states of capture will be higher as well. This means the *n*-state of capture is proportional to Q. This makes the target capture naturally compatible with the higher-*n* states that can be detected with the CO_2 laser. However, two problems occur with capturing into higher-*n* states. The first is that since the *n* states are closer together in energy, more *n* states will capture, reducing the fractional capture into a given *n* state. The second is that with higher-*n* states there are more *L* states, so the fractional capture into a given *L* state goes down. Combining these two effects, the capture into a given *n, L* state should go down as $1/Q^2$. This means that a charge 6+ ion's signals from a single *L* level would be expected to be about 36

times smaller than a charge 1+ ion. This means that larger beams may be required to effectively work with Rydberg ions.

Another change that needed to be made in going to Rydberg ion experiments is changing the pre-ionizer to a repeller lens. It still serves the purpose of Stark ionizing high-*n* Rydberg states. For low charge ions the repeller can be tuned to repel the beam that did not capture a Rydberg electron (primary beam) due to its lower energy/charge. For higher charged ions (such as charge 6+), this is more difficult since the energy/charge is relatively similar between the beams. The focal length will still be different between the two beams, meaning the ideal tuning for the charge capture beam will be different than the primary beam. That being said, for the higher charges the some primary beam could still make it to the detector.

The desired studies of Rn-like Th^{4+} and U^{6+} required an ion source capable of producing multiply charged metal ions by sputtering. A proof of principal experiment was needed to obtain the funding for such a source. An experiment to measure the properties of Kr^{6+} was attempted to show that the technique would work with ions with charge 6+. This experiment was successful, and a paper was published with the results in 2007 [6]. A representative RESIS spectrum is shown in figure 1.5 showing the Kr^{6+} n = 55 to 109 transition. This demonstrated that the higher charge, and *n* states could be accommodated with the RESIS technique, and funding was obtained to purchase an Electron Cyclotron Resonance (ECR) ion source. This new source produced beams of high charge states of thorium and uranium by sputtering from solid metal targets in a Xenon discharge.

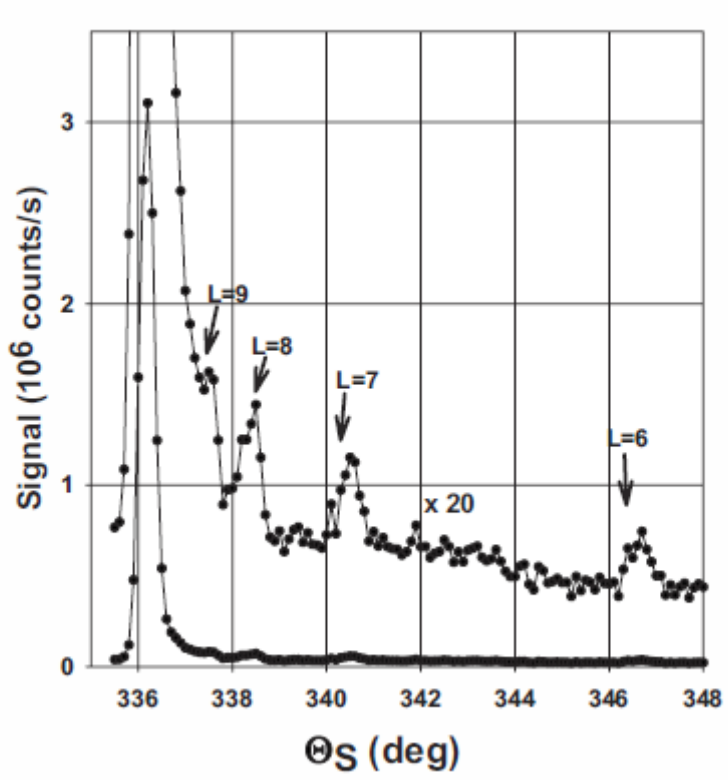

Figure 1.5: Representative RESIS spectrum of Kr^{6+} taken from reference [6]. The horizontal axis is the stage angle. The resolved low-*L* peaks are labeled. The transition was the $n = 55$ to 109 at 48 keV.

1.4 History of Uranium and Thorium RESIS

Graduate student Mark Hanni carried out the initial studies on U^{6+} and Th^{4+}, and the differences in difficulty were documented in his Ph.D. dissertation [7]. Specifically there are two major problems seen in the uranium experiment versus the thorium experiment: uranium had smaller resolved signals and had a larger background. The presence of the background was unexpected, and that will be discussed in greater detail later in this chapter, but was present for both uranium and thorium.

Figure 1.6 is taken directly from Mark Hanni's dissertation, and shows the RESIS spectrum of 100 keV Th^{4+} core states in the $n = 37$ to 73 transition taken in 240 seconds per point [7].

Clearly visible are the n = 37, L = 10, 9, 8, and 7 transitions to the n = 73, L = 11, 10, 9 and 8 states respectively, as well as an unresolved signal from very high-L levels. The resolved signals range from ~1% to 3% of the high-L signal. The background was ~1.3 times the size of the high-L signal for this work. The analysis of this spectrum is covered in detail within the Hanni dissertation, but it is obvious that the resolved peaks are visible to a degree where it would be possible to fit them with Gaussians and determine their perturbation in energy from hydrogenic. Doing this allowed various properties of the Th^{4+} core ion to be determined to a high precision [8-10]. This demonstrates the success of the RESIS technique on a highly charged actinide ion.

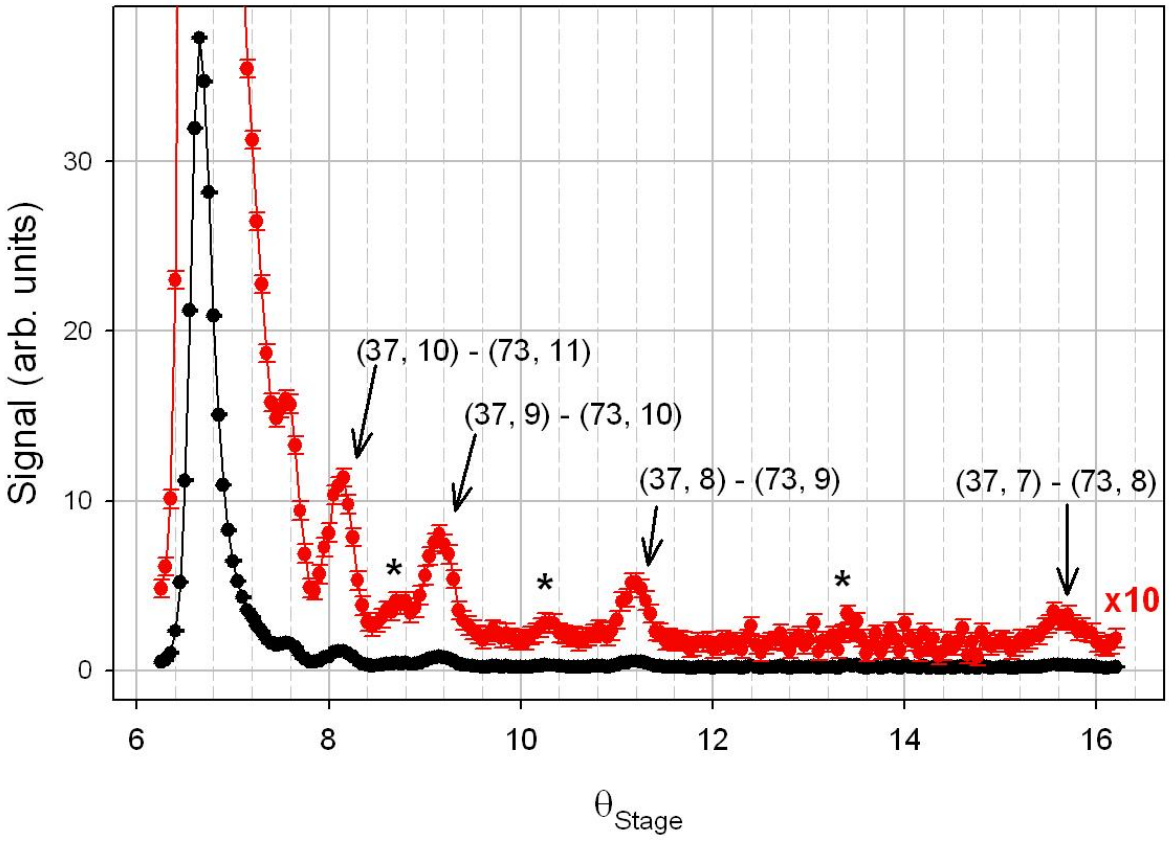

Figure 1.6: Example RESIS spectrum of the Th^{4+} at 100 keV n = 37 to 73 transition. The red line is 10 times the spectrum. Clearly seen are multiple resolved transition peaks labeled with their n,L values above each peak.

The success of thorium is easily contrasted with the difficulty of uranium. Figure 1.7 is taken from reanalyzed data from Mark Hanni's dissertation. It is the spectrum of the U^{6+} 150 keV n = 53 to 93 transition that corresponds to the best high-L signal/uncertainty obtained for U^{6+} (with a signal/uncertainty of ~1300 from 660 seconds of collection time per point). The blue bar on the right side of the spectrum shows the size of the signals if they were 1% of the high-L. It is very clear that there is nothing close to that size visible in this spectrum. This makes it seem like the resolved signals are much smaller than anticipated for U^{6+}. Naively the relative size might have been expected to be reduced by $(4/6)^2 = 0.4$. The resolved signals were about 1% to 3% of the high-L for thorium, and yet the uranium didn't show anything that was even 0.25% of the high-L. This is the first problem seen in the U^{6+} experiment, that the resolved signals are surprisingly small.

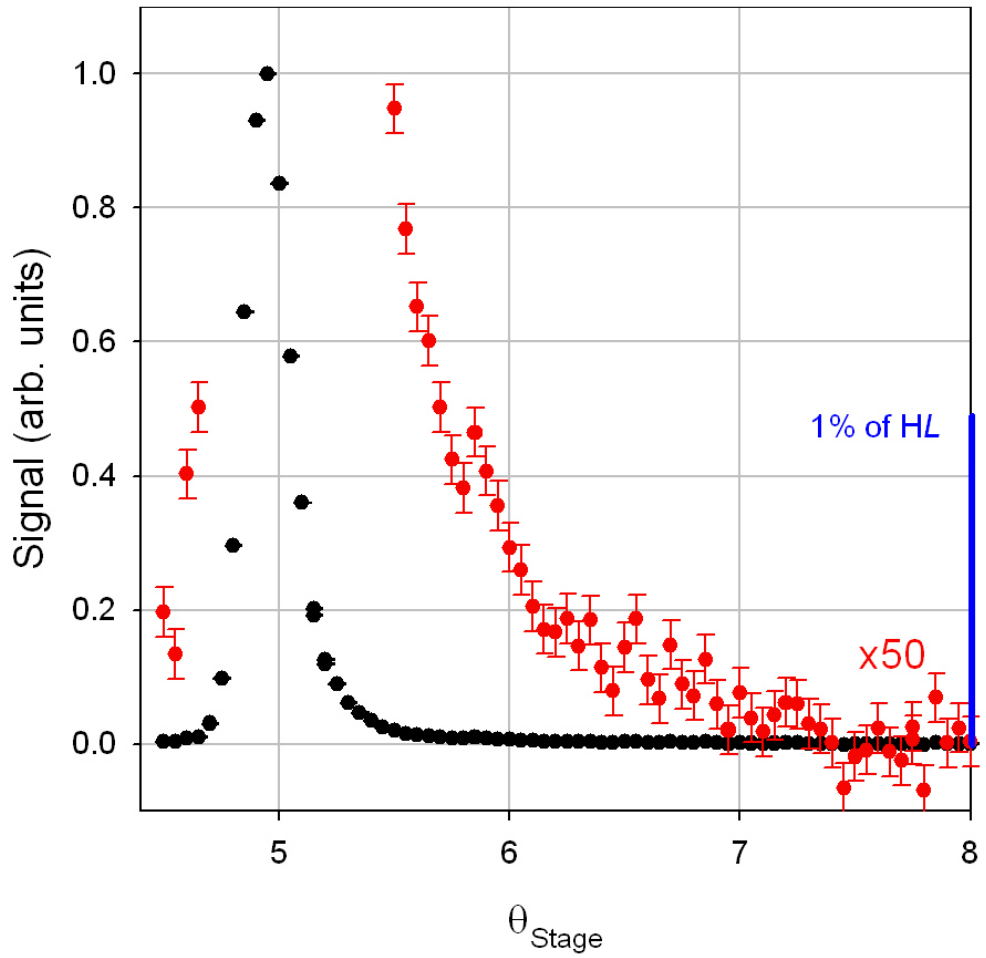

Figure 1.7: Example RESIS spectrum of the U^{6+} at 150 keV n = 53 to 93 transition. The red line is 50 times the spectrum. The blue bar on the right demonstrates a signal size of 1% of the high-L.

The size of the U^{6+} resolved signals can also be compared to figure 1.5 that shows the Kr^{6+} spectrum taken as a precursor to the current actinide experiment. The L = 8 resolved signal was seen at about 1.3% of the high-L. Nothing anywhere close to this size was seen in the U^{6+} scan. This is especially surprising since the Kr^{6+} experiment is so similar to the U^{6+} experiment. Since they are both hydrogenic Rydberg states with a core charge of 6+, there are only minor differences between the two experiments. Yet, the Kr^{6+} resolved signals are on the order of 1% of the high-L and the U^{6+} resolved signals were not seen with error bars that were .07% of the high-L. This reinforces the idea that the resolved U^{6+} signals are much smaller than anticipated.

The second difficulty seen in the U^{6+} experiment was a larger background than that of Th^{4+}. The background for the spectrum seen in figure 1.7 was ~3.2 larger than the high-*L* signal. As mentioned, for the Th^{4+} work the background was ~1.3 times the size of the high-*L* signal. That means the U^{6+} had 2.5 times more background than the Th^{4+} experiment. This larger background makes the U^{6+} experiment very difficult since it already has smaller resolved signals that need to be detected.

Both Th^{4+} and Kr^{6+} demonstrate successful measurements carried out using the RESIS technique with ions that are very similar to U^{6+}, but they also demonstrate the need for further analysis of the U^{6+} RESIS experiment since there must be factors that make U^{6+} much more difficult than anticipated.

1.5 Practical Difficulties

In comparing the description of the RESIS experimental method given earlier with what was actually seen in carrying out the experiments, there are three observations that were unexpected: the small resolved signal sizes for uranium, the presence of the background, and the presence of a regenerated primary. These three observations will be described in some detail below.

The first observation is the small resolved signal sizes seen in the U^{6+} RESIS technique. These were detailed in the last section, and the conclusion is that the resolved signals appear to be smaller than Th^{4+} and Kr^{6+} signals by around a factor of 5. The main question related to this observation is whether the signals are actually smaller than expected. Since the resolved signals are generally seen in the RESIS technique, relatively little analysis has been given to their expected magnitude. The lack of signals for U^{6+} however demands a more careful analysis, and

will be a central topic of this dissertation. For now the simple analysis of the last section seems to indicate the signal sizes are abnormally small for U^{6+}.

The second observation is the presence of the background. Since the high-*n* states that can be Stark ionized within the detector are pre-ionized within the repeller region, the only states that should be ionized within the detector are the signal ions that got excited to high-*n* states in the LIR region. The signal ions should therefore be the only states that get energy tagged in the Stark ionizer, and nothing should be ionized if the CO_2 is off. Surprisingly, this was not the case. A background was seen that was independent of the CO_2 laser, and was energy tagged in the Stark ionizer. Since it is energy tagged, it must ionize in the Stark ionizer, but doesn't have to be Stark ionized. What was actually seen experimentally was a background that was 1.3 times the high-*L* for thorium, and 3.2 times the high-*L* for uranium. This background may not sound terrible, but analysis can be done to determine how hard it makes seeing resolved signals in the uranium case.

Figure 1.8 illustrates two situations that will be analyzed to determine the effect the background has on the signal to noise. The first case is what would be the case in the RESIS experiment if there were no background. This means that when the CO_2 laser is on, then there will be signal ions detected, but when the CO_2 laser is off then there will be nothing detected. This means that if the total collection time is defined to be T, then the signal would be detected for half of that time, T/2. Therefore the total signal counts detected would simply be given as:

$$Counts = \frac{S \cdot T}{2}$$

The uncertainty would come from the simple counting uncertainty, or the square root of the number of counts, where S is the count rate of signal ions:

$$\sigma = \sqrt{\frac{S \cdot T}{2}}$$

This means the signal over noise would be:

$$\left.\frac{S}{\sigma}\right|_{BackgroundFree} = \frac{\frac{S \cdot T}{2}}{\sqrt{\frac{S \cdot T}{2}}} = \sqrt{\frac{S \cdot T}{2}} \tag{1.1}$$

Equation 1.1 shows that if there is no background, then the signal to noise gets larger with the square root of both the signal rate and the time. For a typical U^{6+} beam, the primary beam is about 2 nA, corresponding to 2.1 x 10^9 ions/second. Assuming 5% of the primary capture a Rydberg electron, the charge capture beam would be 100 pA, corresponding to 10^8 ions/second. The high-*L* signal is generally about 2% of CXRT, corresponding to 2.1 x 10^6 ions/second. The resolved signals then might be about 1% of the high-*L* peak making them 10 fA, corresponding to 2.1 x 10^4 ions/second. The resolved signals would then have a signal to noise of ~450 in twenty seconds. This means the resolved signals would still be extremely easy to see if the RESIS technique was in fact background free as expected.

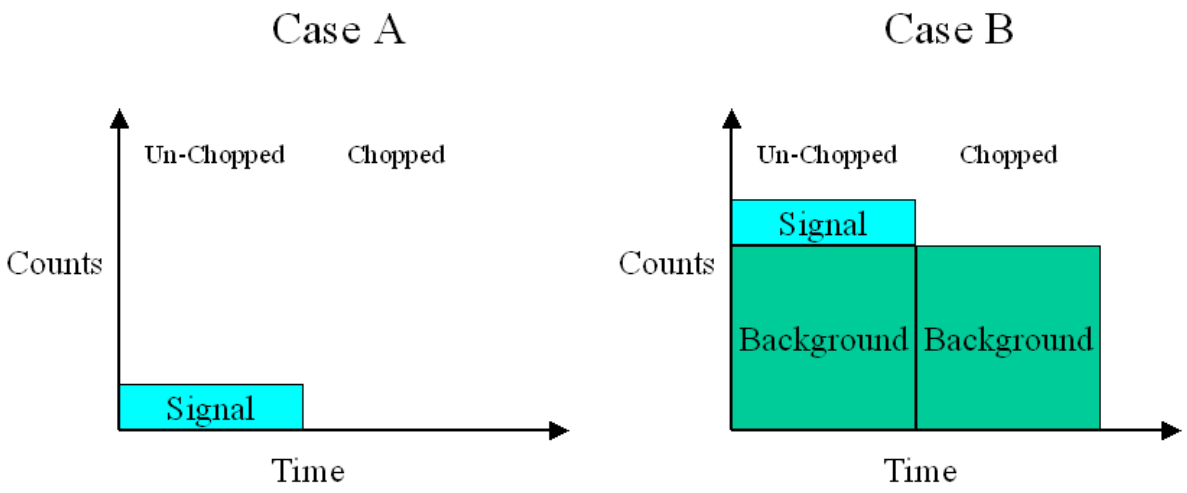

Figure 1.8: Schematic showing where counts in the detector come from when the CO_2 laser is either chopped (not going in) or un-chopped (going in). Case A is the hypothetical situation in the RESIS technique where there is no background. Case B is the actual experimental situation in the RESIS technique where there is a background that is significantly larger than the signal.

The actual RESIS signal to noise can be analyzed in the second case where there is a background that is present whether or not the CO_2 laser is chopped. The signal is the difference of the counts S*T/2. The shot noise in the difference is the square root of the total counts in time T.

$$Total\ Counts = \frac{S \cdot T}{2} + B \cdot T = T \cdot \left(\frac{S}{2} + B \right)$$

Meaning the noise is simply:

$$\sigma = \sqrt{T \cdot \left(\frac{S}{2} + B \right)}$$

Putting this together, the signal to noise is:

$$\left. \frac{S}{\sigma} \right|_{Background} = \frac{\frac{S \cdot T}{2}}{\sqrt{T \cdot \left(\frac{S}{2} + B \right)}} = \frac{\sqrt{\frac{S \cdot T}{2}}}{\sqrt{1 + \frac{2B}{S}}} \qquad (1.2)$$

Equation 1.2 shows that the signal to noise still gets better with the square root of collection time, but the relationship between the signal to noise and the number of signal counts is much more complicated. The background for U^{6+} was often ~10 times larger than the high-*L* signal, so assuming the same 2×10^6 counts/second for the high-*L* signal, it would be reasonable to assume $B = 2 \times 10^7$ counts/second. The background is still the same size at the resolved signals i.e. 1000 times larger than a signal that is 1% of the high-*L*. The signal to noise for the resolved signals in twenty seconds would be 10, down by a larger factor of 45.

This relatively simple analysis of the background demonstrates the severity of the unexpected presence of the background. Its existence makes the signal to noise on a resolved signal worse by a factor of ~45. Since the signal to noise is proportional to the square of the time, then the collection time would have to be ~2,000 times as long to compensate for this factor. This does not mean the RESIS technique is impossible with the presence of this background, but does demonstrate how much harder this background makes it.

The third observation is the presence of what becomes dubbed the "regenerated primary". Before the actinide experiments were carried out a 15˚ magnet was installed downstream of the Rydberg target. This serves the purpose of separating the ions that did not capture a Rydberg electron (primary beam) from the ions that did capture (charge capture beam). This was meant to ensure that after the 15˚ magnet there would be no primary beam. This was not the case though. It was observed that there was a very large primary beam present at the detector. Since this beam must be composed of ions that began as ions that captured a Rydberg electron, but have ionized by the time they make it to the detector, it is called the "regenerated primary."

An analysis of the regenerated primary (RP) begins with understanding which beams are present within the detector. For a U^{6+} 150keV beam, there are three beams present at the

detector. The first is the U^{5+} charge capture (CX) beam that has the nominal 150keV energy and the 5+ charge. As stated previously, this is comprised of ions that have captured an electron in the Rydberg target. The second is the regenerated primary (RP) beam that has a charge of 6+ and is also at the nominal 150keV energy. It is the ions that made it through the 15˚ magnet as U^{5+} but changed into U^{6+} before the detector. The third and final beam at the detector is comprised of the signal ions. This is composed of U^{6+} ions that were Stark ionized in the detector and therefore were energy tagged to have a decreased energy of (145keV for example). When these three beams are sent through the vertical deflector plates, their charge and energy separate them. Specifically a higher charge ion will be deflected more, and a lower energy (slower moving) ion will be deflected more since it spends more time in the field. This means the ratio of charge/energy is the parameter that determines the deflection and therefore the separation of beams. Figure 1.9 shows a schematic of these beams, and their relative deflections for an arbitrary field within the vertical deflector plates. Since the signal ions have both the highest charge, and least amount of energy, they are deflected the most, and the lower charge of the charge capture beam compared to the regenerated primary means it is deflected the least.

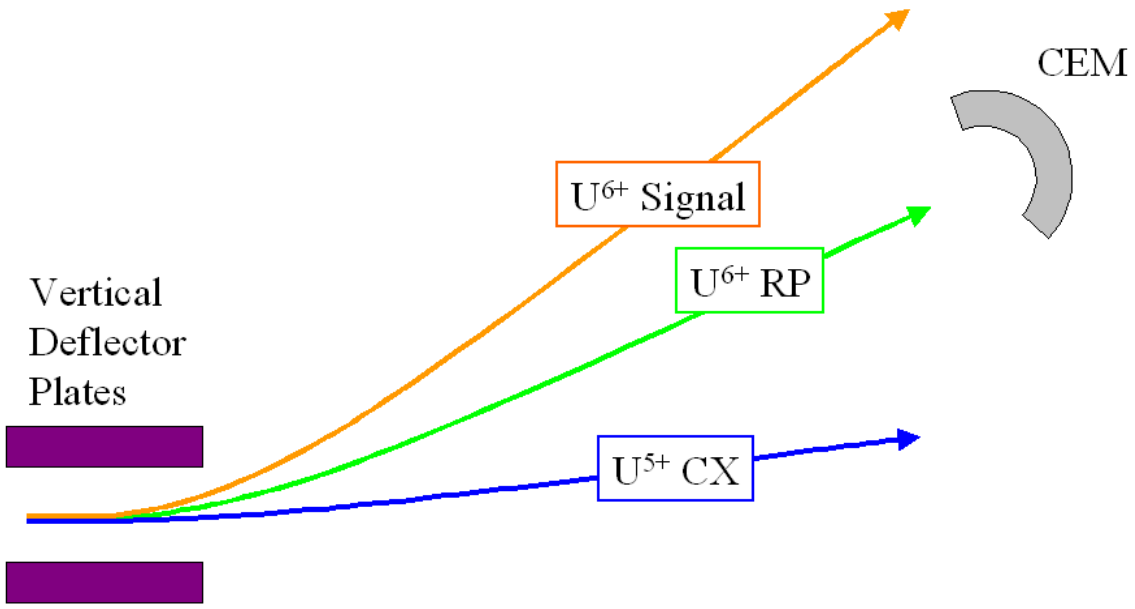

Figure 1.9: Schematic of the beams present within the detector for U^{6+}, and their relative deflections due to the vertical deflector plates.

Figure 1.9 demonstrates how the beams are separated for a set potential on the vertical deflector plates, however the most convenient experimental measurements vary the potential on the vertical deflector plates to document the beams incident on the CEM as a function of that potential. This is dubbed a vertical deflector scan. By doing such a scan it can be learned what beams are present, what their relative charge/energy is, and what their relative sizes are. Figure 1.10 shows a scan such as this for 150keV U^{6+} with the background, regenerated primary, and charge capture peaks labeled. Note that the vertical axis is the log scale, and that the small contribution from the signal has been removed from this scan.

The regenerated primary and background peaks shown in figure 1.10 are entirely from ions that captured an electron from the Rydberg target. Simply blocking the L3 laser (effectively turning off the target), and seeing if these peaks go away tests this. The charge capture peak however, is comprised of ions that capture from the Rydberg target, and those that capture from other sources, principally ground state Rb atoms. By blocking the Rydberg target and measuring the

change in size of the charge capture beam, the charge capture from the Rydberg target (CXRT) can be determined.

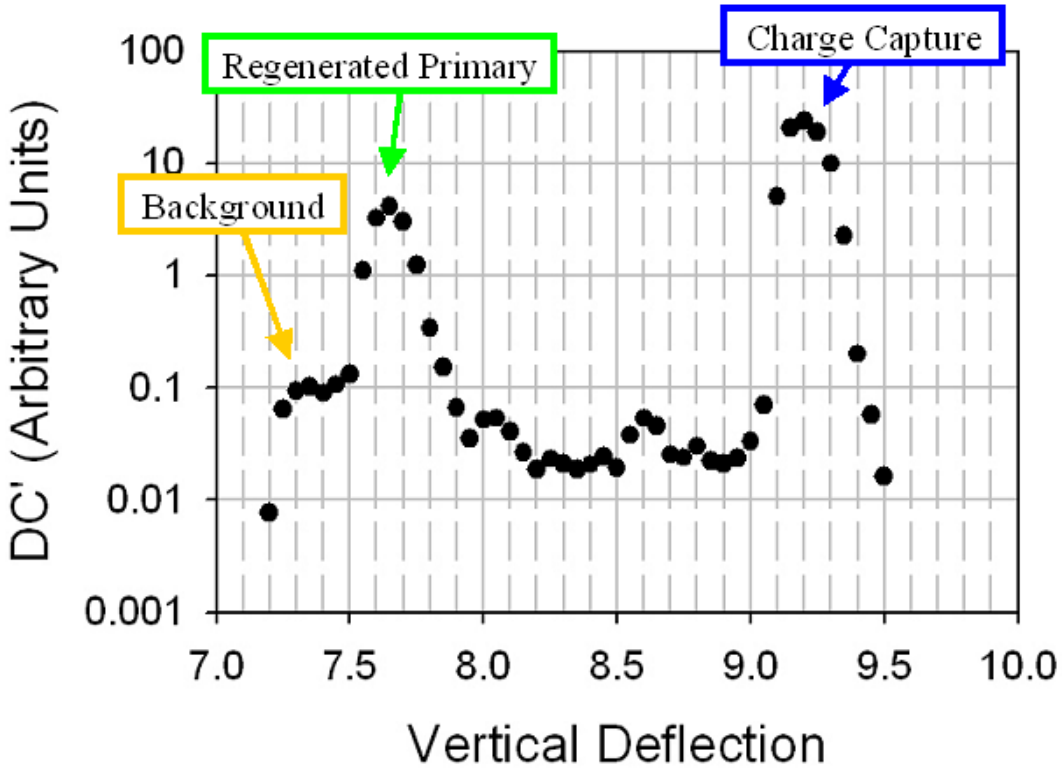

Figure 1.10: Vertical deflection for 150keV U^{6+}. The horizontal axis is proportional to the potential applied to the vertical deflector plates. The background peak is centered at ~7.35, the regenerated primary peak is centered at ~7.65 and the charge capture peak is centered at ~9.2.

The charge capture is the largest peak, but the unexpected regenerated primary peak is less than an order of magnitude smaller than it, making it very significant. Comparing the regenerated primary to the CXRT, it is found that they are usually about equal. This means that about half the ions that capture a Rydberg electron show up in the regenerated primary beam. The background is down less than two orders of magnitude than the regenerated primary. At first glance this may seem small, but since the background was about 18 times the size of the high-*L* signal for this scan, it is actually quite important. This also means that the regenerated primary is about 270 times the size of the high-*L* signal, making it massive compared to the only

expected peak other than the charge cature peak. As alluded to earlier, the fact that the signal is energy tagged separates it from the regenerated primary which has the same charge. This helps immensely, but there is no escaping the background that is at the same location in vertical deflection as the signal.

1.6 Questions and Goals

This chapter has introduced high-*L* Rydberg states and the RESIS technique used to study their spectroscopy and extract measurements of properties of their core ions. The recent studies of Rydberg levels bound to the Rn-like ions Th^{4+} and U^{6+} were briefly reviewed, illustrating the problems encountered in the uranium studies. Specifically, the problems with uranium are a background that was larger than thorium, and resolved signal sizes that were smaller than thorium. In analyzing these problems, a greater understanding of the RESIS technique at large may be gained. Three questions can be posed that will be addressed in this dissertation.

1) What is the dominant source of the background in the RESIS technique?
2) Can the background be reduced?
3) Why are the U^{6+} signals so small?

Answering these three questions effectively, and possibly pointing the way to a successful study of the uranium ions, is the goal of this thesis.

Chapter 2: Experimental Apparatus and Technique

2.1 RESIS Experimental Technique

The RESIS studies analyzed in this thesis were carried out in the J. R. MacDonald Laboratory at Kansas State University using an apparatus that was only slightly modified from that used by Mark Hanni in his earlier Ph.D. dissertation work. The Hanni dissertation describes that apparatus in detail. The first section of this chapter will briefly describe that apparatus using the Th^{4+} study as an example. The intent of this section is to clarify the function of the various parts of the RESIS apparatus.

In the course of the present study, several parts of the apparatus were slightly modified. In particular, the Stark ionization detector was redesigned and a new device was constructed and installed. The second section of this chapter will describe these apparatus modifications and document the details of their construction.

A block diagram showing the beamline is seen in figure 2.1. The ion beam is generated using an Electron Cyclotron Resonance (ECR) ion source. The ions are extracted from the source and accelerated to an energy of choice, for Th^{4+} it was 100keV. After extraction the ion beam passes through an electric quadrupole doublet lens to focus the beam, a 20^{o} magnet to select the proper charge state, and another quadrupole doublet lens for further focusing. At this point the beam intersects a thermal beam of Rubidium atoms that are injected into the beamline by heating an oven containing liquid Rubidium metal. Three lasers intersect within the beam of Rubidium in order to excite a Rydberg electron on the Rubidium. The first two laser excitations are of set wavelength. The first is an excitation from the $5S_{1/2}$ ground state of Rubidium to the

$5P_{3/2}$ state using a 780 nm wavelength laser, and the second excitation is from the $5P_{3/2}$ state to the $4D_{5/2}$ state using a 1529 nm laser. The last excitation comes from a Ti:Saph laser that allows the particular *n* state to be chosen. In general the laser was used to excite to the $10F_{7/2}$ state using 756 nm. Experimental evidence indicates that a few percent of the ion beam captures a Rydberg electron, and capture occurs into a range of *n*'s depending on the target and charge state of the ion, but most capture occurs very roughly between $n = 30$ to $n = 70$. In the example of Th^{4+}, the resulting beam would then be about 95% Th^{4+} that did not capture an electron, and about 5% Th^{3+} Rydberg states that captured a Rydberg electron.

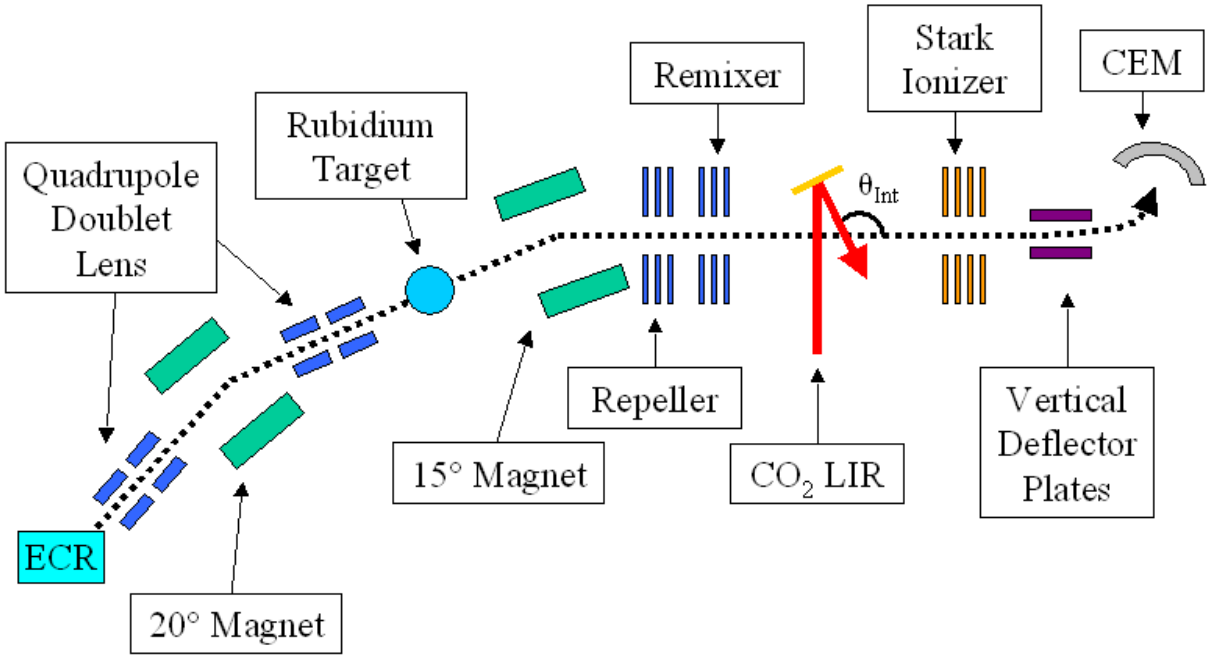

Figure 2.1: Schematic of the RESIS optical technique beamline at the time of the Th^{4+} experiments.

The ion beam then passes through a 15° magnet that selects only the ions that have captured a Rydberg electron, so for Thorium the Th^{3+} Rydberg states would be selected. After the magnet, the beam passes through two more einzel lens that both allow focusing of the beam,

but each also serves another purpose. The first einzel lens is referred to as the repeller and is set to have an electric field large enough to ionize Rydberg states that are bound weakly enough to be Stark ionized within the detector. Rydberg states of core charge Q and principal quantum number *n* ionize at a range of electric fields. The exact field required for ionization depends on the Stark quantum numbers. This range of fields for a given *n* and Q is given by [11]:

$$\frac{1}{9}\frac{Q^3}{n^4} \leq E_{Ionization} \leq \frac{2}{9}\frac{Q^3}{n^4} \text{ a.u.} \qquad (2.1)$$

where 1 a.u. = 5.1 x 10^9 V/cm. All of the states within a given *n* level should ionize at the larger field, regardless of their Stark level. Equation 2.1 holds in the case known as "diabatic" ionization. This applies when the slew rate of the electric field is high enough that the Stark patterns of adjacent *n*-levels don't mix. Experimental evidence supports this description of Stark ionization in RESIS studies.

The repeller was generally set to 10.0 kV over the 2.54 cm gap within the repeller for the thorium experiments, which would imply full ionization of Rydberg states down to $n = 66$. This allows states that are excited to the $n = 73$ state within the experiment to be the only Rydberg states with $n > 65$. The second einzel lens is referred to the remixer and serves the purpose of redistributing a fraction of the populations within the long lived high-*L* states to the shorter-lived low-*L* states that are of more interest experimentally.

Following the remixer is the CO_2 Laser Interaction Region (LIR) where a nominally 50W CO_2 laser is used to excite a transition of choice. The CO_2 laser has tunable lines around ~1000 cm^{-1} which gives the flexibility in choosing a transition, for Th^{4+} it was the $n = 37$ to 73 transition. The CO_2 enters the beamline, and is reflected off a rotate-able mirror before it intersects the beamline. This allows adjustment of the intersection angle (θ_{Int}) and thus change the Doppler tuning of the laser to give a way to scan through the energies of a given hydrogenic

transition and probe the energy level structure. After passing through the CO_2 beam, the beam enters the detector region. Upon entry of the detector there is a rectangular aperture to collimate the beam. This aperture is a 6mm in the vertical and 3mm in the horizontal direction. The signal ions are then Stark ionized. This is done in an electric field region that has a 4 plates spaced an inch apart constituting a 3" ramp down in voltage region, and another plate spaced an inch apart constituting a 1" ramp up in voltage region as seen in figure 2.2.

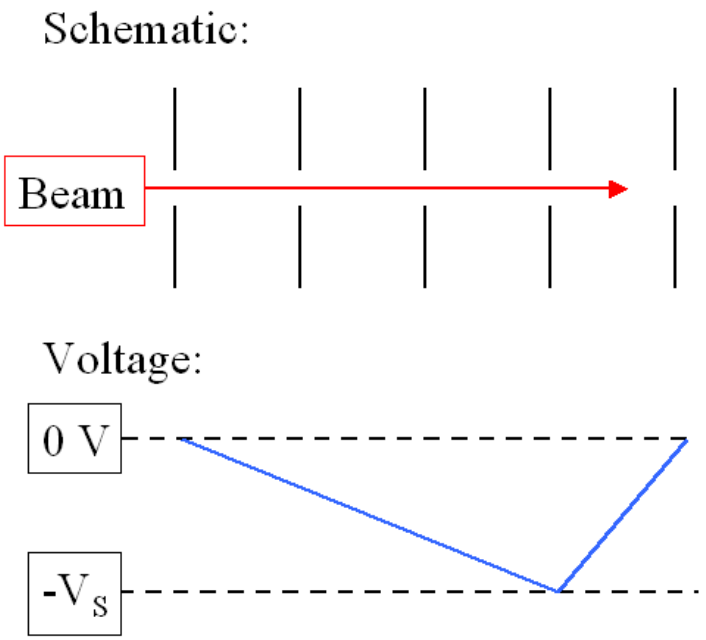

Figure 2.2: Schematic showing the Stark ionizer plates, and the potential present throughout.

The potential V_S is chosen so the electric field in the 1" region is large enough to Stark ionize all states within the upper state of the transition using equation 2.2. For the Th^{4+} the potential was 4.5 kV to fully ionize the n = 73 state. This means the electric field in the 3" ramp down region is 1/3 the field to Stark ionize the signal ions. This field is small enough to not ionize any of the n = 73 ions diabatically, but provides a field that can Stark ionize other higher n residual ions that may be present. It is also important to note that the Stark ionization happens at a negative potential that energy tags the signal ions so they can be separated from other ions of

the same charge that may be present. For the thorium experiment, the beam begins at 100 keV, but the signal ions would be slowed down by 4.5 keV meaning they are at 95.5 keV after the Stark ionizer.

The beam then passes through an aperture lens to help focus the beam. After the lens, the beam passes through horizontal and vertical deflector plates that allow the beam to be deflected upwards into a Channel Electron Multiplier (CEM) for detection. The CEM is offset vertically from the beam by 5.9" so any beams can be separated by their charge to velocity ratio. Since the signal ions have been energy tagged within the Stark ionizer, the potential to deflect them into the CEM should, in principal, be unique and separate them from other ions that are present. It is also worth noting that there is a beamviewer that is below the CEM, but above the beam by ~2.9". The beamviewer consists of a microchannel plate for amplification of the incident beam with secondary electron emission, and a phosphor screen that luminesces for detection [12]. The light from the phosphor screen can then be monitored with a camera to have a real time image of the cross-sectional view of the beams at the detector.

The RESIS apparatus just described was used successfully in the Th^{4+} studies conducted by previous graduate students Mark Hanni and Julie Keele.

2.2 Construction of New Stark Ionizer

In order to fully explore a few possible sources of background, as well as give a greater versatility in useable transitions, it was decided to redesign the Stark ionizer. In designing the new detector, there were a few requirements that needed to be met. The first requirement was versatility in the electric field that could be applied to Stark ionize the signal ions. Previously there was only a 1" (2.54 cm) gap to work with, and although the potential applied is variable there are experimental limits. The potential has to be large enough such that the energy tagging

of the signal ions is sufficient to separate the signal ions from the regenerated primary of the same charge. Also, much more than 8 kV can't be applied, otherwise there is the risk of arcing within the MHV vacuum feedthrough. For this reason only potentials from approximately 3 kV to 8 kV could be used for Stark ionization. Table 2.1 shows the range of *n* states that the previous Stark ionizer could ionize in the first row, and the states that could be ionized with a 0.5", 0.25", and 2.5" gaps in the lower rows. This means by designing a Stark ionizer that could give multiple gap lengths the versatility of the Stark ionizer could be increased significantly. Previously the only states that were able to be Stark ionized were *n* states from 93 to 120, while now *n* states from $n = 67$ to 151 can be Stark ionized.

This versatility is important in exploring the efficiency of the initial ionization that occurs within the repeller region. Within that region Rydberg states with high-*n* are ionized so that only states excited within the CO_2 laser will have high enough *n* values to be Stark ionized in the detector. The field applied within the Repeller is relatively fixed based on the velocity and terminal potential since those determine the optimal setting of the lenses for focusing. This means that if it is not clearing out low enough *n* states, the Repeller is contributing to the background, and this can't be explored by changing the field within the Repeller. The flexibility of the new Stark ionizer allows investigation into the completeness of depletion of states by the Repelling region. Since extremely high *n* states can now be seen, the difference in energy between states cleared out by the Repeller and those that are signal ions can be varied to really evaluate the effectiveness of the Repeller.

Table 2.1: Various Stark ionizer gap lengths and the resulting fields and range of ionizable *n* states of U^{5+} assuming the potential that can be applied is from 3 kV to 8 kV.

Stark Ionizer Gap Length	Range of Stark Ionization Fields	Range of Upper *n* States Ionizable
2.54 cm	1180 – 3150 V/cm	93 – 120
1.27 cm	2362 – 6300 V/cm	79 – 101
0.64 cm	4688 – 12500 V/cm	67 – 85
6.35 cm	472 – 1260 V/cm	118 – 151

A further requirement for the new Stark ionizer was versatility in the ramp down potentials length. The previous Stark ionizer was in a 3:1 ratio, that is to say the ramp down region was 3" and the ramp up region was 1". This ratio was chosen such that the ramp down electric field strength is small enough to not ionize any of the signal ions. This is not to say that this ratio is ideal. It was decided that having control over the ramp down length would be an advantage. For each Stark ionization length (0.25", 0.5", 1", 2.5") there was going to be available four times the ionization length for the ramp down region. This would provide a small enough field to ensure no adiabatic ionization would occur in the ramp down region. Adiabatic Stark ionization might take place at fields as small as $\frac{1}{16}\frac{Q^3}{n^4}$ a.u., and if even partial Stark ionization of the upper RESIS *n*-level occurred this way in the ramp down region, it could reduce the size of the energy-tagged ion signal. This did require a total Stark ionizer length of at least 12.5" to accommodate a 4:1 ratio and a 2.5" Stark ionization region. The final change was to install a better lens in the detector region. The previous aperture lens showed mediocre results, and going to an einzel lens might prove to provide better focusing.

With these considerations in mind, a new Stark ionizer was constructed. Figure 2.3 shows a schematic of the final design for what was dubbed the Super Long Gap Stark Ionizer (SLG) as well as the new einzel lens that is referred to as the detector lens.

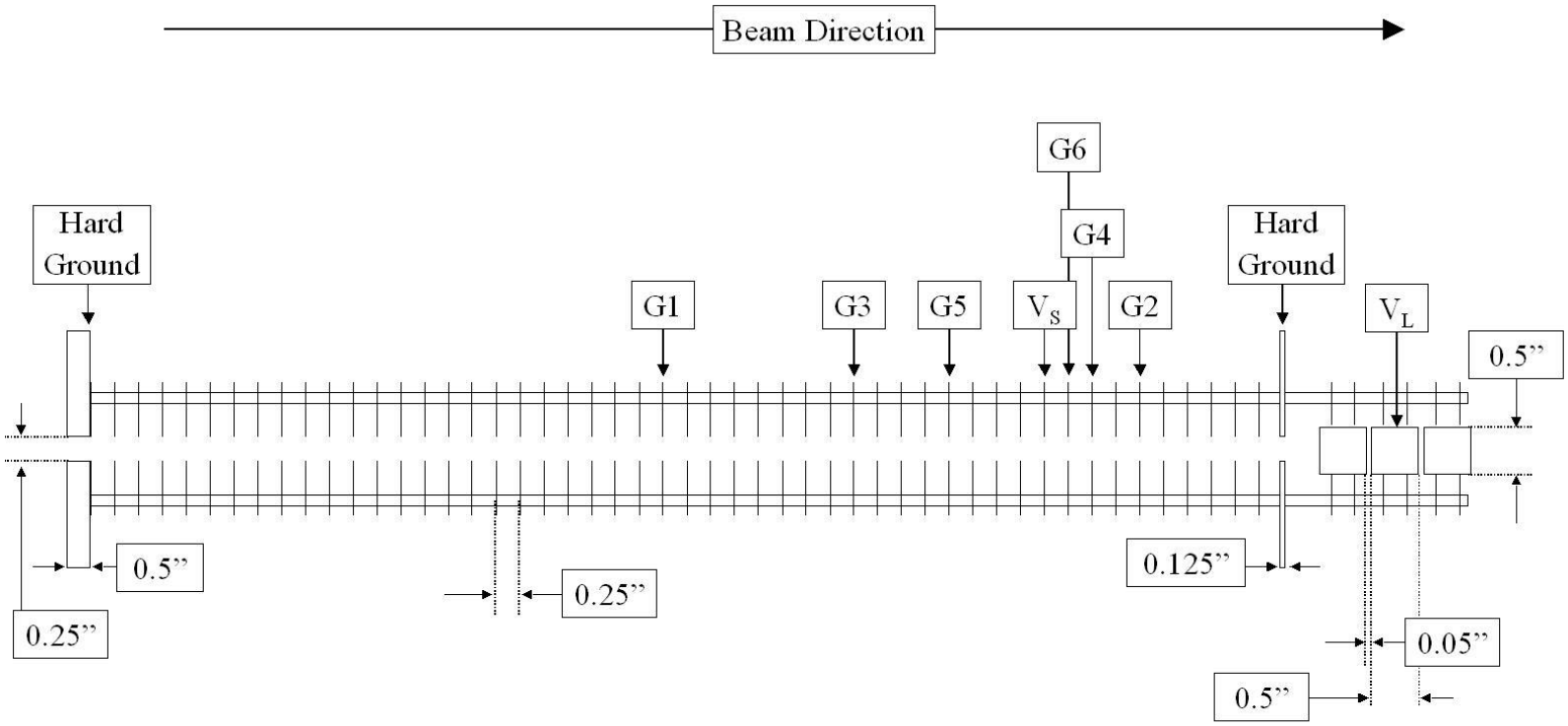

Figure 2.3: Schematic of the Super Long Gap Stark Ionizer (SLG) and the new einzel lens. Important distances are labeled, and the locations of feedthrough connections are labeled as G1 to G6 as well as the hard grounds. Where the Stark ionization potential (V_S) and the detector lens potential (V_L) are applied are also denoted.

It was constructed using mainly commercial parts from Kimball Physics Inc. The Stark ionization component of the Stark ionizer is 12.5" long comprised of 51 plates spaced by ¼". The plates were mainly from Kimball Physics of part number SS-PL-C5x5-R250. They are 1.4" square with a ¼" center hole surrounded by 1/8" holes for ceramic support rods in a square pattern around the center hole. For support, specialty ceramic rods were obtained from Ortech Inc. that when obtained were 24" long and an 1/8" thick, but the length was reduced to ~15.5" to accommodate support of the SLG and the einzel lens. The ceramic rods were at times too large to smoothly fit through the Kimball Physics support holes, at which point the support holes were filed open to accommodate the rods. In order to obtain uniform spacing, ¼" ceramic spacers of part number AL2O3-SP-C-250 were obtained from Kimball Physics and placed over the ceramic support rods between adjacent plates. Two custom plates were constructed in order to mount the structure to the to a 10" conflat end flange that using the same mounting system that was previously used and is detailed in Dan Fisher's dissertation [11]. These plates' dimensions are detailed in figure 2.4, but the hole pattern is the same as those plates acquired by Kimball Physics. These custom plates are attached with connectors to three ½" diameter steel support rods that are mounted directly to the 10" conflat flange. The steel support rods used for the previous Stark ionizer were no longer long enough to support the new SLG, so 7" extensions were added to the previous 12" long rods bringing the total length to 19". The extensions screw on to the previous rods.

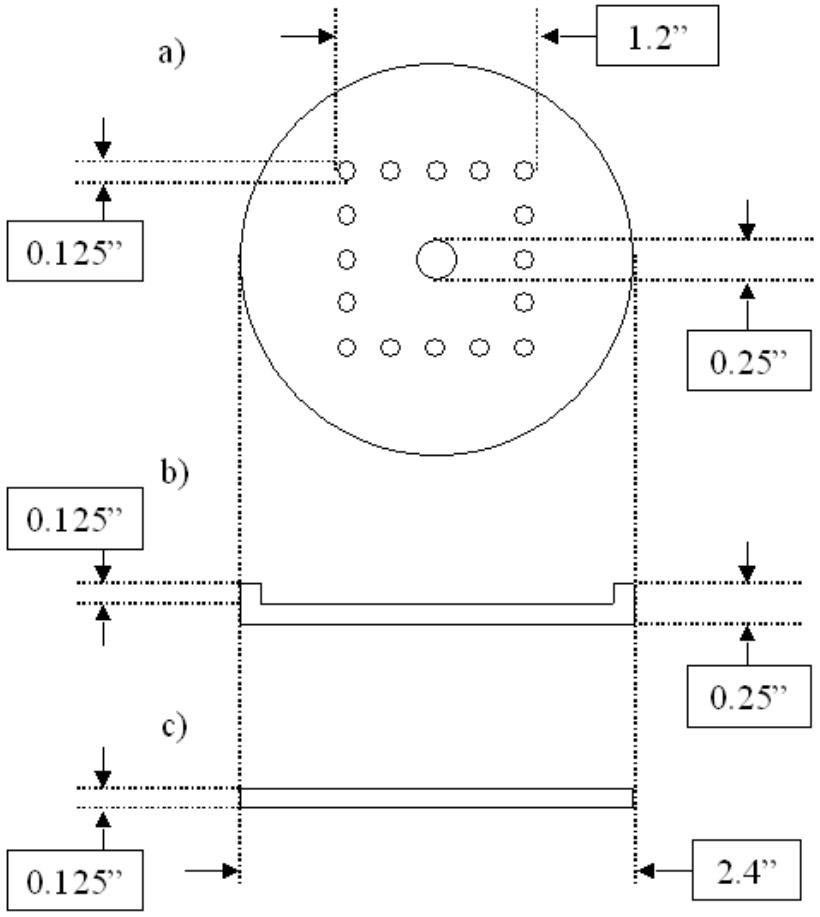

Figure 2.4: Schematic showing the dimensions of the two specialty plates used in the SLG construction. a) Looking along the beam axis showing the center hole where the beam passes, and the support rod holes. b) The horizontal crossectional view of the base plate (first plate seen by beam entering detector) and the lip that is around the plate. c) Horizontal view of the last plate in the SLG.

Each of the plates within the Stark ionizer is connected to the plates on either side with 1 Watt, 18 MΩ resistors. In order to set up the Stark ionizer in the scheme of choice, the Stark ionization voltage of choice is applied onto the same plate within the Stark ionizer, and then external shorts are used to ground plates on either side of the high voltage plate to determine the ramp down and up lengths. The locations of the feedthroughs are seen in figure 2.3 and are labeled as G1 through G6, and the Stark ionization feedthrough is labeled V_S. The resistors

between the plates means that the voltage on each plate is stepped down by an equal amount between each plate between the potential plate and the ground plate giving a relatively constant electric field. The U^{6+} n = 53 to 93 transition (requires ~3150 V/cm to ionize n = 93) can be used as a demonstration of how the Stark ionizer would be used. If –8000 V over a 1" gap is needed for Stark ionization, 8000 V would be applied to the V_S plate, the G2 plate would be grounded giving the proper field for ionization. There is then flexibility as to how long the ramp down region is. If a 4":1" ratio is wanted, the G1 plate is grounded, and if a 2":1" ratio is wanted, the G3 plate is grounded. This flexibility along with the flexibility of the Stark ionization length flexibility demonstrates the greatest strength of the SLG detector. Figure 2.5 demonstrates the potential versus position for the four possible Stark ionization lengths assuming a 4:1 ratio.

The detector lens is also detailed in figure 2.3, and consists of three steel cylinders acquired from Kimball Physics of part number SS-CY-500/500 that have a half inch diameter, and a half inch length. Each of these was welded by Bob Adame in the physics shop to two support plates also from Kimball Physics of part number SS-PL-C5x5-R500 which have the same support hole configuration, but a center hole with a half inch diameter to accommodate the steel cylinders. The plates were welded such that there was a 1/8" distance between the plate and the end of the cylinder. When the plates were then separated by a 0.25" and 0.05" ceramic spacers from Kimball Physics, then there would be a 0.05" gap between the cylinder edges. When the center cylinder is then put at potential, while the two end cylinders are hard grounded, then an einzel lens is created that can be used to focus the beam adjustably by changing the potential applied.

The 10" flange that supports the SLG also has four 2 ¾" conflat flange openings used for feedthroughs. Two of the openings contain 2 ¾" conflat flanges with four MHV feedthroughs.

One of these flanges is used for the horizontal and vertical deflector plates, while the other contains the feedthroughs for G3 through G6. Another of the flanges has two MHV feedthroughs used for G1 and G2. The last flange has two SHV-10 feedthroughs, one for the Stark ionization voltage, the other for the detector lens.

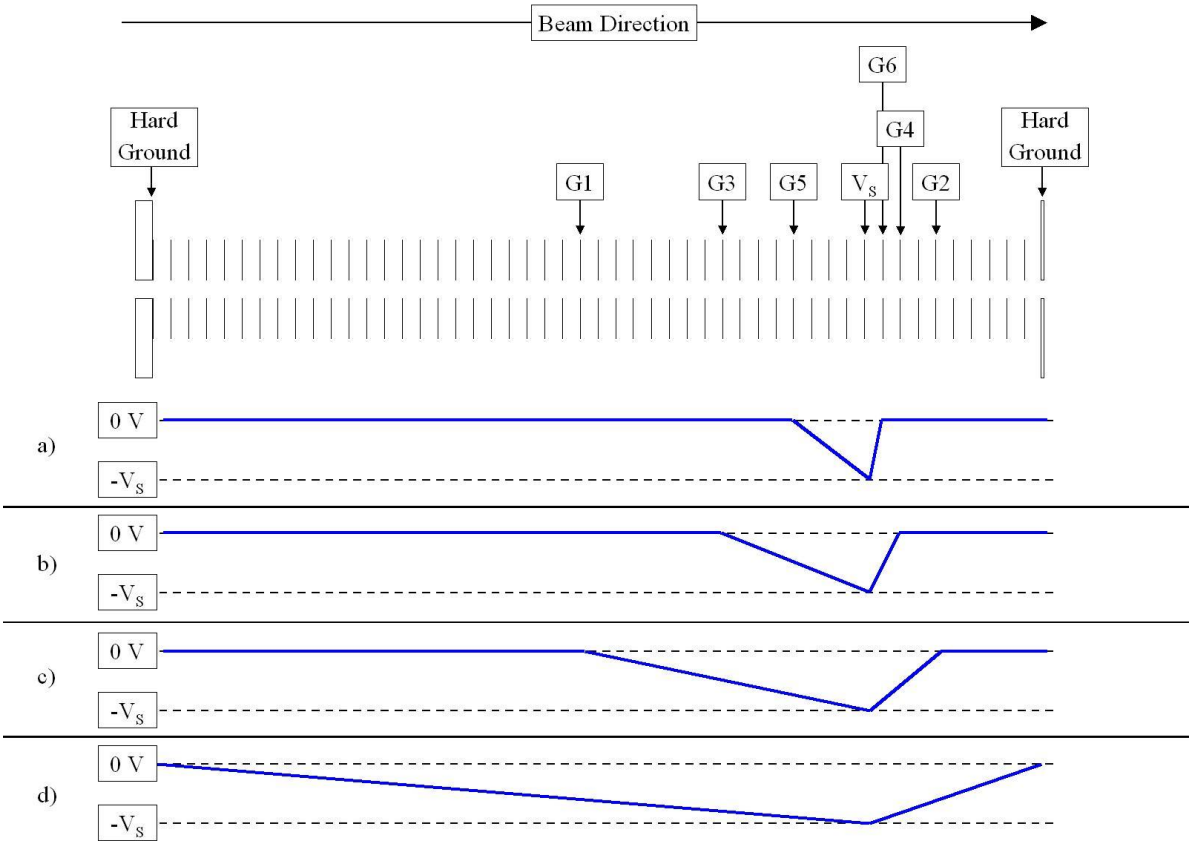

Figure 2.5: Schematic showing the voltage as a function of position along the SLG in the four configurations that have a 4:1 ramp down:ramp up ratio. a) Quarter inch Stark ionization gap with G5 and G6 grounded externally. b) Half inch Stark ionization gap with G3 and G4 grounded externally. c) One inch Stark ionization gap with G2 and G1 grounded externally. d) Two and a half-inch Stark ionization region with nothing grounded externally

Following the detector lens are the horizontal and vertical deflector plates. They are the same deflector plates that were used previously, but with the vertical deflector plates extended. The horizontal deflector plates come first, and are two SS-PL-C5x5-B (same as used for the Stark ionizer without the center hole) and are separated by ~0.6". These plates are attached to

support ceramic rods with standard Kimball Physics mounting brackets. After the horizontal deflector plates, there is the support plate that was previously used, and is very similar to the ones detailed in figure 2.5c, except with a different support hole schematic to accommodate the separation of plates desired. This plate holds the ceramic rods that the deflector plates are mounted to. It was mounted ~17.5" past the 10" conflat end plate that supports the structure. After the support plate are the vertical deflector plates which are very similar to the horizontal deflector plates, except they have a spacing of ~1.4". Previously the horizontal deflector plates were only two SS-PL-C5x5-B plates, making them 1.4" in length. They were modified by adding two more SS-PL-C5x5-B plates that were bolted directly to the original plates. This increased the vertical deflection length to 2.6". This is clearly seen in figure 2.6, which shows the deflector plates region. This additional length allows a greater angle of deflection to be reached to allow the beams to be deflected into the CEM even though the horizontal distance between the end of the vertical deflector plates and the CEM has been reduced by 12" (due to the longer Stark ionizer and lens). Previously the deflection angle required to be incident was about 9.6˚, but due to the lengthening of the detector, it is now about 19.1˚. The longer vertical deflection plates make this larger deflection angle possible without having to increase the deflection voltage to unrealistic values. A photograph of the complete detector region can be seen in figure 2.7.

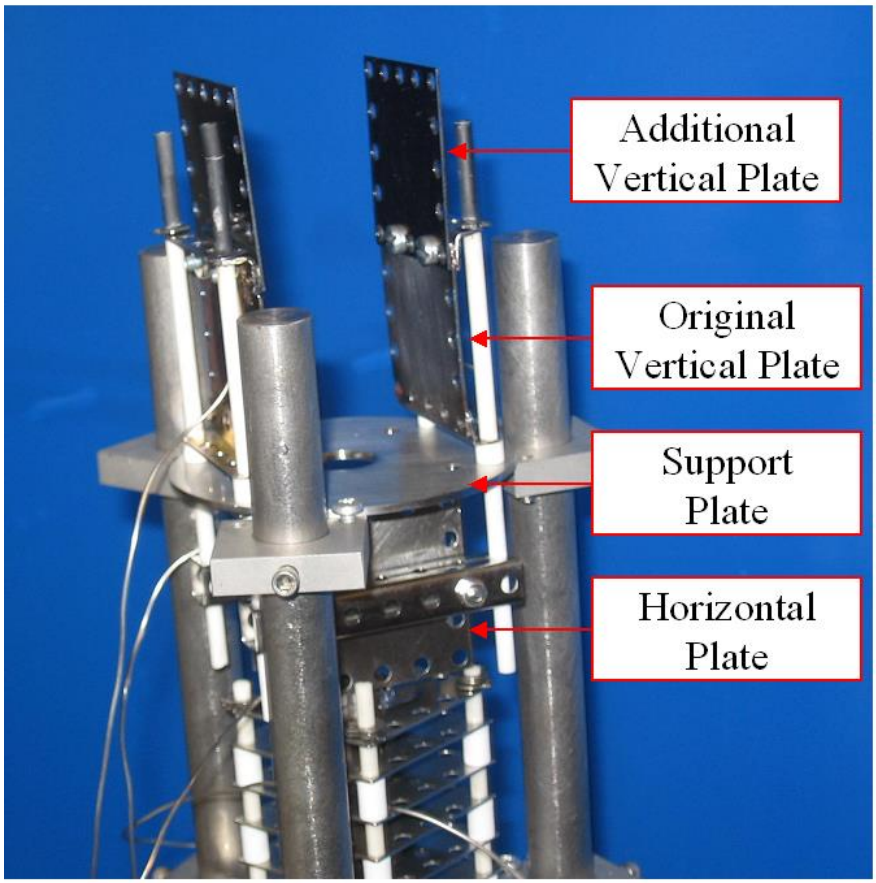

Figure 2.6: Photograph of the deflector plate region within the new detector. Labeled are the horizontal deflector plates, the support plate for mounting, and the original vertical deflector plates. The additional vertical deflector plates added to increase the vertical deflection are shown on top. Visible are the two bolts used to connect the new vertical deflection plates to the old ones.

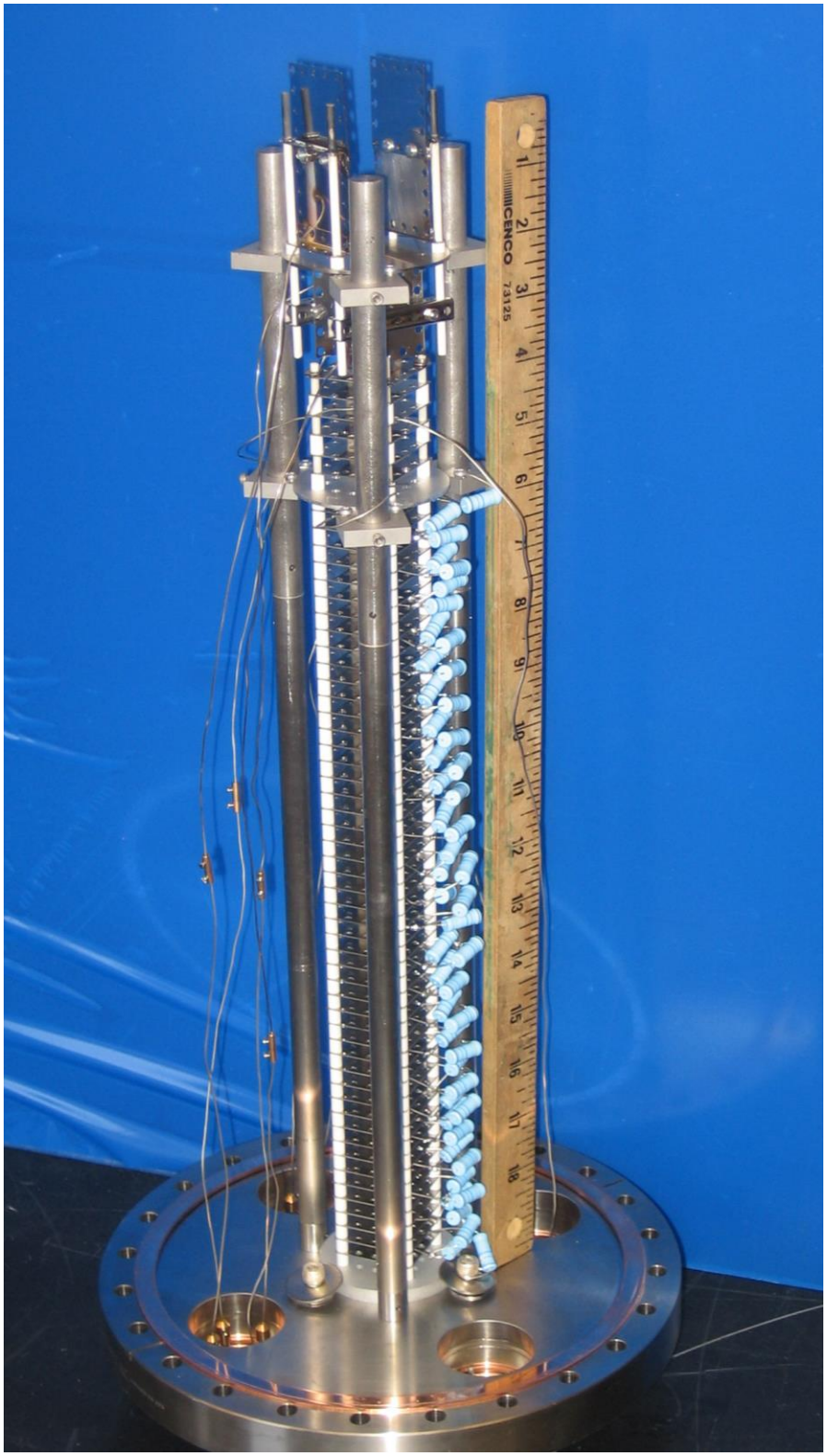

Figure 2.7: Photograph of the completed SLG Stark ionizer, detector lens, and horizontal and vertical deflector plates with a ruler for scale. Not all feedthrough wires were present for this photograph.

2.3 Construction of 10” Preionizer

The advantage of the flexibility of the SLG Stark ionizer also presents itself in unexpected ways. For instance, additional electric fields can be added before the Stark ionizer. This means new experiments can be designed that would require an electric field before the Stark ionization region, which weren’t possible before. The flexibility of the SLG Stark ionizer allows the addition of such a field easily. For reasons that will become clear later, the use of this electric field is referred to as preionization, and the apparatus is referred to as the 10” preionizer since it is within the 10” conflat detector region.

This addition of the electric field was easy, only requiring a different configuration than previous discussed to be used. This configuration, seen in figure 2.8, involves using a 2:1 ratio on the Stark ionizer with a 1” Stark ionization gap. This is achieved by grounding feedthroughs G3 and G2 and by applying the negative Stark ionization potential in the normal place. For preionization, a positive potential, $V_{10”}$, is then placed on the G1 feedthrough. This means there is then an electric field in the 8 inches from the initial entrance to the SLG to the grounded G3 plate that is at positive potential. For the U^{6+} n = 53 to 93 transition, as long as the potential applied to G1 is less than 8000 V none of the n = 93 levels will be Stark ionized in this region. The positive potential is an important distinction from the negative potential in the Stark ionization region because any autoionization that occurs within the positive potential region will be energy tagged with a positive energy and will be distinguished from the signal.

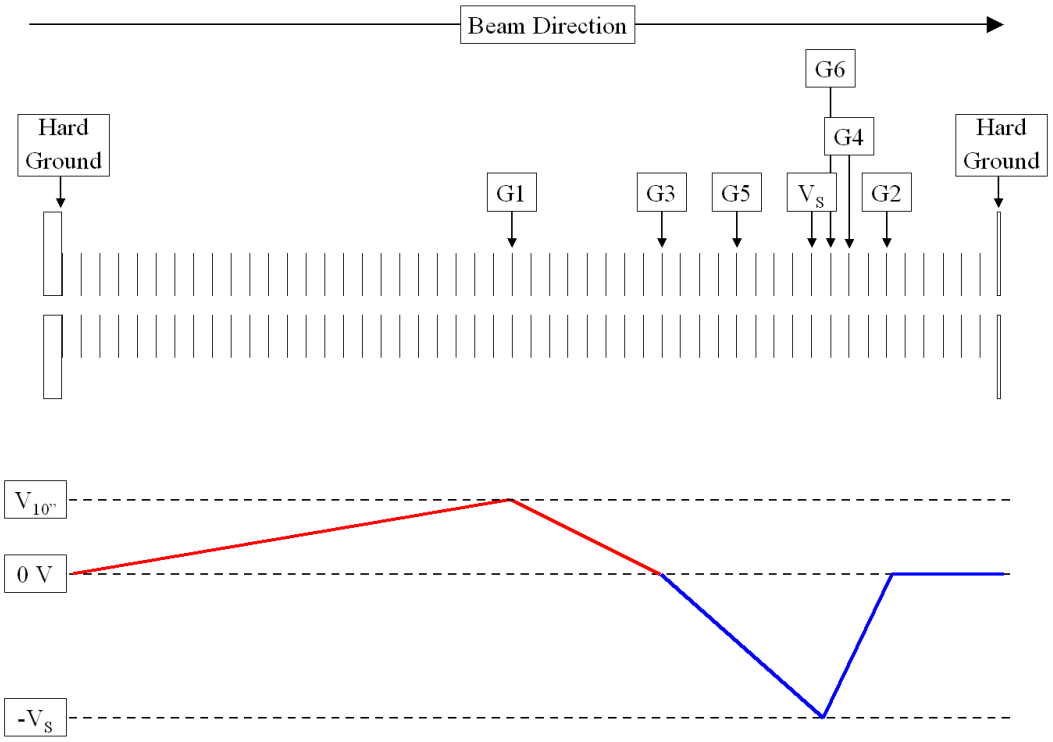

Figure 2.8: Schematic showing the electric potentials within the SLG when it is set up to have the 10" preionization region and then the Stark ionization region. The potential until the G3 plate is positive and corresponds to the preionization region. The potential from plate G3 to G2 corresponds to the Stark ionization region in a 2:1 ratio with a 1" ionization gap. The magnitude of $V_{10"}$ and V_S does not inherently have to be the same, so it was drawn where they were significantly different to emphasize this fact, but the ratio between them is variable and chosen during the experiment.

2.4 Design of the 6" Preionizer

After the successful tests of the 10" preionizer, it was decided to construct an additional preionizer region before the entrance to the detector. The second preionizer was dubbed the 6" preionizer since it is within 6" conflat components. The design of the 6" preionizer is very similar to that of the SLG, and is meant to maintain a large degree of flexibility to accommodate the variety of experiments wished to be carry out to try and understand the background within the RESIS technique. The 6" preionizer is supported by the same system used within the RF

region designed by Julie Keele and is detailed in her dissertation [13]. It is done by using two custom support pieces as seen in figure 2.9 that fit within a 6" conflat flange with three set screws to center it within the flange and mount it firmly. These two support pieces then have four support holes for ceramic rods that fit the pattern of Kimball Physics plates that are then used to apply the electric field to the region. The plates used for the 6" preionizer are 2" square of part number SS-PL-C7x7-B rather than the 1.4" square plates used in the 10" preionizer.

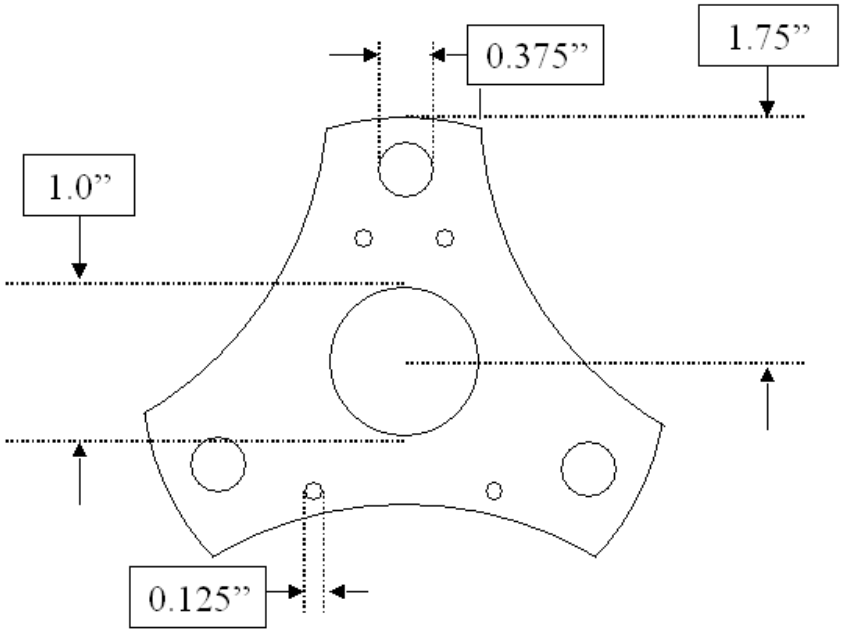

Figure 2.9: Custom built piece with a few key dimensions labeled. The 1/8" inch holes are placed to fit with the hole pattern in commercially acquired plates. The thickness of the plate is ¼".

A schematic of the 6" preionizer is seen in figure 2.10. The ceramic support rods are spare rods from the SLG Stark ionizer, except cut to ~10.25" in to fit the length desired. There are four support rods used in a trapezoid pattern seen with the 1/8" holes in figure 2.9. The rest of the plates are separated by a half inch using two quarter-inch ceramic spacers from Kimball Physics of part number AL2O3-SP-C-250. Each plate is connected to the plates on either side of it using the same 18 MΩ, 1 Watt resistors used within the SLG Stark ionizer. Since the support

plates are grounded to the conflat that they are connected to, these resistors allow varying potential to be placed on the plates with relatively few feedthroughs. That being said, in order to maintain flexibility, there are 8 feedthroughs so a large number of potential schemes can be used. The feedthroughs are every half-inch and are shown in figure 2.10. The 6" preionizer is housed within a 6-way conflat cross. The 6" preionizer is symmetric, but feedthrough 1 is upstream. The top flange of the 6-way cross contains an ion gauge for measuring pressure, the bottom flange contains a turbo pump. The two side flanges contain 6" to 2 ¾" conflat converter flanges, and then a 2 ¾" flange with 4 MHV feedthroughs on each side. One side contains the feedthroughs for F1, F3, F5, and F7, while the other side contains the feedthroughs for F2, F4, F6 and F8.

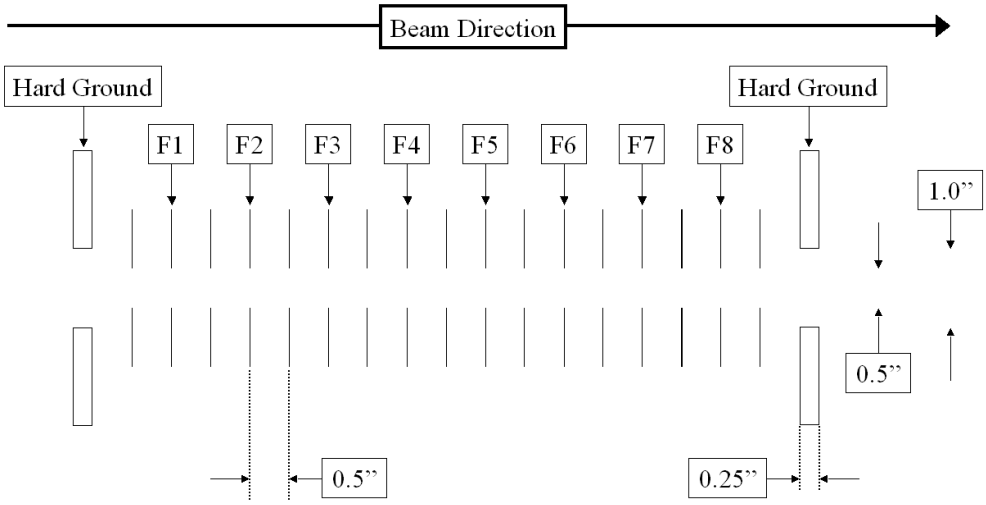

Figure 2.10: Schematic of the 6" preionizer. Feedthrough locations are labeled as F1 through F8. Important distances are labeled. Resistors connect adjacent plates (not shown).

2.5 Rydberg Target Region Pressure Reduction

The pressure within the beamline could be a source of concern when it comes to background creation within the experiment. If a redistribution of *n* states within the Rydberg beam due to collisions is causing some of the background, then the majority of it would most

likely happen in the Rydberg target region since its pressure is ~100 times higher than any other region. For this reason, reducing the pressure in this region became a goal, as well as isolate this region from the LIR region in order to improve the pressure of the beamline at large.

Figure 2.11 shows the previous location of the diffusion pump, and three turbo pumps used relative to the various parts of the beamline. The diffusion pump is mounted below the Rydberg target oven, and principally only pumps out the oven region. It is only able to pump out the beamline at large through the 2mm aperture that allows the Rubidium beam to be injected into the beamline. This means that the vast majority of pumping in the Rydberg target region is done by the turbo pumps downstream.

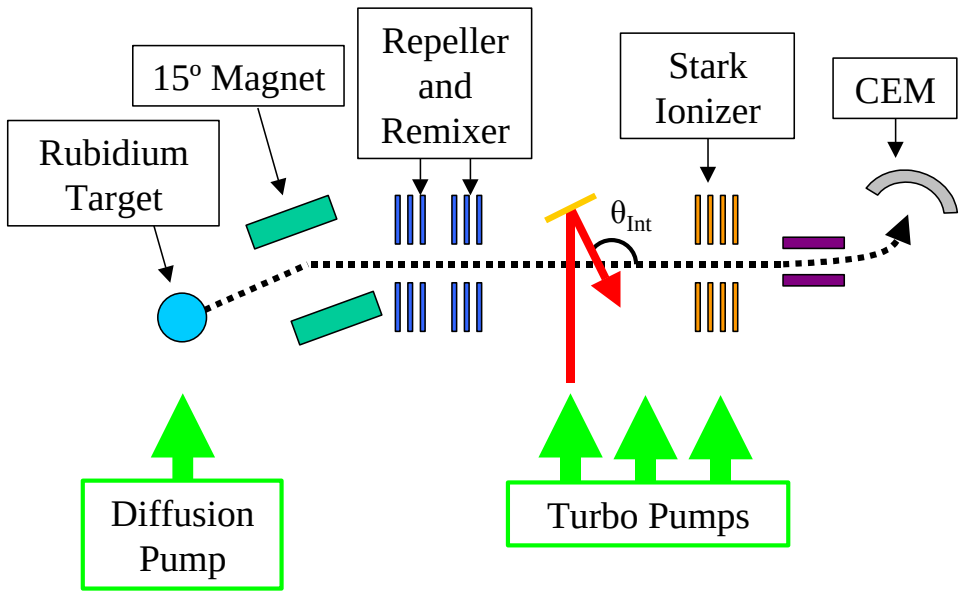

Figure 2.11: Schematic of the beamline showing the location of the four pumps relative to the components of the beamline. The diffusion pump is mounted directly below the Rydberg target. One turbo pump is directly below the LIR, one turbo pump is below the connection between the LIR and the detector, and the last turbo pump is directly below the Stark ionizer.

The main source of pressure within the beamline is residual Rubidium atoms that diffuse from the Rydberg target region. Since there was no separation between the Rydberg target and the LIR region, this Rubidium could diffuse relatively freely between the two regions, causing

the LIR regions pressure to be affected by the target region's pressure. This would result in typical pressures that were mid 10^{-6} Torr for the Rydberg target region, mid 10^{-7} Torr for the LIR region, and mid 10^{-8} Torr for the detector region. These could vary depending on how hot the oven was, but generally there was about an order of magnitude lower pressure between each successive region.

In order to increase the isolation between the Rydberg target region, and the repeller region, a custom built Dependex baffle was designed. A schematic of the baffle is seen in figure 2.12, but it is essentially a Dependex o-ring centering ring that only has a half inch inner diameter rather than the normal ~6" inner diameter. This was placed immediately after the 15˚ magnet, and before the 6" Dependex to 4" Dependex converter. This provides a relatively small aperture that should isolate the pressures between the two regions effectively. The exact location of the baffle is seen in figure 2.13.

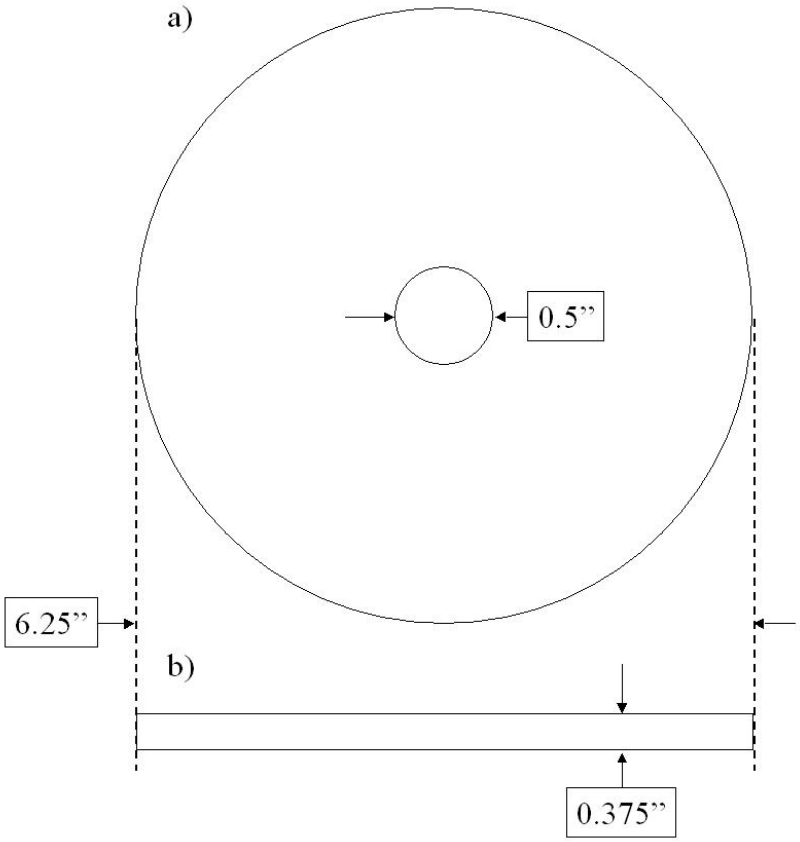

Figure 2.12: Schematic of the baffle used to isolate the Rydberg target region from the repeller region. a) Looking at the baffle as the beam sees it, and b) side view of baffle.

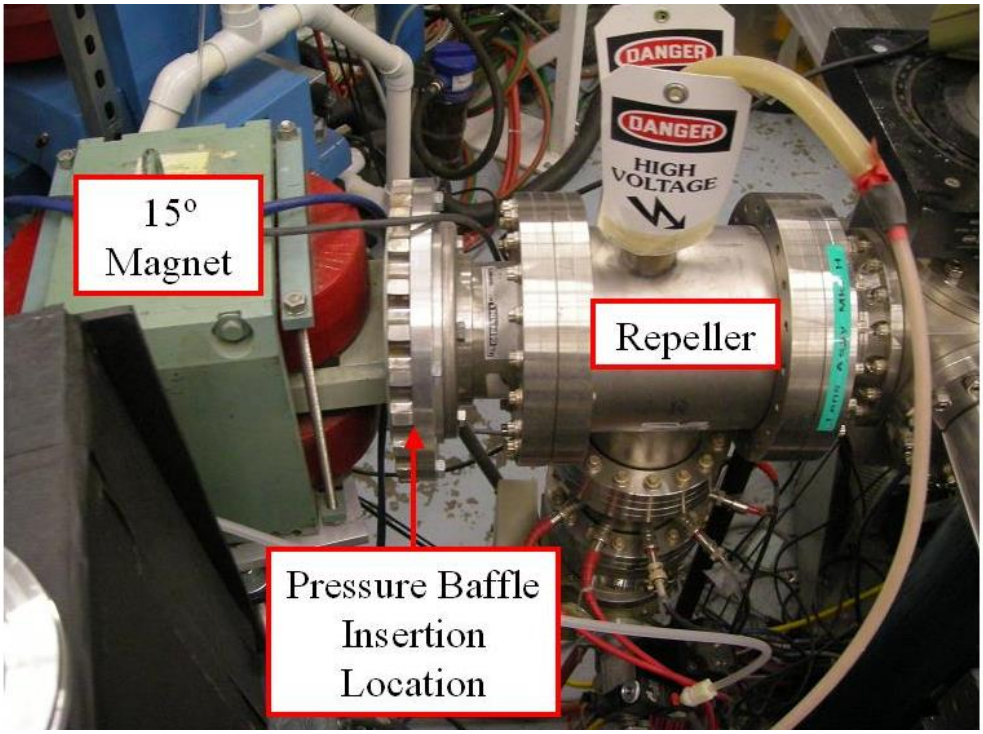

Figure 2.13: Location of the Pressure baffle used to isolate the Rydberg target region.

The baffle between the Rydberg target and LIR 1 region eliminated the effect of the turbo pump at LIR 1 on the Rydberg target pressure making it essential to add a pumping source directly at the Rydberg target. This was done by adding a turbo pump to the Rydberg target region. By adding a turbo pump specifically for the target region it was hoped to decrease the pressure in the region at large. To accommodate the turbo pump, a horizontal window was replaced by a 90˚ ISO100 elbow obtained from the Kurt J. Lesker Company of part number QF100-E90KR so a turbo ISO turbo pump could be mounted vertically. The turbo pump was on hand and provided by the J. R. McDonald facility.

The effectiveness of the baffle can be seen by looking at the ratio between the Rydberg target regions pressure and the LIR region pressure when the Rydberg target has been on for a while causing the Rydberg target regions pressure to be quite high. Table 2.2 shows the pressures and Table 2.3 shows the ratios in pressure in the day before installation of the baffle and the day after installation. The ratio of pressures between the RT and LIR regions is

magnified by a factor of 21 with the installation of the baffle, whereas the LIR compared to the detector doesn't change, indicating the effectiveness of the baffle in isolating the RT region.

Table 2.2: The pressures in the three regions of beamline before and after the baffle was inserted between the Rydberg target region and the LIR region. The pressures were taken after the Rydberg target was hot and therefore the Rydberg target regions pressure was relatively high.

	Pressure in Rydberg Target Region	Pressure in LIR Region	Pressure in Detector Region
Before Baffle Installation	4.1×10^{-5} Torr	1.1×10^{-5} Torr	2.8×10^{-6} Torr
After Baffle Installation	1.4×10^{-5} Torr	1.8×10^{-7} Torr	4.8×10^{-8} Torr

Table 2.3: Data showing the reduced ratio between the Rydberg Target (RT) region's pressure and the LIR region before and after installation of the baffle indicating increased isolation between the two regions. Also shown is the ratio between the LIR region's pressure and the Detector region's pressure to demonstrate relative consistency.

	Before Baffle Installation	After Baffle Installation	After Ratio/ Before Ratio
RT Pressure/ LIR Pressure	37	778	21
LIR Pressure/ Detector Pressure	3.9	3.8	0.97

The improvement in overall pressure can be seen in the average starting pressure in the four days before the installation of the new turbo pump compared to the average starting pressure in the four days after installation as seen in table 2.4. The starting pressure in the LIR is decreased by a factor of 6.2, and the pressure in the Rydberg target region is decreased by a factor of 2.7. This shows the increase in pumping ability that the newly installed turbo pump gains us. These two improvements to the pressure in the Rydberg target region should reduce any influence of collisions on the background.

Table 2.4: Data showing the decrease in pressure seen in the LIR region and the Rydberg Target (RT) region before and after installation of the turbo pump in the RT region.

	Before Turbo Pump Installation	After Turbo Pump Installation	Before Pressure/After Pressure
Average Pressure in LIR Region at Start of Day	2.9×10^{-7} Torr	0.47×10^{-7} Torr	6.2
Average Pressure in RT Region at Start of Day	5.3×10^{-6} Torr	1.95×10^{-6} Torr	2.7

Chapter 3: Overview of the Background

This chapter first serves to provide experimental evidence about the properties of the background. Possible explanations of this evidence will then be considered with the ultimate goal of creating a hypothesis that can explain all of the experimental evidence gathered.

3.1 Background Properties

There are many properties of the background that have been determined through various experimental studies. These properties are key to identifying the dominant source of the background.

1) The first observation is that the background comes from Rydberg states. This is easily determined by measuring the size of the background with the Rydberg target on and off. It has always been seen that when the Rydberg target has been turned off that the background goes away completely. This test is so simple that it was done virtually daily (if not more often), so the fact that the background comes from Rydberg states is extremely well established. Any explanation of the background must explain why a background is created when Rydberg states are present, and no background is created when there are no Rydberg states.

2) The second observation is that the background creation is concentrated at the full Stark ionization voltage, $-V_S$. If the ionization rate was constant throughout the Stark ionizer then there would be approximately equal amounts of energy tagged ions at all potentials between 0 and $-V_S$. Figure 3.1 shows a vertical deflection scan of the U^{6+} n = 53 to 93 transition at 150 keV. If the ionization was continuous throughout the Stark ionizer this would result in a plateau being seen from ~6.0 to 6.3 kV in figure 3.1. The fact that the amount of energy tagged counts decreases by more than order of magnitude between the regenerated primary and the signal

indicates that that there is a significant increase in background creation at the Stark ionization potential.

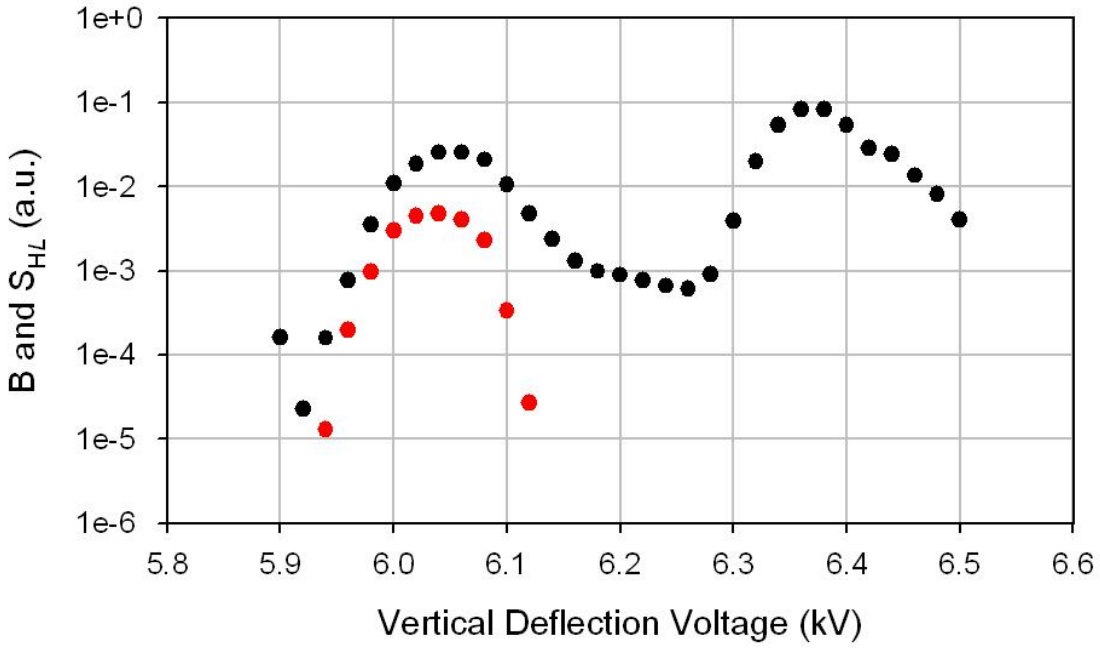

Figure 3.1: Vertical defection scan demonstrating the increased background production at the Stark ionization potential. The high-*L* signal is seen in red, and the B is in black. The peak in B around 6.38 kV is the regenerated primary, and the fact that a peak in B is seen at the signal location (6.05 kV) demonstrates the increased background production rate at the field flipping location.

Figure 3.2 is another visual of this phenomenon. It is a photo taken of the beams present on the beamviewer taken just before the vertical deflection scan in figure 3.1 was taken. The largest and brightest peak seen on the beamviewer is the regenerated primary, and the bright signal that is only partially resolved from the regenerated primary corresponds to ions that were positively energy tagged within the metastable preionizers. The relatively dim peak above the regenerated primary is the background. It is clearly separated from the regenerated primary, and it is clear that there is a lot of background created at the peak voltage within the Stark ionizer (at the field flip), but little to none seen between the regenerated primary and the background peak.

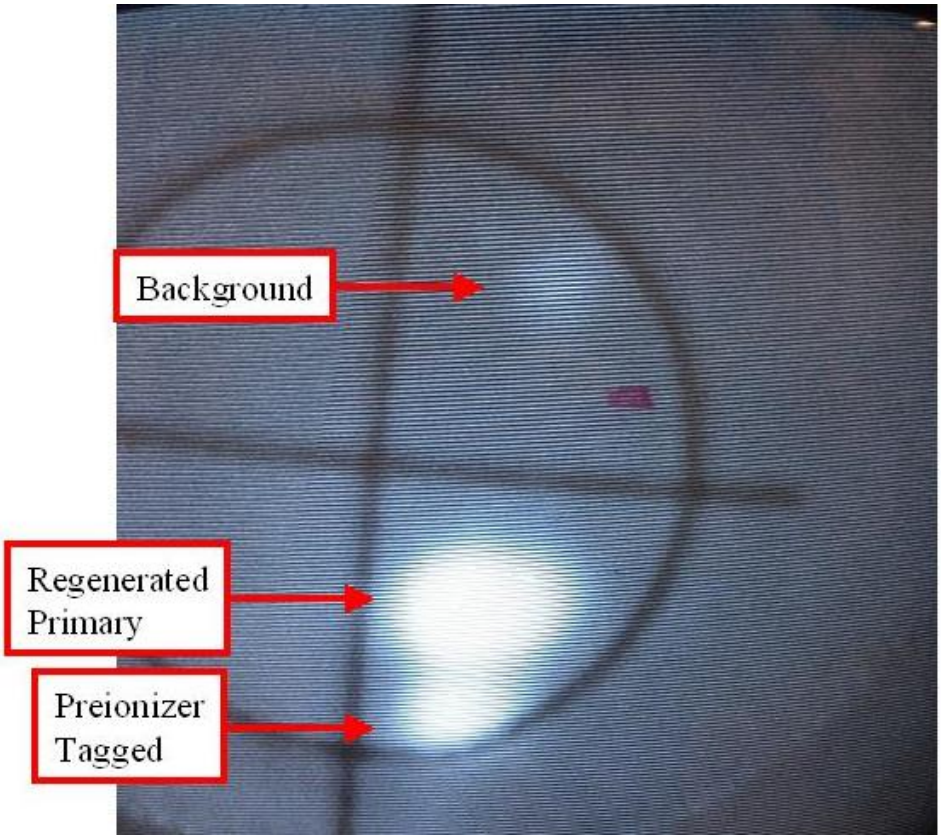

Figure 3.2: Photo of the beamviewer showing the regenerated primary, energy tagged preionized ions, and the background created at the signal. The isolation of the background peak from the regenerated primary indicates that the creation of background is isolated at the peak voltage within the Stark ionizer.

This indicates that there is an increase in background production at the peak potential, or equivalently, at the field flip within the Stark ionizer. Any hypothesis for the source of the background must explain why the production of background is concentrated at the peak potential in the Stark ionizer (same location as the electric field flip).

3) The third observation is that the size of the background is dependent on the geometry of the Stark ionizer. With the installation of the super long gap Stark ionizer, a wide range of Stark ionizer schemes could be tested. Table 3.1 shows the background size for three Stark ionizer schemes. Clearly seen is the increased size of the background as the Stark ionization region becomes larger. This is dramatically seen with the background becoming

approximately 15 times larger with the longest Stark ionizer compared to the shortest. Once again, this observation must be explained to have confidence in the hypothesis about the background.

Table 3.1: Data showing the background normalized to the high-*L* signal versus the field size in the repeller versus the field size in the Stark ionizer. The first column is the transition, the second column is the Stark ionizer schematic used, the third column is the electric field in the Stark ionizer, and the last column is the background compared to the high-*L* signal.

Transition	Stark Ionizer Schematic	$E_{\text{Stark Ionizer}}$ (V/cm)	B/S_{HL}
U^{6+} 150 keV n = 55 to 123	2.5":10"	1024	46.3
U^{6+} 150 keV n = 53 to 93	1":4"	3150	6.11
U^{6+} 150 keV n = 53 to 93	0.5":2"	4724	2.95

4) The fourth observation is that the background is relatively independent of the system pressure. Figure 3.3 shows the high-*L* signal and background size for the U^{5+} n = 45 to 85 transition at 125 keV. The high-*L* signal was monitored after all three turbo pumps in the beamline were turned off to raise the pressures in the beamline more than an order of magnitude throughout the beamline. The background does change with the pressure, but not more than a factor of two, while the pressure changed by a factor of 25. The signal experiencing a greater effect, and gets smaller by ~4 over the same pressure range. The fact that the signal goes down faster than the background as the pressure gets higher means the background/signal gets higher with higher pressure. The background to signal gets worse with higher pressure, but only by a factor of 2 over the 25 times higher pressure. This leads to the conclusion that the pressure can affect the background and signal, but relatively minimally over pressure changes that are reasonable in physical situations.

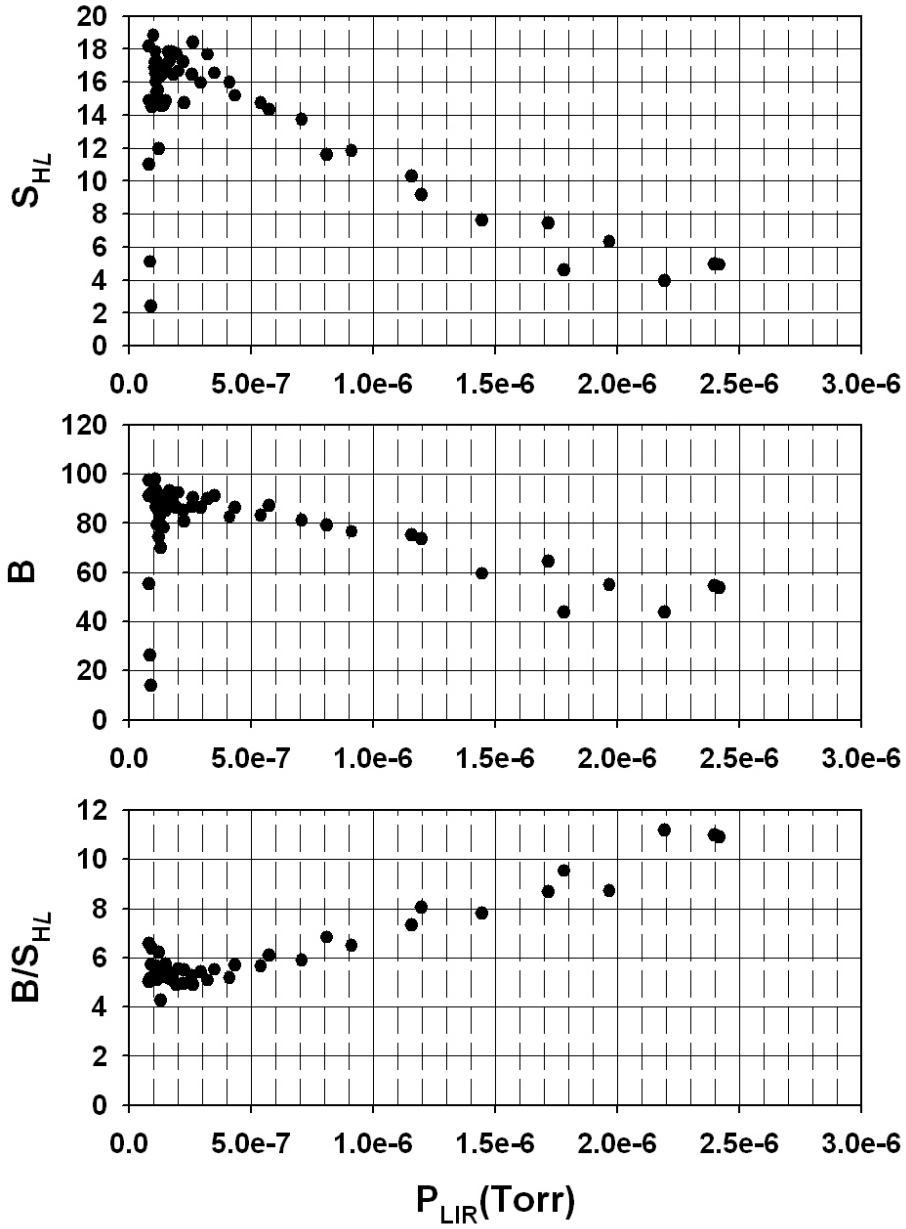

Figure 3.3: The background and the high-*L* signal for the U^{5+} n = 45 to 85 transition at 125 keV versus the pressure measured in the LIR region in Torr. All turbo pumps were turned off to raise the pressure, then turned back on to ensure the signal went back to where it was to start. The top graph is the high-*L* signal versus the LIR pressure, the middle graph is the background size versus the LIR pressure, and the bottom graph is the background over the high-*L* signal versus the LIR pressure.

5) The fifth observation is that the background is not dependent on the system temperature. Other than a cold trap above the Rydberg target, the beamline is kept at room

temperature. This means by and large the beamline is at room temperature, and the temperature is not regulated. An experiment was designed to determine how the temperature affects the background.

Modifications were made to the detector region that allowed for cooling to occur below the Stark ionization apparatus. It consisted of a 5" by 7" plate mounted about 2" below the beam axis. This plate was then thermally connected to a liquid nitrogen trap mounted below the detector region. This allows this plate to be cooled to liquid nitrogen temperatures. This plate was then placed at liquid nitrogen temperature and allowed to heat back up to room temperature while the B/S_{HL} for the Xe^{6+} at 150 keV n = 53 to 92 transition. Figure 3.4 shows the B/S_{HL} versus the temperature measured within the cold trap with the assumption that the trap temperature and the plate temperature are approximately equal.

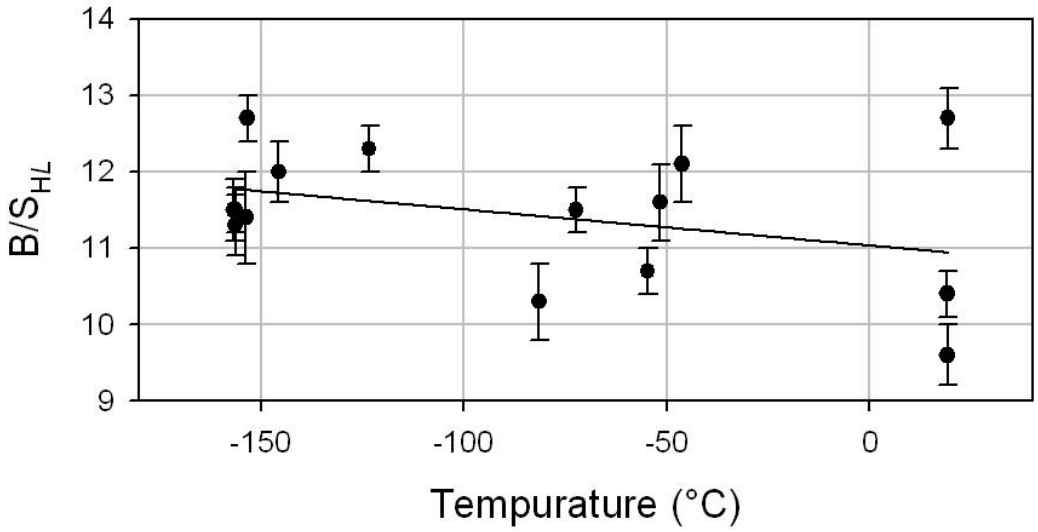

Figure 3.4: The background compared to the high-L signal versus the temperature of the plate mounted below the Stark ionizer. The transition used was the Xe^{6+} at 150 keV n = 53 to 92 transition. The fitted line had a slope = -0.0047(33) and an intercept = 11.03(36).

The data in figure 3.4 was fit with a line found to have a slope = -0.0047(33). This is easily consistent with 0, which would be expected if the temperature had no effect on the production of background. This drastic change of temperature below the Stark ionization region

had no effect on the background. This leads to the conclusion that the background size is independent of the detector temperature.

6) The sixth observation is that the background is proportional to the size of the charge capture from the Rydberg target (CXRT). One way this was observed is by monitoring the background, high-*L* signal, and CXRT as the Rydberg target heated up at the start of the day. The CXRT can change orders of magnitude at the start of the day from the first time the signal is measured till an equilibrium is reached. Figure 3.5 shows the background for the U^{6+} $n = 53$ to 93 transition at 150 keV as the Rydberg target heats up at the start of data collection. When figure 3.5a and 3.5b are compared it is obvious that the background is directly proportional to the charge capture from the Rydberg target since they are virtually identical. Also shown is the ratio of background to signal to show that this ratio is essentially constant. This analysis leads to the conclusion that the background is in fact proportional to the CXRT.

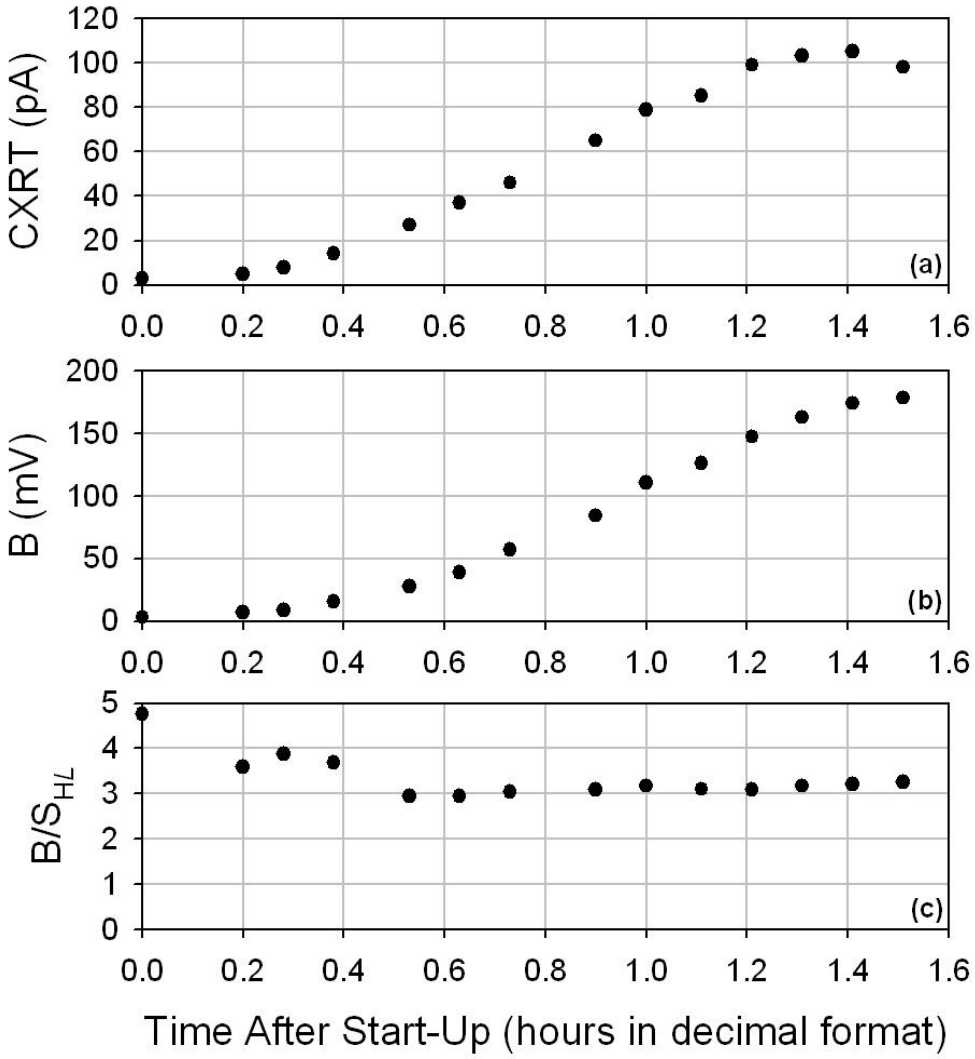

Figure 3.5: Data looking at the background (B) versus the charge capture from the Rydberg target (CXRT) at the start of data collection. Graph a) shows the CXRT versus the time (in decimal format). Graph b) is the background versus the time, and graph c shows the background over the high-*L* signal versus time.

7) The seventh observation is that the background is insensitive to the ratio of the electric field in the repeller (E_R) over the electric field in the Stark ionizer (E_S). Figure 3.6 shows a test done on the 90 keV $n = 50$ to 89 transition of Xe^{6+}. Sitting on the high-*L* signal, and keeping the repeller voltage constant. This allowed the background normalized to the signal to be studied versus E_R/E_S. There is little overall trend, if anything it appears to be increasing as the Stark ionization voltage goes down. This is due to incomplete separation from the regenerated

primary. This is most drastically seen with the point at E_R/E_S of ~2.2, which clearly has a very large background. The other points show little trend, and there is little reason to the E_R/E_S ratio has an affect on the background.

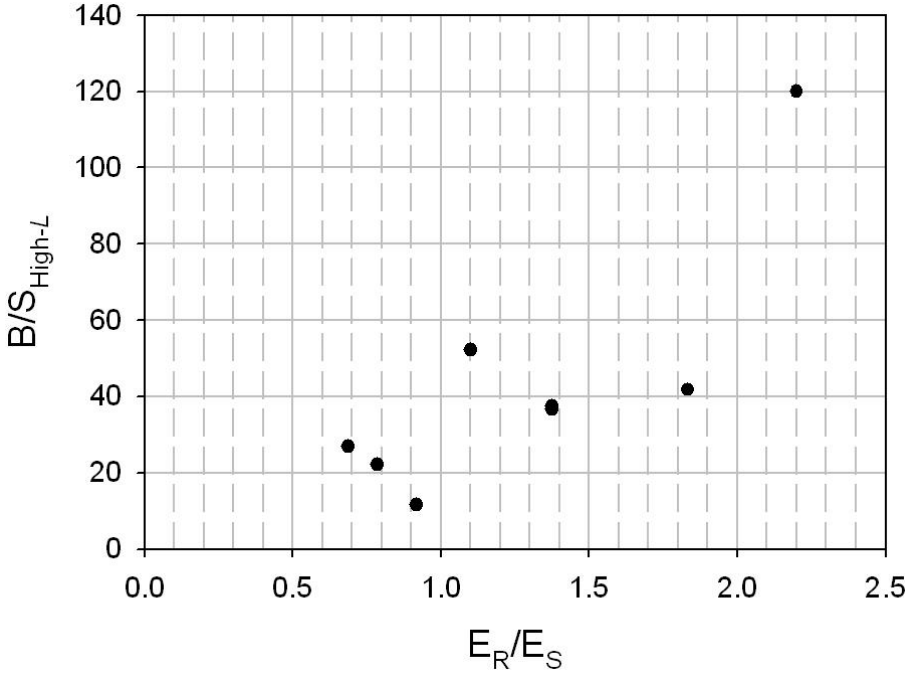

Figure 3.6: Data looking at the background (B) normalized to the high-*L* signal size versus the ratio of the repeller field to the Stark ionization field (E_R/E_S).

8) The eighth observation is that the background is reduced with the preionizers that were described in the last chapter. This is easily demonstrated with a typical scan where the background was monitored as a function of the potential on the 10" preionizer ($V_{10"}$). Figure 3.7 shows the background versus $V_{10"}$ for the U^{5+} n = 44 to 76 transition at 125 keV. The 10" preionizer clearly reduces the background compared to the signal even with small potentials applied. Even at just 2 kV on the 10" preionizer the background is decreased by a factor of approximately 2.4. The largest electric field within the 10" preionizer when 2 kV is applied to it is about 260 V/cm. This is a sixteenth the field for Stark ionization of the signal, and an eighth the field size in the ramp down region. This means even a small electric field applied to the

beam before detection has large effects on the size of the background. This phenomenon was observed for a range of transitions in U^{6+}, as well as several other ions (U^{5+}, Th^{3+}. Th^{4+}, Xe^{6+}, Pb^{2+}, Pb^{4+}). This makes it clear that the preionizers reduce the size of the background, and at small fields.

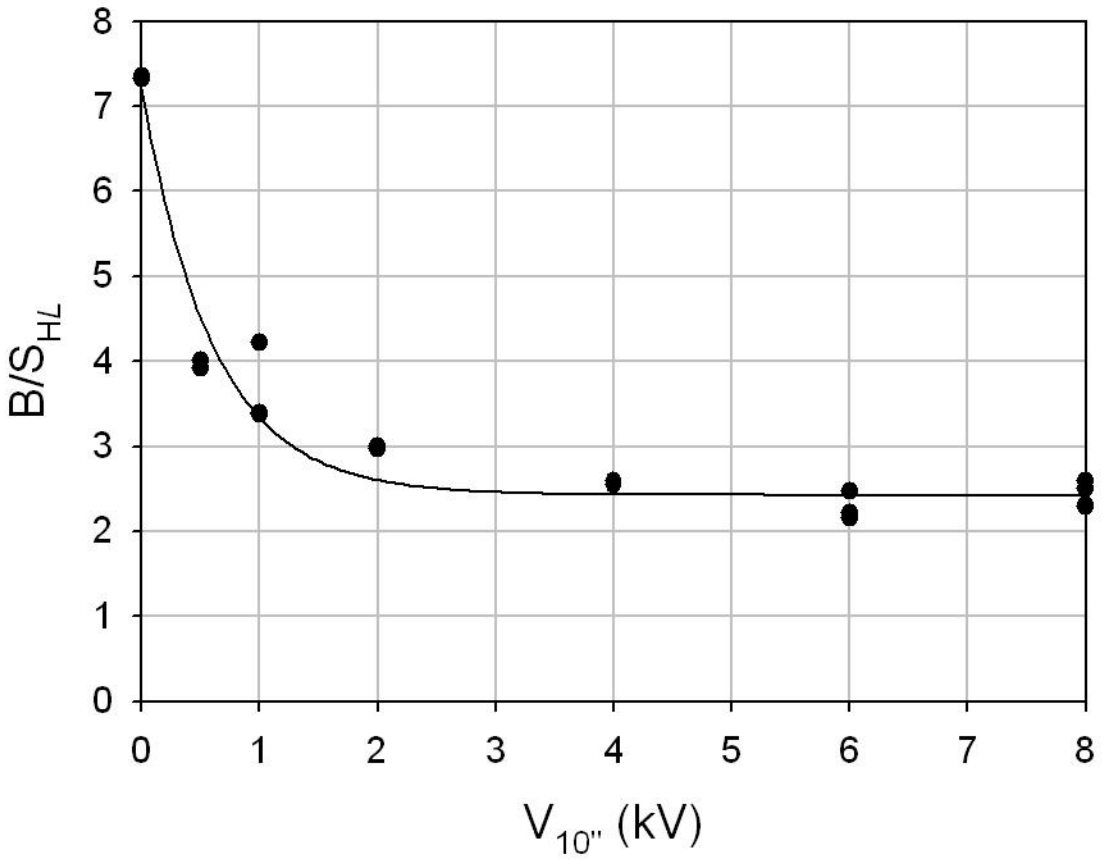

Figure 3.7: The background compared to the high-*L* signal for the U^{5+} n = 44 to 76 transition at 125 keV versus the voltage applied to the 10" preionizer ($V_{10"}$). The exponential fit is to guide the eye.

9) The ninth (and final) observation is that the size of the background is insensitive to the size of the entrance aperture to the detector. The aperture at the entrance to the detector is generally the smallest aperture in the detector. As mentioned in chapter 2, there was a 6mm by 3mm aperture at the entrance to the detector for the first U^{6+} experiment to colimate the beam. To experimentally check if the background was dependent to the beam size entering the detector,

a 1/8" diameter circular aperture was used instead. This reduced the size of the aperture by a factor of ~2 in the vertical. There was no change seen in the background size after this installation was made. After this observation no entrance aperture was used (and was the standard for most of the current work) which means the tiniest aperture was from the detector plates themselves (¼" aperture).

These nine observations give a range of properties now known about the background. Ideally, a hypothesis that explains the dominant source of the background would also explain these observations. At the very least, any hypothesis about the dominant source of the background can't provide predictions that are contrary to the observations described. To recap, these observations are:

1) The background comes from Rydberg states.
2) The creation of background is concentrated at the peak Stark ionization field flip (same location as electric field direction flip).
3) The size of the background is dependent on the geometry of the Stark ionizer.
4) The background is independent of the system pressure.
5) The background is independent of the system temperature.
6) The background is directly proportional to the CXRT.
7) The background is insensitive to the ratio of the repeller's electric field over the Stark ionizer's electric field (E_R/E_S).
8) The preionizers reduce the background with small fields.
9) The background is insensitive to the aperture size at the entrance to the detector.

These observations give a range of properties about the background that allow hypotheses to be tested by determining if they explain these properties. The next section will analyze

several hypotheses that have been created in an attempt to explain the presence of the background, and determine if they hold up under scrutiny of attempting to explain these observations.

3.2 Background Creation Mechanisms

Several possible mechanisms of the creation of the background need to be addressed. These mechanisms can be laid out into four categories:

A) Stark ionization of Rydberg states
   i) Rydberg states that are left over after the Repeller
   ii) Rydberg states that were excited to higher-*n* states by collisions
   iii) Rydberg states that were excited to higher-*n* states by blackbody radiation

B) Direct ionization within the Stark ionizer
   i) Ionization by collisions
   ii) Ionization by Rydberg-Rydberg collisions
   iii) Ionization by blackbody radiation
   iv) Ionization by slow moving electrons trapped in the space charge potential of the beam

C) Edge ionization in the Stark ionizer

D) Autoionization of metastable Rydberg states

The first category of mechanism is the Stark ionization of Rydberg states within the Stark ionization field that are not the signal. The RESIS technique is set up such that the repeller should ionize any Rydberg states that are bound weakly enough to be ionized in the Stark ionization field. In the case of U^{6+}, the repeller would ionize Rydberg states with $n > 84$. The

signal ions are then excited to $n \sim 93$ after the beam has passed through the repeller. The Stark ionizer is set to ionize the signal ions, and since the repeller ionized every other Rydberg state with an n state as large as the signal ion, then only the signal ion should ionize in the detector. If however, some high-n Rydberg states existed at the Stark ionizer that are not signal ions then they would show up as background.

This category of hypothesis can be compared to the observations laid out in the last section. One obvious advantage to all the hypotheses in category A is that it would easily explain why the background is centered at V_S. One large problem with this category of hypothesis is that the background is insensitive to the ratio E_R/E_S. If the repeller Stark ionizes states much lower than the states ionized in the detector, then fewer states will be present at the detector to be Stark ionized. This is true whether the high-n states come from being excited by collisions, blackbody radiation, or are just left over from the repeller.

A major problem with all of these hypotheses in category A is observation 8, which is that small electric fields before the detector reduces the background. As described in the last section, the fields needed to reduce the background in the preionizers are quite small, with only 260 V/cm decreasing the background by a factor of 2.4. An electric field strength of 260 V/cm would Stark ionize only Rydberg states with $n \geq 181$ for U^{6+}. Even in the unlikely event that states of this type were present at the entrance to the detector, they would certainly Stark ionize in the ramp down field and could not contribute to the energy tagged background.

Although the first hypothesis for Stark ionization of Rydberg states seems unlikely, there are still two ways Rydberg states could make it to the detector: Excitation by collision, and excitation by blackbody radiation. Both of these revolve around the idea that Rydberg states are in fact cleared out as expected by the repeller, but then states that pass through the repeller ($n \leq$

83 for U^{6+}) are excited to higher *n* states that could ionize in the Stark ionizer. Neither of these could explain why the preionizers work (observation 8). In addition, the two specific excitation sources in Aii) and Aiii) are ruled out by observations 4) and 5) respectively.

All of the previous analysis about the properties of the background rules out the possibility of Stark ionization of Rydberg states. The next set of hypotheses are similar, but revolve around Rydberg states being directly ionized. These hypotheses have problems when it comes to describing the observations related to the Stark ionizer. They don't explain why the background would be concentrated at the peak Stark ionization voltage. All of these processes have the property of having a relatively constant ionization rate throughout the beamline, and the Stark ionizer would not alter that since it is no different from other parts of the beamline as far as these hypotheses are concerned. Therefore, the ionization would be uniform throughout the Stark ionizer and no peak in background would be seen at the Stark ionization voltage. Observation 2 rules out all hypotheses in this category. In addition, the two hypotheses Bi) and Biii) are further ruled out by observations 4) and 5). Hypotheses Bii) and Biv) are further ruled out by observation 6, since both of these would be proportional to a higher power of CXRT.

Hypothesis C is that Rydberg states could ionize due to their proximity to the edge of apertures within the Stark ionizer. This would occur when electric field from the image charge from the Rydberg ion creates a field large enough to ionize the Rydberg ion itself. If this were the case then the background should be dependent on the dimensions of the beam as it enters the detector. This however is not the case, as demonstrated by observation 9. When the size of the aperture to the detector was varied, no change in the background was seen. Another major problem with this hypothesis is Observation 2. Hypothesis C would require a majority of the Rydberg states that ionize in the detector to pass through ~40 apertures only to ionize at the one

aperture where the signal ions ionize. This is extremely hard to explain. All of this appears to eliminate this hypothesis.

The final hypothesis, D, is autoionization of metastable Rydberg states. A metastable state is one in which the core ion is not in its electronic ground state. Once a Rydberg electron is added to this excited core, there is a decay channel for this state making it metastable. This would happen when the excited core de-excites, transferring energy to the Rydberg electron and moving it to a continuum state. This process would cause autoionization throughout the beamline, which would explain the regenerated primary. Some of this autoionization might happen within the Stark ionizer, which would produce the energy tagged background. There easily could be metastable states coming from the ion source since core ions could be excited in the hot conditions of the ion source.

This hypothesis is fully consistent with observations 1, 4, 5, 6, 7, and 9, but not obviously with observations 2, 3, and 8. Also, since there is a large amount of ionization that occurs before the detector to form the regenerated primary, it seems very likely that autoionization of metastable states does occur in the experiment. All of these support the metastable autoionization hypothesis, but there still observations 2, 3, and 8 to explain. Observation 2 is that the background is concentrated at the electric field flip in the Stark ionizer. Observation 3 is that the background creation rate is dependent on the geometry of the Stark ionizer. Observation 8 is that the preionizers decrease the size of the background. The metastable hypothesis must explain these properties to be accepted as correct.

A detailed analysis of the metastable autoionization hypothesis, carried out in the next chapter, will show that it is consistent with these last three observations.

Chapter 4: Metastable Autoionization as Source of Background

The last chapter discussed various properties of the background, and discussed several possible explanations of the background. The autoionization of metastable states appears to be the most likely explanation of the background. This chapter will provide a theoretical basis that explains some of the observations detailed in the last chapter that are not obviously explained by metastable autoionization.

The Rydberg ions in the beamline can be broken into two categories that will be considered within this chapter. The first is autoionizable metastable states, which are all metastable states that have a channel to autoionize. The second are ions that can't autoionize. The ground state ions clearly fit in this category, but there could in principle metastable states that are forbidden to autoionize. The focus of this chapter is on the first category of ion, metastable states that can autoionize, and when metastable states are referenced it will mean metastable states that can autoionize unless stated otherwise.

4.1 Predicting U^{6+} Metastable Autoionization Rates

One important detail in the metastable autoionization hypothesis is the actual autoionization rates of these states. This is a crucial prediction that needs to be made to determine if this hypothesis can be correct. For instance, if the longest lived metastable state is on the order of femtoseconds, it is extremely unlike any metastable states would survive the microseconds it takes to get from the target to the detector. Even knowing the order of magnitude can therefore be a first test of this hypothesis. With this in mind, the calculations

involved in determining the autoionization rates will be discussed, followed by reporting the predicted autoionization rates.

The autoionization rates can be calculated using Fermi's golden rule [14]:

$$A = \frac{2\pi}{\hbar}\left|\langle \Psi | V | \Psi' \rangle\right|^2$$

where $|\Psi\rangle = |J_C, nLm_i K\rangle$, and $|\Psi'\rangle = |J'_C, \varepsilon L' m_j K\rangle$ with $K = L + J_C$, and J_C is the core total angular momentum, and where:

$$V = e\vec{Q}\cdot\frac{C^{[2]}(\hat{r})}{r^3}$$

$$\vec{Q} \equiv e\sum_{i=1}^{N_e} r_i^2 C^{[2]}(\hat{r}_i)$$

in which $\vec{Q}$ is the 2nd rank quadrupole moment operator of the core ion, $C^{[2]}$ is the spherical harmonic in the Rydberg electrons angular position, and r is the Rydberg electron's radial coordinate. In Hanni's dissertation [7], it is discussed how this becomes:

$$A = \frac{2\pi}{\hbar}(2L+1)(2L'+1)\begin{pmatrix} L & 2 & L' \\ 0 & 0 & 0 \end{pmatrix}^2 \begin{Bmatrix} K & L & J_C \\ 2 & J'_C & L' \end{Bmatrix}^2 \left\langle J'_C \left\| \vec{Q} \right\| J_C \right\rangle^2 \left\langle nL \left\| r^{-3} \right\| \varepsilon L' \right\rangle^2 \quad (4.1)$$

for the autoionization rate between core states in the bound and continuum channels, where $\left\langle J'_C \left\| \vec{Q} \right\| J_C \right\rangle$ is the quadrupole matrix element. The autoionization rate for arbitrary J'_C and L' averaged over all possible K states can be written as:

$$\bar{A}_{J'_C, L'} = \frac{1}{(2L+1)(2L'+1)}\sum_K (2K+1)A(K) \quad (4.2)$$

Using equations 6.2.4, 6.2.5, and 6.2.9 from [15] it is known that:

$$\sum_K (2K+1)\begin{Bmatrix} K & L & J_C \\ 2 & J'_C & L' \end{Bmatrix}^2 = \frac{1}{5} \quad (4.3)$$

Combining equations 4.2 and 4.3:

$$\overline{A}(J'_C, L') = \frac{2\pi}{\hbar}\frac{(2L'+1)}{5(2J_C+1)}\begin{pmatrix} L & 2 & L' \\ 0 & 0 & 0 \end{pmatrix}^2 \left\langle J'_C \left\| \vec{Q} \right\| J_C \right\rangle^2 \left\langle nL \left| r^{-3} \right| \varepsilon L' \right\rangle^2 \tag{4.4}$$

For quadrupole transitions the selection rule is $L' = L \pm 2,0$, which means the total autoionization rate from an initial state (J_C,n,L) into a final continuum state with J_C' is:

$$\overline{A}_{Tot}(J'_C) = \overline{A}(J'_C, L-2) + \overline{A}(J'_C, L) + \overline{A}(J'_C, L+2) \tag{4.5}$$

In each of the terms in equation 4.5 there will be a three-J symbol that can be simplified using equation 3.7.17 in reference [15], which gives the relationships:

$$\begin{aligned}
\begin{pmatrix} L & 2 & L+2 \\ 0 & 0 & 0 \end{pmatrix}^2 &= \frac{3}{2}\frac{(L+1)(L+2)}{(2L+1)(2L+3)(2L+5)} \\
\begin{pmatrix} L & 2 & L \\ 0 & 0 & 0 \end{pmatrix}^2 &= \frac{L(L+1)}{(2L-1)(2L+1)(2L+3)} \\
\begin{pmatrix} L & 2 & L-2 \\ 0 & 0 & 0 \end{pmatrix}^2 &= \frac{3}{2}\frac{L(L-1)}{(2L-3)(2L-1)(2L+1)}
\end{aligned} \tag{4.6}$$

Using equations 4.4, 4.5 and 4.6 it can be written:

$$\begin{aligned}
\overline{A}_{Tot}(J'_C) = \frac{2\pi}{\hbar}\frac{\left\langle J'_C \left\| \vec{Q} \right\| J_C \right\rangle^2}{5\cdot(2J_C+1)}\Bigg[&\left(\frac{3}{2}\frac{(L+1)(L+2)}{(2L+1)(2L+3)}\right)\left\langle n, L \left| r^{-3} \right| \varepsilon, L+2 \right\rangle^2 \\
&+\left(\frac{L(L+1)}{(2L-1)(2L+3)}\right)\left\langle n, L \left| r^{-3} \right| \varepsilon, L \right\rangle^2 + \left(\frac{3}{2}\frac{L(L-1)}{(2L+1)(2L-1)}\right)\left\langle n, L \left| r^{-3} \right| \varepsilon, L-2 \right\rangle^2\Bigg]
\end{aligned} \tag{4.7}$$

This can be simplified assuming $L >> 1$ (this is the case for states of interest) to remove the L dependence of the coefficients:

$$\overline{A}_{Tot}(J'_C) \approx \frac{2\pi}{\hbar}\frac{\left\langle J'_C \left\| \vec{Q} \right\| J_C \right\rangle^2}{40(2J_C+1)}\left[3\left\langle n, L \left| r^{-3} \right| \varepsilon, L+2 \right\rangle^2 + 2\left\langle n, L \left| r^{-3} \right| \varepsilon, L \right\rangle^2 + 3\left\langle n, L \left| r^{-3} \right| \varepsilon, L-2 \right\rangle^2\right] \tag{4.8}$$

Equation 4.8 gives an easy way to calculate the average autoionization rates if the quadrupole matrix element, and the radial matrix elements are known.

The radial matrix elements were calculated using a Matlab program based heavily on a Fortran code developed by Julie Keele [16]. This code follows the Runge-Kutta method [17] to solve for the discrete and continuum states that are not easy to calculate for high *L* and *n* states otherwise. The discrete wavefunction is normalized in the normal fashion, namely by forcing:

$$|\psi_D|^2 = 1$$

The normalization of the continuum wavefunction is more complicated. At large radii, the continuum wavfunction becomes a cosine function:

$$\psi_{\varepsilon,L}(r) \to C(\varepsilon)\cos(kr + \varphi_\varepsilon)$$

Where C(ε) is the is a normalization constant, and $k = \sqrt{2\varepsilon}$ in atomic units. To normalize, it is required that:

$$\int_0^\infty \psi_{\varepsilon,L}(r)\psi_{\varepsilon',L}(r)dr = \delta(\varepsilon - \varepsilon')$$

This leads to the condition that:

$$|C(\varepsilon)|^2 = \frac{\pi}{2}\sqrt{2\varepsilon}$$

Once the discrete and continuum functions were calculated, a numerical integration was done that summed the discrete points for:

$$\langle \psi_D | r^{-3} | \psi_C \rangle = \sum_r \frac{\psi_D(r)\cdot\psi_C(r)}{r^3}\Delta r$$

where Δr is the step size taken between discreet points. This program was used to calculate the radial matrix elements in equation 4.8.

In order to proceed, theoretical values for the energy levels are neccesary. These were unknown duriong the previous work done by Mark Hanni, but since that time there have been theoretical predictions published [18]. Table 4.1 shows the electron configuration, the *J* value,

and the predicted energy relative to the ground state for the lowest 12 excited states in U^{6+}, all of which are metastable. They consist of a single hole in the otherwise full 6p shell and a valence 5f electron. The last column in table 4.1 is the label assigned to the state. The letter in the label refers to the hole-electron configuration of the state (A for $\overline{6p_{3/2}}5f_{5/2}$, B for $\overline{6p_{3/2}}5f_{7/2}$, C for $\overline{6p_{1/2}}5f_{5/2}$, D for $\overline{6p_{1/2}}5f_{7/2}$, and G for the ground state) and the number is the angular momentum of the state. This notation is used throughout this text for reference to the states. Figure 4.1 is an energy diagram showing the states from table 4.1.

Table 4.1: Predicted energies of the lowest 12 excited states of the U^{6+} ion. The first column is the configuration of the states hole-electron, the second column is the angular momntum of the state, the third column is the energy above the ground state in cm^{-1}, and the last column is the label assigned to the state.

State	*J*	Energy (cm^{-1})	Label
$\overline{6p_{3/2}}5f_{5/2}$	1	55084	A1
$\overline{6p_{3/2}}5f_{5/2}$	2	57270	A2
$\overline{6p_{3/2}}5f_{5/2}$	4	64483	A4
$\overline{6p_{3/2}}5f_{7/2}$	3	68332	B3
$\overline{6p_{3/2}}5f_{7/2}$	5	70664	B5
$\overline{6p_{3/2}}5f_{5/2}$	3	73117	A3
$\overline{6p_{3/2}}5f_{7/2}$	4	79433	B4
$\overline{6p_{3/2}}5f_{7/2}$	2	86091	B2
$\overline{6p_{1/2}}5f_{5/2}$	3	151076	C3
$\overline{6p_{1/2}}5f_{7/2}$	3	158903	D3
$\overline{6p_{1/2}}5f_{5/2}$	2	159384	C2
$\overline{6p_{1/2}}5f_{7/2}$	4	161277	D4

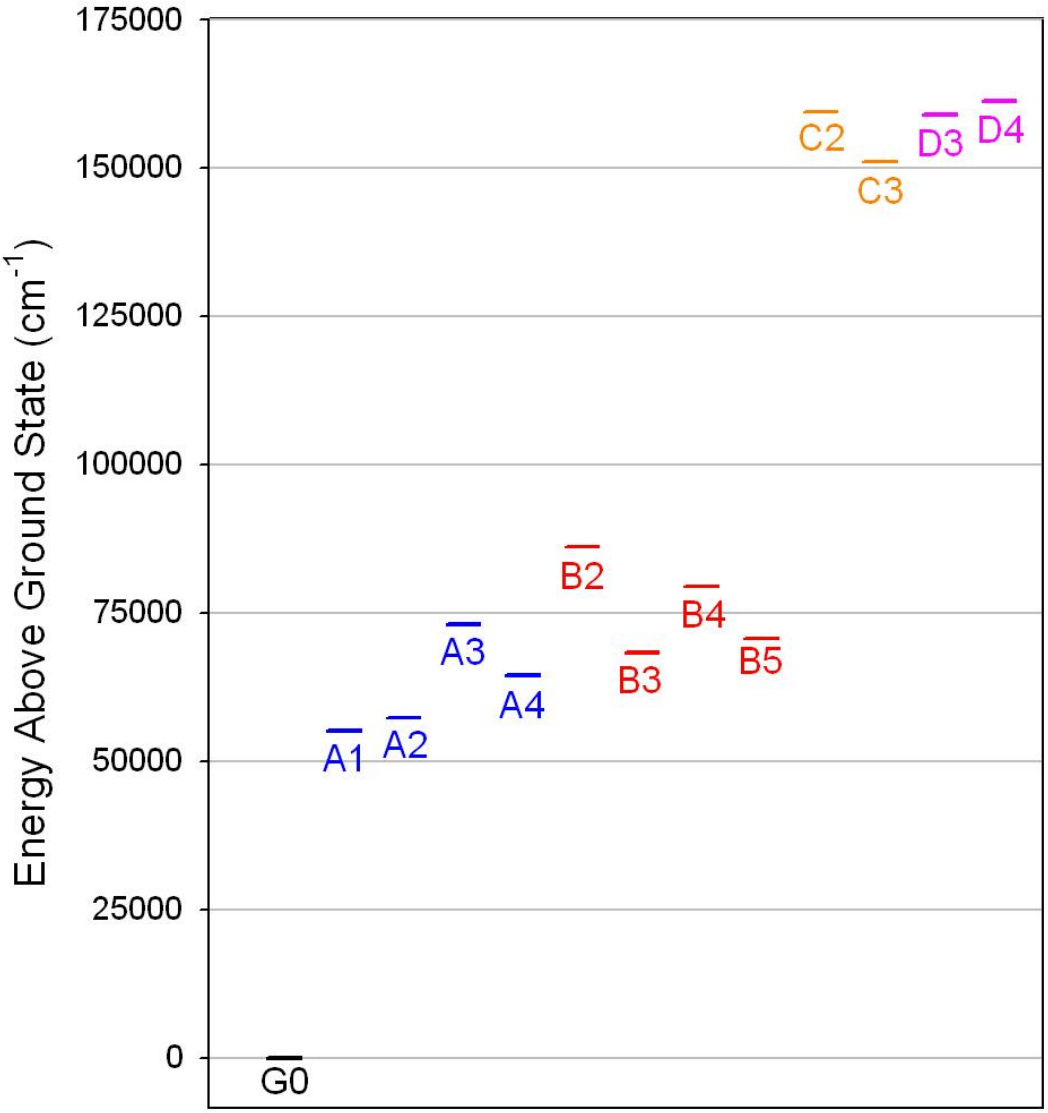

Figure 4.1: U^{6+} energy level diagram showing the energy levels detailed in table 4.1. The states are organized horizontally by their hole-electron configuration.

It is important to note that all of the excited energy levels shown in figure 4.1 have the same parity, meaning spontaneous electric quadrupole transitions can occur between any two ionic states so long as the final state is lower in energy than the initial state, and $\Delta J \leq 2$. This means every state has a spontaneous electric quadrupole decay channel, except A1 (only the ground state is lower, but $J = 1 \rightarrow J = 0$ is forbidden). Each excited level of U^{6+} can support a whole series of Rydberg levels that can decay by electric quadrupole autoionization to the

continuum of a lower energy ion if E2 decay to that level is allowed. This means the Rydberg levels bound to the A1 state can't autoionize. It is therefore not a relevant state when it comes to the metastable autoionization hypothesis as the source of background and would fit into the second category of ions discussed at the start of this chapter, with the ground state ions.

The knowledge of the energy level diagram allows a better analysis of the metastable autoionization rates, but before this is possible, the quadrupole matrix elements need to be known in order to evaluate equation 4.8. The quadrupole matrix elements can be inferred from the calculated spontaneous electric quadrupole transition rates, using equation 2 in reference [18]:

$$A = \frac{5.70332 \times 10^4 \cdot (\Delta E)^5}{(2J_C + 1)} \left\langle J'_C \left\| \vec{Q} \right\| J_C \right\rangle^2 \tag{4.9}$$

where A is the spontaneous E2 decay rate in 1/s, ΔE is the energy difference between the two states in atomic units, and the quadrupole matrix element is in atomic units. Predicted decay rates were taken from reference [19].

Once the quadrupole matrix element is known, equation 4.8 can be evaluated. One question that arises is how to determine the dependence on n and L? The n states that would matter are those that are captured into from the Rydberg target, but would not be cleared out in the repeller, roughly from n = 25 to 70. This would correspond to ~1500 n,L states that would need to be calculated for each decay channel, which is not practical. Instead, the decay rate was determined for multiple L states with a fixed n value, and vice versa to find the average decay rate for a decay channel as a function of n and L. It was found that the decay rate could be approximated as:

$$\overline{A}(n, L) = A_C \frac{1}{n^3 \cdot L^6} \tag{4.10}$$

where A_C is a coefficient found for each decay channel. Table 4.2 shows the calculated quadrupole matrix element, and the decay rate coefficient for almost all decay channels that are possible (channels C2 to D3, D4 to D3, and D4 to C2 are not included due to absence of predicted E2 spontaneous decay rates). The predicted decay rates following this method are similar in trend with n and L as those predicted previously by Mark Hanni, and give overall rates very similar as well [7]. The better theoretical knowledge of the energy levels and quadrupole matrix elements likely make the current predictions more accurate than previous predictions. The decay rate coefficients in table 4.2 vary greatly, more than 9 orders of magnitude. Combining this with the n^{-3} and L^{-6} dependence means that there is great variation in decay rate within an excited energy level, as well as between energy levels.

Table 4.2: Overview of predicted autoionization rates. The first column is the decay channel, the second column is the quadrupole matrix element, and the last column is the decay coefficient in equation 4.10.

Decay Channel	$\left\langle J'_C \left\| \vec{Q} \right\| J_C \right\rangle$	A_C (1/s)
A2 to A1	1.1885	1.70×10^{25}
A2 to G0	0.2192	1.02×10^{20}
A3 to A1	0.1759	6.48×10^{21}
A3 to A2	0.5266	7.58×10^{22}
A3 to A4	0.5747	2.60×10^{23}
A3 to B3	0.2736	1.17×10^{23}
A3 to B5	0.1284	1.52×10^{22}
A4 to A2	0.3644	7.78×10^{22}
B2 to A1	0.164	1.28×10^{22}
B2 to A2	0.1637	7.68×10^{21}
B2 to A3	0.9795	6.91×10^{23}
B2 to A4	0.243	2.30×10^{22}
B2 to B3	0.4793	6.91×10^{22}
B2 to B4	0.0748	1.28×10^{22}
B2 to G0	2.8422	1.45×10^{21}
B3 to A1	0.5906	1.47×10^{23}
B3 to A2	1.2909	1.05×10^{24}
B3 to A4	1.1692	1.50×10^{24}
B4 to A2	0.5276	7.58×10^{22}
B4 to A3	0.9991	1.00×10^{24}
B4 to A4	0.4641	3.81×10^{22}

B4 to B3	0.9887	2.74×10^{23}
B4 to B5	1.1682	4.11×10^{23}
B5 to A4	0.9111	8.28×10^{23}
B5 to B3	0.4666	1.99×10^{23}
C2 to A1	0.0899	8.10×10^{17}
C2 to A2	0.0916	9.72×10^{17}
C2 to A3	0.0178	6.48×10^{16}
C2 to A4	0.0331	1.09×10^{17}
C2 to B2	0.015	1.22×10^{17}
C2 to B3	0.0656	4.36×10^{17}
C2 to B4	0.0575	1.01×10^{18}
C2 to C3	0.8125	5.25×10^{23}
C2 to G0	2.2845	5.20×10^{19}
C3 to A1	0.025	4.38×10^{16}
C3 to A2	0.0954	7.22×10^{17}
C3 to A3	0.0185	6.80×10^{16}
C3 to A4	0.054	2.62×10^{17}
C3 to B2	0.0282	4.23×10^{17}
C3 to B3	0.0595	5.57×10^{17}
C3 to B4	0.0464	6.35×10^{17}
C3 to B5	0.0125	2.50×10^{16}
D3 to A1	0.0573	1.30×10^{17}
D3 to A2	0.0751	2.81×10^{17}
D3 to A3	0.0359	1.17×10^{17}
D3 to A4	0.0605	2.98×10^{17}
D3 to B2	0.0004	4.48×10^{13}
D3 to B3	0.1208	1.46×10^{18}
D3 to B4	0.1749	4.90×10^{17}
D3 to B5	0.0595	3.13×10^{17}
D3 to C3	0.2881	5.05×10^{22}
D4 to A2	0.0643	1.23×10^{17}
D4 to A3	0.13	1.18×10^{18}
D4 to A4	0.0413	6.72×10^{16}
D4 to B2	0.0096	1.50×10^{16}
D4 to B3	0.1041	6.06×10^{17}
D4 to B4	0.0388	1.83×10^{17}
D4 to B5	0.0903	4.54×10^{17}
D4 to C3	0.8386	1.27×10^{23}

Since predictions for the decay rates are now known, it is possible to predict the fastest decay channels for each state. In most cases, the fastest decay channel dominates, but the C3 state is an exception, where the total decay rate was about 4 times larger than just the fastest

decay channel. For this reason table 4.3 shows the fastest decay channel for most states, and the total decay rate for the C3 state. Figure 4.2 shows the energy level diagram, but with the fastest decay rates for each state shown as a green arrow. These predicted decay rates are important for analysis of the metastable population within U^{6+}, and more detailed predictions can now be made.

A quick analysis can be done to determine if these predicted decay rates are extremely fast, or slow for the current experiment. The time from the Rydberg target to the detector for 150 keV U^{6+} is 4.35 microseconds. Looking at $n = 40$ (a state with a lot of capture) large and small decay rates can be calculated. The fastest decay rate would be the A2 state and a low L such as $L = 2$, making the lifetime for this state $2.4*10^{-13}$ microseconds. This is extremely short lived, and these states would autoionize well before the detector. A longer-lived state would be the C3 state with $L = 39$, giving a lifetime of 1300 microseconds. This is a couple of orders of magnitude larger than the time to the detector meaning most of this state would make it to the detector. The main thing this indicates is that the range of lifetimes for the uranium metastable states is massive (at least 17 orders of magnitude), and there seem to be some metastable states that could survive to the detector. This is important to note, but not many concrete conclusions can be drawn from this wide a range of values. This calls for more detailed modeling to be done that can account for the large number of n and L states that would occur.

Table 4.3: Predicted fastest decay coefficients for each metastable state, except C3. For that case, the total rate from table 4.2 is shown.

State	A_C (1/s)
A1	0
A2	1.70×10^{25}
A3	2.60×10^{23}
A4	7.78×10^{22}
B2	6.91×10^{23}
B3	1.50×10^{24}
B4	1.00×10^{24}
B5	8.28×10^{23}
C2	5.25×10^{23}
C3	2.74×10^{18}
D3	5.05×10^{22}
D4	1.27×10^{23}

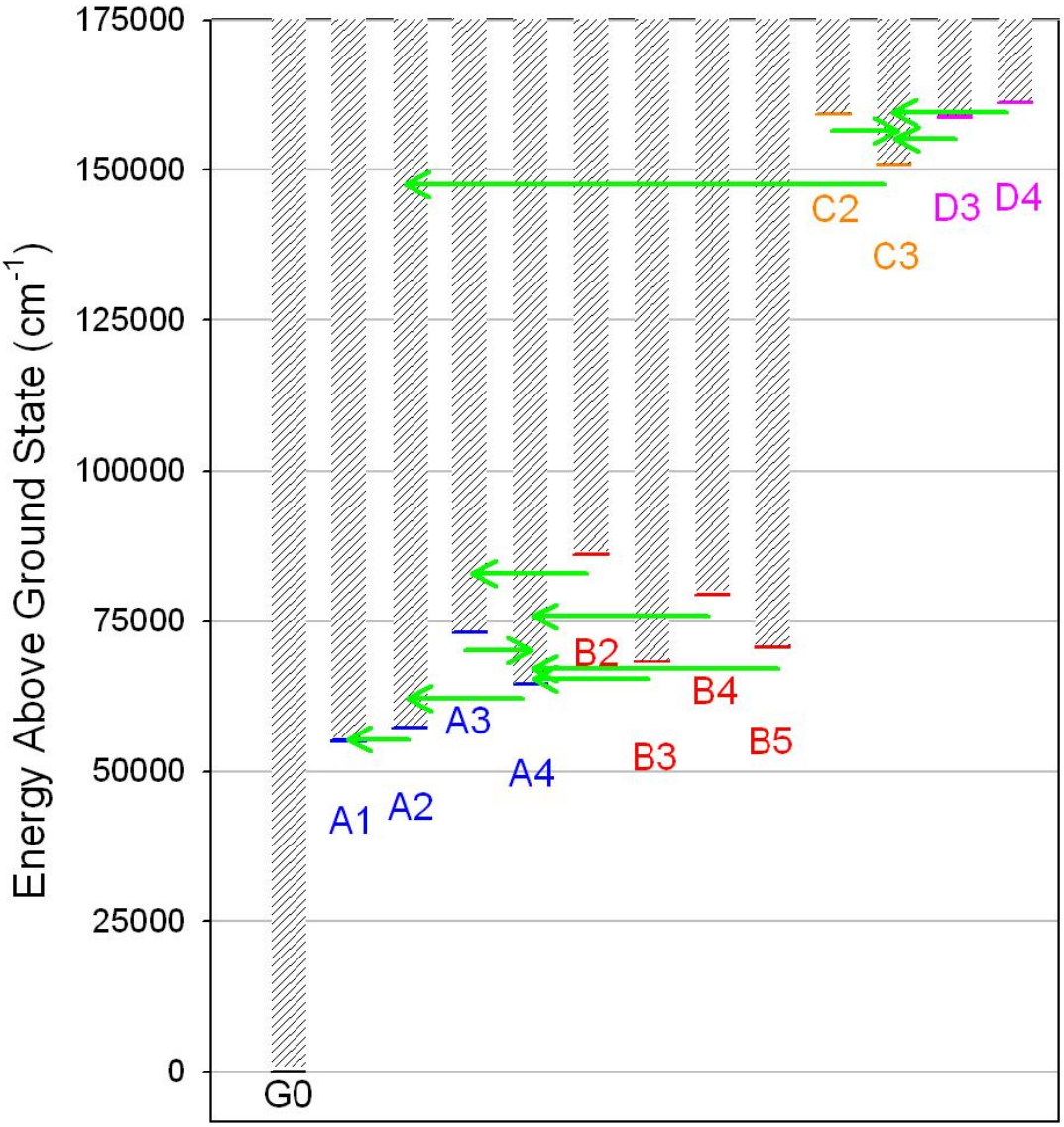

Figure 4.2: Energy level diagram showing the energy levels as well as the electric quadrupole autoionization decay channel that is fastest for each Rydberg series.

4.2 Stark Mixed Autoionization Rates

The last section provided predictions for the electric field free autoionization rates for metastable U^{5+} Rydberg states. Within a sufficiently large electric field *L* is no longer a good quantum number, and the *m* value of the state determines the decay rate. This section serves to determine the autoionization rates of metastable U^{5+} Rydberg within an electric field.

A field can be said to be large enough if all the states within one *n* are Stark-mixed. Without knowing the exact energies of the *L* states it is difficult to say what magnitude electric field would do this, but it is certainly the case when adjacent *n* levels overlap. The *n* = 53 and *n* = 54 hydrogenic levels are separated by 1500 GHz, so if the Stark manifold has this width than complete *L* mixing can be assumed. The width of the Stark manifold for a given *n* state in an electric field is [20]:

$$\Delta E = 3F\,\frac{n(n-1)}{Q}$$

where F is the magnitude of the electric field, and Q is the charge of the core. Using this, an electric field of 850 V/cm would be sufficient to overlap the *n* = 53 and *n* = 54 states. Any electric field in the beamline whose magnitude is greater than this can be assumed to cause complete *L* mixing and autotionization will be dependent on the *m* value of the states.

When in a field of this magnitude, then the decay rate can be assumed to be the average of the field free decay rates for the states that are mixed. This means that an *m* state will decay as the average of all field free *L* values that can have that *m* value, specifically:

$$A(n,m) = \frac{\sum_{L \geq |m|} A(n,L)}{n - |m|}$$

where A(*n*,*L*) is the field free decay rate, and A(*n*,*m*) is the electric field decay rate. Using the field free decay rate, this can be written as:

$$A(n,m) = \frac{\frac{A_C}{n^3}\sum_{L \geq |m|}\frac{1}{L^6}}{n - |m|}$$

This equation can be used to calculate the electric field autoionization rate for arbitrary *n*,*m* states. Table 4.4 shows the decay rate for a few select n,m states as a function of the decay

coefficient. The decay rate within an *n* value varies by three to five orders of magnitude, but only about an order of magnitude within an *m*. This means even within an *n* state there is a large variation in decay rate.

Table 4.4: The predicted autoionization rates for a range of *n*,*m* values as a function of the decay coefficient for a arbitrary decay channel. Table 4.3 shows that the coefficient A_2 ranges from 10^{18} to 10^{25} 1/s.

$\|m\|$	$n = 35$	$n = 40$	$n = 45$	$n = 50$
5	$7.94 \times 10^{-11} A_C$	$4.56 \times 10^{-11} A_C$	$2.80 \times 10^{-11} A_C$	$1.82 \times 10^{-11} A_C$
10	$2.37 \times 10^{-12} A_C$	$1.33 \times 10^{-12} A_C$	$7.99 \times 10^{-13} A_C$	$5.10 \times 10^{-13} A_C$
15	$3.57 \times 10^{-13} A_C$	$1.93 \times 10^{-13} A_C$	$1.13 \times 10^{-13} A_C$	$7.07 \times 10^{-14} A_C$
20	$1.04 \times 10^{-13} A_C$	$5.36 \times 10^{-14} A_C$	$3.05 \times 10^{-14} A_C$	$1.87 \times 10^{-14} A_C$
25	$4.32 \times 10^{-14} A_C$	$2.14 \times 10^{-14} A_C$	$1.18 \times 10^{-14} A_C$	$7.02 \times 10^{-15} A_C$
30	$2.26 \times 10^{-14} A_C$	$1.07 \times 10^{-14} A_C$	$5.70 \times 10^{-15} A_C$	$3.31 \times 10^{-15} A_C$
35		$6.28 \times 10^{-15} A_C$	$3.23 \times 10^{-15} A_C$	$1.82 \times 10^{-15} A_C$
40			$2.05 \times 10^{-15} A_C$	$1.12 \times 10^{-15} A_C$
45				$7.56 \times 10^{-16} A_C$

The autoionization rates for U^{5+} Rydberg metastable states are now known within an electric field of a large enough magnitude to mix all the states. This does not consider what happens in more complicated electric fields that change magnitude and direction. The next section will serve to analyze what happens in one of these fields.

4.3 Modeling Metastable Population Mixing in a Time-Varying Electric Field

The next question that needs to be answered is what happens when the metastable Rydberg states pass through a changing electric field. The electric field within the detector serves to Stark ionize the signal ions, but is also where the background is created. Understanding what happens to metastable states as they pass through this field is necessary to understand their properties, and whether they could be the source of the background.

To understand what the electric field in the Stark ionizer does, it is first necessary to better understand the field itself. Previously, the electric fields within the Stark ionizer have been viewed as simply an electric field that starts and stops without addressing it as a physical electric field that has complications beyond this naïve analysis. The electric field really has four distinct regions: 1) Entrance to the electric field, 2) relatively constant electric field, 3) a flip in direction of electric field, and 4) exiting the electric field. When the electric field begins, flips, and ends there are components of the electric field perpendicular and parallel to the beam direction except when directly on the center axis (every field discussed is cylindrically symmetric). This means it is a field rotation in two dimensions, rather than the naive view of a change in one dimension. As an example, figure 4.3 shows the electric field that is present within the half-inch Stark ionizer region with a one-inch ramp down region when looking 0.5 mm off the central axis. This electric field was found by modeling the Stark ionization region in the program Simion 7.0 that then calculates the electric field numerically. This clearly shows the non-negligible perpendicular field that needs to be considered to fully understand the electric fields' affects on the ion beam.

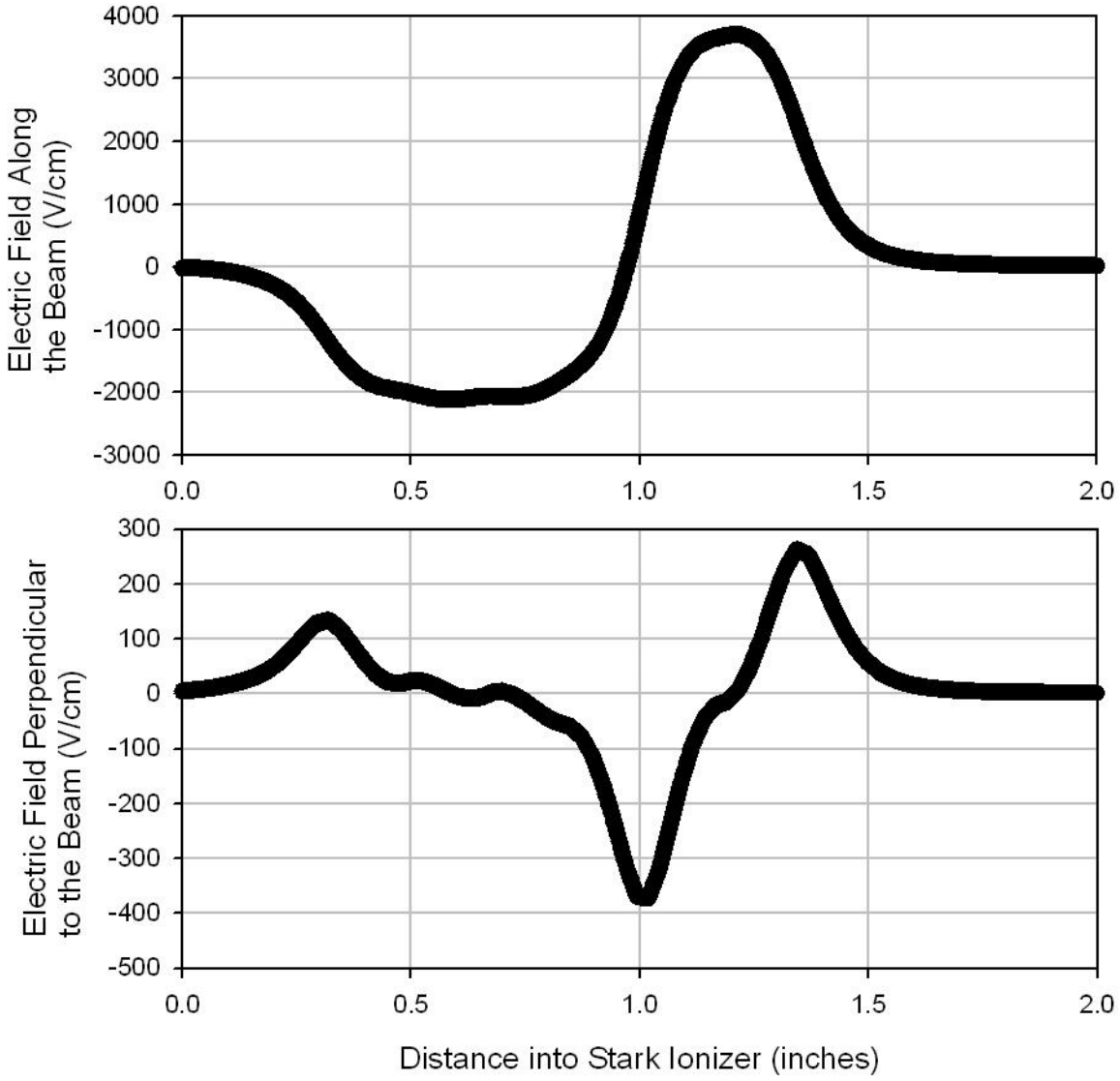

Figure 4.3: Magnitude of the components of the electric field at 0.5 mm off the beam axis within a half inch Stark ionizer with a one inch ramp down region with V_S = -5000 V as a function of the distance into the region in inches as taken from the Simion 7.0 program. a) Electric field parallel to the beamline in V/cm. b) Electric field perpendicular to the beamline in V/cm.

Determining what happens to the metastable states passing through this electric field can be complicated, and modeling is needed in order to try to understand what happens. Ideally, the metastable *n* values that are most highly populated are the ones that would modeled since they are of the most interest. The most highly populated states after capture are of the order of $n = 45$. The Hamiltonian for these *n* states becomes quite large. To analyze these states it would involve

the diagonalization of a n^4 term matrix, or for $n = 45$ it would mean diagonalizing a matrix of ~4 million terms. Working with matrices of this size would make the modeling extremely complicated, but some intuition into what sort of mixing might occur in hydrogenic states could be gathered from modeling more reasonable n state Rydberg levels. For this reason, $n = 3$ hydrogen was chosen as an example before expanding to higher-n states.

The first step is to determine the Hamiltonian for the hydrogenic states in an arbitrary electric field. The electric fields are always cylindrically symmetric within the regions being discussed. This means the electric field can always be broken down into a component parallel to the beam that will be defined as the z-axis, and a component radial to the beam that will be defined as the x-axis. The Hamiltonian of a Rydberg ion is then given as:

$$H = e\left(E_x x + E_z z\right) \tag{4.11}$$

Within an n each state can be tagged with its L and m value, which means that the matrix elements of the Hamiltonian between state $\left|n, L, m\right\rangle$ and $\left|n, L', m'\right\rangle$ is given by:

$$\left\langle n, L', m'\middle|H\middle|n, L, m\right\rangle = eE_x\left\langle n, L', m'\middle|x\middle|n, L, m\right\rangle + eE_z\left\langle n, L', m'\middle|z\middle|n, L, m\right\rangle \tag{4.12}$$

The matrix element of z in equation 4.12 can be calculated with the help of eq. 60.7 and eq. 63.5 in Bethe and Salpeter [20]. Combining these equations the z matrix element is given as:

$$\left\langle n, L-1, m\middle|z\middle|n, L, m\right\rangle = \sqrt{\frac{L^2 - m^2}{(2L+1)(2L-1)}}\frac{3}{2}n\sqrt{n^2 - L^2} \tag{4.13}$$

A similar procedure can be used to calculate the x matrix element using eq. 60.11 from [20]. Doing this there are two equations that will give the matrix elements of x:

$$\begin{aligned}\left\langle n, L-1, m+1\middle|x\middle|n, L, m\right\rangle &= -\frac{3}{4}\sqrt{\frac{(L-m)(L-m-1)}{(2L+1)(2L-1)}}n\sqrt{n^2 - L^2} \\ \left\langle n, L-1, m-1\middle|x\middle|n, L, m\right\rangle &= \frac{3}{4}\sqrt{\frac{(L+m)(L+m-1)}{(2L+1)(2L-1)}}n\sqrt{n^2 - L^2}\end{aligned} \tag{4.14}$$

Combining equations 4.13 and 4.14 with the symmetry of the Hamiltonian from it being self-adjoint the Hamiltonian for a Rydberg ion in an electric field can be relatively easily computed.

What can be learned by analyzing the $n = 3$ Rydberg states is the change in m state that will occur as an ion passes through an electric field like those found within the Stark ionizer. As shown in figure 4.3, with the help of the program Simion, numerical values for the electric field within the Stark ionizer can be obtained. Mathematically speaking, small time interval steps can be made through this electric field, and at each step the Hamiltonian can be diagonalized and the evolution of an arbitrary state can be determined. This computation was done in MATLAB 7.0 language in an m-file named efieldn3.m that imports the electric field values from an excel file named efieldn3.xls, and exports results to another worksheet within the same excel file. The Hamiltonian for $n = 3$ hydrogen can be written as (tagging each state as $|L,m\rangle$:

	$\|2,2\rangle$	$\|2,1\rangle$	$\|2,0\rangle$	$\|2,-1\rangle$	$\|2,-2\rangle$	$\|1,1\rangle$	$\|1,0\rangle$	$\|1,-1\rangle$	$\|0,0\rangle$
$\langle 2,2\|$	ε_2	0	0	0	0	$5.75E_x$	0	0	0
$\langle 2,1\|$	0	ε_2	0	0	0	$5.75E_z$	$4.07E_x$	0	0
$\langle 2,0\|$	0	0	ε_2	0	0	$-2.36E_x$	$6.64E_z$	$2.36E_x$	0
$\langle 2,-1\|$	0	0	0	ε_2	0	0	$-4.07E_x$	$5.75E_z$	0
$\langle 2,-2\|$	0	0	0	0	ε_2	0	0	$-5.75E_x$	0
$\langle 1,1\|$	$5.75E_x$	$5.75E_z$	$-2.36E_z$	0	0	ε_1	0	0	$6.64E_x$
$\langle 1,0\|$	0	$4.07E_x$	$6.64E_z$	$-4.07E_x$	0	0	ε_1	0	$9.41E_z$
$\langle 1,-1\|$	0	0	$2.36E_x$	$5.75E_z$	$-5.75E_z$	0	0	ε_1	$-6.64E_x$
$\langle 0,0\|$	0	0	0	0	0	$6.64E_x$	$9.41E_z$	$-6.64E_x$	ε_0

where ε_2, ε_1, and ε_0 are the energy of the states in the field free region, E_x and E_z are in V/mm giving each term units of MHz. The electric field values taken from Simion for each step are imported from an excel file called efieldn3.xls. At each step through the electric field, the eigenvalues, λ_i, are found as well as the eigenvectors, $|\lambda_i\rangle$. The wavefunction at a given step is

first projected into the eigenvector basis state. For instance, if $|\psi_I\rangle$ is the initial state, then in the field free basis it can be written as:

$$|\psi_I\rangle = \sum a_{L,m} |L,m\rangle$$

Which written in the eigenvector basis of the first step:

$$|\psi_1\rangle = \sum a_{1,\lambda_i} |\lambda_i\rangle$$

where:

$$a_{1,\lambda_i} = \langle \lambda_i | \psi_I \rangle$$

Once the state is known in the basis of the first step, then it is able to evolve in time for one time step Δt. The step size depends on the number of steps used through the Stark ionizer, N, and the total time to travel through the electric field flip, t. Figure 4.4 shows the electric fields used within the model for varius radii off the central axis and shows that it takes about 1.4 cm for the electric field flip to occur. The total time the beam takes to pass through this 1.4 cm will be an important metric to label how quickly this field flips from the perspective of the beam. At each step the states spend t/N seconds at that particular field, where N is the total number of steps taken. The states evolve in time using a diagonal matrix whose diagonal is given by:

$$Evolve = \exp\left[-i \cdot \lambda_i \cdot \frac{t}{N} \cdot 2 \cdot \pi \right]$$

The newly evolved states are then projected back to the original basis by, meaning the final state $|\psi_F\rangle$ is:

$$|\psi_F\rangle = \sum a_{2,\lambda_i} |\lambda_i\rangle$$

where:

$$a_{2,\lambda_i} = \langle \psi_I | \lambda_i \rangle$$

The program then moves forward a step into the field and $|\psi_F\rangle$ becomes $|\psi_I\rangle$ for the next step, and the procedure continues as described.

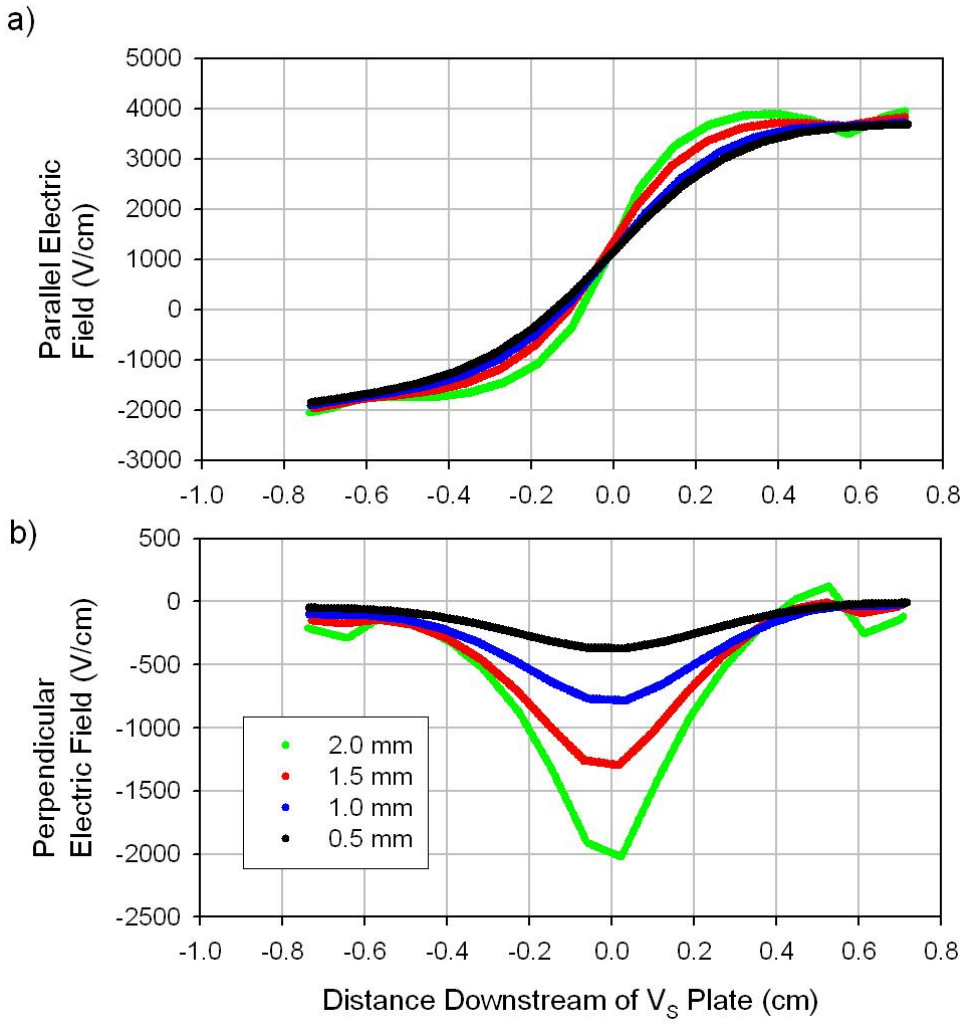

Figure 4.4: The electric fields for 2, 1.5, 1.0, and 0.5 mm off the central axis used for the calculations within this section. The values were taken from Simion 7.0. Part a) shows the electric field component parallel to the beam axis, and part b) shows the electric field component perpendicular to the field axis.

This evolution can then be done for every step through the electric field found from Simion to give the final state after the field. By varying the total time through the Stark ionizer insight can be gained into the mixing dependence versus how adiabatic the field change is. It might be expected that if the beam passes through the field extremely rapidly then the field

change is diabatic and there would be no change in state. If however, the field changes very slowly the change would be adiabatic and the state would evolve with the flip in electric field and end in the same *m* state in the new basis, or equivalently go to –*m* in the original basis. Figure 4.5 shows the mixing that occurs within a 1":0.5" Stark ionizer at V_S = -5000V with the amount of time spent passing the through the electric field flip in the aperture is varied. The probabilities are averages from varying off axis radii, scaled to the area at that radii assuming equal ion distribution per cross-sectional area. The initial state was $n = 3$, $L = 2$, $m = 2$, and the plot shows the probability of ending in the other possible *m* values.

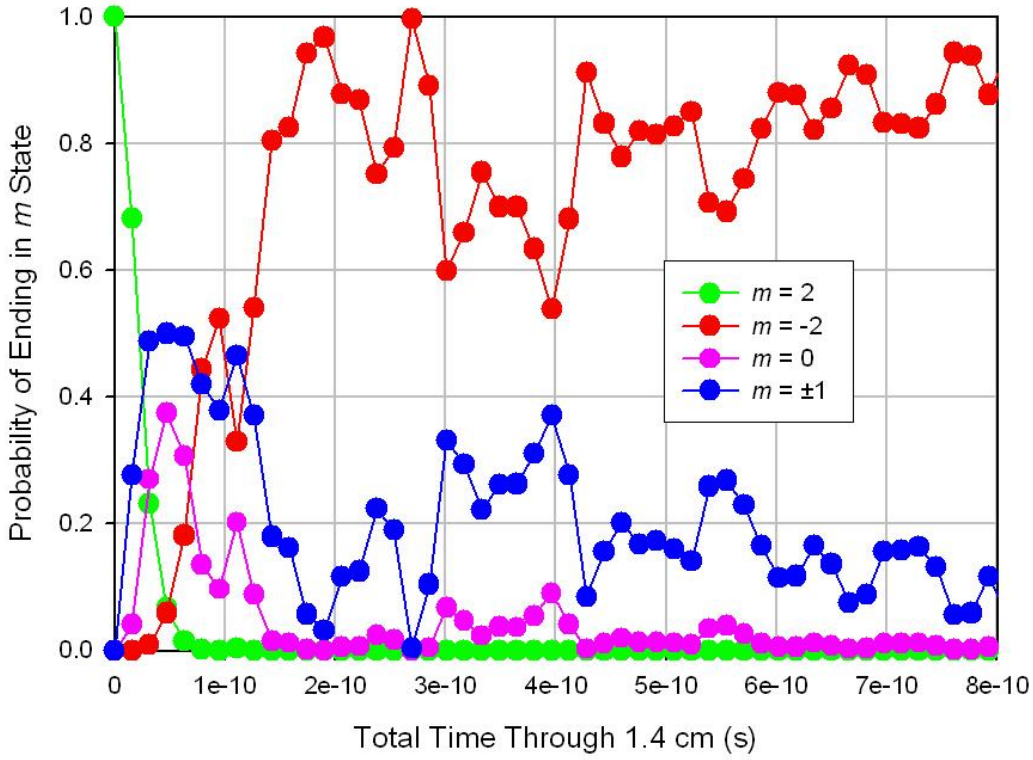

Figure 4.5: Probability of ending in a given *m* state after starting in the $m = 2$ state and passing through the aperture within the 1":0.5" Stark ionizer at V_S = -5000V. Probabilities were averaged for multiple radii scaled for the fraction of ions that would be found at that radius assuming equal density of ions across the beam.

There are a few qualitative ideas that can be taken from figure 4.5. The first thing is that if the time through the detector is short enough then the the transition is "diabatic" and the *m* state doesn't change. This is seen clearly at the very short times where $m = 2$ is maintened after passing through the electric field. The second observation is that if the time through the detector is long enough then the transition is "adiabatic" and the *m* value goes to $-m$. This is seen as for the longer times (approaching 1 ns) then the $m = -2$ is by far the most likely state. The third observation is that between these diabatic and adiabatic limits there is substantial mixing to lower *m* states. The probability of ending in $m = 0$ peaks at about 38% and of ending in $m = \pm 1$ peaks at about 50%. This means there is a range of times that it takes to pass through the electric field flip that mixes the *m* states a large amount. Another observation was that the mixing times were insensitive to the zero-field energy splittings (ε_0, ε_1, and ε_2 in the Hamiltonian). This would be expected if the range of Stark energies is much greater than the range of zero field energies. This was tested by changing the values of the zero-field energies over a range on the order of hundreds of MHz and determining if there was a substantial change

The next issue is how to expand the results in figure 4.5 to higher, more relevant *n* states. One way to do this is to look at the average *m* value resulting from an initial state n, $L = n-1$, $m = 1$ for multiple *n* states, as seen in figure 4.6. The calculation is easily generalized to these states. The adiabatic and diabatic limits are still clearly seen for all *n* states in figure 4.5. At very short times to pass through the field flip the *m* value is maintained, and for long times through the detector then the *m* state flips sign. Also seen though is that the times through the field flip that cause mixing changes as a function of the *n* state. Two metrics can be used for comparison between the different *n* states: the time through the field flip where the average *m* value is 0, and the time through the field flip that gives the peak of the hump feature seen. Table 4.5 details

these values. Both of these times appear to be inversely proportional to *n*, as documented in columns 3 and 5 in table 4.5.

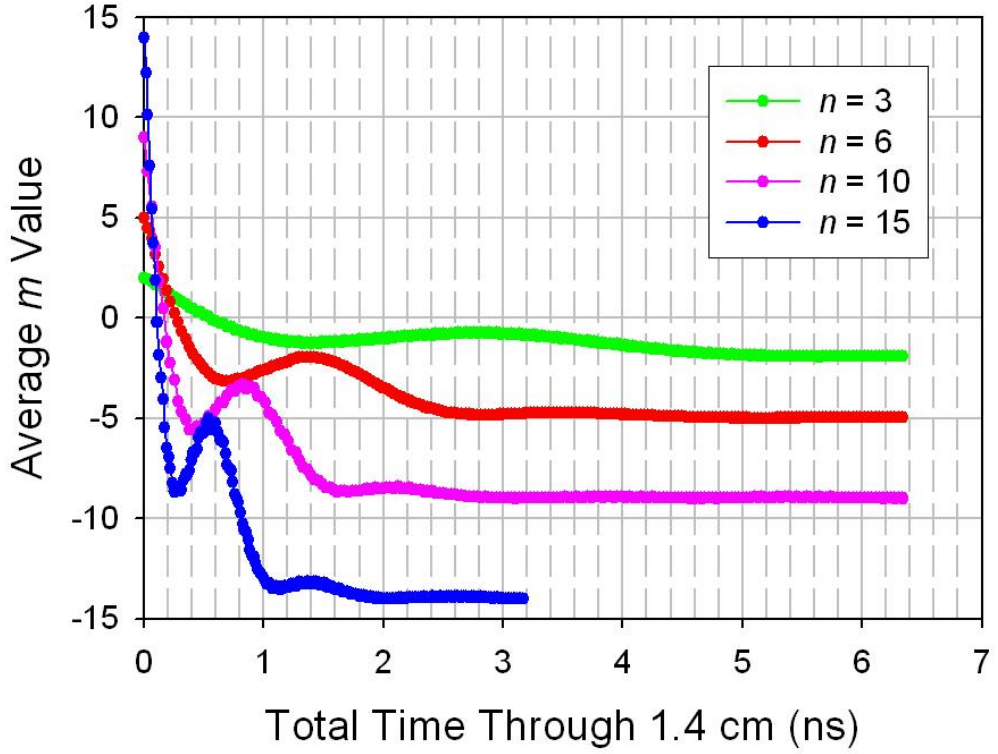

Figure 4.6: Average *m* value after exiting the Stark ionizer electric field 0.5 mm off-axis and V_S = -5000 V for a range of *n* values. The initial *L* and *m* state was always *n*-1.

Table 4.5: Important times taken from figure 4.6. The first column is the *n* value. The second column is the time through the field flip that gives an average *m* value of 0. The third column is the *n* value multiplied by column 2. The fourth column is the time through the detector that gives the peak value of the hump seen. The fifth column is *n* times column 4.

n	Time for Average *m* = 0 (ns)	*n* * column 2	Time for Peak of Hump (ns)	*n* * column 4
3	0.55	1.65	2.76	2.76
6	0.27	1.59	1.43	2.86
10	0.17	1.65	0.82	2.73
15	0.10	1.50	0.54	2.70

The critical time that determines whether the transition acts adiabatically or diabatically could be dependent on the maximum perpendicular electric field at the time of the flip. This electric field would dictate the separation of adjacent Stark states during the flip, and therefore

how many cycles between these states could occur during the field flip. The separation of states is given by:

$$\Delta\varepsilon = \frac{3Fn}{Q} \tag{4.15}$$

where Δε is the separation between adjacent Stark states, F is the magnitude of the electric field, and Q is the charge of the Rydberg core. For the cases shown in figure 4.6 there is a perpendicular field of 370 V/cm. For n = 3, and Q = 1 this corresponds to a separation of adjacent states of ~4200 MHz. This frequency corresponds to a period of 0.24 ns. This compares very well with what is seen for n = 3 in figure 4.5 where the time through the electric field flip is of this order mixing starts occuring. These results indicate that the maximum perpendicular electric field F, n state, and Q value are the parameters that dictate the critical time that determines whether mixing will occur. Specifically, the transition can be viewed as diabatic if:

$$t_{FieldFlip} << t_{critical} = \frac{Q}{3Fn}$$

and it can be viewed as adiabatic if:

$$t_{FieldFlip} >> t_{critical} = \frac{Q}{3Fn}$$

This predicts the critical time should be inversely proportional to the n value, which fits very well with the observations documented in table 4.5. Equations 4.15 now gives a way to determine what times through the Stark ionizer will cause mixing to occur for arbitrary n, Q assuming the perpendicular electric field can be predicted. For example, at F = 370 V/cm, n = 45, and Q = 6, equation 4.15 gives Δε = 10.76 GHz, or $t_{critical}$ = 0.09 ns. By comparison the 150 keV U^{6+} beam passes through the 1.4 cm aperture in 40 ns, making the transition close to adiabatic.

For the previous analysis, the electric field used was for a potential of –5000 V, and a beam that is 0.5 mm off axis. Although these values might be typical, they are certainly not the only ones that need to be considered. The potential on the Stark ionizer depends on the transition, and a wide range have been used. Figure 4.7 shows the average m value versus the total time through the electric field flip (the ~1.4 cm seen in figure 4.4) for a range of potentials applied to the Stark ionizer for $n = 3$ hydrogen. All other parameters remained the same as for figure 4.5 (0.5mm off the center axis, initial state was $L = 2$, $m = 2$). The perpendicular electric field at the flip should be propotional to the potential applied to the Stark ionizer so the critical time for the two extremes should be about a factor of 4 shorter for the maximum field than for the minimum field. Figure 4.7 matches this prediction well.

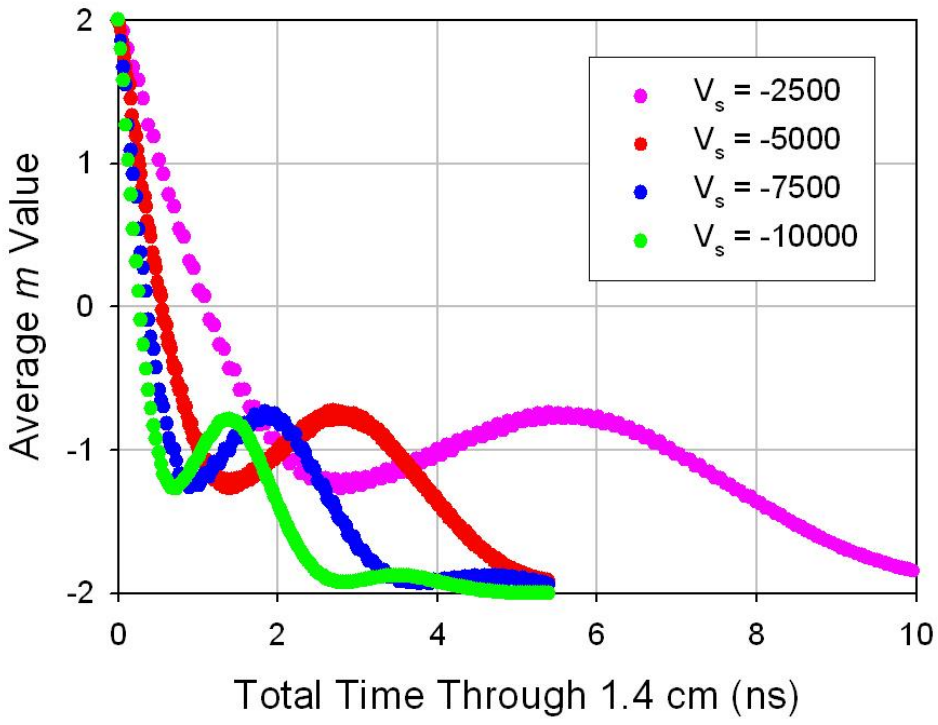

Figure 4.7: Average m value upon exiting the Stark ionizer after starting in the $m = 2$ state and passing through the aperture that would be present within the 1":0.5" Stark ionizer at various Stark ionization potentials, assuming a trajectory that is 0.5 mm off axis.

Looking at how the probability changes as a function of the radius can also be of interest. This indirectly affects the critical time since the perpendicular electric field will be dependent on the distance off axis. Since the ion beam will occur at a range of radii from the center axis (beam could have a maximum of ~6mm diameter), the different fields seen by different ions will change their mixing. The perpendicular field will get larger with larger radii. Figure 4.8 shows that there would be a large amount of variation in mixing depending on the offset of the ion from the central beam. The diameter of the background beam is ~1 mm (visual shown later in this chapter), which means the beam's average *m* value versus time through the detector could follow closely any of the plots in figure 4.8. The tuning of the beamline could induce large changes in the mixing depending on whether the beam is centered on-axis, or centered 2 mm off-axis, or anywhere inbetween. The width of the beam would also introduce a wider range in mixing times since a 1 mm beam would have ions at a 1 mm range of radii off axis.

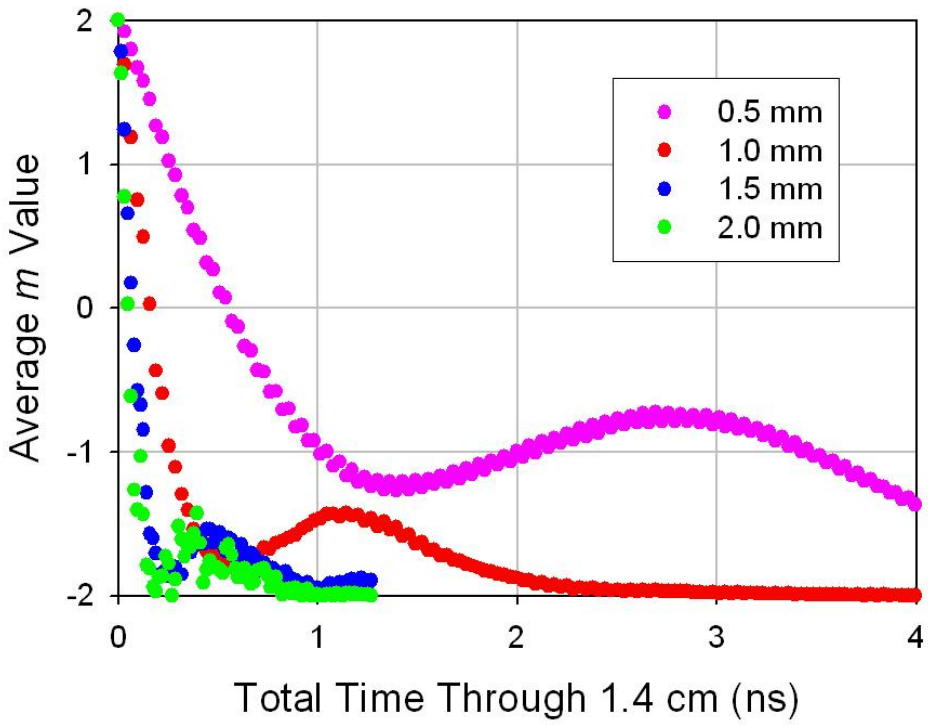

Figure 4.8: Average *m* value upon exiting the Stark ionizer after starting in the *m* = 2 state and passing through the aperture that would be present within the 1":0.5" Stark ionizer at various radii from the center axis of the beam, assuming V_S = -5000 V.

This hydrogen modeling demonstrates the potential *m* mixing that would occur at the field flip within the Stark ionizer. In order analyze what happens to the metastable population as it travels through the beamline, this mixing must be accounted for in order to accurately model the population changes. The next section will detail how the population of the metastable U^{6+} states vary throughout the beamline.

4.4 Modeling U^{6+} Metastable Populations

At this point the theoretical analysis of the metastable states in U^{6+} has given the autoionization rates of the metastable states both in field free and Stark-mixed conditions, and evidence showing the Stark ionizer field can mix *m* states significantly. The question now becomes, what happens to the metastable state populations throughout the beamline? Since the

autoionization rates are known, their populations can be modeled as a function of the distance traveled throughout the beamline. The mixing of the electric fields within the beamline (10" preionizer, Stark ionizer) can also be taken into account. This section serves to describe this model, and present some of its predictions.

The modeling of the metastable population throughout the beamline was carried out using Matlab 7, within an m-file named metpredictps.m, and exports results to an excel file named metpredictps.xls. The main outline of the program is to use (n,n) matrices whose elements correspond to ($|m|$,L) states. The model predicts the fraction of metastables left in an n state within a particular metastable manifold as a function of the distance traveled through the beamline.

Since it appears m state mixing is crucial in understanding the Stark ionizer, it was assumed that the 10" preionizer and Stark ionizer mix m states at their entrances, and at their flips in electric field. The 6" preionizer was left out of the modeling since it was turned off for experimental measurements that will be used for comparison.

One question is how to treat the beamline. Figure 4.9 shows a schematic of the beamline, including distances that were used for the various regions. It is important to model the magnet to infer the initial metastable population at capture. The repeller and remixer are ignored for the purpose of this modeling since their electric fields occur for a relatively short amount of time. The Stark ionizer modeled was the 2":1.0" since that corresponds to the 53-93 transition used for experimental comparisons.

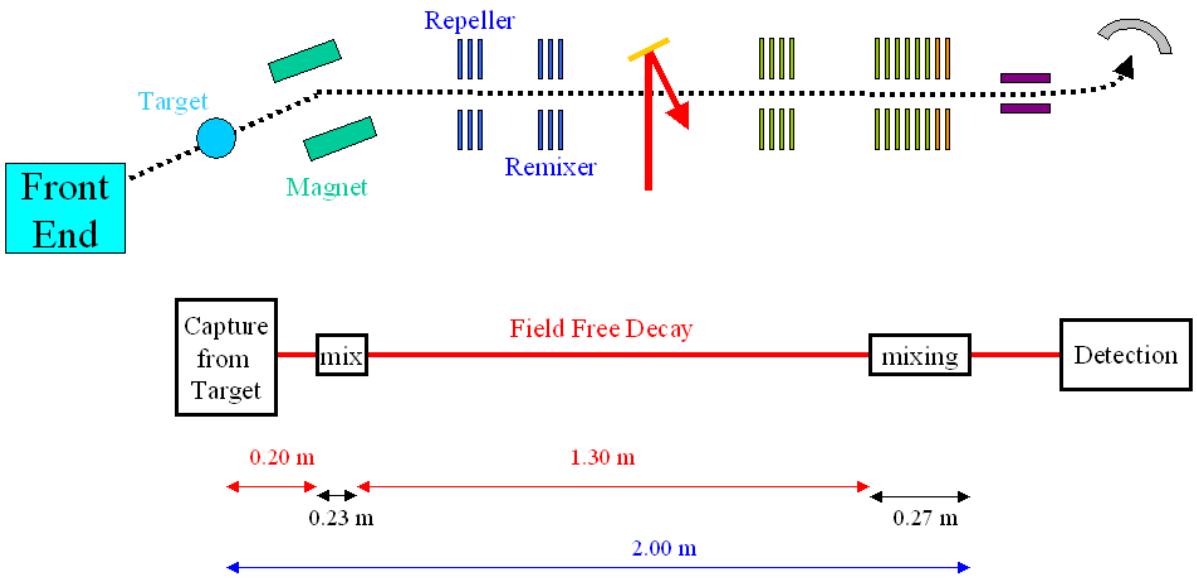

Figure 4.9: Schematic showing the important parts of the beamline when modeling the autoionization of metastable states.

As discussed earlier, the decay rate for a particular *n*, *L* state is:

$$A_{n,L} = \frac{A_C}{n^3 L^6} \tag{4.16}$$

where A_C for each state is shown in table 4.2. This was assumed to be the decay rate in all field free parts of the beamline. Within the fields of the Stark ionizer, the 15˚ magnet, and the 10" preionizer it was assumed that an *m* state decays as the average decay rate of all *L* states that can have that *m* value. Specifically:

$$A_m = \frac{\sum_{L=m}^{n-1} \frac{A_C}{n^3 L^6}}{(n-1)-m} \tag{4.17}$$

Between equation 4.16 and 4.17, the decay rate can be known for every part of the beamline between the Rydberg target and detection. The question then becomes how to account for mixing within field flips, and in the field free regions.

One assumption is that there is some level of *m* mixing that occurs both in the field free regions, and at a flip in electric field direction. The difficult part is determining how much mixing occurs. All states could become equally mixed such that they all have equal populations, or there could just be a slight redistribution that increases the population of lower *m* values slightly, or any amount of mixing in between. The field free region between the 15º magnet and the start of the preionizer was assumed to completely mix *m* states within an *L* state due to its length. This assumed mixing is due to the earth's magnetic field (~0.5 G). The separation is a function of *m*, but is about 0.7 MHz times the *m* value. This is a time per cycle of 1.4/*m* microseconds. For U^{6+} at 150 keV, the amount of time in the field free region is several microseconds, meaning many cycles between states has occurred, and complete mixing is likely. The *L* states were assumed to be unchanged in this region. Of course the autoionization rates depend only on *L* in the field-free region.

The mixing at the field flips within the 10" preionizer and the Stark ionizer was left as variable. A parameter for each that allowed mixing to be varied from no mixing, to the population in each state being equal was used. This means the population in a given *L*, *m* state is mixed using:

$$P'_{L,m} = C_M \frac{\sum_{m'} P_{L,m'}}{2L+1} + (1-C_M)P_{L,m} \tag{4.18}$$

where C_M is the mixing coefficient, $P_{L,m}$ is the population in the state before mixing, and $P'_{L,m}$ is the population after mixing. This means if C_M is 0 the population in an *L*, *m* state after mixing is the same as it was before (no mixing occurs). If C_M is 1, then the population of each *m* state within an *L* value was equalized. This mixing does alter the autoionization rates since there is full Stark mixing after the field flip.

Another assumption is for the initial distribution of *L* and *m* values within an *n* state, and the *n* state distribution itself. The initial distribution in *n* was assumed to be uniform from *n* = 25 to 80, which are the states predicted to capture from CTMC. It is difficult to know the exact initial distribution in *L* and *m*, but one logical initial distribution is to assume that each *L* level has the same population, and within an *L* state each *m* state has an equal population. This was chosen as the initial population distribution. This initial distribution travels through 20 cm of field-free space and is then sent through the 15º magnet where the decay rate is dictated by the decay rate of the *m* values. That is to say it decays following equation 4.17 dependent on the *m* value of the state for the 0.23 meters within the magnet.

After the 15º magnet the remaining population within each *m* state is distributed equally amongst the *L* values that can contain that *m* value. Decay in the field free region is then dictated by equation 4.16 once again for the 1.30 meters between the end of the magnet and the start of the 10" preionizer. Once the start of the 10" preionizer is reached, the population within each *L* value is distributed equally amongst the *m* value for that *L* value, corresponding to the complete *m* state mixing that is assumed to occur within the field free region. Decay then occurs following equation 4.17 for the ramp up region until the field-flip within the 10" preionizer. At the field-flip, the total population within each m state is mixed (a varying amount depending on input parameter C_M from equation 4.18) and decay occurs once again following equation 4.17. Since there is a minimal change in field between the preionizer and the Stark ionizer, no mixing of *m* states is assumed to occur. An analogous procedure is then followed for the Stark ionizer.

This program was then used to determine the fraction of each metastable state formed at the Rydberg target that would survive to the entrance of the Stark ionizer. It was assumed that each metastable state would decay at the rate shown in table 4.3. Table 4.6 shows the decay

coefficient used for each metastable state. Only the C3 metastables have any population remaining after the 15˚ magnet, and most of the states that even make it to the 15˚ magnet are from the C3 state. That being said, only 8% of the original C3 population makes it to the entrance of the detector. Also shown in table 4.6 is the statistical weight for each state.

Table 4.6: The first column is the metastable state, the second column is the statistical weight of that state, the third column is the fastest decay channel for that state, the fourth column is the decay coefficient for that channel, the fifth column is the fraction of metastables present after the Rydberg target that survive to the start of the 15˚ magnet, the sixth column is the fraction of metastables present that survive to the end of the 15˚ magnet, and the seventh column is the fraction of metastables present that survive to the end of the detector entrance

Metastable State	Weight	Channel	A_C (1/s)	Fraction Surviving from the RT to the start of the 15˚ Magnet	Fraction Surviving from the RT to the end of the 15˚ Magnet	Fraction Surviving from RT to the Entrance of the 10" Preionizer
A2	5	A2 to A1	1.70×10^{25}	0.00	0.00	0.00
A3	7	A3 to B3	2.60×10^{23}	0.01	0.00	0.00
A4	9	A4 to A2	7.78×10^{22}	0.01	0.00	0.00
B2	5	B2 to A3	6.91×10^{23}	0.00	0.00	0.00
B3	7	B3 to A4	1.50×10^{24}	0.00	0.00	0.00
B4	9	B4 to A3	1.00×10^{24}	0.00	0.00	0.00
B5	11	B5 to A4	8.28×10^{23}	0.00	0.00	0.00
C2	5	C2 to C3	5.25×10^{23}	0.00	0.00	0.00
C3	7	C3 to A4	2.74×10^{18}	0.53	0.20	0.08
D3	7	D3 to C3	5.05×10^{22}	0.02	0.00	0.00
D4	9	D4 to C3	1.27×10^{23}	0.01	0.00	0.00

One prediction that can be made from the results shown in table 4.6 is the ratio of autoionizing metastable levels to the total U^{5+} beam at the 15˚ magnet. This is a number that can be deduced from measurements described in section 4.5. If it is assumed that the initial populations of Rydberg ions are proportional to the statistical weights of their core ions, e.g. G:A1:C3 = 1:3:7, and that 80% of the C3 Rydberg ions autoionize prior to leaving the 15˚

magnet (as predicted in table 4.6), then the ratio of metastable Rydberg ions to the total U^{5+} beam at the exit of the 15˚ magnet is:

$$f_{M,15^\circ} = \frac{7 \cdot 0.20}{4 + 7 \cdot 0.20} = 0.26 \tag{4.19}$$

Further insight can be gained by analyzing the decay of state C3 in more detail. Although the mixing coefficients are irrelevant for the short-lived states, it is very important for the C3 state since it has large effects on the overall survival. Figure 4.10 shows the fraction of C3 metastable ions left as a function of distance after the 15˚ magnet. There is an increased decay at the start of fields, and field flips due to the changes in decay rate and mixing that occurs there. It is also clear that about 40% of the metastable population that was present at the 15º magnet is still present after the field free region. It is also clear in figure 4.10 that the metastable decay rate is greatly increased within the electric fields, accounting for an approximately 80% decrease in population over the final 0.25 m compared to a 40% decrease over the first 1.27 m. The quick decreases seen at mixings (most easily seen at the entrance to the preionizer) indicates that mixing to extremely short-lived states occurs. This means that a lot of the decay that occurs due to mixing happens very shortly after the mixing event. This would explain why the background is centered around the ionization aperture. Mixing at the location of the Stark ionization aperture would greatly increase the autoionization rate by populating extremely short-lived states. These decay virtually immediately, meaning a relatively large amount of ions get energy tagged with the full potential.

This model also clearly shows why the preionizers work. The mixing that occurs when the Rydberg states enter the preionizer's field, as well as the mixing that occurs at the field flip within the preionizer causes an increased autoionization rate within the preionizer. This would

decrease the total number of metastable states that would make it to the Stark ionizer, meaning there were fewer states that could contribute to the background.

This model also demonstrates the presence of the regenerated primary. Even though figure 4.10 shows only the C3 metastable state's population (the only state that has any survival to the detector), half of its initial population ionizes in a field free region. This would already result in a regenerated primary that was larger than the background, but taking into account all the other states that don't survive to the detector, the regenerated primary could be quite large, which fits experimental observation.

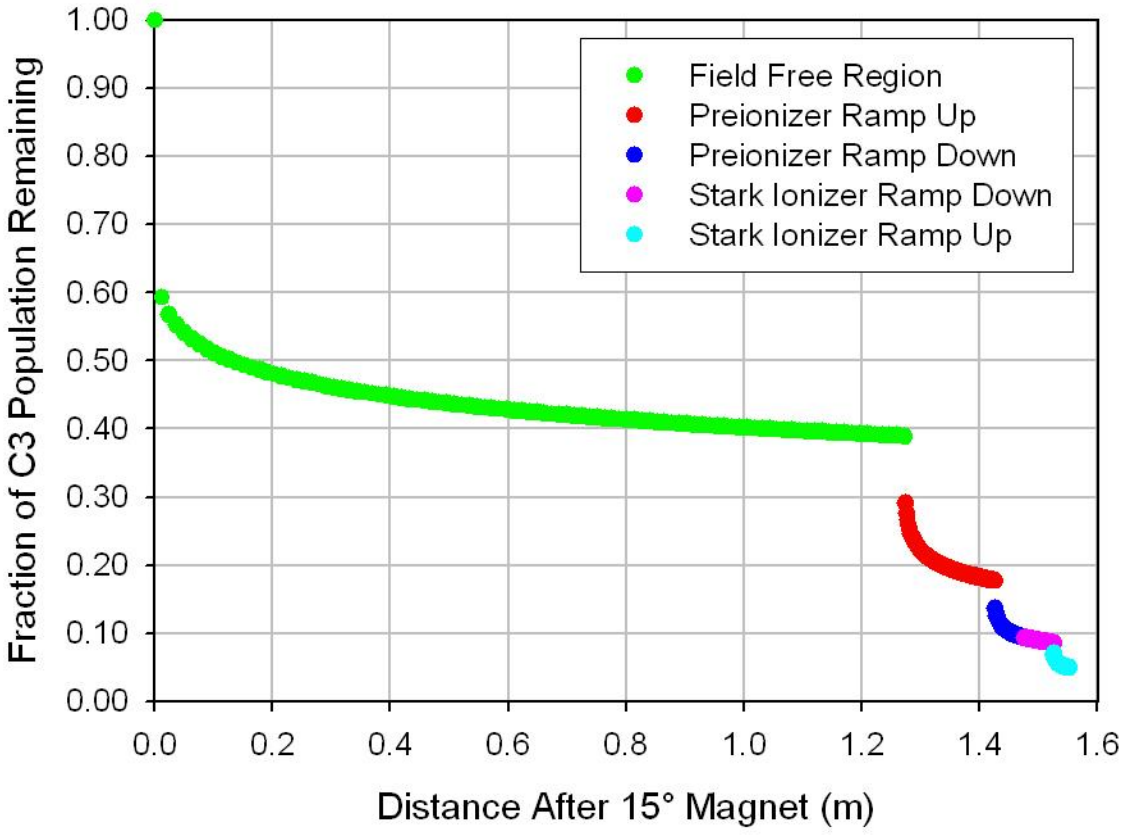

Figure 4.10: Fraction of C3 metastable ions remaining as a function of distance traveled after the 15˚ magnet assuming the mixing coefficients are both 1. The different colors correspond to the individual decay regions as separated by mixing events. According to table 4.6, only 20% of the C3 metastable Rydberg levels survive to the end of the 15˚ magnet, where figure 4.10 shows the C3 population as 1.0.

Ideally, predictions made by this modeling would be compared to experimental measurements. Previously there was no way to measure metastable beam concentrations experimentally. For this reason, both theoretical and experimental methods were developed and will be discussed. The next section will explain the experimental method in detail. The rest of this section will explain the theoretical predictions that can be made with the model that was just explained, specifically referencing values that can be measured experimentally.

First a few important values need to be defined. There are four important values that correspond to absolute ion counts that can be directly measured on the CEM. The first is the regenerated primary from the preionizer (RPP). The RPP is the ions that ionize and are energy tagged within the preionizer region. This would be the ions that ionize in the region around the plate at $V_{10"}$. The second value is the background (B), which is the metastable states that ionize and our energy tagged within the Stark ionizer when the preionizer is off. The third value is the change in background when the preionizer is on (ΔB). This can be easily measured experimentally by comparing the size of the background when the preionizer is on and off. This also means that the size of the background when the preionizer is on is simply $B-\Delta B$. These four values (RPP, B, ΔB, and $B-\Delta B$) are all easily measured on the CEM.

The next value that is important is the amount of metastable states that are present at the start of the electric field flip in the Stark ionizer (M_S). Specifically this would be the metastable population ¼" (6.4 mm) before the plate in the Stark ionizer that is at $-V_S$. This is when there begins to be a perpendicular electric field, indicating that the electric field begins to change directions. Unlike the previous values, this value can't be measured directly on the CEM. This is because some fraction of these metastable states don't autoionize within the Stark ionizer and will show up as CXRT at the CEM. These would be inseparable from other ions that contribute

to the CXRT (ground state ions, non-autoionizable metastable states), and therefore it is not known how many of them that there are. For this reason, M_S can't be directly measured. It is however very important, and measuring its size is one of the goals of this analysis.

The next type of values that need to be defined are fractional changes in metastable beam populations. These can't be directly measured in the experiment, but can be calculated from values that can directly be measured on the CEM. The first is the efficiency of the Stark ionizer field flip in creating autoionization (ε_{SI}). This is defined as the fraction of metastable states that autoionize within the Stark ionizer field flip (B) compared to the metastable states that enter the electric field flip (M_S), explicitly it is:

$$\varepsilon_{SI} = \frac{B}{M_S} \tag{4.20}$$

This value is indirectly related to the mixing that occurs at the electric field flip in the Stark ionizer since the size of the background depends on the amount of mixing, so this value gives a metric for the amount of mixing. The second fractional value of importance is the total killing efficiency of the 10" preionizer (K_{PI}). This is defined in terms of the decrease in M_S when the preionizer is on compared to when the preionizer is off. To discuss this value, two situations can be considered. In situation A, the preionizer is off and the Stark ionizer is on. In situation B both the preionizer and the Stark ionizer are on. In situation A, there is a certain amount of metastable states entering the Stark ionizer, $M_{S,A}$. In situation B, since the preionizer is on, fewer metastable states reach the electric field flip and could contribute to the background, $M_{S,B}$. The difference between $M_{S,A}$ and $M_{S,B}$ (ΔM_S) would be the amount of metastable states that autoionize in the preionizer that wouldn't autoionize if the preionizer was off. The killing efficiency of the preionizer is then just what fraction of metastable states that would reach the detector when the preionizer is off are killed in the preionizer, explicitly:

$$K_{PI} = \frac{\Delta M_S}{M_{S,A}} \tag{4.21}$$

Assuming ε_{SI} is the same in both situation A and situation B, then the killing efficiency of the preionizer can also be written in terms of the background:

$$K_{PI} = \frac{\varepsilon_{SI} M_{S,B} - \varepsilon_{SI} M_{S,A}}{\varepsilon_{SI} M_{S,A}} = \frac{\Delta B}{B} \tag{4.22}$$

Since both B and ΔB are measurable, then K_{PI} can be calculated easily. The final fractional value that needs to be defined is the fraction of K_{PI} that occurs at the electric field flip in the preionizer. The total decrease in metastable ions has been defined as ΔM_S, but a certain fraction of these will be ionized at the electric field flip in the preionizer, and will be energy tagged at the full $V_{10"}$ potential which were defined to be RPP. This fraction is called f_{PI}, and is thus defined as:

$$f_{PI} = \frac{RPP}{\Delta M_S} \tag{4.23}$$

The definition of these values now enables further analysis on the metastable population within the experiment to be carried out.

The model discussed in this section will now be used to make predictions that can be compared to experimental values. For this analysis the C3 states decay rate is still used within the model since it appears to be the only state that survives to the detector. Since both situation A (preionizer off, Stark ionizer on) and situation B (preionizer on, Stark ionizer on) each situation will be modeled. Figure 4.11 shows what the voltage scheme looks like for situation A, and shows the fraction of the C3 metastable population remaining as a function of the distance traveled past the 15˚ magnet. Within the model used to create figure 4.11 it was assumed that the mixing coefficient for the Stark ionizer was 1 ($C_M = 1$). Labeled in figure 4.11 is the decay that

occurs within .064 m (0.25”) on either side of the plate at $-V_S$. The metastable states that autoionize in this region are assumed to be energy tagged with the full $-V_S$ potential and would show up as background (B).

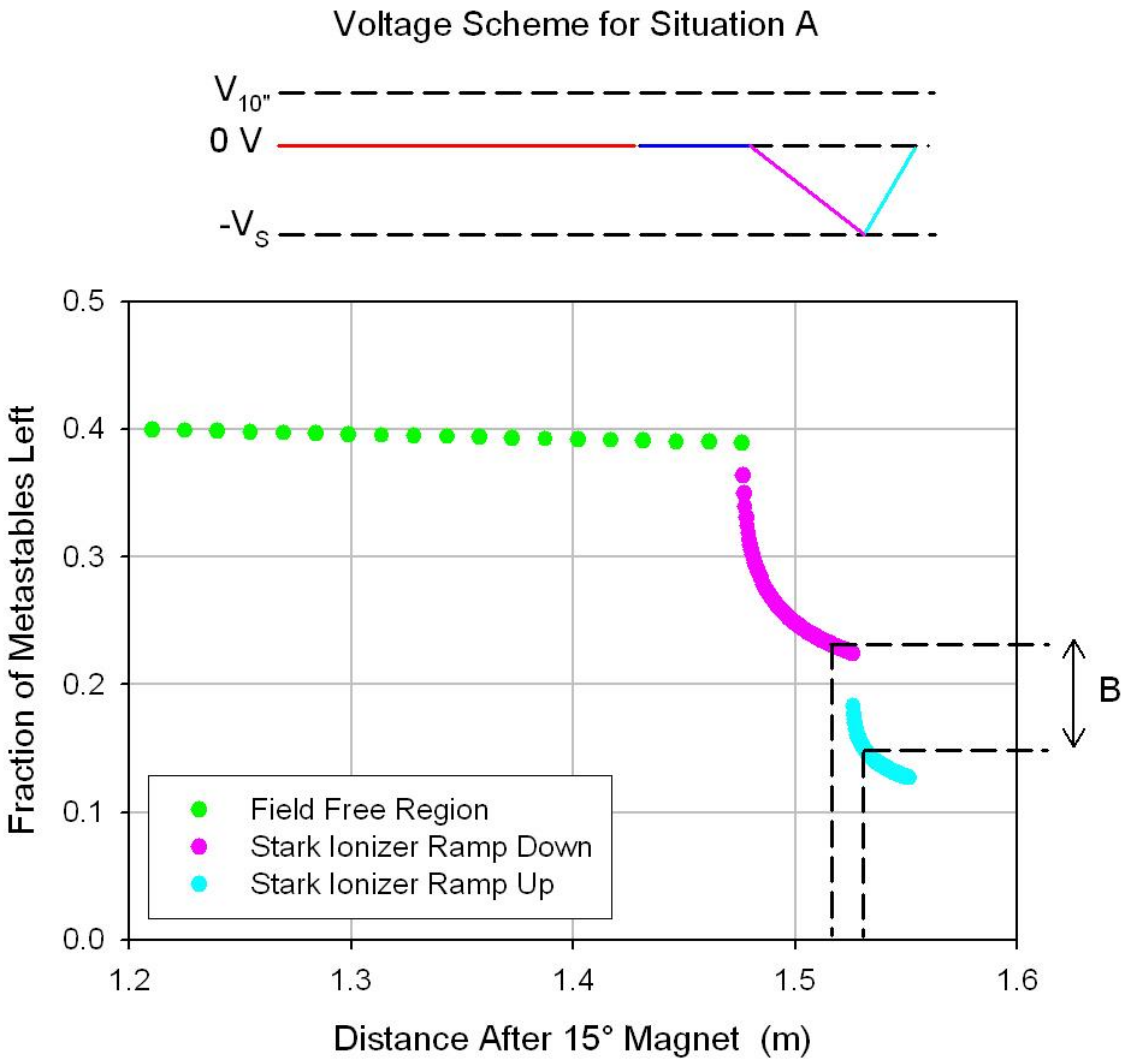

Figure 4.11: Voltage scheme and metastable decay for situation A. The voltage scheme at top shows the preionizer as off and the Stark ionizer potential. The graph shows the fraction of C3 metastable states that are present as a function of the distance traveled beyond the 15˚ magnet. Labeled on the graph is the autoionization that would contribute to the background (B).

Figure 4.12 shows what the voltage scheme looks like for situation B, and shows the fraction of the C3 metastable population remaining as a function of the distance traveled past the 15˚ magnet. Within the model used to create figure 4.12 it was assumed that the mixing

coefficient for both the preionizer and the Stark ionizer was 1 (C_M = 1 for each). Labeled in figure 4.12 is the decay that occurs within 0.064 m (0.25") on either side of the plate at $V_{10"}$. The metastable states that autoionize in this region are assumed to be energy tagged with the full $V_{10"}$ potential and would show up as regenerated primary from the preionizer (RPP). Also shown are the ions that would contribute to the background when the preionizer is on (B- ΔB).

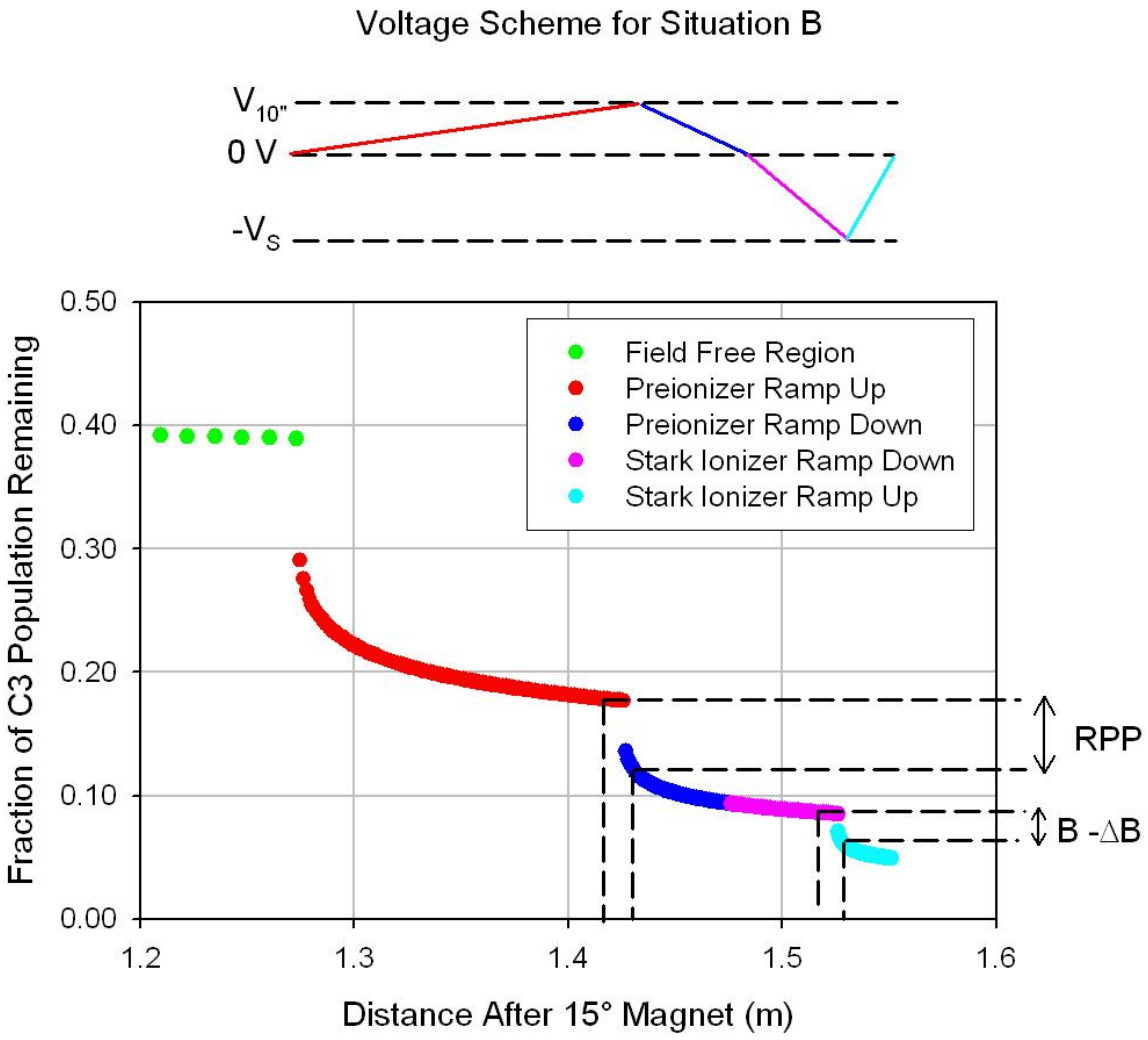

Figure 4.12: Voltage scheme and metastable decay for situation B. The voltage scheme at top shows the preionizer, and the Stark ionizer potentials. The graph shows the fraction of C3 metastable states that are present as a function of the distance traveled beyond the 15˚ magnet. Labeled on the graph is the autoionization that would contribute to the background with the preionizer on (B-ΔB). Also labeled on the graph are the ions that would contribute to the regenerated primary from the preionizer (RPP).

Figures 4.11 and 4.12 demonstrate how the B, B-ΔB, RPP, $M_{S,A}$, and $M_{S,B}$ can be predicted as a fraction of the initial metastable population at the 15˚ magnet (scaled to 1). Specifically, from figure 4.11 $M_{S,A}$ is found to be about 0.24 of the metastable population leaving the 15˚ magnet, M_{15°, whereas from figure 4.12 $M_{S,B}$ is found to only be about 0.09 (meaning ΔM_S is 0.15). This shows that the killing efficiency is about 63%. These figures also show that there are a lot of factors that contribute to the total K_{PI}. By turning on the preionizer, the ionization within the preionizer is clearly greatly increased, but the ionization in the Stark ionizer ramp down is decreased since there is no mixing between the preionizer and the Stark ionizer. These two competing factors are both taken into account with the definition of K_{PI} since it takes into account the net increased autoionization between the two cases, and not just the increase in the preionization region. The RPP can be read as being roughly 0.06, which gives f_{PI} as also roughly 40%. This sort of analysis allows meaningful predictions to be made that will be compared to experiment in the next section.

Table 4.7 shows the predictions for values for two mixing coefficient possibilities. One of the situations considered is when both the preionizer and the stark ionizer have the same mixing coefficient ($C_M = 1$). The third possibility considered is where the preionizer has more mixing than the Stark ionizer ($C_{M,PI} = 1$, and $C_{M,SI} = 0.5$). The values for ε_{SI} and K_{PI} are the same so long as the mixing coefficients are the same since the distances that contribute to it are the same. For both cases f_{PI} is predicted to be about 50%. This means that if the RPP were measured, this would correspond to about half the total increased killing that occurs by turning the preionizer on. This is a factor that will be used in the experimental section.

Table 4.7: Comparison of some key observations from modeling metastable state decay between different mixing coefficients used in the model.

Property	$C_{M,PI} = 1$ $C_{M,SI} = 1$	$C_{M,PI} = 1$ $C_{M,SI} = 0.5$
ε_{SI}	36%	22%
K_{PI}	62%	62%
f_{PI}	44%	44%

This modeling so far provides insight into what might be expected to occur with the metastable state populations as they pass through the beamline. It appears metastable autoionization can explain the presence of a large regenerated primary, and the presence of the background. It also explains the background's isolation at the peak Stark ionization potential. It also has an explanation of why the preionizer works. All of this analysis helps settle many of the questions about the metastable autoionization hypothesis. This makes it not only the only hypothesis that has no direct evidence against it, it also explains most of the properties known about the background. There are only a few remaining things that need to be considered to have a good deal of faith with the conclusion that autoionization of metastable states causes the background. These are:

1. Can the metastable population at the detector be experimentally measured?
2. Why do the different Stark ionizer configurations result in different background sizes?
3. How well do the preionizers work?

The rest of this chapter will be devoted to investigating these questions.

4.5 Measuring U^{6+} Metastable Populations

One difficulty that arose when attempting to analyze the possible effects of metastable population in the U^{6+} RESIS technique was the lack of knowledge about the metastable content

of the ion beam. Previous studies have measured metastable content of ion beams [21,22], but they required a precise knowledge of metastable ion levels, and involved fewer metastable states. This meant a novel technique would have to be developed that could help this research project, as well as directly contribute to the scientific community at large. This section outlines the method that was developed.

The method developed to determine metastable concentrations revolves around the metastable preionization. It is important to note that this analysis assumes that the regenerated primary and background are created through metastable autoionization. Due to the evidence discussed throughout this chapter, this seems to be true. Making this assumption allows further analysis to be made, and if the results appear to be consistent with experimental observation then it helps justify this assumption.

To understand the procedure, a review and better analysis of the beams that are present within the detector is needed. U^{6+} will be used as an example ion to demonstrate this procedure, but it is applicable to any arbitrary ion. Figure 4.13 shows a block diagram of the beamline as it pertains to the beams that are present. At the start of the beamline, after front end tuning, the ion beam is exclusively U^{6+}. After passing through the Rydberg target, the beam is comprised of U^{6+} that did not capture a Rydberg electron, and U^{5+} Charge Exchange (CX) Rydberg states that did. The purpose of the 15˚ magnet is to separate the Rydberg U^{5+} from uranium that did not capture, so after it the beam is exclusively U^{5+}. Part of this beam is excited within the CO_2 LIR region. Since excitation only happens from a single *n* state, there are plenty of *n* states that would still be populated, but not excited. Once the beam reaches the detector, the relatively small fraction of the beam that was excited in the LIR will be Stark ionized and energy tagged to have a lower

kinetic energy. The beam therefore is mainly U^{5+} that was not Stark ionized, and some U^{6+} that is the signal ions separated by charge and energy from the U^{5+}.

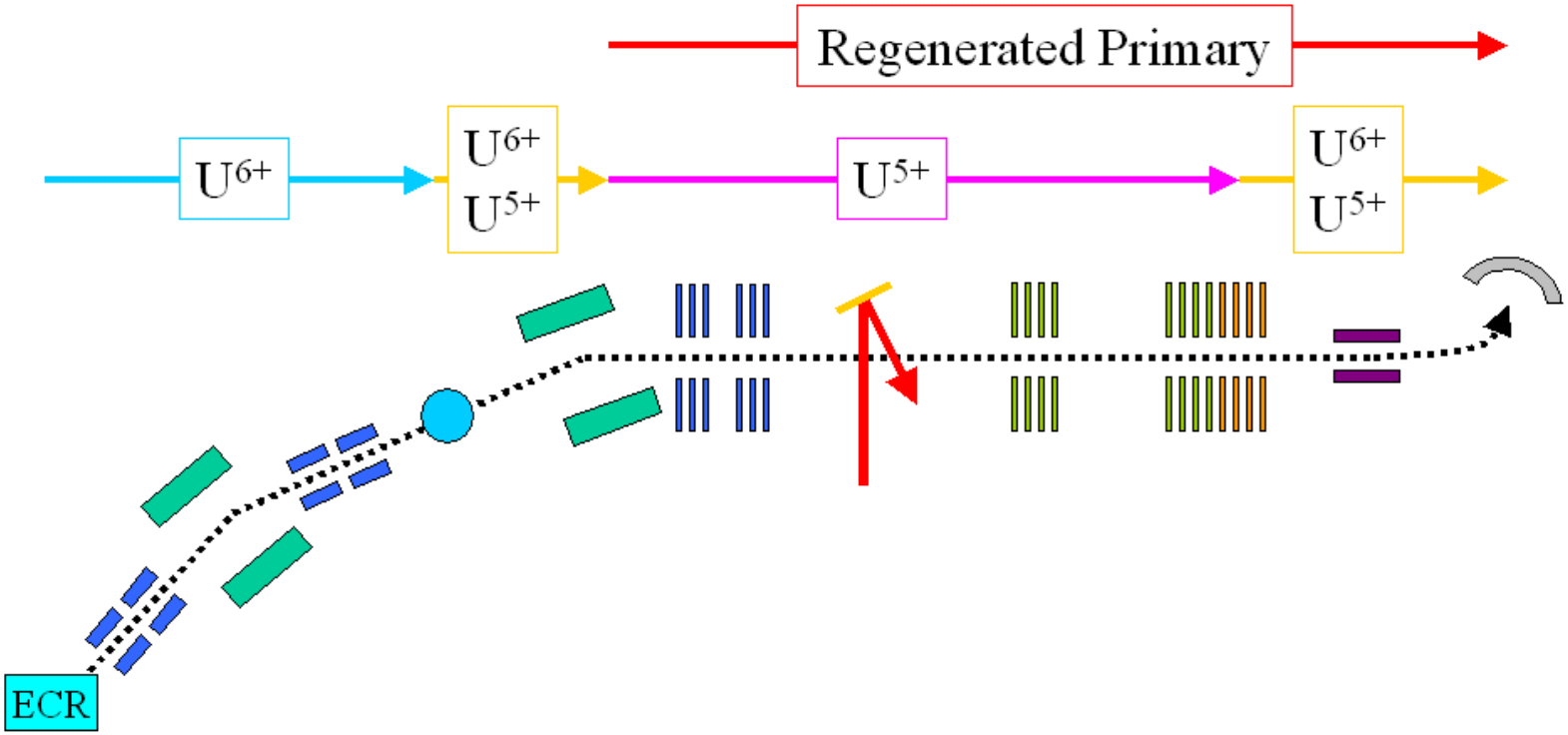

Figure 4.13: Schematic of the beamline showing what beams are present. The part of the beamline where autoionization of metastables can create the regenerated primary is also shown

As discussed, there is also the production of a Regenerated Primary (RP) beam throughout the beamline due to the autoionization of metastable states that complicates things. This means after the 15˚ magnet there are U^{5+} states ionizing back to the primary charge of U^{6+} that will make it all the way to the CEM as U^{6+}. These are different in energy from the Stark ionized U^{6+} signal ions since they have not been energy tagged. However, the autoionization that occurs within the preionizers and Stark ionizer would be energy tagged. The autoionization within the preionizers which are at positive potential will increase their kinetic energy separating it from the signal ions and constitutes a beam referred to as the Regenerated Primary from the Preionizers (RPP) peak. The autoionization that occurs within the Stark ionizer, however, will be energy tagged in the same way, and has the same charge and energy as the signal ions. These autoionized ions constitute the Background (B). This means there are four distinct beams present within the detector. For clarity, lets examine a standard case where for a U^{6+} beam at 150 keV where the Stark ionizer is at –5000 V, and the 10" preionizer is at 3000 V (6" preionizer is not needed for any of this analysis and is therefore off). The beams in the detector are separated from each other within the vertical deflector plates by their energy/charge (E/Q). For a set voltage on the vertical deflector plates, the lower the E/Q ratio, the larger the deflection. In this case the signal and background are tagged with –5 keV making their net kinetic energy 145 keV and their net charge is 6+. Since they have the largest charge, and the lowest energy they have the lowest E/Q ratio, ~24. The next beam in E/Q is the regenerated primary, which is charge 6+, but has not been energy tagged and is therefore still at the nominal kinetic energy of 150 keV (E/Q ~25). The RPP follows in E/Q since it also has a 6+ charge, but has been accelerated to a kinetic energy of 153 keV (E/Q ~25.5). Finally comes the CX beam that is still

at charge 5+ and 150 keV giving it an E/Q of ~30. A visual of these four beams is shown in figure 4.14.

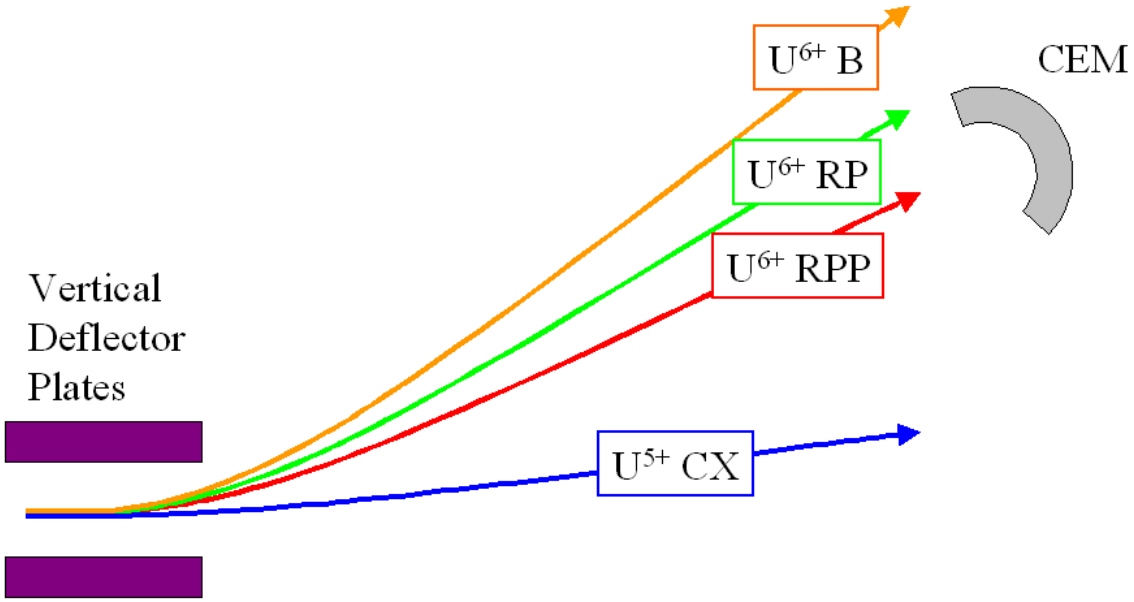

Figure 4.14: The beams that are present in the detector, and their vertical separation from the vertical deflector plates set to a constant voltage that would deflect the RPP into the CEM.

These beams can be seen on the beamviewer to give a qualitative look at them. Figure 4.15 shows the same photograph discussed shown earlier on page 50, but with the four beams within the detector labeled similarly to figure 4.14. The background, regenerated primary, and regenerated primary from the preionizer are all clearly seen as separate peaks, although not necessarily completely resolved. The charge capture is off the beamviewer screen at the time of the photo, but is clearly seen, and much brighter than any other beam. For reference, the dark circle on the screen in figure 4.15 has a diameter of 0.8 cm, while the aperture in front of the CEM has a diameter of 0.32 cm. Thus, it seems reasonable to assume that, when properly tuned, the CEM collection efficiency is close to 100%.

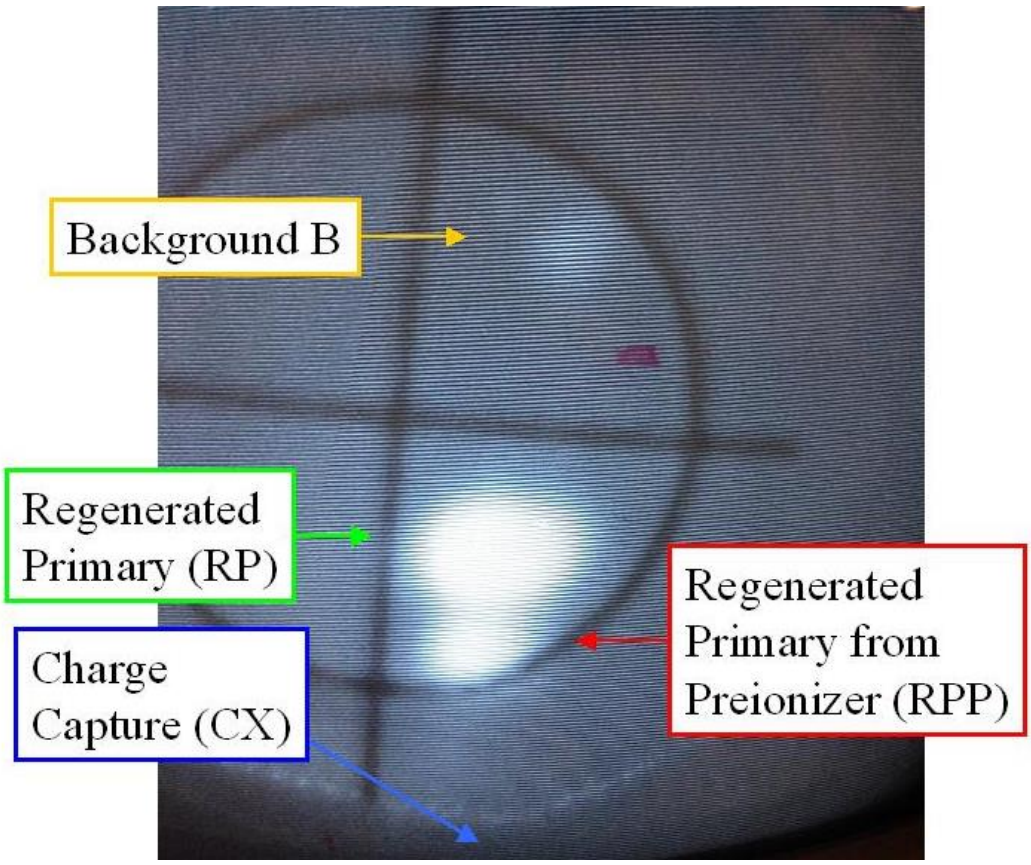

Figure 4.15: Photograph of the beamviewer showing the beams within the detector. Not shown is the charge capture beam.

Also shown in figure 4.14 is the CEM to emphasize the idea that a beam of choice can be directed into the CEM for quantitative detection by choosing the proper voltage on the vertical deflection plates. Figure 4.16 shows a vertical deflection scan for U^{6+} at 150 keV showing the presence of the beams discussed (note the vertical axis is on a log scale).

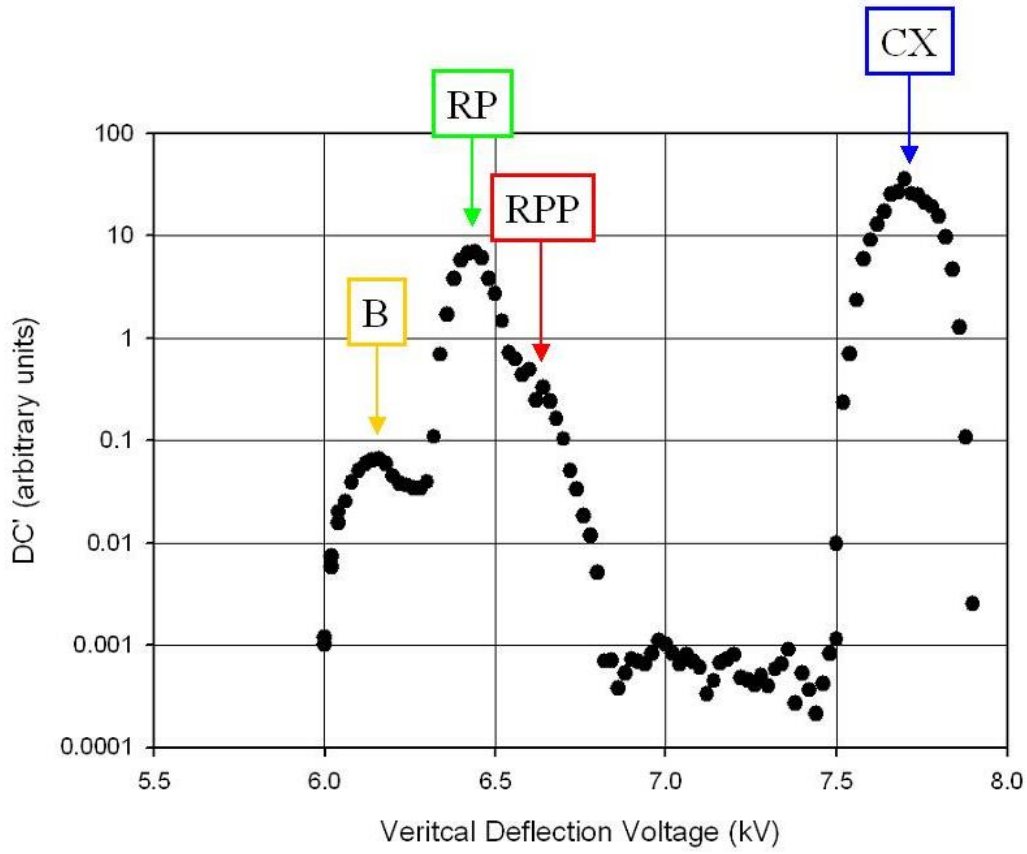

Figure 4.16: Vertical deflection scan showing the relative positions and sizes of the Background (B), Regenerated Primary (RP), Regenerated Primary from Preionizer (RPP) and the Charge Exchange (CX) beams.

There are five key values that can be measured from these beams that will allow something to be learned about the metastable fraction content of the beam. The first is to measure the change in the size of the background with (B-ΔB) and without (B) the 10" preionizer. This is easy to determine by tuning the detector for the background, and simply taking a few points with the 10" preionizer on, then a few with the 10" preionizer off. In order to account for beam fluctuations, normalization of the background to the size of the high-*L* peak was done since it was also measured while the background is measured, and it doesn't change size as a result of the preionizer. The third value needed is the size of the regenerated primary (RP). This is easy to do by simply tuning the detector for the regenerated primary. The next is

the size of the regenerated primary from the preionizer (RPP). This is a bit harder than measuring RP since it is not completely separated from the regenerated primary. For this reason, the detector is tuned for the RPP peak, and then data is collected with the 10" preionizer on and off in order to determine the change in size at that location. This change in size due to the 10" preionizer is defined as the RPP. The final value needed to measure is the charge exchange from the Rydberg target (CXRT). The charge capture peak seen in figure 4.16 is comprised of ions that capture an electron from the Rydberg target, and also ions that capture an electron from other sources (primarily ground state rubidium) but how much comes from the target is what is needed. By tuning the detector to look at the charge exchange, then taking data with L3 open and blocked, it can be determined how much of the charge exchange is from the Rydberg target. These are the five (the RP, RPP, ΔB, B, and CXRT) key values needed to continue. All of these are measured as mV outputs of the CEM, correcting to a constant value of CEM gain.

In the previous section, these values were related to metastable populations that can now be used to link experimentally measurable values to metastable populations. The first value needed is the killing efficiency of the preionizer, which is the fractional decrease in background due to turning on the preionizer:

$$K_{PI} = \frac{\Delta B}{B} \tag{4.24}$$

which is also equivalent to:

$$K_{PI} = \frac{\Delta M_S}{M_S} \tag{4.25}$$

where M_S is the metastable flux entering the electric field flip in the Stark ionizer when the preionizer is off, and ΔM_S is the change in this flux by turning on the preionizer. Since ΔB and B

are measurable, K_{PI} is known using equation 4.24. The RPP was linked to ΔM_S by definition of f_{PI} in equation 4.23, which can be related to M_S using equation 4.25 to give:

$$RPP = f_{PI} \cdot \Delta M_S = f_{PI} \cdot K_{PI} \cdot M_S \tag{4.26}$$

Rearranging equation 4.26 gives:

$$M_S = \frac{RPP}{f_{PI} \cdot K_{PI}} \tag{4.27}$$

Both the RPP and K_{PI} are known, but f_{PI} can't be determined experimentally. The theoretical model used in the previous section found that $f_{PI} = 0.44$. This theoretical value was used in order to find a value of M_S from experimental values. This then gives a way to measure the metastable flux of the beam entering the electric field flip, something that was completely unknown before this work.

Although the metastable content of the beam at the electric field flip in the Stark ionizer is important, ideally it would be good to know the initial fraction of the beam that is metastable. It is difficult to learn anything directly about the beams before the 15˚ magnet. For instance, any metastable ions that capture a Rydberg electron and auto-ionize before the 15˚ magnet would not be transported down the rest of the beamline, and therefore knowledge of them is lost. For this reason, the metastable fraction immediately after the 15˚ magnet (M_{15°) is the earliest fraction that can be measured. It is known that the regenerated primary corresponds to metastable ions that have autoionized before the energy tagging in the Stark ionizer, meaning the total metastable population at the 15˚ magnet is the regenerated primary (population that has autoionized before the detector), combined with the population left at the Stark ionizer:

$$M_{15^\circ} = M_S + RP \tag{4.28}$$

This can also be related to the total beam size at the 15˚ magnet. The total Rydberg beam that is not metastable is simply the CXRT. This means the total beam at the detector ($Beam_{15^\circ}$) is:

$$Beam_{15^\circ} = M_{15^\circ} + CXRT \tag{4.29}$$

Which means the fraction of the beam that is metastable at the 15˚ magnet ($f_{M,15^\circ}$) is:

$$f_{M,15^\circ} = \frac{M_{15^\circ}}{Beam_{15^\circ}} \tag{4.30}$$

Another important metric to look at is the fraction of metastable ions that have decayed between the 15˚ magnet and the detector ($f_{Decayed}$):

$$f_{Decayed} = \frac{RP}{M_{15^\circ}} \tag{4.31}$$

The killing efficiency of the Stark ionizer electric field flip can also be determined by comparing the background, B, to M_S. It was defined as the fraction of the metastables arriving at the Stark ionizer show up as background:

$$\varepsilon_{SI} = \frac{B}{M_{\det}} \tag{4.32}$$

This procedure and set of equations gives the ability to relatively simply measure 5 key values and determine a lot about the metastable concentration of the beam having used only one value taken from theoretical modeling. There are a few simplifying assumptions made within this procedure. The first is the collection of the beams with the CEM. At the front of the CEM is a $1/8^{th}$-inch aperture. It is assumed that all of a beam of interest is collected. Also, the lack of resolution between the RPP and RP that is obtained with this aperture means that it can be difficult getting an accurate size reading for the RPP. The collection of beams can therefore give relative beam sizes that have a degree of uncertainty to them.

This method was used to determine the metastable composition of the U^{6+} beam at 150keV. Table 4.8 shows the measured values from the best experimental measurement in the first section, and the values calculated from the measured values in the second section. This now gives numbers that can be compared to theory for analysis of the metastable autoionization hypothesis. The main things to be noticed in table 4.8 are the large fraction of metastable states that decayed between the 15˚ magnet and the detector, 92%. The killing efficiencies for the 10" preionizer, and the Stark ionizer are also of note, each one being fairly large, around 40%. These shows just how effective even a small field can be in increasing the metastable autoionization rate.

Table 4.8: Overview of U^{6+} at 150keV metastable measurements. The first section shows the measured values outlined in this chapter. The second section shows the values that were calculated from the measured values. The n = 53 to 93 transition was used and the data is from the file CSS6-151. The potential used on the Stark ionizer was –8000 V on the 1":2", and the potential used on the preionizer was 7000 V.

Measured Values	
B (mV at 1300)	70
S_{HL} (mV at 1300)	3.9
RP (mV at 1300)	2688
CXRT (mV at 1300)	3768
RPP (mV at 1300)	55.4
ΔB (mV at 1300)	31.3
K_{PI}	45%

Calculated Values	
Time to Detector from the 15˚ magnet (μs)	4.52
M_S (mV at 1300)	246
M_{15° (mV at 1300)	2934
$Beam_{15^\circ}$ (mV at 1300)	6702
$f_{Decayed}$	92%
$f_{M,15^\circ}$	44%
ε_{SI}	28%
$M_S/Beam_{15^\circ}$	3.7%
$S_{HL}/ Beam_{15^\circ}$	0.06%
$B/ Beam_{15^\circ}$	1.04%

Table 4.9 is a comparison of some theoretically predicted values from the last section, and values measured. The measurements reported are from a standard experimental measurement, but there were fluctuations in the measured killing efficiencies found to be within a factor of about 1.2 of the values reported here. These comparisons are quite good all things being considered. The efficiency of the Stark ionizer is consistent with a medium amount of mixing. The overall killing efficiency of the 10" preionizer is smaller than the fully mixed case in the preionizer, $C_M = 1$. The theoretical value for M_S/ M_{15° was taken from the modeling of the C3 decay shown in figure 4.11. The experimental measurement matches to within a factor of three. The measurement of $f_{M,15^\circ}$ matches the prediction from equation 3.19 to within a factor of two. The predictions of these two ratios are particularly significant because they do not depend on the choice of the parameter C_M, but only on the calculated autoionization lifetimes and the initial populations. If it is assumed that the initial populations of ground and metastable levels in the original U^{6+} beam are in the ratios of the statistical weights of the several levels, then the calculated lifetimes predict that only the C3 metastable levels survive to the exit of the 15˚ magnet, and that they do so with probability 0.20. This immediately yields the prediction of $f_{M,15} = 0.26$, which is found to be low by about a factor of two. Similarly, if it is assumed that, as predicted, only the C3 metastables survive beyond the 15 degree magnet, then their calculated lifetimes predict that $M_S/M_{15^\circ} = 0.23$, a value that is found to be too high by a factor of three. These two discrepancies together suggest that perhaps some of the autoionizing metastable Rydberg levels beyond the 15˚ magnet are actually not C3 metastables, but other shorter-lived metastables. This would require some modifications of the autoionizing lifetimes, or (less likely) some different assumptions about the initial populations at the Rydberg target. In any case, the

agreement between model and observations is sufficient to support the main conclusions that metastable Rydberg levels are the main source of the background.

Table 4.9: Comparison of theoretical and experimental values from metastable population analysis. ε_{PI} is the efficiency of the 10" preionizer. ε_{SI} is the killing efficiency of the Stark ionizer. M_{det}/ M_{15° is the fraction of metastable states at the 15˚ magnet that survive to the detector.

Value	Experimental Value	Theoretical Value
ε_{SI}	28%	22%-36%
K_{PI}	45%	62%
M_S/ M_{15°	8.4%	23%
$f_{M,15}$	44%	26%

4.6 Fraction of Metastable States at Capture

The last section demonstrates that the modeling of metastable populations after the 15˚ magnet matches well with experimental values. The model in section 4.3 not only analyzes the metastable populations after the 15˚ magnet, but also in the region between capture and the 15˚ magnet. This allows some suggestions about the composition of the Rydberg beam, and the preceding ion beam at the time of capture. A main conclusion of the model, based on the calculated autoionization lifetimes, is that only a small fraction of autoionizing metastable Rydberg levels formed at capture survive beyond the 15˚ magnet, where they can be measured. Consequently, the initial metastable fraction in the Rydberg beam at capture is very likely to be much more than the 44% measured after the 15˚ magnet. There is some evidence to suggest that the U^{6+} excited levels may be populated near statistical weights. One measurement shows that the resolved RESIS signals are at least a factor of four smaller than predicted in Chapter 5, consistent with the hypothesis that 75% of the stable Rydberg levels are bound to the A1 excited level of U^{6+}. The factor of four would be consistent with statistical weighting of the relative populations of the ground state and A1 state. Another line of evidence is the measurement of

$f_{M,15}$. This is found to be a factor of two larger than the value predicted based on statistical population of the C3 metastable level and the model's prediction that only these autoionizing metastable levels survive beyond the 15 degree magnet. Had this measurement been smaller than this prediction, it might have suggested that the metastable levels were populated at less than statistical levels. So, while there is no direct evidence about the population of any of the metastable levels other than A1 and C3, it is entirely possible that they are all initially populated at statistical levels.

Something that could affect these predictions is the spontaneous E2 decay of metastable states to the ground state. There are three states where this is possible A2, B2 and C2. As mentioned earlier, theoretical values for the decay rate are known [19]. The spontaneous E2 decay rate to the ground state is 8.2 s^{-1} for the A2 state, $3.8x10^3$ s^{-1} for the B2 state, and $3.4x10^4$ s^{-1} for the C2 state. These rates are far too small to affect the distribution of population in the 1.2 μs of transit time between the Rydberg target and the end of the 15˚ magnet.

To summarize, estimates of the metastable content of the Rydberg beam are consistent with the hypothesis that the initial U^{6+} beam obtained from the ECR ion source has metastable content consistent with the statistical weight of the first excited configuration of U^{6+} consisting of a 6p hole and a 5f valence electron. The statistical weight of these levels is 2*3*2*7 = 84, while the statistical weight of the $6p^6$ ground state is 1. Thus, it appears that the initial U^{6+} beam could be 84/85 = 98.8% metastable. The same would be true of the initial Rydberg beam formed by charge capture from this ion beam, meaning that only 1.2% of the initial Rydberg beam consists of Rydberg electrons bound to the ground state of U^{6+}. Of the 98.8% metastable Rydberg levels, most can autoionize. Only those bound to the A1 metastable level are forbidden to autoionize. These form 3.5% of the initial Rydberg beam, and since they are stable, they

contribute both to the measured U^{5+} beam current, the CXRT as it is denoted in chapter 5, and to the RESIS signals. Because of their higher statistical weight, the A1 Rydberg levels actually account for 75% of the RESIS signal, and this may be the primary reason for the very small resolved RESIS signals seen in U^{6+}, as discussed in chapter 5. The other metastable Rydberg levels, 95.3% of the initial Rydberg beam, are allowed to autoionize, and most are predicted to do so very rapidly. Only one metastable Rydberg series, the one bound to the C3 metastable level, is predicted to autoionize slowly enough that some of it remains at the detector where it can contribute to the background. Calculations suggest that the small fraction of the C3 Rydberg levels that survive to the detector produce a background that is 0.13% of the size of the total initial Rydberg beam flux at the Rydberg target. This, however, is much larger than even the high-*L* RESIS signal which is found (in Chapter 5) to be approximately 0.2% of the stable Rydberg flux, or about 0.01% of the initial Rydberg beam. Thus, the metastable U^{6+} levels contribute critically to the explanation of both of the difficulties encountered in the U^{6+} RESIS studies, the large background and the small signals.

4.7 Stark Ionizer Configuration and Background Production

One major question that remains is why do different configurations of the Stark ionizers produce different amounts of background? As discussed, one property of the background is that the SLG Stark ionizer had background sizes that were ten times the size of the half-inch Stark ionizer. The metastable autoionization has a possible explanation for this, that the amount of mixing that occurs within the Stark ionizer is dependent on the properties of the electric field flip in the Stark ionizer. The idea would be that the relatively small transverse field that occurs in the longer Stark ionizers does a more effective job of mixing than the shorter field flips, and therefore more autoionization is induced. As discussed when analyzing the mixing of $n = 3$

hydrogen, the adiabaticity of the passage through the electric field determines the amount of mixing that can occur. Thus the question can really be posed, does the background size depend on how adiabatic the field flip in the Stark ionizer is?

The first question is how adiabatic a field flip might be for a typical $n = 45$ metastable state. Using equation 4.15 for calculating the critical time for the passage through the ¼" aperture for U^{6+} metastable states with $n = 45$ and a typical perpendicular field, the critical time is found to be ~.09 ns. This critical time is much smaller than a typical experimental time through the ¼" aperture which is tens of nanoseconds. This means that all of the transitions are on the adiabatic end of things. Presumably becoming less adiabatic would create more mixing within the Stark ionizer and result in a greater background. This hypothesis can be tested by looking at various U^{6+} transitions that have varying degrees of "adiabaticity" Stark ionizer transitions and determine if the background gets larger as the electric field transition becomes less adiabatic.

One question is how to judge how adiabatic the electric field flip is? As mentioned, the two main factors are the size of the perpendicular field, and the time to pass through the detector. To determine the relative size of the electric fields in the Stark ionizer, Gauss' law was used. There are no enclosed charges in the detector, which means $\nabla \cdot \vec{E} = 0$ or more conveniently that the net electric field flux must be zero. The perpendicular field flux must therefore be proportional to the net flux along the axis. It follows that the perpendicular field must be proportional to the change in electric field along the beam axis, ΔE_Z. The "adiabaticity" is therefore proportional to this parameter. The "adiabaticity" also increases with the amount of time it takes to pass through the field flip. The time is inversely proportional to the square root

of the kinetic energy. This means a metric to determine how adiabatic the transition is can be defined as:

$$\alpha = \frac{\Delta E_Z}{\sqrt{KE}}$$

This can be referred to as the "adiabaticity" of the transition. As this parameter goes up, the transition becomes more adiabatic, and as it goes down the transition can be said to be more diabatic.

Using this metric as a way to measure the adiabaticity of the transition, the killing efficiency of the Stark ionizer can be compared to how adiabatic the field flip is. Table 4.10 shows the transition looked at, all of which were U^{6+}. Figure 4.17 shows the ratio of background to high-*L* signal as a function of α. The data is separated by the velocity of the beam since it is easier to visualize how transitions compare within a velocity. At all velocities the general trend is what is predicted. As the transition becomes more diabatic, the background gets worse. It is reassuring to see the overall trend that is expected, and that within a velocity the trend is as expected.

Table 4.10: Comparison of Stark ionizer schematics for U^{6+} transitions that experience varying degrees of adiabatic field changes. The first column is the potential put on the Stark ionizer for detection, the second column is the schematic used on the Stark ionizer, the third column is the kinetic energy of the beam, the fourth column is the change in electric field along the beam axis, the fifth column is the "adiabaticity", and the last column is the killing efficiency of the Stark ionizer.

Transition	V_S (V/cm)	Stark Ionizer Scheme	KE (keV)	ΔE_Z (V/cm)	α	B/S_{HL}
n = 51 to 91	-4500	0.5":1"	150	5314	434	5.75
n = 53 to 93	-8000	1":2"	150	4724	386	9.40
n = 55 to 104	-5300	1":2"	120	3129	286	9.30
n = 54 to 99	-3750	0.5":1"	120	4429	404	6.00
n = 55 to 120	-3000	1":2"	90	1771	187	36.3
n = 53 to 105	-5000	1":2"	90	2952	311	11.3
n = 52 to 102	-3000	0.5":1"	90	3543	373	7.6

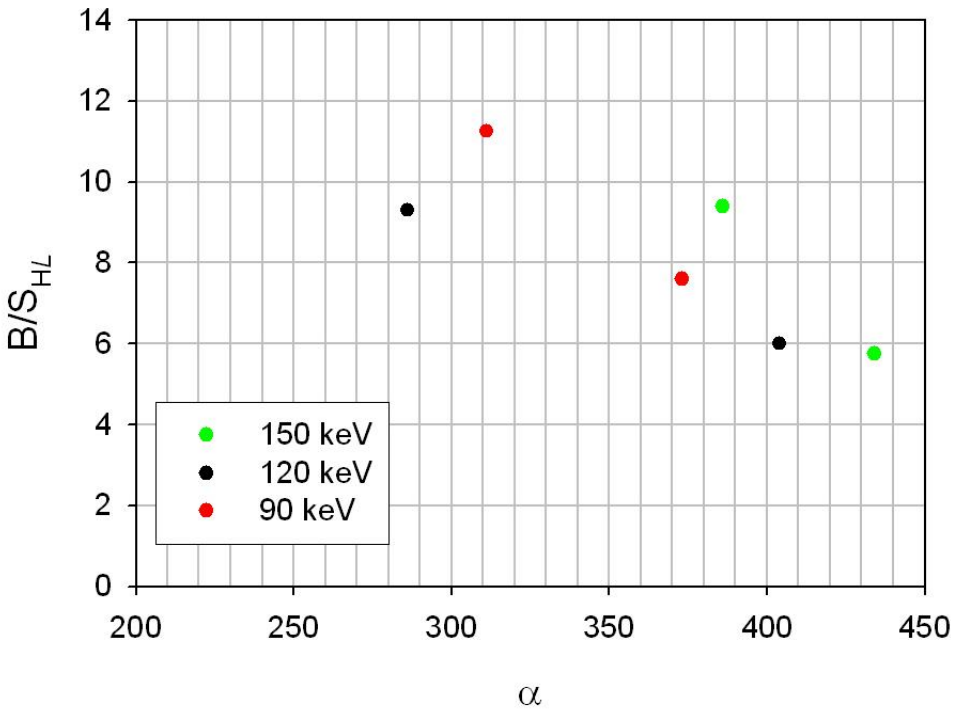

Figure 4.17: Comparison of the background normalized to the high-*L* signal size of the Stark ionizer versus the "adiabaticity" of electric field flip.

These results continue to demonstrate that the metastable as background source has no contrary evidence. This is another case where the metastable hypothesis provides a prediction that appears to be confirmed by experiment.

4.8 Analysis of Preionizers Efficiency

The 10" preionizer has been discussed previously within this chapter, but the 6" preionizer has yet to be analyzed. Comparisons can be made between the functionality of the 6" preionizer and the 10" preionizer, to test the understanding of them. Since they are just viewed as two mixing and killing events in a row before the detector, the total amount of metastable states that make it through the preionizers can be predicted. The fraction of the metastable states that survive through the 6" preionizer are all states that aren't killed, i.e. $1-K_{6"}$. The fraction

that survives through the 10" preionizer is similarly $1-K_{10"}$. This means the total fraction that makes it through both the preionizers should be:

$$1-K_{Tot}=(1-K_{6"})(1-K_{10"})$$

Table 4.11 shows the two most recent tests, these were performed on thorium ions. The second column shows the measured survival through just the 6" preionizer, and the third column shows the measured survival through just the 10" preionizer. The fourth column shows the measured survival through both the 6" and 10" preionizers. The fifth column shows what the total survival through both the preionizers might be expected to be based on the survival through each preionizer individually. The last column shows that the effectiveness of the survival through both preionizers is very similar to the predicted survival assuming the killing events are unrelated and don't saturate.

Table 4.11: Two tests of the 10" and 6" preionizer's killing efficiency. The first column is properties of the beam. The second and third columns are 1 minus the killing efficiencies of the 6" and 10" preionizers corresponding to the survival of metastable states. The fourth column is the experimentally measured survival fraction found by turning them both on. The fifth column is the predicted survival fraction found by multiplying columns two and three together. The last column is a comparison of the experimental survival fraction over the theoretical.

Beam Properties	$1-K_{6"}$	$1-K_{10"}$	$1-K_{Tot}$ Experimental	$(1-K_{6"})*(1-K_{10"})$	Experimental /Theoretical K_{Tot}
Th^{4+} 100 keV	0.71	0.56	0.38	0.40	0.94
Th^{3+} 75 keV	0.68	0.51	0.38	0.34	1.12

The killing efficiencies found were not always as in table 4.11. There would be times when the 6" preionizer did very little killing, or when the combined killing measured was not as high as predicted. There is a possible explanation of this observation. As shown in figure 4.8, how far an ion is off axis can greatly affect the amount of mixing scene. It could be that the

tuning on certain days sent the beam off axis more than others in passing through the preionizers affecting their killing efficiencies

Overall the preionizers can be regarded as a big success since previously there had been no way to reduce the background in the RESIS technique, whereas the preionizers can reduce the background by as much as a factor of 5.

4.9 Overview of Metastable Autoionization Hypothesis

Within this chapter, the autoionization of metastable Rydberg states has been analyzed as it applies to a wide range of issues, but the main goal was to explain the observations about the background described in the previous chapter. Table 4.12 serves to summarize the reasons for those observations that have been discussed throughout the chapter.

Table 4.12: Explanations of observed background properties based on the autoionization of metastable Rydberg states being the source of the background.

Observation of Background	Metastable Explanation of Observation
The background comes from Rydberg states.	Requirement for autoionization.
The creation of background is concentrated at the peak Stark ionization field flip (same location as electric field direction flip).	The electric field flip mixes to extremely short-lived states that ionize virtually immediately, creating a large rate of autionization at the field flip.
The size of the background is dependent on the geometry of the Stark ionizer.	The geometry of the Stark ionizer changes how adiabatic the electric field change is that is experienced by the ion beam. The amount of mixing that occurs is dependent on the adiabaticity, and thus different geometries mix varying amounts creating differing amounts of background.
The background is independent of the system pressure.	No reason the pressure should be a factor.
The background is independent of the system temperature.	No reason the temperature should be a factor.
The background is directly proportional to the CXRT.	The amount of metastable Rydberg states is directly proportional to the CXRT, so it follows that the background would be as well.
The background is insensitive to the ratio of the repeller's electric field over the Stark ionizer's electric field (E_R/E_S).	The metastable Rydberg states that would pass through the repeller explain the background.
The preionizers reduce the background with small fields.	The fields in the preionizer decrease the amount of metastable states that make it to the detector by increasing autoionization before the detector.

The ability of this hypothesis to explain all of these properties of the background gives a lot of confidence that this hypothesis is correct. There is no evidence that directly contradicts this hypothesis, unlike all other hypotheses discussed in chapter 3. This in depth analysis of the

background serves to explain its source with the motivation of improving future experiments. The preionizers success also is a large step forward in improving the background size. The ability to measure the metastable concentration provides a novel technique that provides a way to measure metastable content, a problem that had no easy solution previously.

Chapter 5: Predicting RESIS Signal Sizes

5.1 Factors Determining RESIS Signal Size

Predicting the RESIS signal sizes requires consideration of several processes that occur along the RESIS beamline.

1. Charge capture in the Rydberg target determines the population that is initially present in any particular Rydberg level (n, L, m).
2. Radiative decay in electric field free regions of the beamline reduces the population of all Rydberg levels by some amount.
3. Within regions where a sufficiently large electric field produces Stark mixing of all L levels within a given n, radiative decay proceeds at different rates depending on the value of m with respect to the electric field. Furthermore, the relative population of various L, m levels can be altered as the beam enters or exits these regions and where the direction of the electric field changes.
4. Within the magnetic field of the 15° bending magnet, both Zeeman and Stark mixing affect the populations and radiative decay rates.
5. The excitation probability within the CO_2 laser varies, depending on the Rydberg level.
6. Once excited, there could still be radiative decay before the excited level reaches the Stark ionization detector.
7. Stark ionization and collection of the resulting ion is expected to be highly efficient (100%).

All of these processes will be discussed in turn.

In order to illustrate the degree of significance of the processes described in 3) and 4) above, two models predicting RESIS signal sizes will be discussed. Model A ignores processes 3) and 4), while model B includes them.

5.1.1 Charge Capture

The first step in calculating the signal size is knowing the distribution of capture as a function of *n* from the Rubidium target. This is a problem that has been analyzed in detail previously. A Classical Trajectory Monte Carlo (CTMC) code to predict capture of an electron from a Rydberg target by an ion beam was created by Ron Olson [23]. This code is also examined in detail in Dan Fisher's dissertation [11], and its predictions were largely confined in the experimental study of Fisher [24]. Using this program, predictions can be made about the capture fraction into a given *n* for the ion beam of choice. Figure 5.1a shows the predicted fractional capture as a function of *n* for U^{6+} at 150keV capturing from a 10F Rubidium target. Figure 5.1b shows the same distribution plotted as a function of binding energy. This distribution is approximately Gaussian centered at a binding energy that is approximately $\sqrt{Q} \cdot E_b(n_T)$ where $E_b(n_T)$ is the binding energy of the Rydberg electron on the target. The energy width of the distribution (~0.45 eV) in this case is expected to be proportional to the ion beam velocity for fixed n_T.[24]

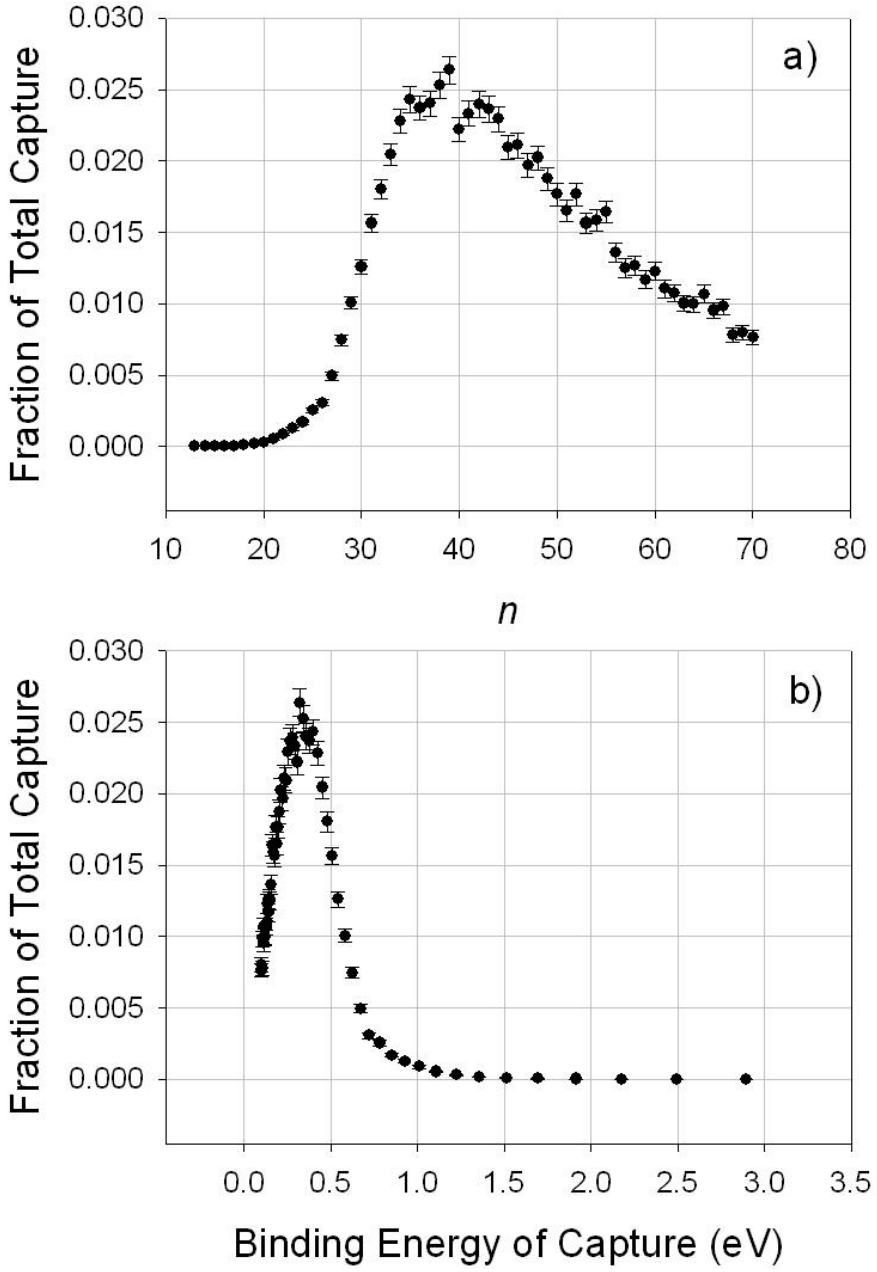

Figure 5.1: The fraction of the total capture for a U^{6+} at 150 keV beam from a 10*F* Rydberg target as a function of a) captured *n* values and b) the binding energy.

Using data taken from the CTMC predictions for capture the height of a signal compared to the total charge capture from the Rydberg target (CXRT) can be predicted. From figure 5.2, it is estimated that ~1.5% of the total charge capture from the Rydberg target is into the $n = 53$ state. All other *n* values will contribute to the CXRT seen at the detector, but only the lifetimes

of the n = 53 state need to be considered to predict the signal size. The L and m value distributions also need to be considered. The L-distribution in charge capture has been studied in detail previously [25]. For simplicity here, the L values were assumed to have equal populations within an n state after capture, and the m states are assumed to have equal population within an L. When the effects of the 15° magnet are discussed, it will become clear that this assumption is not critical.

5.1.2 Radiative Decay in Regions Free of Electric Field

The field free hydrogenic decay rate is predicted from the equation developed by Chang and depends on the n and L values of the state [26]:

$$A(Q,n,L) = \frac{1.08\times10^{10}Q^4}{n^3(L+0.5)^2}\,\mathrm{s}^{-1} \tag{5.1}$$

Using this assumption the fractional population left in a given L state as a function of time spent in a field free can be calculated using:

$$f_L = \exp(-A_L \cdot t) \tag{5.2}$$

where f_L is the fraction left of state L, A_L is the decay rate for a given L state from equation 5.1, and t is the time. These equations allow predictions to be made for the amount of total decay that occurs for a particular L state in a field free region. This adequately addresses the total population in an L state in a field free region, but the decay rate within an electric field need also be considered.

By convention, we choose to label the m-levels with respect to an axis along the beam direction. Since the earth's magnetic field is largely perpendicular to this direction, it leads to Zeeman precession which redistributes the m populations. If there are differences in the m-state population, and if there is sufficient time for evolution of the m states in the earth's magnetic

field, the population may mix. The separation of *m* states in the field free region comes from the Zeeman splitting due to the earth's magnetic field (~0.5 G). The separation is a function of Δm, but is about 0.7 MHz times the Δm value. This is a time per cycle of $1.4/\Delta m$ microseconds. For U^{6+} at 150 keV, the shortest time spent in a field free region is 0.3 microseconds. As soon as Δm gets to 5 then there is a full cycle experienced.. Seeing as most m states are far larger than this, it seems like a valid assumption that complete mixing of *m*-levels occurs in an electric field free region.

5.1.3 Stark-Mixed Radiative Decay

Within a sufficiently large electric field the angular momentum is no longer a good quantum number, and then the *m* values become important. In order to model effectively the parts of the beamline that are within an electric field, equations are needed that describe the decay rate of different *m* states. Equations developed by DePaola et. al. [27] determine the average decay rate for an arbitrary *m* value:

$$\begin{aligned}
\overline{A}(Q,n,m=0) &= \frac{1}{2n-1}\sum_{L=0}^{n-1}(2-\delta_{L,0})\cdot A(Q,n,L) \cong \frac{Q^4}{n^4}\left[106-\frac{108}{n}\right]\times 10^8 \text{ s}^{-1} \\
\overline{A}(Q,n,m=1) &= \frac{1}{n-1}\sum_{L=0}^{n-1}A(Q,n,L) \cong \frac{Q^4}{(n-1)n^3}\left[101-\frac{108}{n}\right]\times 10^8 \text{ s}^{-1} \\
\overline{A}(Q,n,m=2) &= \frac{1}{n-2}\sum_{L=0}^{n-1}A(Q,n,L) \cong \frac{Q^4}{(n-2)n^3}\left[53-\frac{108}{n}\right]\times 10^8 \text{ s}^{-1} \\
\overline{A}(Q,n,m\geq 3) &= \frac{1}{n-|m|}\sum_{L=|m|}^{n-1}A(Q,n,L) \cong \frac{Q^4}{n^4}\frac{108}{m}\times 10^8 \text{ s}^{-1}
\end{aligned} \tag{5.3}$$

These decay rate can then be used to find the population after time t as the same way as equation 5.2 did for field free decay. These equations hold when the electric field is large enough to completely mix all *L* values within an *n* state. The width of a the Stark manifold for a given *n* state in an electric field is [20]:

$$\Delta E = 3F\frac{n(n-1)}{Q}$$

where ΔE is the width in energy, F is the electric field strength, and Q is the charge of the ion. If the Stark width is on the same order as the energy separation of *L* states in a field free region, then all states can be assumed to be mixed. The exact field free width is unknown for U^{6+}, but it is certainly less than 1500 GHz, the difference in energy between $n = 53$ and $n = 54$. In order to have a Stark width of this size, an electric field of 850 V/cm would be needed. This gives an idea of how large an electric field would need to be for equation 5.3 to be used to estimate the decay. There are several places within the beamline that have fields that are of this magnitude or more (15˚ magnet with E = 3000 V/cm, the repeller with E = 4300 V/cm, the remixer with E = 3800 V/cm).

The effects of this mixed decay rate on the lifetimes of states can be evaluated by looking at example rates. Table 5.1 shows the lifetimes for $n = 53$ U^{6+} both within and out of a field. The last column shows the ratio of the two. It can be seen that a field compresses the total range of lifetimes. This means that the shortest lived states' lifetimes become longer within a field, and the longest lived states' lifetimes become shorter. This has the effect of making the change in population between low *L* states and high *L* states less severe when in an electric field.

Table 5.1: Average lifetimes for various L values in $n = 53$ U^{6+} for field free regions and within a field. The last column shows the ratio of the field free regions lifetime over the lifetime within a field.

L Value	Field Free Lifetime (μs)	In Field Lifetime (μs)	Field Free/In Field
5	0.32	1.52	0.21
10	1.17	2.88	0.41
15	2.56	4.27	0.60
20	4.47	5.67	0.79
25	6.92	7.07	0.98
30	9.89	8.48	1.17
35	13.40	9.88	1.36
40	17.45	11.29	1.55
45	22.02	12.70	1.73
50	27.13	14.11	1.92

Mixing of states can also occur within the electric field regions of the beamline. As discussed, upon entering fields such as these, decay follows the m values using equation 5.3 since it is assumed that complete mixing of all L states occurs in this field. The question is, what happens to the population distribution once the populations start leaving these fields and L becomes a good quantum number again. Upon leaving the repeller, L becomes a good quantum number again, so the population of each L state needs to be determined. Stark mixing in the electric field mixes all the L states that have that m value. It is assumed that there is enough time within the field to randomize the phase between all these Stark levels. This means that when leaving the field it is plausible to assume that an equal amount of each m states' total population will go to each L state that can have that m state. Explicitly this means:

$$P'_{L,m} = \frac{\sum_{L} P_{L,m}}{n - |m|} \tag{5.4}$$

This has the effect of repopulating the lower L states that had decayed before the reaching the electric field. In fact, this is precisely what the remixer was designed to do in order to enhance the size of resolved RESIS signals in the Kr^{6+} experiment. [6]

5.1.4 Radiative Decay and Population Changes in 15˚ Magnet

The second region to be considered when it comes to mixing is the 15˚ magnet. Once the population is within the magnet the size of the perpendicular magnetic field and electric field causes large enough Stark broadening and Zeeman splitting that all *L*-states would become mixed. The size of the fields can be determined for U^{6+} at 150keV. By setting the magnitudes of the centripetal force equal to the Lorentz force in the magnetic field, the magnitude of the magnetic field for the 15° magnet can be determined:

$$\frac{m \cdot v^2}{r} = qvB$$

$$B = \frac{m \cdot v}{q \cdot r}$$

where v is the velocity of the beam, m is the mass of the ion, q is the charge of the ion, B is the magnitude of the magnetic field, and r is the radius of curvature for the magnet which is 20.3 cm from its manual. This means that the magnetic field for the U^{6+} beam at 150keV ($\beta = .001159$) is ~0.85 Tesla, giving a $\Delta m = 1$ Zeeman splitting of 12 GHz, sufficient for major Zeeman mixing during the transit time of 0.58 μs. The magnitude of the motional electric field is then given as:

$$E = v \cdot B$$

For U^{6+} at 150keV, the motional field is then 3000 V/cm, easily sufficient to mix all *L*'s. With two large perpendicular fields it is difficult to determine exactly what will happen, but it is likely that very significant mixing will occur. For simplicity, it is assumed that the population of every *L*, *m* state would be equalized. Therefore the population in each state at the start of the magnet is set to be:

$$P'_{L,m} = \frac{1}{n^2} \sum_{L,m} P_{L,m} \tag{5.5}$$

where $P_{L,m}$ is the population entering the magnet, and the factor n^{-2} corresponds to the total number of states.

The decay rate within the magnet is also determined using the assumption that all states are fully mixed. Under this assumption, it is reasonable to assume that the decay for each state would be the average decay rate for all states. Explicitly, this meant:

$$\overline{A} = \frac{1}{n^2}\sum_{L}(2L+1)A(Q,n,L) \tag{5.6}$$

where A(Q,n,L) is from equation 5.1. This overall decay rate is then used to calculate the decay of all states for the 0.3072 meters within the magnet. This means the relative population of each state is equal throughout the magnet, and only the overall population changes. This treatment of the magnet also means the initial population distribution before the magnet is unimportant. The total population decrease before the magnet does depend on the initial L-distribution, but under the assumption that complete mixing occurs within the magnet all correlation with the initial distribution is lost.

5.1.5 Excitation in CO_2 Laser

Another factor in the beamline that affects the signal size is the CO_2 excitation. The probability of excitation within the CO_2 laser interaction region was modeled using equations developed for a $TEM_{0,0}$ laser beam using time dependent perturbation theory by C.R. Quick and H.C. Bryant [28]. The probability of excitation from state $|n,L\rangle$ to state $|n',L'\rangle$ is given by:

$$P_{n,L\to n',L'} = \frac{e^2\pi}{4\hbar^2}\langle n,L|Z|n',L'\rangle^2 E_0^2 T^2 \frac{\omega_0}{\omega(z)}\exp\left[-\frac{1}{2}(\omega'-\omega_0)^2T^2\right] \tag{5.7}$$

where $\omega(z)$ is the distance from center of the laser beam where the intensity is 1/e of the peak intensity, ω_0 is the waist of the laser the minimum value of $\omega(z)$, T is the transit time through the

laser waist, E_0 is the amplitude of the electric field at the beam waist, and $\langle n, L | Z | n', L' \rangle$ is the root mean square matrix element for the dipole transition between the two states. The matrix element can be evaluated with the help of equations 60.7 and 3.17 in reference [20], as well as equation 13.145 in reference [29]. All of these values can be calculated for the CO_2 laser. The waist of the CO_2 laser (ω_0) is given as 0.9mm in the documentation for the laser. The magnitude of $\omega(z)$ can be calculated with the help of equation 3.3.10 within [30]:

$$\omega^2(z) = \omega_0^2 \left[1 + \left(\frac{\lambda_0 z}{n \omega_0^2 \pi} \right)^2 \right] \tag{5.8}$$

where λ_0 is the wavelength of the laser, and z is the distance from the output of the laser to the intersection with the beamline, 0.158m. The transit time through the laser waist is given by:

$$T = \frac{\omega_0}{v \times \sin(\theta_{Int})} \tag{5.9}$$

where v is the velocity of the beam, and θ_{Int} is the angle of interception between the ion beam and the CO_2 laser. The electric field, E_0, can be found using equation 3.4.3 from [30]:

$$E_0^2 = \frac{4P\eta}{\omega_0^2 \pi} \tag{5.10}$$

where P is the power of the laser, typically around 20 Watts, and η is the wave impedance given by:

$$\eta = \sqrt{\frac{\mu_0}{n\varepsilon_0}} \tag{5.11}$$

where *n* is the index of refraction of the medium. In a vacuum $\eta = 376.73\Omega$, and at P = 20 W then E_0 = 1089 V/cm. These equations allow the probability of excitation to be calculated for all *L* values. If the probability is found to be larger than 0.5 then the excitation is assumed to be saturated and the probability is set to 0.5. Since likelihood of excitation is dependent on *L*

through the matrix element, it can affect the size of the high-L, and the relative size of the resolved signals compared to the high-L.

5.1.6 Stark Ionization and Ion Collection

Since the Stark ionizer is designed to have an electric field that ionizes all L states at the same potential, it should ensure the signal ions are all ionized and energy tagged in the same manner, and therefore it is assumed Stark ionization and detection is 100% efficient.

5.2 Models of RESIS Signal Size

At this point, the theory of how the populations evolve within the beamline is in place, and consequences for signal size can be discussed. Two models will be used to predict the signal size within the experiment, one simplified one, and one that is more detailed. Figure 5.2 shows a schematic of the beamline, as well as how it will be viewed theoretically for the two models. Model A treats the entire beamline as having field free decay and the probability of excitation in the CO_2 being the only things that affect the populations in predicting the signal sizes, i.e. it ignores items 3) and 4). Model B takes model A, and adds the effects of 3) and 4). By including both models, the significance of the mixing effects described in 3) and 4) can be evaluated.

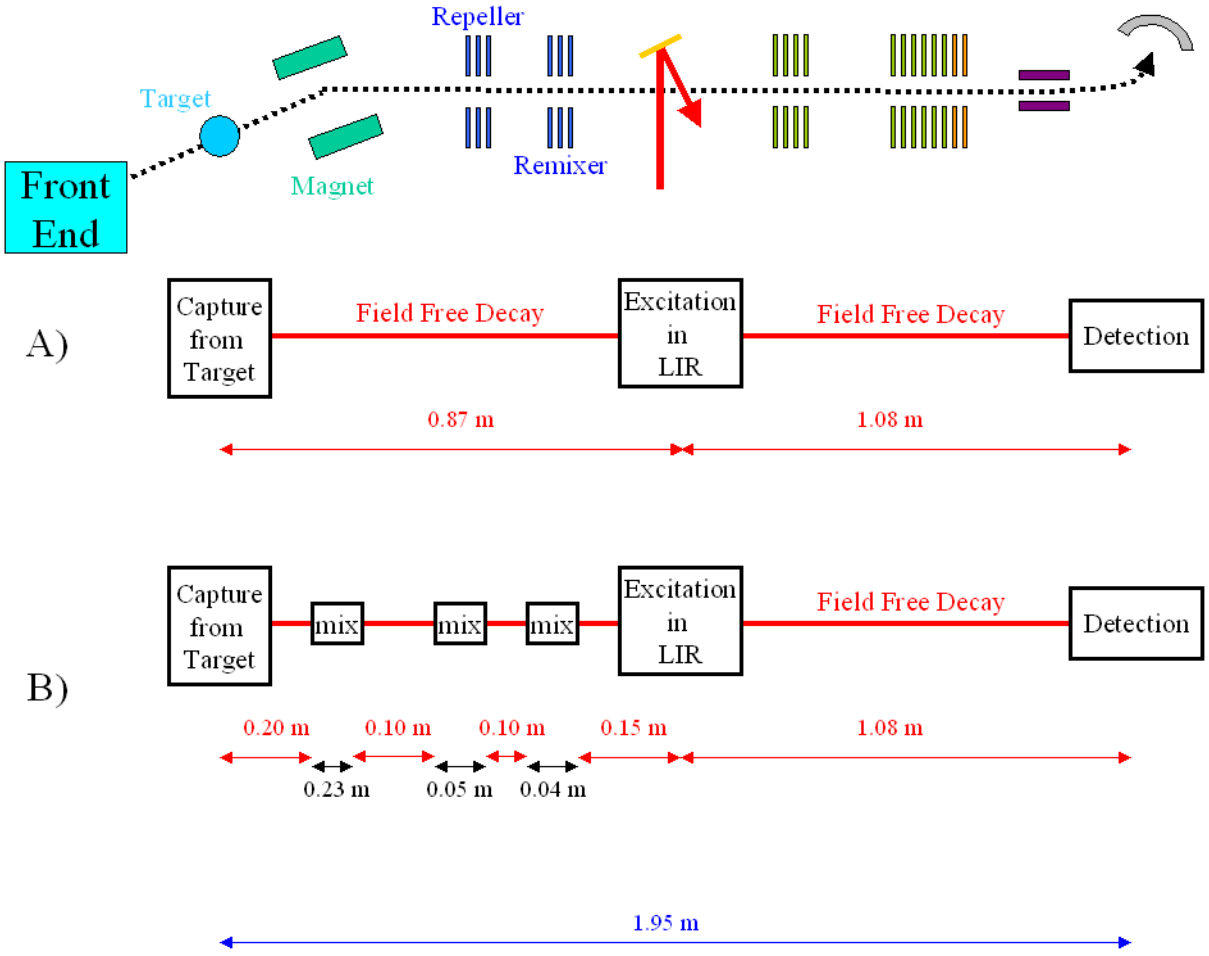

Figure 5.2: Schematic of the beamline, with the population models shown below. The distances are not to scale. Model A) is the simplistic model where only the excitation in the laser and field free decay are considered. Model B) is the detailed model that adds the 15˚ magnet, repeller and remixer.

5.2.1 Model A Predictions for U^{6+} n = 53 to 93 RESIS Signals

The predictions of model A are easily calculated using the equations previously discussed. Table 5.2 outlines the values at key points in the beamline found using model A for U^{6+} at 150keV and the n = 53 to 93 transition for an example. This model has the initial population after capture that was described before, where each L state has the same population. It is important to note that since model A doesn't involve any electric fields, the m states are

irrelevant and therefore ignored. Field-free decay is assumed for the 0.87 meters between the Rydberg target and the LIR. Within the LIR, the excitation probability is calculated using equation 5.7. Following excitation, field-free decay is assumed for the 1.08 meters between the LIR and the detector. Since this decay occurs after excitation, the *L* values are increased by one, and the *n* state is now the upper state of the transition of interest when determining the decay rate of a population. The population that survives until the detector is what would be expected to show up as signal, assuming that the Stark ionization and collection is 100%.

Table 5.2: Details of signal state populations throughout beamline. Column 1 is the *L* value. Column 2 is the fraction of the initial *L* population left at the LIR. Column 3 is the probability of that *L* being excited to the upper state within the LIR. Column 4 is the fraction of the initial population in an *L* state that makes it to the LIR and gets excited. Column 5 is the fraction of the initial population in each *L* state that makes it to the detector as a signal ion.

L	Fraction Left of Initial Population at LIR	Probability of Excitation in the LIR	Fraction of Initial Population Excited in LIR	Fraction of Initial Population Contributing to Signal
0	0.00	0.50	0.00	0.00
1	0.00	0.50	0.00	0.00
2	0.00	0.50	0.00	0.00
3	0.00	0.50	0.00	0.00
4	0.00	0.50	0.00	0.00
5	0.00	0.50	0.00	0.00
6	0.00	0.50	0.00	0.00
7	0.02	0.50	0.01	0.00
8	0.04	0.50	0.02	0.01
9	0.07	0.50	0.04	0.02
10	0.12	0.50	0.06	0.04
11	0.17	0.50	0.08	0.06
12	0.22	0.50	0.11	0.08
13	0.28	0.50	0.14	0.11
14	0.33	0.50	0.16	0.13
15	0.38	0.50	0.19	0.15
16	0.42	0.50	0.21	0.18
17	0.46	0.50	0.23	0.20
18	0.50	0.50	0.25	0.22
19	0.54	0.50	0.27	0.24
20	0.57	0.50	0.29	0.25
21	0.60	0.50	0.30	0.27

22	0.63	0.50	0.31	0.28
23	0.65	0.50	0.33	0.30
24	0.68	0.50	0.34	0.31
25	0.70	0.50	0.35	0.32
26	0.72	0.50	0.36	0.33
27	0.73	0.50	0.37	0.34
28	0.75	0.50	0.37	0.35
29	0.76	0.50	0.38	0.36
30	0.78	0.50	0.39	0.37
31	0.79	0.50	0.39	0.37
32	0.80	0.50	0.40	0.38
33	0.81	0.50	0.41	0.39
34	0.82	0.50	0.41	0.39
35	0.83	0.50	0.41	0.40
36	0.84	0.50	0.42	0.40
37	0.85	0.50	0.42	0.41
38	0.85	0.31	0.27	0.26
39	0.86	0.18	0.15	0.15
40	0.87	0.10	0.09	0.08
41	0.87	0.05	0.04	0.04
42	0.88	0.02	0.02	0.02
43	0.88	0.01	0.01	0.01
44	0.89	0.00	0.00	0.00
45	0.89	0.00	0.00	0.00
46	0.90	0.00	0.00	0.00
47	0.90	0.00	0.00	0.00
48	0.90	0.00	0.00	0.00
49	0.91	0.00	0.00	0.00
50	0.91	0.00	0.00	0.00
51	0.92	0.00	0.00	0.00
52	0.92	0.00	0.00	0.00

The likelihood that an U^{5+} ion within $n = 53$ will make it to LIR, get excited, and make it to the detector is now predicted for all L. It should be noted in table 5.2 that the lowest L states don't make it to the detector due to their short lifetimes, and the highest L states don't get excited within the LIR. This process can be done for any transition of interest, and by knowing the fraction of each initial population that survives to detection for each L state important predictions can be made. This will be demonstrated for the values in table 5.2. Which L states contribute to the high-L needs to be known, so the states that would be resolved from the high-L signal can be

determined. The dipole polarizability of U^{6+} is predicted to be $5.2a_0^3$ [18] and therefore predictions can be made for the energy levels for U^{6+}. There is also plenty of data on the widths of the high-*L* for U^{6+}. By assuming that the resolved peaks are about the width of the high-*L*, a resolved state can be assumed to be one whose predicted energy is larger than the energy width of the high-*L* peak. Using this criterion, all states above $L = 11$ would contribute to the high-*L*. If it is assumed every *L* state had an initial population weight of 1 (keeping with the assumption that all *L* states having the same initial population), then the total initial population in $n = 53$ would be 53. The sum of the fraction left in states that would contribute to the high-*L* $n = 53$ to 93 peak would be 8.17. This means that the high-*L* signal would be comprised of about 15.4% of the ions that begin in the $n = 53$ state. Combining this with the information from CTMC that 1.5% of the total population is in the $n = 53$ state, it can be concluded that the high-*L* peak should be 0.23% of the total U^{5+} beam formed by the Rydberg target. This gives a value that is measurable to compare the theory to experiment. The resolved signal statistical weights are simply the fraction left found in table 5.2 and can then be compared to the high-*L* and the charge capture. Superimposing Gaussian signals with 200 MHz full width at half maximum for each of the $n = 53$ *L* levels shown in table 5.2, assuming $\alpha_D = 5.2$ a.u. and $\Delta E = -\frac{1}{2}\alpha_D \langle r^{-4} \rangle$ predicts the RESIS signal shown in figure 5.3. Note that the $L = 10$ peak is predicted to be 0.5% of the high-*L*.

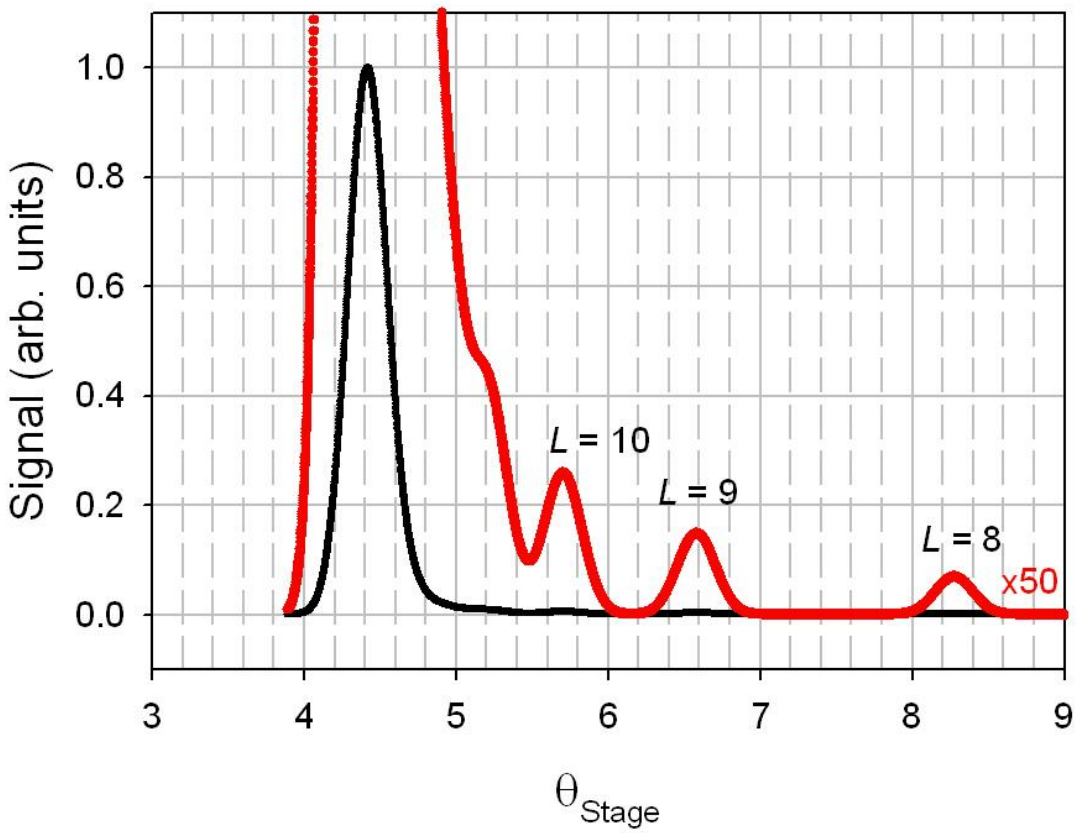

Figure 5.3: Prediction of the signal for the U^{6+} at 150keV n = 53 to 93 transition made by model A. The signals are normalized to the high-L signal, and the red line is 50 times the nominal predicted signal. The high-L signal is predicted to be 0.23% of the CXRT. The L = 8, 9, and 10 resolved peaks are labeled. The tuning rate is ~1150 MHz/˚.

5.2.2 Model B Predictions for U^{6+} n = 53 to 93 RESIS Signals

Model B adds the affects of mixing in the magnet, repeller, and remixer. This more complicated model attempts to accurately model these regions by treating them as mixing events.

The preionizers and initial part of the Stark ionizer are ignored within both models. After excitation in the LIR, the states of interest are in a much higher n state than they began in. Although the fields in and near the detector might cause a deviation away from field free decay, the relative change in population between L states is assumed to be negligible due to the size of the upper n state. The lifetimes go as n^3, so a much larger n state after excitation means that the

lifetimes of all states are large, and mixing would only provide small changes in relative populations. Therefore, it is assumed that field free decay after the LIR is an appropriate approximation.

Model B is written in the MATLAB Version 7 language within an m-file called gauspredictfinal.m, and uses no additional package other than those that come with the Version 7 program. It also imports and exports data to an associated excel file with the name transitiongpplot.xls that must be located within the same directory as the m-file in order to work.

One important change between model B and model A is that the *m* states of the ions need to be considered. For this reason, the model revolves around an (*n*, *n*) matrix whose elements contain the population of a given *L*, and *m* value. Since the *m* and –*m* states are mathematically identical, only the positive values are used, but with double the statistical weight of the $m = 0$ states when applicable. The columns in the matrix correspond to the *L* value, ranging from 0 to *n*-1, and the rows correspond to *m* values, ranging from 0 to *L*. The initial population follows the analysis discussed previously where each *L* state has the same population, and within an *L* state, each *m* state has the same population. Figure 5.4 shows a two dimensional plot that shows the relative population of each state within $n = 53$ for the U^{6+} at 150keV. The total initial population was set to be 53.

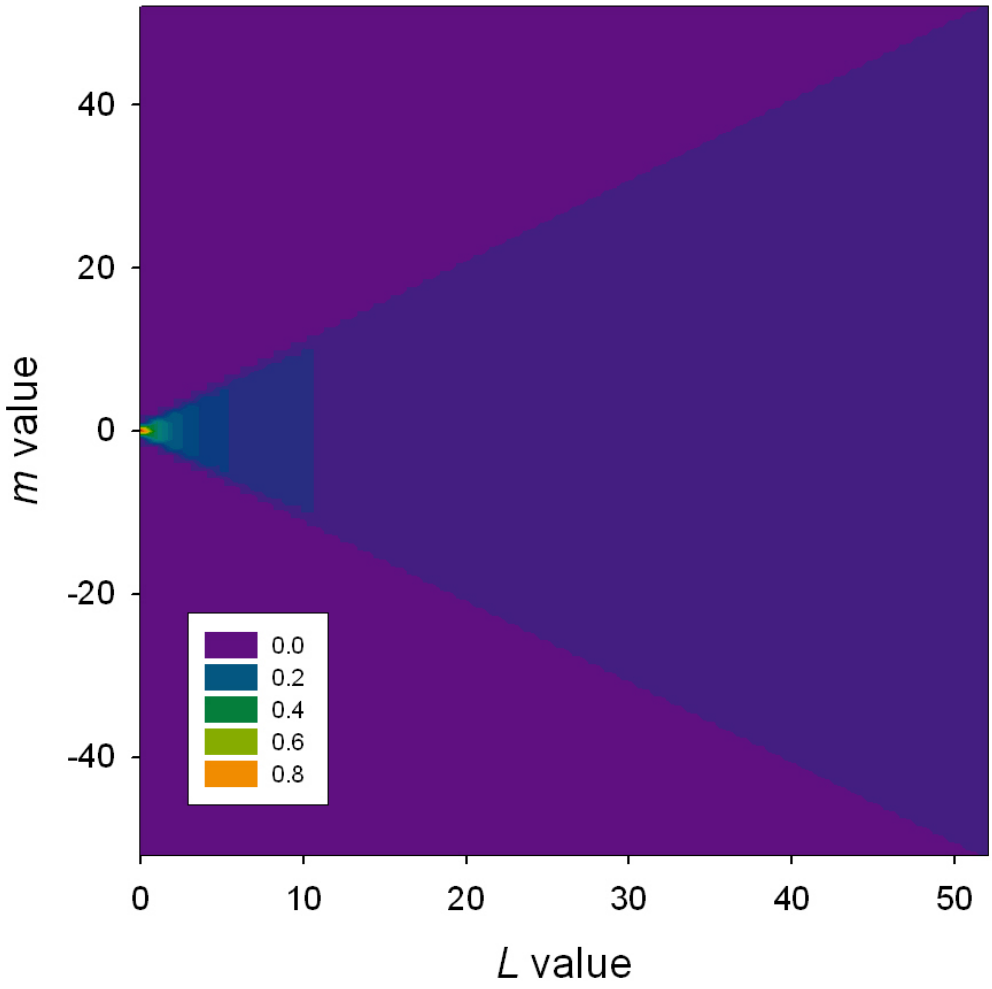

Figure 5.4: Two dimensional plot of the initial population distribution within $n = 53$ for the U^{6+} at 150keV. The total initial $n = 53$ population was taken to be 53. The x-axis is the L value, and the y-axis is the m value.

After the initial population is set, free field decay is assumed for the first 0.20 meters to the 15˚ magnet (as shown in figure 5.2). Figure 5.5 shows the populations of all states of the ensemble as it reaches the 15˚ magnet. Note that the lowest *L*-levels have decayed, and that the *m*-states within an *L*-state have equal population since nothing has yet occurred that is *m* dependent. The total $n = 53$ population reaching the 15˚ magnet is 40.9 (77% remaining from capture).

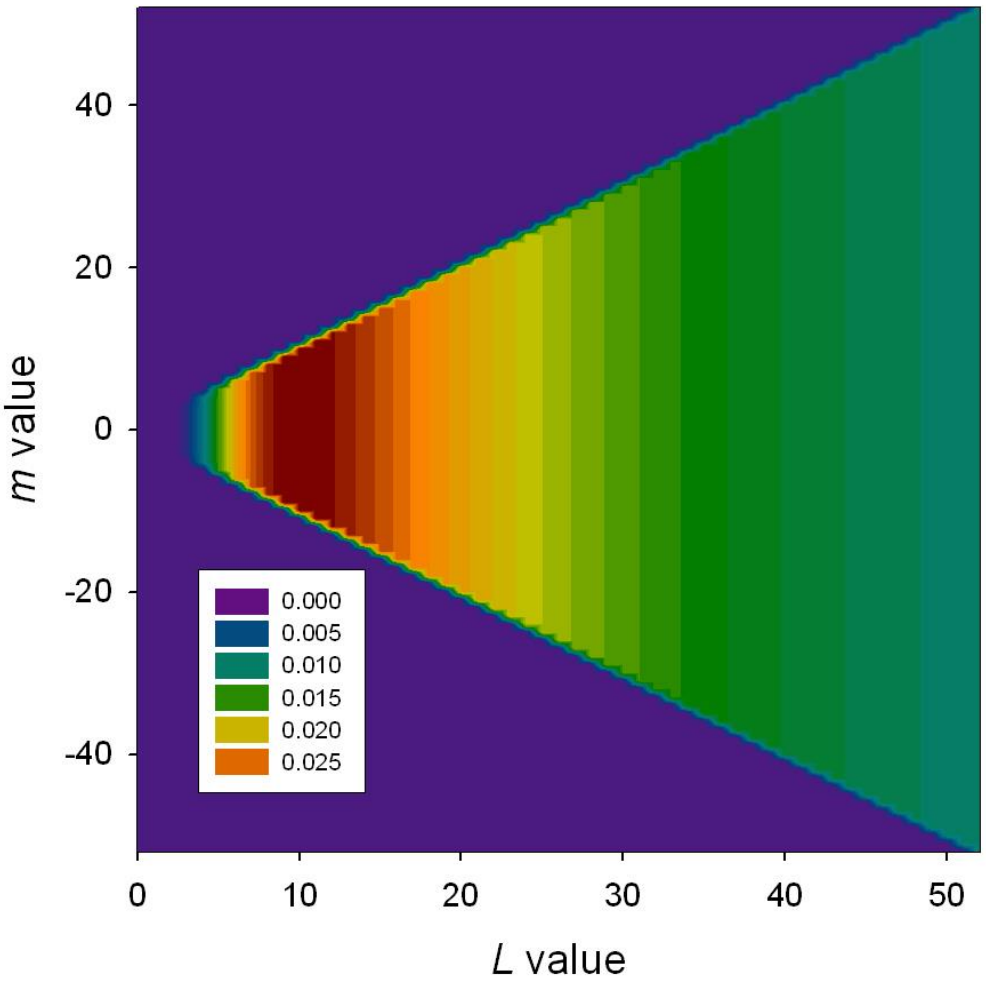

Figure 5.5: Two dimensional plot of the population distribution entering the magnet for the U^{6+} at 150keV $n = 53$ to 93 transition. The x-axis is the *L* value, and the y-axis is the *m* value.

Upon entering the magnet, complete mixing is assumed as described before and all states decay with the average decay rate of all the states. Figure 5.6 shows the population leaving the

magnet, and under the assumptions just stated, every state has the same population. This also demonstrates the relative lack of importance of the initial distribution assumed. It is important for the overall population that enters the magnet, but all information about the distribution is lost in the magnet. At the end of the magnet the total population is 34.8 (66% remaining from capture).

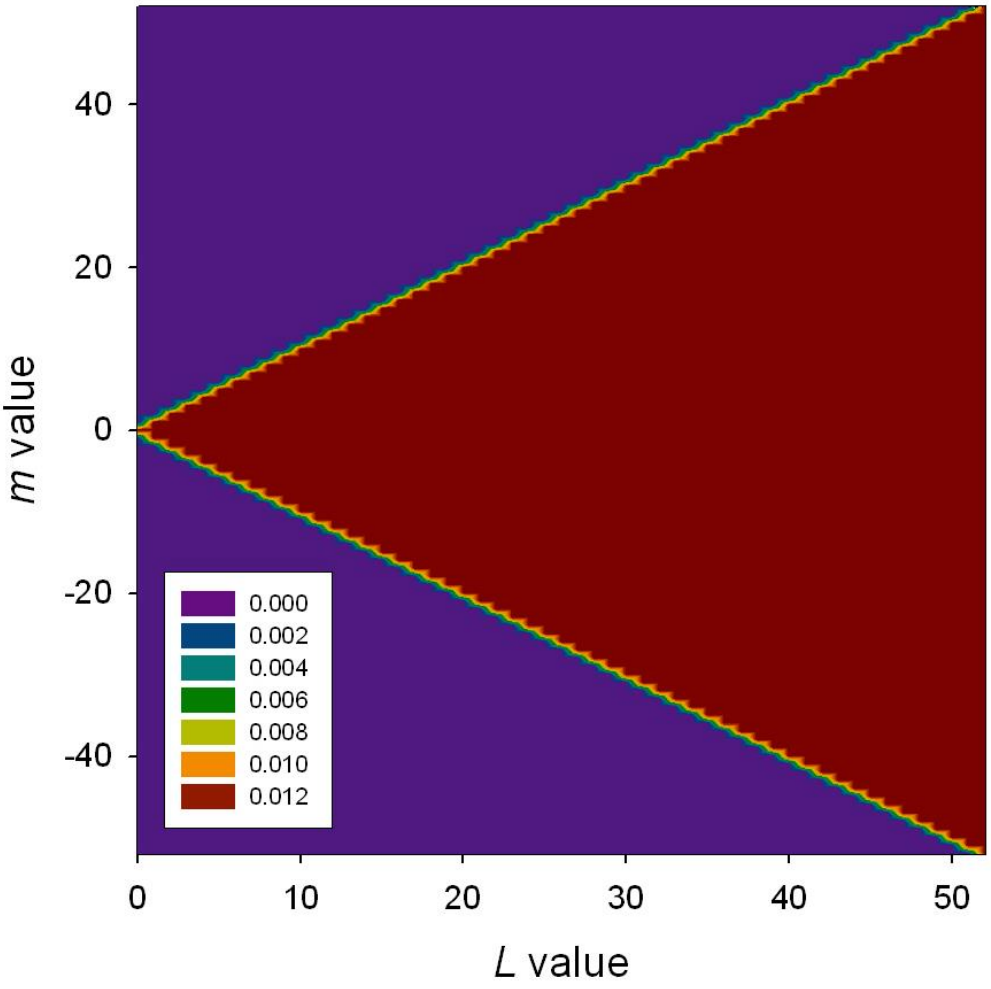

Figure 5.6: Two dimensional plot of the population distribution exiting the magnet for the U^{6+} at 150keV n = 53 to 93 transition. The x-axis is the L value, and the y-axis is the m value.

After leaving the 15° magnet, the decay becomes field free again, and decay is dependent on the L value. This field free decay then lasts for the 0.10 meters between the magnet and the

repeller. Within an *L* state, each *m* state has the same population since they did upon leaving the 15° magnet. Figure 5.7 shows the population distribution entering the repeller. The equal population in each state has clearly been broken due to the much faster decay rates for the lower *L* values. After this field free region the total population is 33.0 (62% remaining from capture).

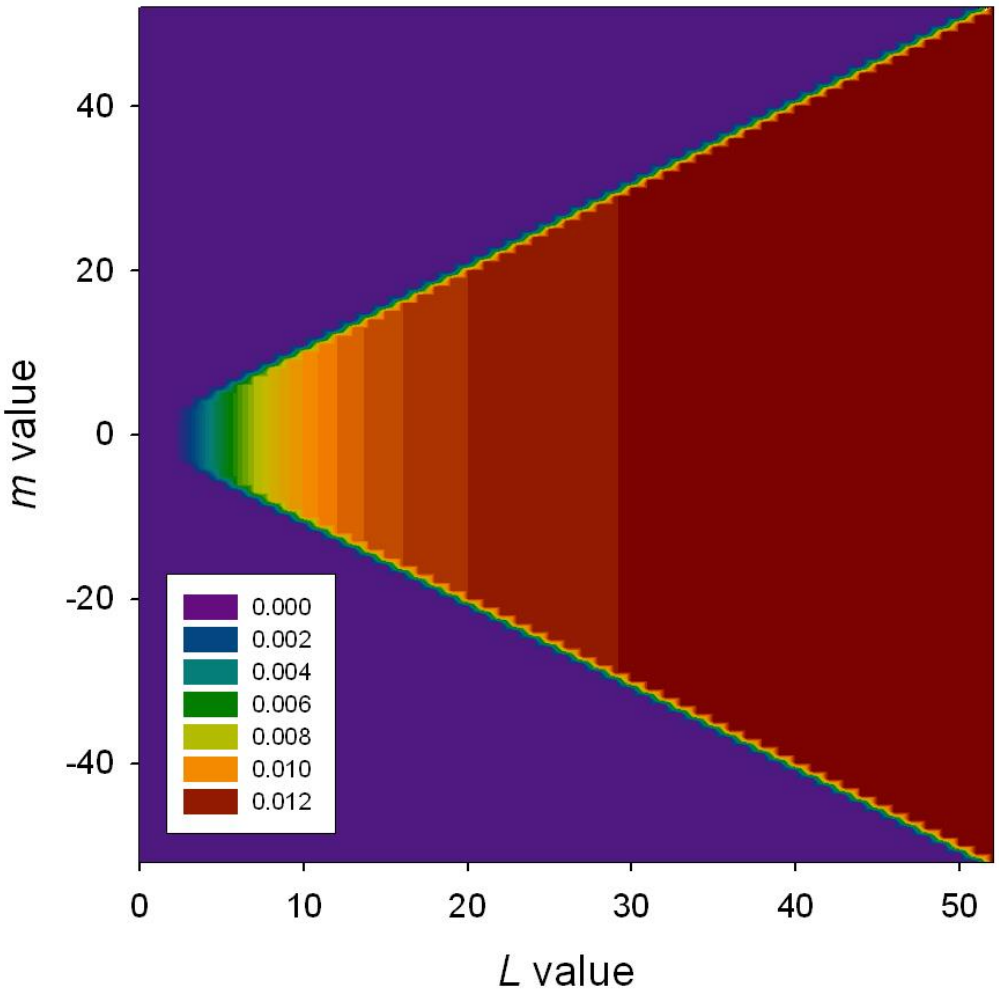

Figure 5.7: Two dimensional plot of the population distribution entering the repeller for the U^{6+} at 150keV n = 53 to 93 transition. The x-axis is the *L* value, and the y-axis is the *m* value.

Upon entering the repeller, the decay follows the electric field decay rates seen in equation 5.3. This means the *m* states are now what determines the decay for the 0.05 meters within the repeller. Upon exiting the field of the repeller, the m states are mixed to all possible *L*

states following equation 5.6. Figure 5.8 shows the population at the end of the repeller. Note that the lower *m* levels have been depleted. At the end of the repeller the total population is 31.9 (60% remaining from capture).

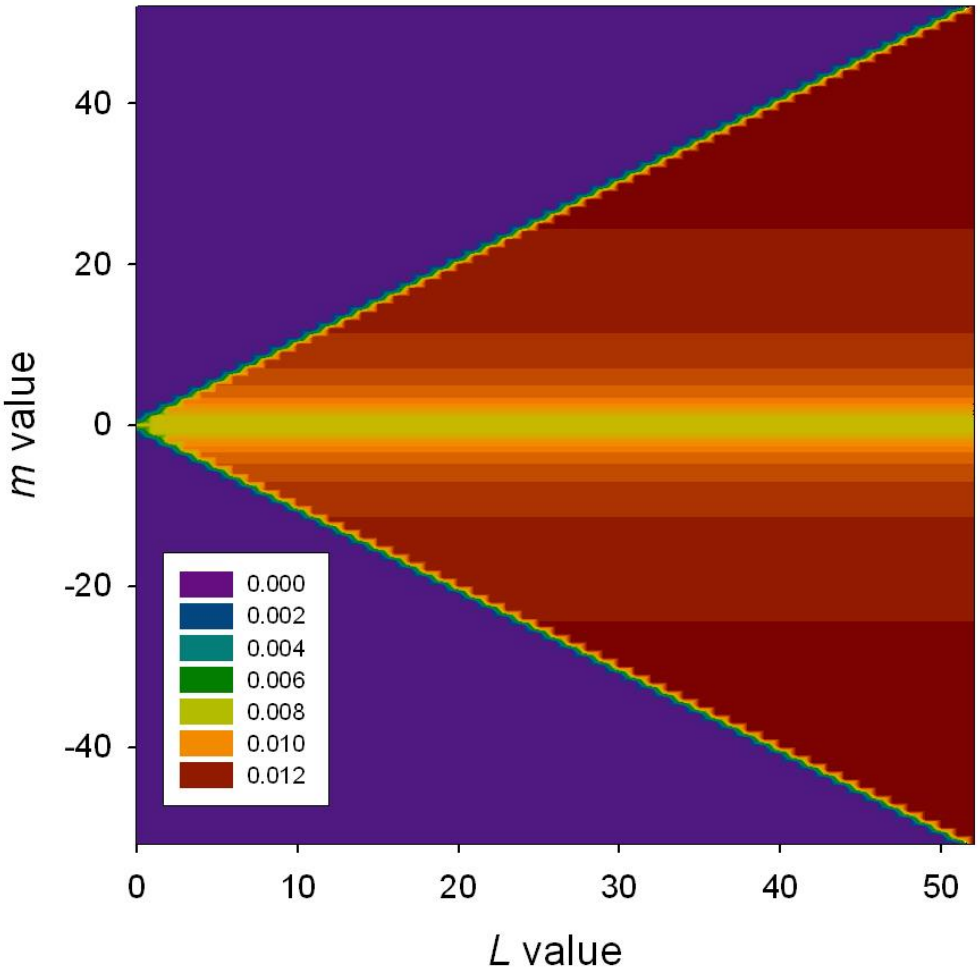

Figure 5.8: Two dimensional plot of the population distribution exiting the repeller for the U^{6+} at 150keV n = 53 to 93 transition. The x-axis is the L value, and the y-axis is the m value.

Field free decay then occurs as previously for the 0.10 meters between the repeller and the remixer. Figure 5.9 shows the population distribution entering the remixer. Clearly seen is the effect of the Zeeman mixing after the repeller, since all *m*-states now have the same population within an L state. Also, the short lifetimes of the low L states in the field free region

is shown since the lowest *L* values are heavily depleted. After this field free region the total population is 30.5 (58% remaining from capture).

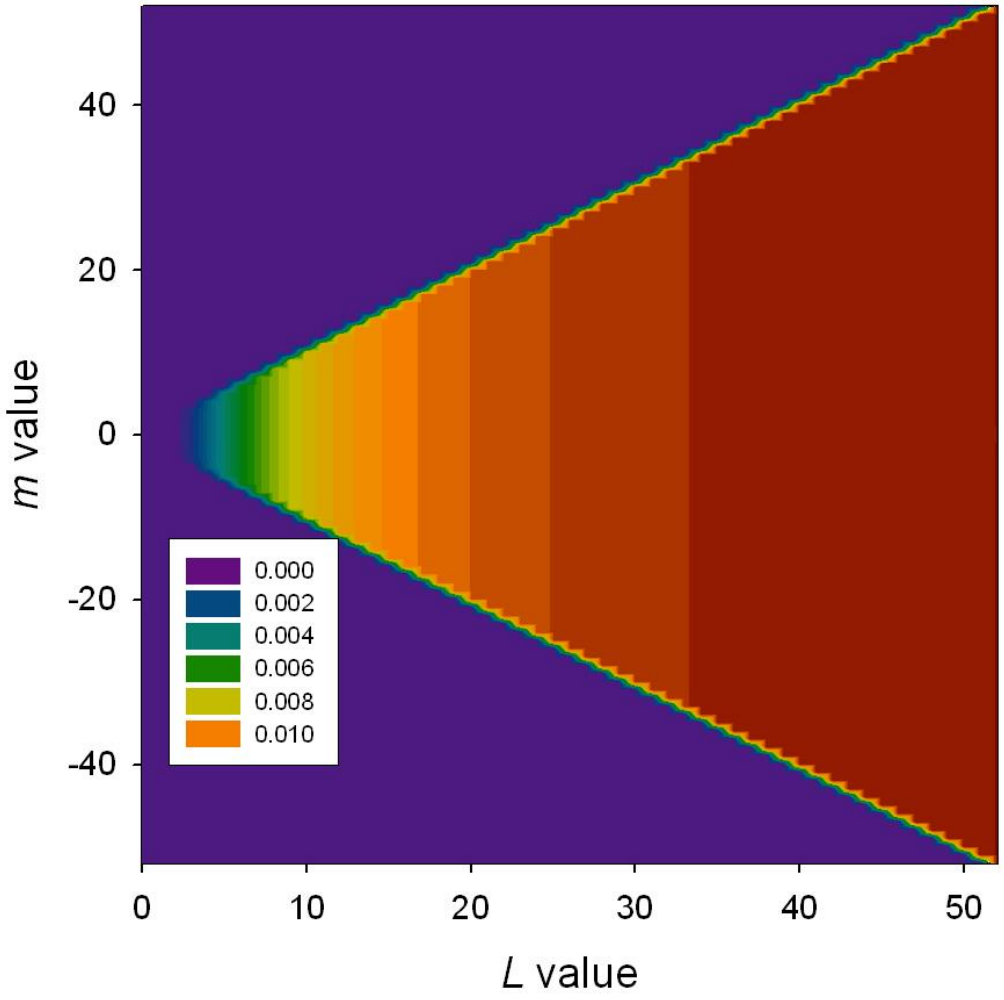

Figure 5.9: Two dimensional plot of the population distribution entering the remixer for the U^{6+} at 150keV n = 53 to 93 transition. The x-axis is the *L* value, and the y-axis is the *m* value.

The remixer is treated exactly like the repeller, except it is only 0.035 meters long. Figure 5.10 shows the population at the end of the remixer. It is exactly like the end of the repeller, except with the overall populations being lower. At the end of the remixer the total population is 29.9 (56% remaining from capture).

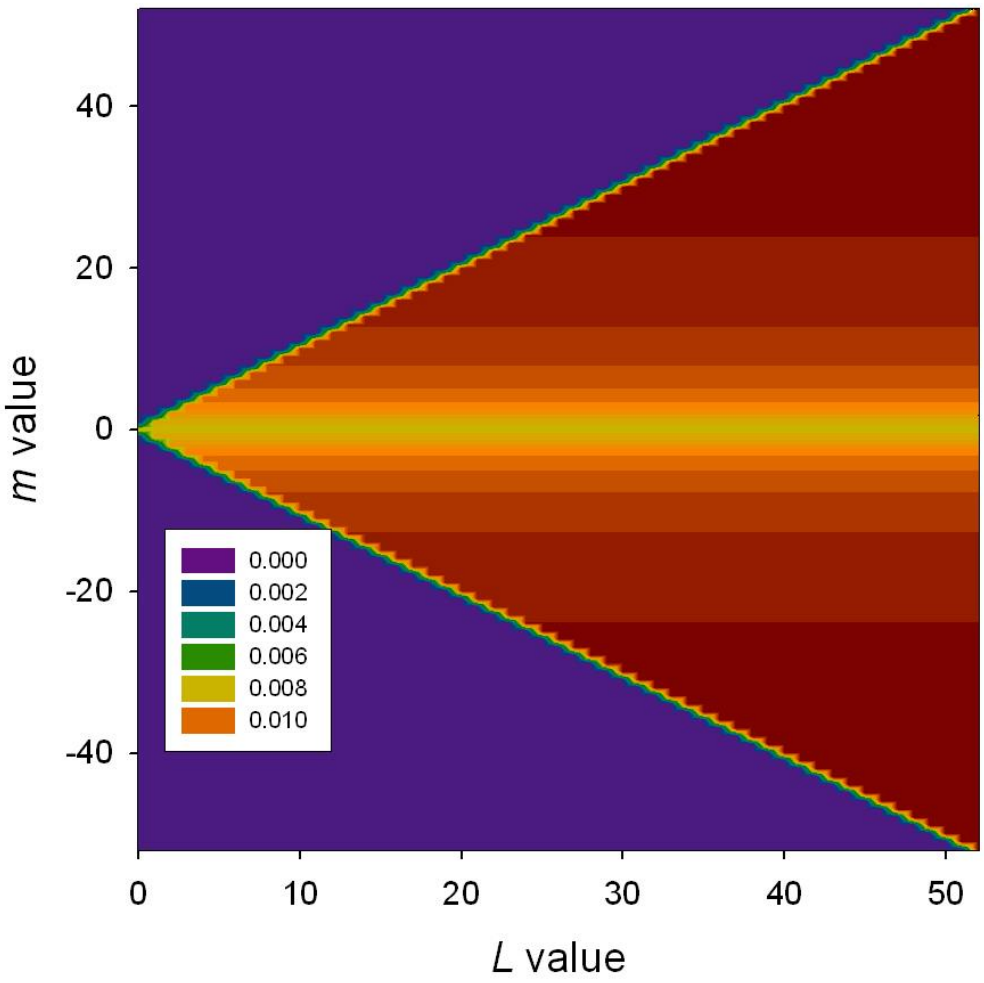

Figure 5.10: Two dimensional plot of the population distribution exiting the remixer for the U^{6+} at 150keV n = 53 to 93 transition. The x-axis is the L value, and the y-axis is the m value.

After the remixer is 0.15 meters of field free decay before the LIR. Once the LIR is reached, the populations are excited in the same way as for model A. The populations now are in the upper n-state of the transition, and the L values have increased by 1. Figure 5.11 shows the population after excitation in the LIR. It is now relatively complicated since the lack of excitation within the LIR depletes the highest L states, and the field free decay prior to the LIR depletes the lowest L states. At the start of the LIR the total population is 28.1 (53% remaining from capture).

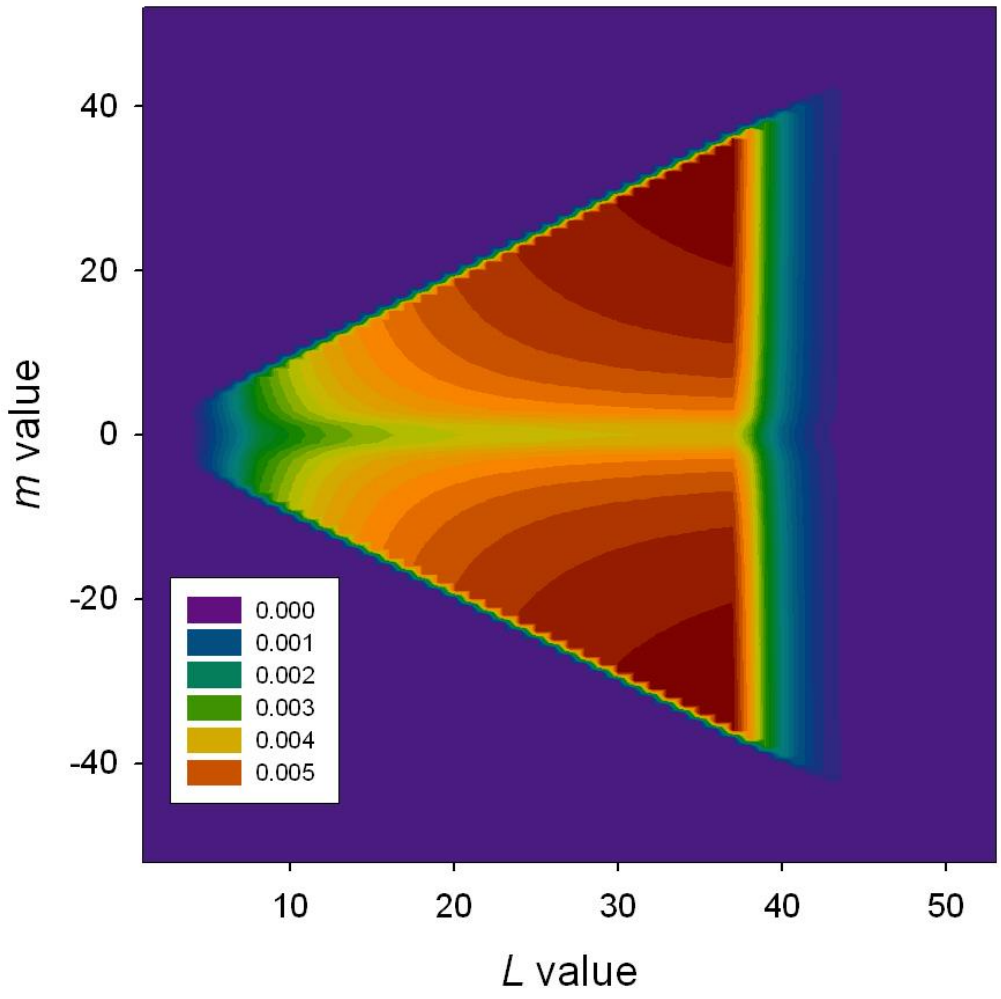

Figure 5.11: Two dimensional plot of the population distribution in $n = 93$ after excitation in the LIR for the U^{6+} at 150keV $n = 53$ to 93 transition. The x-axis is the L value, and the y-axis is the m value.

The total population that makes it to and gets excited in the LIR is 7.15 (13% of the capture in $n = 53$). After the excitation in the LIR, there is field free decay for the last 1.08 meters before the detector. The total population that makes it to the detector as signal ions is 6.43 (12% of the capture population in $n = 53$). Ionization and collection are assumed to be 100% efficient.

After determining the populations that will contribute to the signal, a plot versus frequency is made by adding Gaussian peaks together for each L state, that are centered at the calculated frequency values. Explicitly:

$$f_L(\nu) = A \cdot \exp\left[\frac{-(\nu - \nu_L)^2}{2\omega_T^2}\right] \tag{5.13}$$

where A is the relative amplitude for a particular L as calculated in the preceding section, ν_L is the frequency of the transition for a given L value, ω_T is the width of the Gaussian, and ν is a dummy variable that is calculated in steps that are a 10,000th the total frequency range of interest. The width of the Gaussian is taken to be 200 MHz, the observed width of the high-L signal. This allows the total height of the high-L to be determined since it is composed of many L states that may be similar in frequency, but have at least some variation.

Figure 5.12 shows the predictions for the U^{6+} n = 53 to 93 at 150keV transition made by model A and model B for a comparison. Only when the predictions are multiplied by 50 do any differences become apparent, but it is clear that model B predicts larger resolved signals than model A.

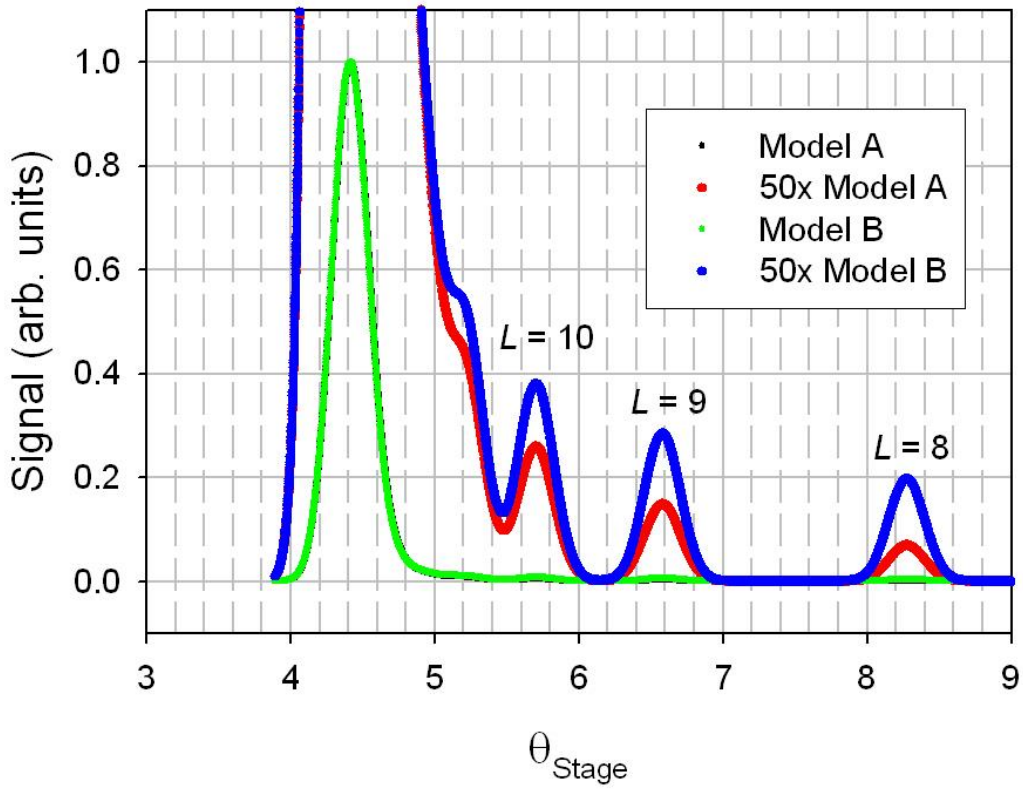

Figure 5.12: Comparison of the predictions made by models A and B for the U^{6+} n = 53 to 93 at 150 keV transition. The black points are the model A prediction normalized to the high-L, and the red points are the model A prediction times 50. The green points are the model B prediction normalized to the high-L, and the blue points are the model B prediction times 50. Model B predicts the high-L signal is 0.17% of the CXRT. The resolved peaks are labeled above.

5.3 Comparison of Models

There are now two methods for predicting the signal size, model A and model B. Before comparing to experimental data, a comparison of the two predictions can indicate the significance of the additional complexity of model B. Although the comparisons made in this section are all theoretical values, the ions and transitions used for comparison will be ones for which there are experimental data. All of the ions analyzed in this section have a J = 0 core for consistency in comparison to U^{6+} although in principal this method can be used for any ion.

Table 5.3 shows a comparison of the size of the predicted high-*L* size for the two models. The high-*L* size is compared to the total charge capture from the Rydberg target taken from CTMC. As seen in table 5.3, while there are differences between model A and model B's high-*L* predictions, overall they are relatively minor, all being within a factor of 1.5 of each other. This might be a bit surprising considering the differences between the two programs (extreme mixing in the magnet especially), but it indicates field free decay and excitation probability in the CO_2 are the biggest factors in determining signal size. It is also seen in the table that it is not consistent as to which model predicts the larger signal for a particular ion, but varies from ion to ion. This may mean the mixing that is taken into account within the model B can be a good or bad thing depending on the ion and transition.

Table 5.3: Comparison of the predicted size of the high-*L* signal from model A and model B for various ions. The first column shows beam conditions. The second column is the predicted fraction of capture into the lower *n* state of interest. Column 3 is the predicted size of the high-*L* compared to the charge capture from the Rydberg target for the model A. Column 4 is the predicted size of the high-*L* compared to the charge capture from the Rydberg target for the model B. Column 5 is model B's prediction over the model A's prediction.

Transition Details	CTMC Fraction of Total Capture in n_{lower}	Model A H*L*/CXRT	Model B H*L*/CXRT	B/A
U^{6+} 150 keV *n* = 53-93	0.015	0.0023	0.0017	0.74
Th^{4+} 100 keV *n* = 37-73	0.029	0.0025	0.0032	1.28
Th^{4+} 60 keV *n* = 37-73	0.029	0.0021	0.0027	1.28
Pb^{4+} 72 keV *n* = 37-73	0.029	0.0025	0.0033	1.32
Kr^{6+} 150 keV *n* = 53-105	0.012	0.0020	0.0017	0.85
Xe^{6+} 90 keV *n* = 54-115	0.016	0.0024	0.0018	0.75

These two models can also be used to predict the size of the resolved signals compared to the high-*L* signal. Using the same analysis as that used to create table 5.3, the fraction that begins in a given *L* value that is predicted to show up as signal at the detector is known. If it is once again assumed that each *L* value has the same initial population, then the ratio of population in a given *L* value can be compared to the total population of *L* values that can contribute to the high-*L*. Table 5.4 shows the predictions made for the resolved signal sizes of various ions. The final column shows the comparison of model B's prediction versus model A's prediction. Once again the two models compare fairly well, but with a bit more variation than was seen on the high-*L* predictions. Once again, it is not consistent which as to which model predicted larger signals, but varied on a ion by ion basis. Model A has a greater variation between resolved signals within an ion. For instance, the predicted resolved signals change by about a factor of 4 for model A, and only a factor of 2 for model B. This is due to the repopulation of lower *L*-levels depleted by radiative decay that is caused by the repeller and remixer fields.

Table 5.4: Predicted size of resolved signals using model A and model B. The first column details the ion and transition of interest, and the second column is the *L* value of the resolved peak. The third column is the predicted size of the resolved peak from the model A compared to the high-*L*, and the fourth column is model B's prediction. The last column is the predicted size from model B over model A's prediction.

Transition Details	Resolved Peak	Model A Percentage of H*L*	Model B Percentage of H*L*	B/A
U^{6+} 150keV *n* = 53-93	*L* = 10	0.48%	0.58%	1.20
	L = 9	0.28%	0.41%	1.47
	L = 8	0.13%	0.29%	2.27
Th^{4+} 100keV *n* = 37-73	*L* = 10	2.84%	1.94%	0.68
	L = 9	1.97%	1.57%	0.80
	L = 8	1.19%	1.21%	1.02
Th^{4+} 60keV *n* = 37-73	*L* = 11	2.96%	2.05%	0.69
	L = 10	2.07%	1.67%	0.81
	L = 9	1.30%	1.31%	1.01
Pb^{4+} 72keV *n* = 37-73	*L* = 9	1.57%	1.33%	0.85
	L = 8	0.89%	1.00%	1.12
	L = 7	0.40%	0.70%	1.75
Kr^{6+} 150keV *n* = 53-105	*L* = 9	0.89%	1.33%	1.49
	L = 8	0.56%	1.00%	1.79
	L = 7	0.29%	0.70%	2.44
Xe^{6+} 90keV *n* = 54-115	*L* = 9?	0.44%	0.81%	1.85
	L = 8?	0.23%	0.61%	2.70
	L = 7?	0.09%	0.43%	4.76

The size of the resolved signals in U^{6+} 150keV *n* = 53 to 93 transition are of particular note since this is the ion of greatest interest. Both models predict it to have the smallest resolved signals of any ion looked at, but the Kr^{6+} ion is comparable. In both cases it is predicted that the U^{6+} might be less than a factor of 2 smaller than those seen in Kr^{6+}. This is mostly due to a difference in velocities since the charge and the lower *n* levels are the same and the upper *n* level are similar.

The overall similarity between the two models for a range of ions indicates that the additions within model B are mainly corrections to the signal size on top of more dominant factors (field free decay and excitation probability). This means that the assumptions taken to

create model B, though believed to be valid, have a relatively small effect and don't appear to alter results by more than a factor of 2 from model A. The question is now, how well do these models predict the experimental signal size seen?

5.4 Comparing Predictions to Experiment

Before comparing the predictions to experimental observations, some greater detail needs to be given about how the signal size was measured experimentally. Within this section the experimental size of the high-L signal (S_{HL}), and resolved signals (S_L) will be compared to each other and with the size of the charge capture from the Rydberg target (CXRT). The sizes of the signals were measured by chopping the CO_2 laser to use a lock-in amplifier to help reduce noise. The CXRT, however, was measured by directly looking at the output signal coming from the CEM. In order to compare the signal sizes to each other no adjustments need to be made, but to compare the signal sizes to the CXRT an adjustment needs to be made to account for the use of the lock-in amplifier. By chopping the signal, and measuring the RMS fundamental component with the lock-in amplifier the measured signal is actually:

$$S_{Lock-in} = \frac{\sqrt{2}}{\pi} S_{high-L}$$

where $S_{high\text{-}L}$ is the peak signal rate, and $S_{Lock\text{-}in}$ is the signal measured on the lock-in amplifier. The lock-in therefore reads signals that are 0.45 times smaller than the actual peak signal. This factor is taken into account to compare the signal sizes to the CXRT in an accurate manner. With this in mind, there are really three ratios that are of interest that need to be compared between the models and the experiment. The first is the size of the high-L signal compared to the total charge capture from the target: S_{HL}/CXRT. The second is the size of the resolved signals compared to the CXRT: S_L/CXRT. The last is the size of the resolved signals compared

to the size of the high-L: S_L/S_{HL}. These three ratios allow comparisons to be made between model B's predictions and the experimental data acquired. Only model B will be used for comparison for simplicity, but the as noted in the last section, the two models would have fairly similar results.

Table 5.5 shows the ratio of the high-L signal size to the CXRT for the theoretical model and from experimental values for a range of ions. When comparing the model to the experimental results, the accuracy is quite good. Most of the predictions are within a factor of 2 of the experimental values. The worst comparison is Xe^{6+}, and it is only off by a factor of 2.25. Of particular note is that the U^{6+} model compares well, being off 47%. This comparison is important since there are no visible resolved signal sizes in that case that can be compared. The fact that it compares so well gives confidence that accurate predictions for U^{6+} can be made using the theoretical model.

Table 5.5: Comparison between the model B's prediction of the high-L signal compared to the CXRT and the experimentally measured values.

Transition Details	Model B S_{HL}/CXRT	Experimental S_{HL}/CXRT	Experimental/ Model B
U^{6+} 150keV n = 53-93	0.0017	0.0025	1.47
Th^{4+} 100keV n = 37-73	0.0032	0.0033	1.03
Th^{4+} 60keV n = 37-73	0.0027	0.0044	1.63
Pb^{4+} 72keV n = 37-73	0.0033	0.0039	1.18
Kr^{6+} 150keV n = 53-105	0.0017	0.0038	2.24
Xe^{6+} 90keV n = 54-115	0.0018	0.0013	0.72

Table 5.6 shows the resolved signal size to the CXRT for model B and from experimental values for a range of ions. The accuracy of model B in predicting the resolved signal size is

overall fairly good as well. Generally, model B predicts smaller resolved signals compared to the CXRT than were actually seen, with 100keV Th^{4+} being the main exception. A factor of two is once again the general accuracy, but it can be seen that the accuracy of the theory varies even within an ion. This indicates there is something affecting the signal size that has an *L* dependence that is not adequately modeled with the theory. That being said, this effect isn't large enough for much concern since the resolved signal variation is never more than a factor of 2 within an ion. The U^{6+} ion is not shown since there are no resolved signals observed.

Table 5.6: Comparison between model B's prediction of the resolved *L* signals compared to the CXRT and the experimentally measured values. The values in columns 3 and 4 are in parts per million.

Transition Details	Resolved Peak	Model B S_L/CXRT (ppm)	Experimental S_L/CXRT (ppm)	Experiment/ Model B
U^{6+} 150keV *n* = 53-93	*L* = 10	19	?	?
	L = 9	14	?	?
	L = 8	10	?	?
Th^{4+} 100keV *n* = 37-73	*L* = 10	62	71	1.15
	L = 9	50	53	1.06
	L = 8	39	27	0.69
Th^{4+} 60keV *n* = 37-73	*L* = 11	55	173	3.15
	L = 10	45	118	2.62
	L = 9	35	55	1.57
Pb^{4+} 72keV *n* = 37-73	*L* = 9	44	177	4.02
	L = 8	33	113	3.42
	L = 7	23	69	3.00
Kr^{6+} 150keV *n* = 53-105	*L* = 9	16	55	3.44
	L = 8	12	31	2.58
	L = 7	8.8	19	2.16
Xe^{6+} 90keV *n* = 54-115	*L* = 9?	15	44	2.93
	L = 8?	11	39	3.55
	L = 7?	7.7	24	3.12

Table 5.7 shows the ratio of the resolved signal size to the size of the high-*L* for the theoretical model and from experimental values for a range of ions. Since the high-*L* signal is easily measured, this comparison is the most convenient and precise comparison that can be made. Overall the model predicts this ratio well, always being within a factor of 4 for all

resolved signals, and almost always under estimating the ratio. Figures 5.13 through 5.17 give a visual comparison between model B and the experimental scans. The size of the high-L was always normalized to 1 remove the differences in predicted high-L seen in table 5.5. These visuals allow a better discussion of the information within table 5.7 to be made.

Table 5.7: Comparison between model B's prediction of the resolved L signals compared to the size of the high-L and the experimentally measured values.

Transition Details	Resolved Peak	Model S_L/S_{HL}	Experimental S_L/S_{HL}	Experiment/ Model
U^{6+} 150keV n = 53-93	L = 10	0.76%	?	?
	L = 9	0.57%	?	?
	L = 8	0.40%	?	?
Th^{4+} 100keV n = 37-73	L = 10	1.94%	2.13%	1.10
	L = 9	1.57%	1.59%	1.01
	L = 8	1.21%	0.77%	0.64
Th^{4+} 60keV n = 37-73	L = 11	2.05%	3.88%	1.89
	L = 10	1.67%	2.65%	1.59
	L = 9	1.31%	1.23%	0.93
Pb^{4+} 72keV n = 37-73	L = 9	1.33%	4.54%	3.44
	L = 8	1.00%	2.88%	2.86
	L = 7	0.70%	1.74%	2.5
Kr^{6+} 150keV n = 53-105	L = 9	0.97%	1.48%	1.52
	L = 8	0.71%	0.83%	1.16
	L = 7	0.52%	0.49%	0.94
Xe^{6+} 90keV n = 54-115	L = 9?	0.81%	2.48%	3.03
	L = 8?	0.61%	2.16%	3.57
	L = 7?	0.43%	1.33%	3.13

Figure 5.13 shows the experimental and predicted signals for the Th^{4+} at 100keV n = 37 to 73 and figure 5.14 shows is the Th^{4+} at 60keV n = 37 to 73 transition. The 60keV prediction shows a recurring problem seen in these predictions; the resolved signal sizes decline more quickly with decreasing L than the model predicts. The reason for this is not clear, but it is also not a large enough effect to cause great concern since it appears to only cause differences that are within a factor of two of the prediction. The comparison between the 60keV and 100keV

predictions hint that the size of the resolved signal versus the velocity isn't modeled perfectly. Once again, any problems that are seen are relatively minor.

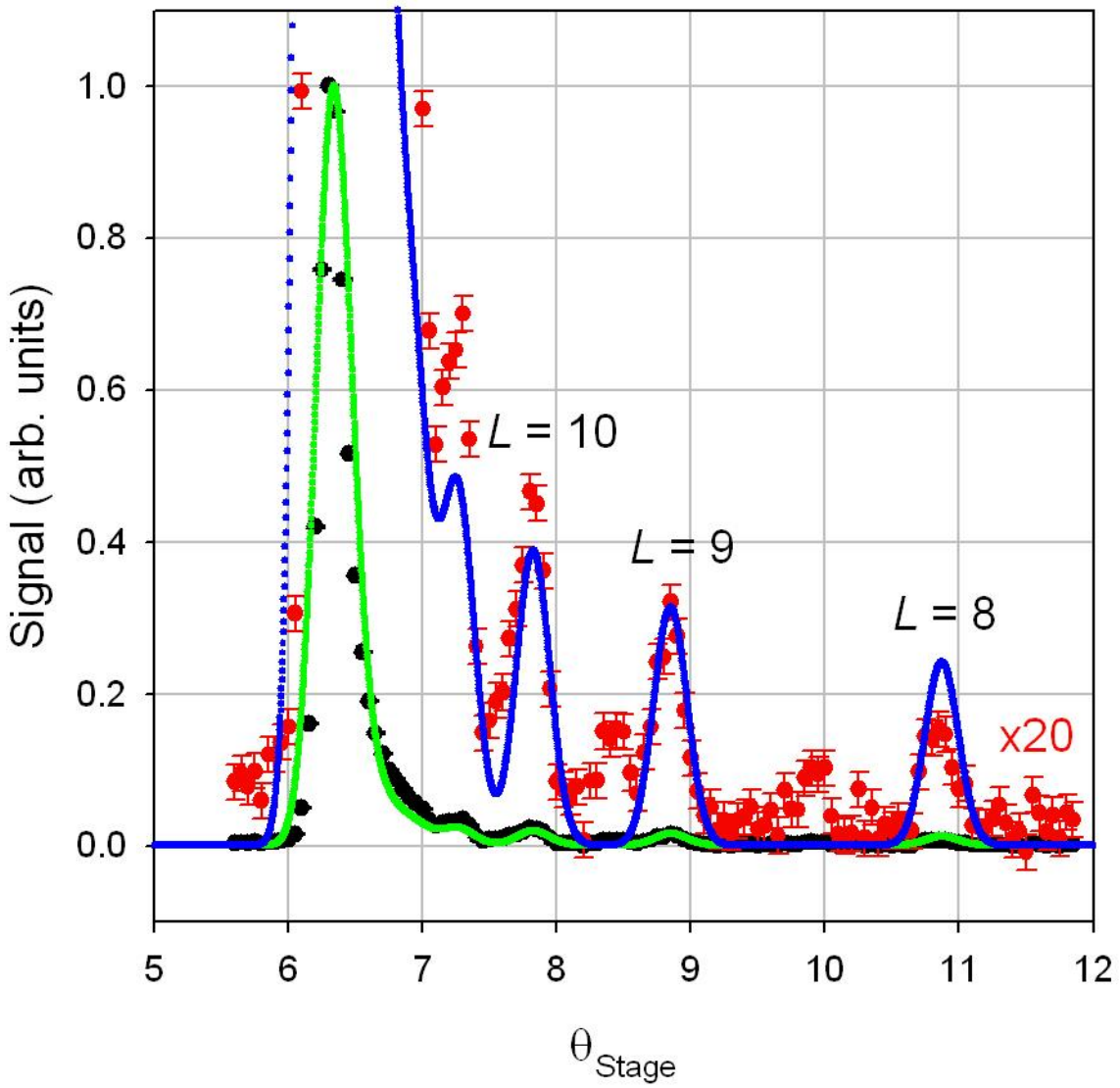

Figure 5.13: Experimental and predicted scans for the Th^{4+} at 100keV n = 37 to 73 transition. The black values are the experimental scan and the red values are 20 times the experimental values. The green values are the predicted scan and the blue values are 20 times the predicted value. The resolved peaks are labeled by the original L value in the transition. Data is taken from CSS10-012.

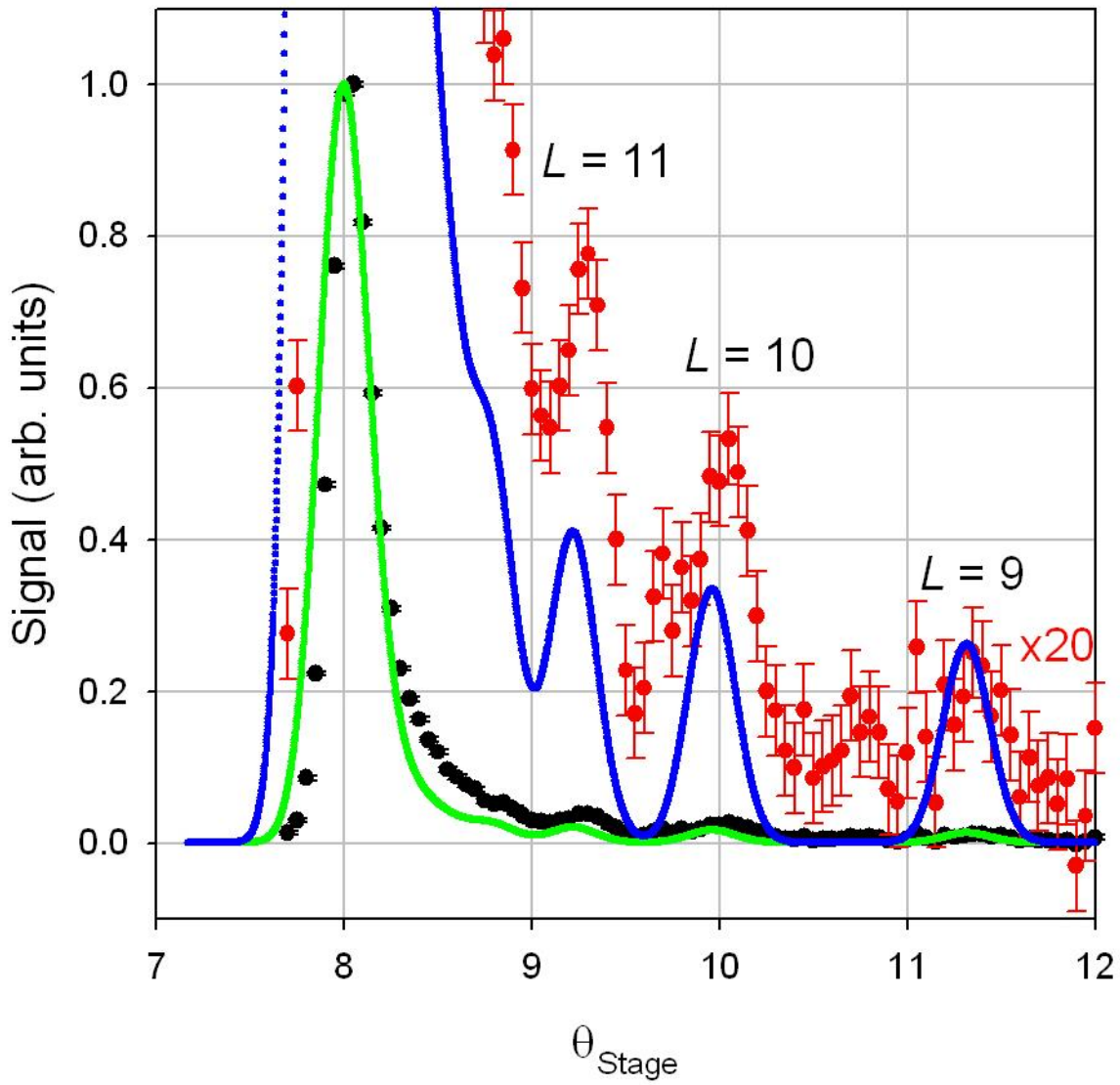

Figure 5.14: Experimental and predicted scans for the Th^{4+} at 60keV n = 37 to 73 transition. The black values are the experimental scan and the red values are 20 times the experimental values. The green values are the predicted scan and the blue values are 20 times the predicted value. The resolved peaks are labeled by the original L value in the transition. Data is taken from CSS10-018 to 019.

Figure 5.15 shows the prediction for the Pb^{4+} at 72keV n = 37 to 73 transition. This gives a collection of three charge 4+ ions that can be compared to the model's predictions. Overall the predictions match well. The Pb^{4+} is the worst with the predictions ranging from being off by a factor of ~2 to 4. The predictions tend to be smaller than the size actually seen, but generally

within a factor of ~2. This gives confidence for the 4+ ions that the size of the resolved signals can be predicted with reasonable accuracy.

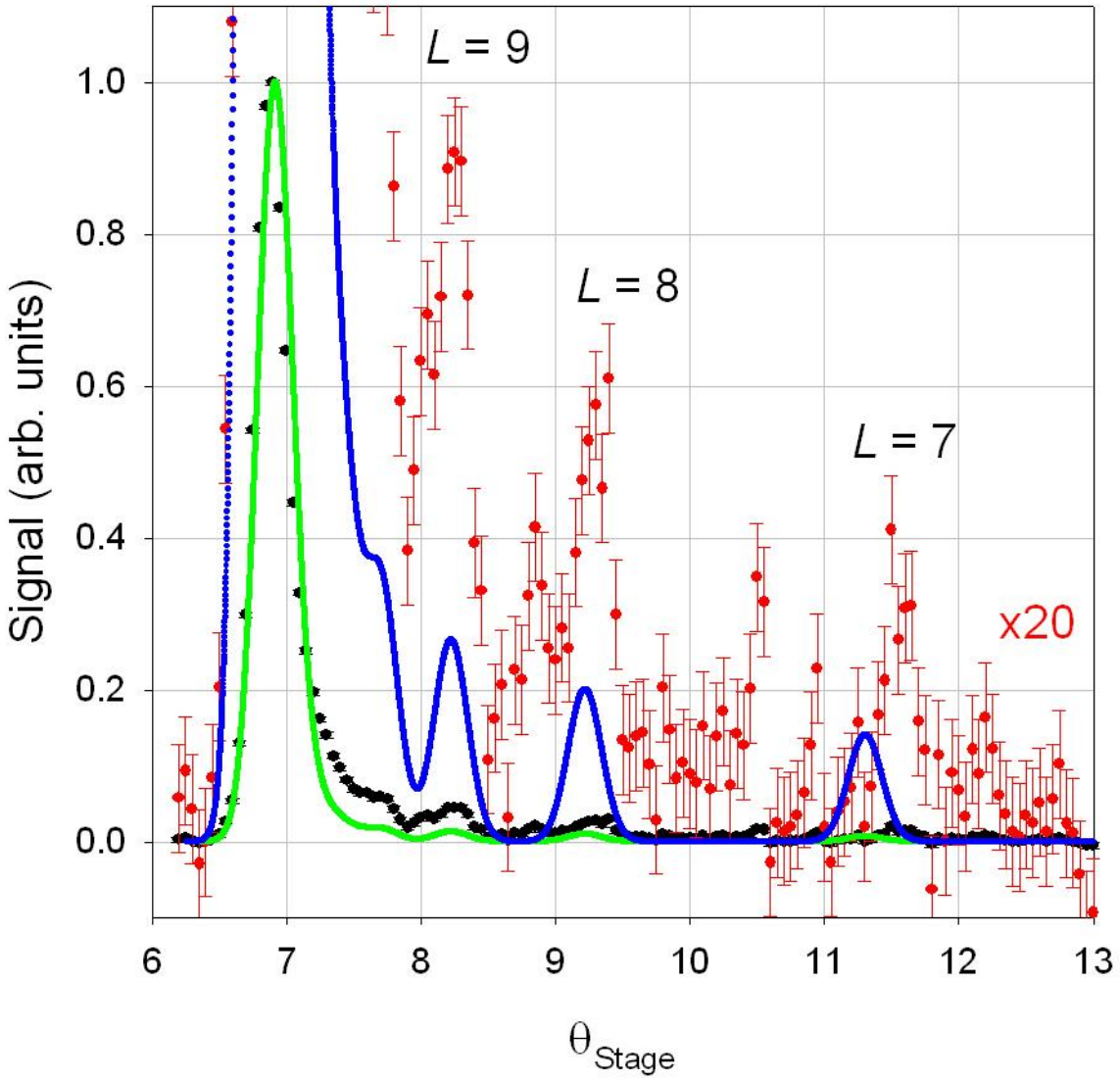

Figure 5.15: Experimental and predicted scans for the Pb^{4+} at 72keV n = 37 to 73 transition. The black values are the experimental scan and the red values are 20 times the experimental values. The green values are the predicted scan and the blue values are 20 times the predicted value. The resolved peaks are labeled by the original L value in the transition. Data is taken from CSS6-091 to 092.

Since it is really the U^{6+} ion that a prediction of the signal size is desired, it would be beneficial if comparisons could be made to other charge 6+ ions to test the accuracy in ions that are similar. There are two transitions that can be compared to: the Kr^{6+} at 150keV n = 53 to 105

transition, and the Xe^{6+} at 90keV n = 54 to 115 transition. The properties of the krypton ion are well known due to the previous study by the Lundeen group [6], but no Xe^{6+} properties are known. For this reason, the dipole polarizability was assumed to be close to that of Kr^{6+} and the exact same value happened to match the resolved signals quite well. The exact classification of the resolved signals could be off, but most likely not off by more than $L\pm1$. This could change the comparison between the model, but most likely not more than the uncertainty already seen in the charge 4+ ions.

Figure 5.16 shows the Kr^{6+} at 150keV n = 53 to 105 transition compared to model B's transition. Once again, the high-L peaks are normalized to 1. The prediction in this case is quite good, with there only being minor differences. Figure 5.17 shows the Xe^{6+} at 90keV n = 54 to 115 transition. The prediction is not as good as the Kr^{6+} showing a predicted size of resolved signals that are ~2 to 4 times smaller than actually seen.

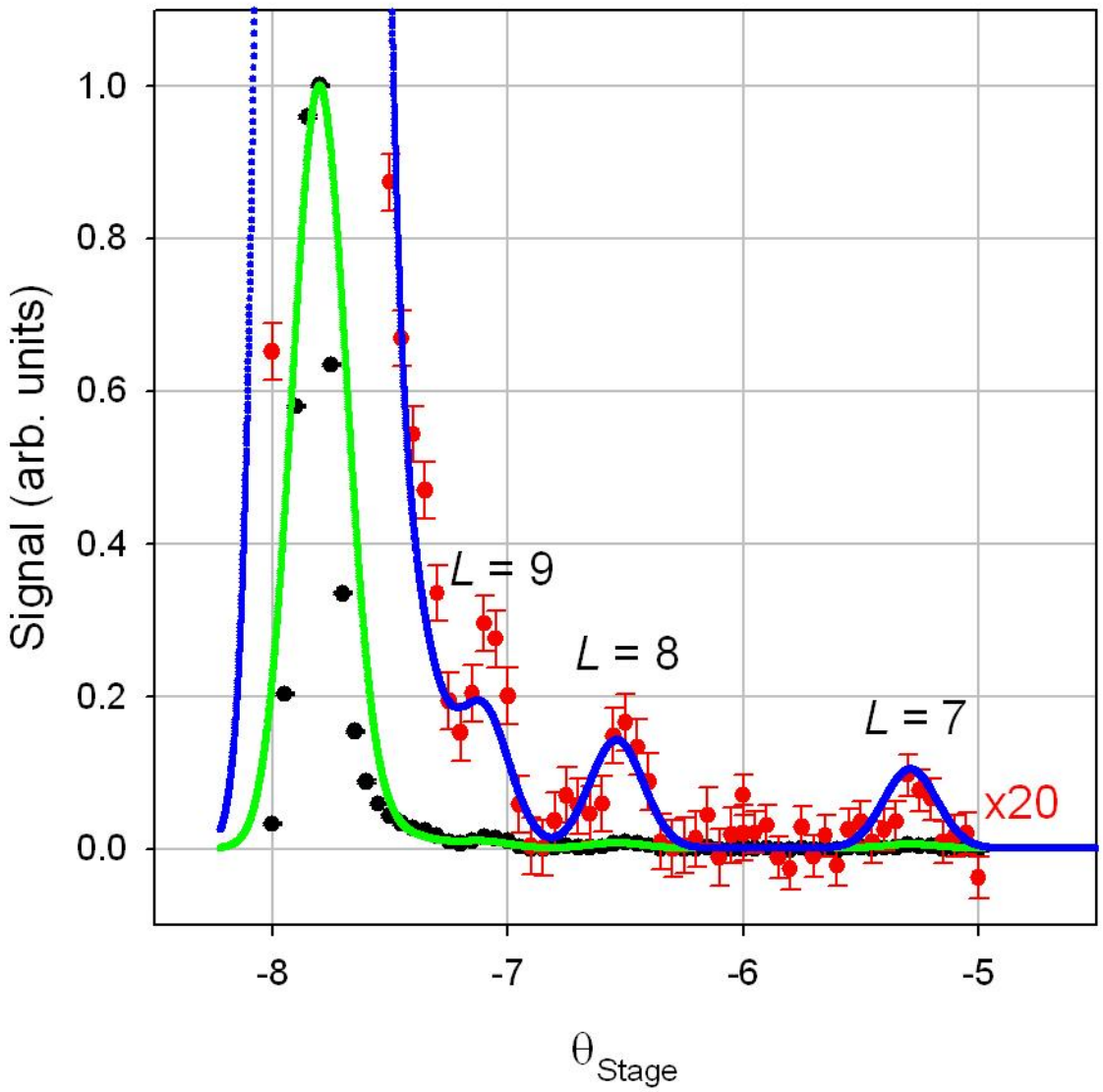

Figure 5.16: Experimental and predicted scans for the Kr^{6+} at 150keV n = 53 to 105 transition. The black values are the experimental scan and the red values are 20 times the experimental values. The green values are the predicted scan and the blue values are 20 times the predicted value. The resolved peaks are labeled by the original L value in the transition. Data is taken from CSS10-042 to 047.

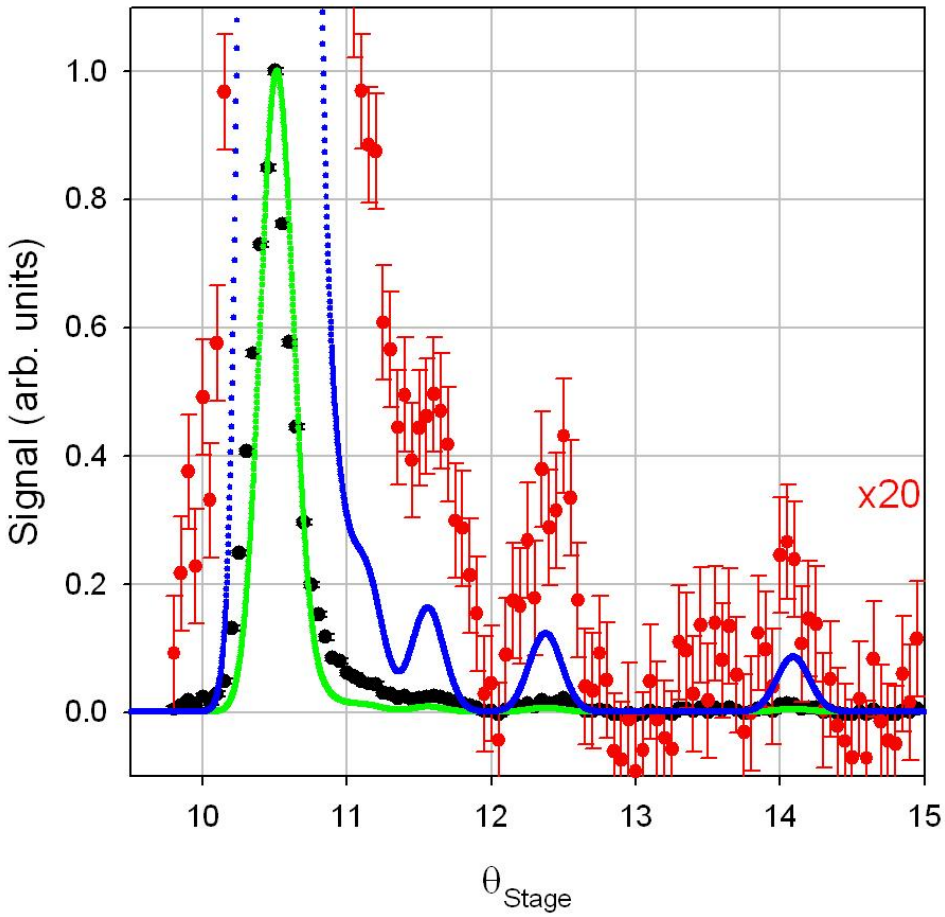

Figure 5.17: Experimental and predicted scans for the Xe^{6+} at 90keV n = 54 to 115 transition. The black values are the experimental scan and the red values are 20 times the experimental values. The green values are the predicted scan and the blue values are 20 times the predicted value. The resolved peaks are labeled by the original L value in the transition, with the caveat that there is a degree of uncertainty within the idenetification of the .resolved peaks. Data is taken from CSS2-056.

The conclusions that can be made are the same as those for the charge 4+ ions, and ones that appear to be universal. The first is that the model is accurate to within a factor of ~2 when looking at all resolved signals involved for an ion. The second is that the model predicts resolved signals that are if anything smaller than actually seen. For this reason model B could be viewed as a minimum signal size that gives a way to judge how big resolved signals should be when compared to the size of the high-L. Model B can therefore be applied to the U^{6+} ion to predict expected resolved signal sizes.

5.5 Uranium Predictions from Model B

Table 5.5 showed that the size of the n = 53 to 93 high-L signal agrees well with the model. This section examines the size of the possible resolved signals. The U^{6+} at 150keV n = 53 to 93 transition shown in chapter 1 of this work has the best signal to noise for a U^{6+} RESIS scan that was achieved. The data for this scan was taken and discussed in Hanni's dissertation [7], although it was reanalyzed to subtract a constant background that is now no longer seen and believed to be separate from any U^{6+} RESIS signal. The data was also independently reanalyzed without normalizing the size of the signal to the DC level. The DC appeared to consistently go down throughout the scan, so this normalization would incorrectly decrease the size of the signal away from the high-L. Figure 5.18 shows the experimental U^{6+} at 150keV n = 53 to 93 transition scan as well as the predicted size of the resolved signals.

The error bars in the scan are 0.073% of the high-L. This is small enough to make anything of the size 0.60% of the high-L easily seen. Figure 5.18 shows that nothing close to this size is visible within the experimental scan. Table 5.8 estimates the possible size of the resolved peaks by fitting the points at the predicted location. Although no obvious resolved peaks are seen, there are apparent positive points in the scan, and this fitting gives a quantitative way to analyze how small these signals might be. Also in table 5.8 is the predicted signal height, and the ratio of experimental over predicted. By taking an average of the two peaks experimental/theoretical ratios, it was found that the average ratio is 0.43(9). This means that the experimental peaks are less than half their predicted size.

Table 5.8: Comparison of the experimental and theoretical U^{6+} at 150keV $n = 53$ to 93 transition resolved peak size. The first column is the resolved peak, the second column is the experimentally seen size taken from fitting the points at the predicted position relative to the high-L size, the third column is the theoretical peak size relative to the high-L size, and the last column is the ratio of the two sizes.

Peak	Experimental	Theoretical	Experiment/ Theoretical
$L = 10$	0.0050(14)	0.0076	0.65(18)
$L = 9$	0.0012(3)	0.0057	0.21(5)

One might attribute this to the accuracy of the model. This seems unlikely for a couple of reasons. The first is that the model never predicted resolved signals larger than observed for any of the other ions looked at. It is difficult to see a reason why U^{6+} would break this rule. This means, the predicted spectra could be viewed as a minimum resolved peak size. This would mean that the U^{6+} peaks are smaller by at least a factor of 2. The second reason is the nature of the RESIS experiment. Since the experiment deals with hydrogenic Rydberg states, the difference between U^{6+} and Xe^{6+} or Kr^{6+} is minimal. They have the same charge, similar velocity (same velocity for Xe^{6+}), and similar lower n states. These are the major factors that dictate the size of the resolved signals. This makes it difficult to see a factor of 2 swing from prediction when comparing U^{6+} to the Kr^{6+} and a factor of 4 swing from prediction when comparing the U^{6+} to the Xe^{6+}. For these reasons, the conclusion is made that the U^{6+} signals are smaller by at least a factor of 4 than the model predictions.

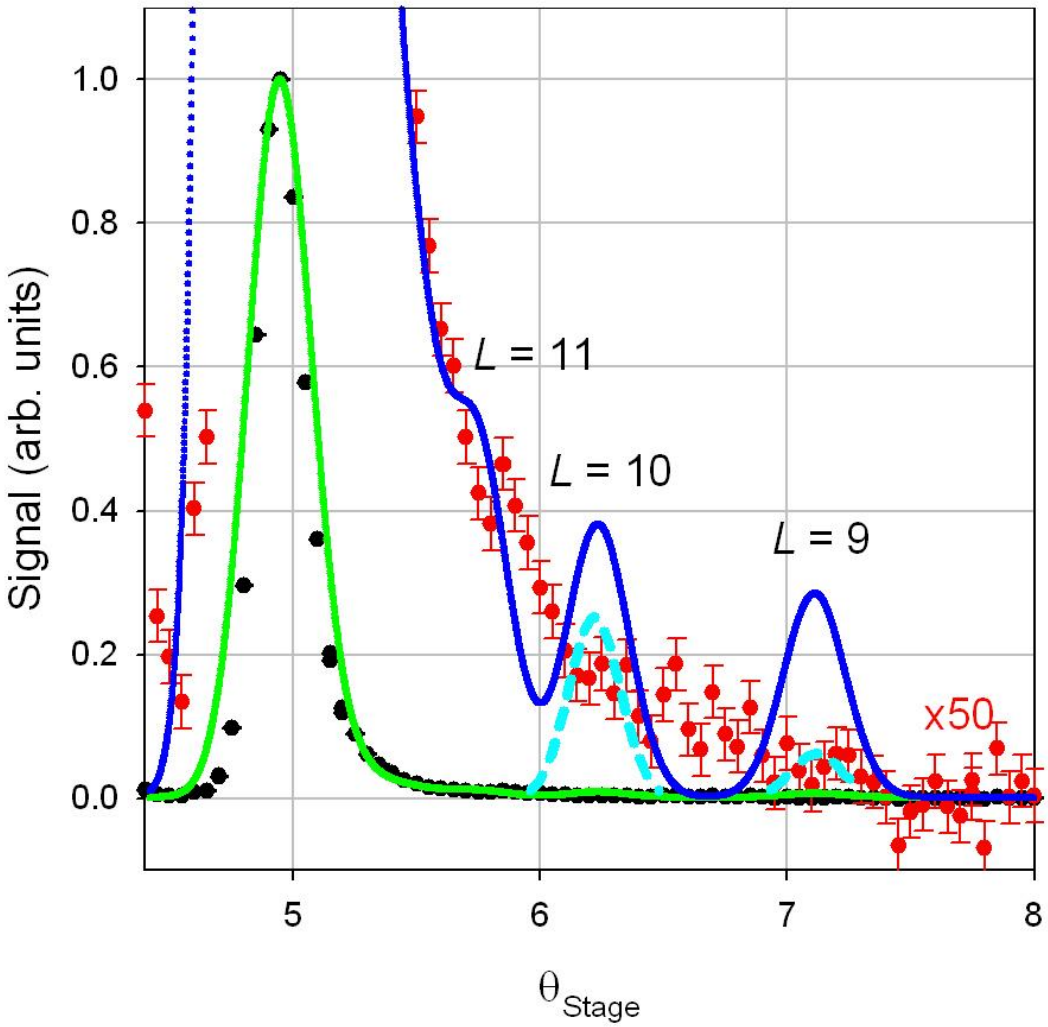

Figure 5.18: Experimental and predicted scans for the U^{6+} at 150keV n = 53 to 93 transition. The black values are the experimental scan and the red values are 50 times the experimental values. The green values are the predicted scan and the blue values are 50 times the predicted value. The light blue dashed peaks are the fitted gaussians to determine possible experimental signal size. The predicted peaks are labeled by the original L value in the transition. Data is taken from MH11-117 to 144.

5.6 Is the 15˚ Magnet a Problem?

The 15˚ magnet is an important part of the beamline since it was added after the successful Kr^{6+} study, and before the problematic U^{6+} study. In order to gain insight about the magnet the population in each L value versus the distance traveled through the beamline can be

looked at for models A and B. This can easily be found by simply summing the population of all *m* states within an *L* value. This is important to look at since it is the population in the resolved *L* values that are of interest. Figure 5.19 shows the relative population in each *L* value throughout the beamline for the U^{6+} at 150keV *n* = 53 to 93 transition for models A and B.

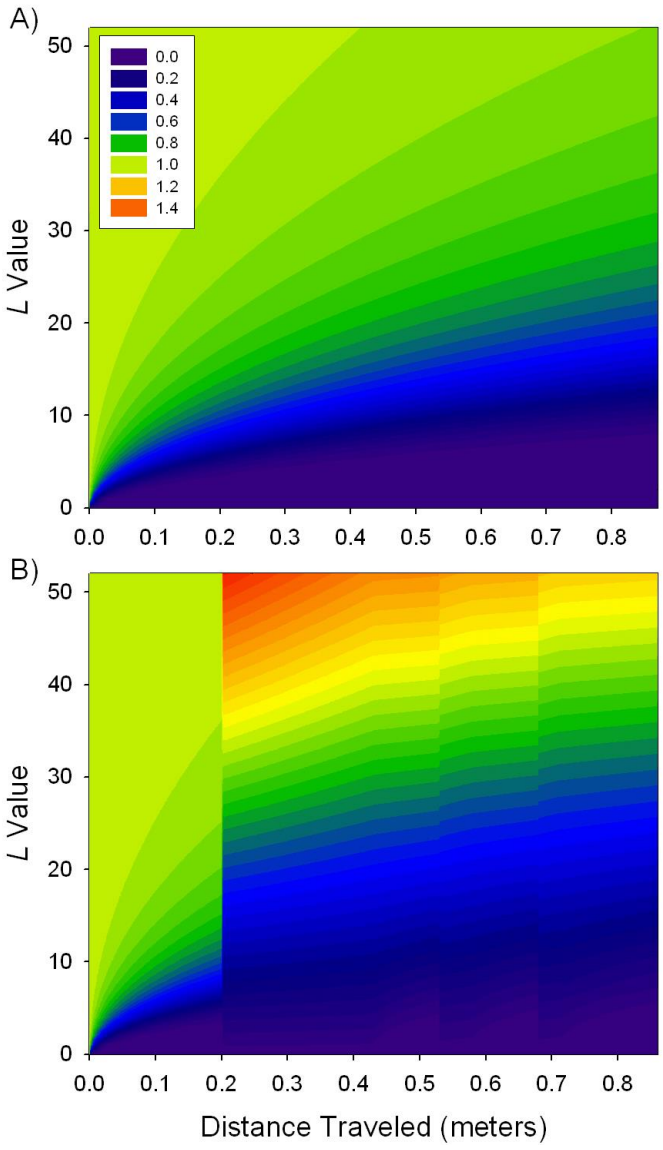

Figure 5.19: Two dimensional plot of the total population within an *L* value as a function of the distance traveled along the beamline for the U^{6+} at 150keV *n* = 53 to 93 transition as determined with A) Model A and B) Model B. The x-axis is the distance traveled in meters between the Rydberg target and the LIR, and the y-axis is the *L* value. At 0.2 meters is the entrance to the magnet in Model B.

This helps put into perspective the importance of the magnet at d = 0.2 meters when it comes to relative populations. The decay after the magnet has some wrinkles in model B caused by the repeller and remixer that shift it away from field free decay a bit, but not much. Clearly the mixing that occurs at the magnet is the largest change between the two models. This essentially has the effect of shifting the population to higher *L* states. For instance, the highest *L* states get a ~40% increase in population. This is due to the magnet equalizing the population in every *L*, *m* state. The higher *L* states have more *m* states, and therefore have more population. This also has the effect of decreasing the *L* state populations in the *L* values that are of most interest (*L* around 11). If the magnet does mix as much as one might expect, it has a negative effect on the resolved signals. Experimental evidence can help determine if this is a significant problem.

The Kr^{6+} experiment was carried out to demonstrate that a charge 6+ ion could be used in this technique in anticipation of carrying out the U^{6+} experiment. Mixing in the 15˚ magnet is one hypothesis for why the resolved signals are so small in U^{6+}. Already this doesn't appear to be the case since the predictions in the last section took into account this mixing, and the U^{6+} signals still appear far too small. In an attempt to further rule out this hypothesis, the Kr^{6+} experiment from before the installation 15˚ magnet was modeled to determine if the 15˚ magnet is causing problems.

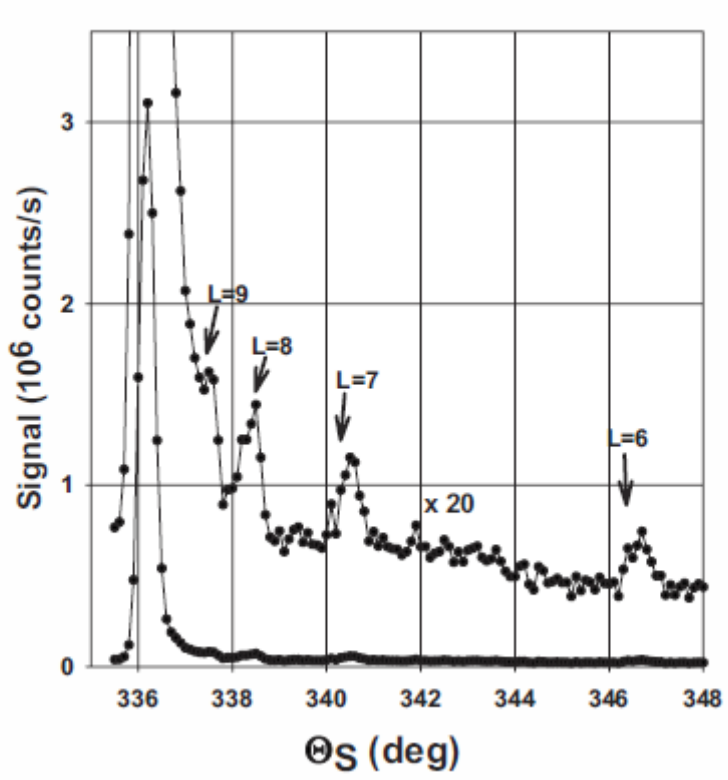

Figure 5.20: Representative RESIS spectrum of Kr^{6+} taken from reference [6]. The horizontal axis is the stage angle. The resolved low-*L* peaks are labeled. The transition was the $n = 55$ to 109 at 48 keV.

Figure 5.20 shows a spectrum taken for the 48keV Kr^{6+} $n = 55$ to 109 transition. The beamline when figure 5.20 was taken is described in reference [6]. A modified model, excluding the 15˚ magnet was used to predict the resolved signal sizes of the peaks seen. Table 5.9 shows the comparison for resolved signals for Kr^{6+} spectra taken before and after the installation of the magnet. In both transitions, the predicted resolved signal sizes are smaller than those actually seen. The size of the resolved signals compared to predicted size does not have the *L* dependence for the transition without the 15˚ magnet that was previously seen. This might indicate that dependence is related to the 15˚ magnet, but exactly how is not obvious.

Since both transitions are modeled fairly accurately, and since the prediction is smaller than experiment for both it is difficult to see how the 15˚ magnet could make the signal sizes for

U^{6+} by at least a factor of 4. The 15˚ magnet may affect the signal sizes, but not greatly. This indicates that the 15˚ magnet is not the source of problems for U^{6+}.

Table 5.9: Comparison between model B's prediction of the resolved *L* signals compared to the size of the high-*L* and the experimentally measured values for Kr^{6+}. The Kr^{6+} at 48 keV was taken before installation of the 15˚ magnet, and the Kr^{6+} at 150keV was taken after installation of the 15˚ magnet.

Transition Details	Resolved Peak	Model S_L/S_{HL}	Experimental S_L/S_{HL}	Experiment/ Model
Kr^{6+} 48 keV n = 55-109	L = 8	0.52%	1.15%	2.22
	L = 7	0.36%	0.80%	2.22
	L = 6	0.23%	0.45%	1.96
Kr^{6+} 150 keV n = 53-105	L = 9	0.97%	1.48%	1.52
	L = 8	0.71%	0.83%	1.16
	L = 7	0.52%	0.49%	0.94

5.7 Hypothesis for Small U^{6+} Resolved Signals

As concluded in this chapter, it appears that the resolved signals for U^{6+} are less than half the predicted size. Also determined was that the high-*L* signal over the CXRT for U^{6+} seen experimentally matched predicted size well (experiment/theory = 1.47 for U^{6+}, and average for all ions was 1.38). One hypothesis that could explain the discrepancy would be if the U^{6+} RESIS spectrum also contains signals from stable A1 metastable Rydberg states. The metastable state Rydberg electron energies would still be very close to hydrogenic, meaning when the n = 53 to 93 transition is being probed, then resonances could still occur for the metastable ions. The high-*L* peak would still be in the same location since it is just the hydrogenic transition, but the resolved peaks for the metastable states would depend on the properties of the A1 ion. These properties are surely different from the ground state ion since the metastable states have J = 1 and would therefore have a quadrupole moment that would shift the resolved signal locations, as well as possibly having a different dipole polarizability that would shift the resolved signals even more. If in the experiment both A1 metastable and ground U^{6+} states are being probed, the

resulting spectrum would be a superposition of their individual spectra. The high-*L* signal would overlay perfectly and look fine, but the resolved signals would become quite complicated and each a smaller fraction of the high-*L* signal.

The resolved signals of the A1 metastable states must then be considered. A possible assumption is that the initial population of the ground and metastable states follows the statistical weight of the states. This would mean that the A1 metastable state would have three times the population of the ground state. Since radiative decay would be the same for either state, the signals from the A1 state would also be three times the size of the ground state. However, due to the quadrupole moment of the A1 state, it would be expected that each *L* state peak would be split into 3 peaks depending on the vector addition of *J* and *L*. These resolved A1 metastable peaks would then be expected to be about the same size as the ground state resolved peaks. The end result would be four times as many resolved peaks seen that were all roughly the same size, only ¼ of which would be from the ground state. Each individual peak would be four times smaller compared to the high-*L* signal than would be expected if the signal was just from the ground state. This fits very well with the spectra seen in figure 5.19, and suggests that the A1 and ground state are statistically populated initially.

Signals from autoionizable metastable states also need to be considered. Although 95% of the initial beam is autoionizable metastable states, only the C3 state survives past the 15˚ magnet. Therefore, the amount of $n = 53$ states within the C3 state survive to the LIR is what needs to be considered (there is little autoionization after the LIR due to the high *n* state). Table 5.10 outlines the key values that need to be compared between the C3 state and the A1 and ground state in order to determine their relative resolved peak sizes. The second row shows their initial fraction of the total beam at capture from their statistical weights. The C3 state has a

larger initial population due to its higher J value. There is differing amount of decay of the n = 53 state between the C3 state, which autoionizes quickly, along with the relatively slow radiative decay all three states experience. Using the model from chapter 4, it is predicted that about 14.7% of the n = 53 C3 metastable levels survives to the LIR to contribute to the signal, the rest autoionizes. For the radiative decay for all three states have only 53.0% of the initial n = 53 state survives to the LIR to contribute to the signal. The C3 states fraction that makes it to the LIR is the autoionization fraction (14.7%) multiplied by the radiative decay fraction (53.0%), which gives an overall survival of the C3 state at the LIR of 7.79%. These values are shown in row 3 of table 5.10. Furthermore, since the C3 state is a J = 3 state, each L population will be distributed amongst 7 peaks depending on the vector addition of J and L. This means only 1/7 = 14.3% of an L state population is in each C3 resolved peak. The equivalent fraction for each state is shown in row 4 of table 5.10. By multiplying rows 2 to 4 together, an overall comparative factor between the resolved signal sizes. This analysis shows that the C3 resolved signals would only be about a 15% of the size of the other resolved peaks. This analysis shows that the resolved signals from the C3 state would be expected to be small compared to the other signals, and therefore not a significant problem in the experiment.

Table 5.10: Comparative factors that determine the relative sizes of resolved signals for the C3, A1, and ground state. The second row is the initial fraction of the beam in each state. The third row is the $n = 53$ state remaining at the LIR. The fourth row is the fraction of an L population in each resolved peak. The fourth row is rows 2 to 4 multiplied together. The last row is the predicted resolved signal size normalized to the predicted size for the ground state.

	C3 State	A1 State	Ground State
Initial Fraction of Total Beam	8.24%	3.53%	1.18%
$n = 53$ Population Remaining at LIR	7.79%	53.0%	53.0%
L Population in Each Resolved Peak	14.3%	33.3%	100%
Overall Fraction	.00091	.0062	.0062
Overall Size Normalized to Ground State	0.15	1	1

Chapter 6: Conclusion and Future Directions

This dissertation has served to explore why U^{6+} RESIS studies have not yet been successful, and develop a better understanding of the RESIS study at large. Specifically three questions were posed that motivated this research:

4) What is the dominant source of the background in the U^{6+} RESIS study?
5) Can the background be reduced?
6) Why are the U^{6+} signals so small?

These questions have been looked at in detail, and answers can be given.

6.1 Conclusions about U^{6+} and Th^{4+}

The main motivation for a detailed analysis of the background and signal sizes within the RESIS technique was the success of the Th^{4+} experiment, and the difficulties encountered the U^{6+} experiment. It was originally observed that there were two major problems with the U^{6+} experiment when compared to the Th^{4+} experiment, the background was larger, and the resolved signals were smaller. These two problems can now be re-evaluated with a greater understanding of each.

The background is larger within the U^{6+} experiment, but really isn't a major hindrance experimentally. Even at the background rates originally detailed in chapter 1 if the U^{6+} signals were the same size as the Th^{4+} signals, then the collection time would need to be approximately doubled for U^{6+} in order to have the same signal to noise. This could be (and was) done and yet no resolved signals were seen. Also, the background has been reduced by using the preionization fields before the detector. These fields reduced the background within the U^{6+}

experiment to levels very similar to those in the Th^{4+} experiment (~1.5 times the high-*L* signal). Despite the better background size, resolved signals were still not seen within the U^{6+} experiment. This further demonstrates that the background seen within the U^{6+} experiment is a negative, but not a major hindrance in the RESIS experiment with U^{6+}.

The major problem that makes the U^{6+} RESIS experiment difficult are the smaller, and apparently more complex, resolved signals. In chapter 5, predictions of the expected signal sizes showed that the U^{6+} resolved signal sizes were at least a factor of 4 smaller than would be expected. A hypothesis was presented there that non-autoionizing $J = 1$ metastable states are contributing to the U^{6+} RESIS signals making the resolved signals smaller by a factor of 4 and much more complex. This could explain the smaller U^{6+} signals, but only if the lowest energy metastable state was a $J = 1$ state, as is predicted to be the case for U^{6+}. If instead, a $J = 2$ state was the lowest energy metastable state, as is predicted for Th^{4+} [18], then there would be a decay channel for all metastable Rydberg states, and there would be no metastable contribution to the RESIS signal. Of course, even today, none of these metastable excited states, in either Th^{4+} or U^{6+}, have been seen spectroscopically, and the uncertainty in theoretical calculations makes it difficult to be sure that the $J = 1$ state is in fact the lowest state in U^{6+} but not in Th^{4+}. Still, if this were in fact the case, it would explain neatly why the Th^{4+} experiment succeeded, but the U^{6+} experiment did not. It's worth noting that when the experiments began, there were no predictions of the order of excited levels in either ion.

6.2 Can the U^{6+} Experiments be Made Practical?

The present U^{6+} experiment didn't succeed because the resolved signals were very small ($S_L \sim 0.002 * S_{HL}$ = 3 ppm of the CXRT), and they had to compete with a background that was much larger ($B \sim 5000 * S_L$). The background comes from autoionizing Rydberg levels that are

produced in great numbers because the original U^{6+} beam extracted from the ion source could be as much as 99% metastable. Some of the metastable Rydberg levels are stable enough that they contribute to the RESIS signal and are responsible for reducing the size of the resolved RESIS signals by about factor of 4.

One may consider two possible approaches for redesigning the U^{6+} experiment

1) Make the resolved signals larger by using a different laser (not the CO_2 laser previously used), that makes it possible to excite a lower *n* level of U^{5+}. It appears *n* = 24 could be probed in this way. Especially if this change were combined with a change of Rydberg target so that the peak of the capture distribution was near *n* = 24, this could result in significant increases in the size of both the high-*L* signal and the resolved signals relative to the total charge capture.
2) Obtain the U^{6+} beam from a different type of ion source that might have a much lower fraction of metastable levels. One possibility might be an EBIS (Electron Beam Ion Source). Reduction in the metastable fraction could significantly reduce the background, and also possibly increase the size of resolved signals if it also reduced the flux of "stable" metastable Rydberg levels bound to the *J* = 1 excited level of U^{6+}. Unfortunately, such an ion source would likely produce a much smaller total U^{6+} beam flux, so some analysis is necessary to predict if the change could be an advantage.

In order to explore these two alternative approaches, it will help to systematically consider the variable factors that determine the signal to noise in the RESIS experiment. Let I_0 represent the initial U^{6+} beam rate, and T be the total data collection time. Let f_{Cap} represent the fractional charge capture, and f_M represent the fraction of autoionizing Rydberg levels formed at

capture. Further, let f_S represent the fraction of the stable Rydberg levels contributing to a resolved RESIS signal and f_B represent the fraction of autoionizing Rydberg levels contributing to the background. This would mean that the resolved signal is given as:

$$S = f_S(1 - f_M) f_{Cap} I_0 \tag{6.1}$$

and the background is:

$$B = f_B f_M f_{Cap} I_0 \tag{6.2}$$

These equations can be used in equation 1.2 from chapter one to give:

$$\frac{S}{\sigma} = \frac{\sqrt{\frac{ST}{2}}}{\sqrt{1 + \frac{2B}{S}}} = \frac{f_S(1 - f_M)}{\sqrt{f_S(1 - f_M) + 2 f_B f_M}} \sqrt{\frac{f_{Cap} I_0 T}{2}} \tag{6.3}$$

In the present U^{6+} experiment based on the n = 53 to 93 transition with the CO_2 laser these values were found to be $I_0 \approx 5nA = 5 \times 10^9 s^{-1}$, $f_{Cap} \approx 0.05$, $f_M \approx 0.95$, $f_S \approx 3.6 ppm$, and $f_B \approx 0.0014$. I_0 and f_{Cap} are estimates. f_M is the statistical weight of autoionizing metastable levels, and f_S is an average over the three signal sizes predicted in Table 6.2. The simulations of Chapter 4, specifically table 4.6 and figure 4.11, predict that only the C3 metastable Rydberg levels contribute to the background, and 0.016 of the initial C3 population at the Rydberg target contributes to the background. If the initial beam is assumed to be statistically populated, then f_B can be taken to be the product of this factor and the statistical weight of the C3 metastable levels, 0.086. Plugging these values into equation 6.3 gives a S/σ of 1.0 in a data collection time of 660 s, which was the data collection time for each point in figure 5.18, just about right. This total beam flux and data collection time will form a useful comparison point in considering possible improvements.

The first approach to improving the experiment would be to use a different excitation laser, to probe a lower n level of U^{5+}. The CO_2 laser is unusual in that it gives a high-power single-frequency laser at modest cost. Recent technological advances in the 1.5 micron region used for fiber communication offer a possible alternative choice. It is now possible to buy a single frequency laser at any of 45 frequencies spaced about 100 GHz in the wavelength range 1530.33 – 1565.50 nm [31]. Of these, one at 1565.50 nm is well suited to excite the n = 24 level of U^{5+} to an upper state of n = 92. This low power single frequency laser can be matched to a high-power fiber amplifier made by IPG Photonics to provide 30 W of CW power for a total price of about $60,000 [32]. This is very comparable to the price of a CO_2 laser of similar power, and it should make excitation of the n = 24 to 92 transition, via Doppler tuning, very practical. The best Rydberg target to populate n = 24 is a 7F Rydberg target, which provides a population fraction of about 6% in n = 24, and a population fraction in a single L level of about 0.25%. This is more than a factor of 10 higher than produced in a single L level of n = 53 with a 10F target. One negative factor of probing n = 24 rather than n = 53 is the much shorter radiative lifetimes of the n = 24 levels. This would require redesign of the RESIS apparatus to shorten the distance between the target and the LIR. It appears this would be possible by removing the 15˚ magnet and the remixer, giving a total distance of 8 cm between the RT and the LIR. Figure 6.1 illustrates a possible geometry.

There could be a 1 cm gap between the Rydberg target and the repeller array, leaving 1.4 cm to be used after the repeller. In order to probe the U^{6+} at 150 keV n = 24 to 92 transition, room needs to be left for the laser to be Doppler shifted. If the mirror is mounted 2.5 cm off axis, then the spectrum for $L > 8$ can be probed in about 0.45 cm along the beam axis. This can be accommodated and still have about a 1 cm gap between the repeller and the LIR.

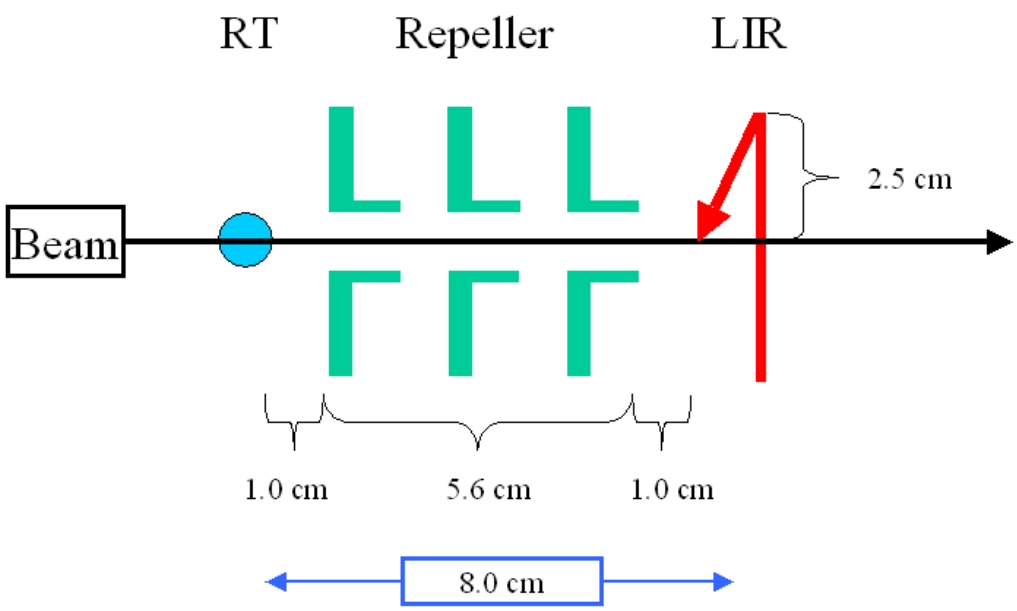

Figure 6.1: Schematic showing the distances that could be used for the probing of the U^{6+} at 150 keV n = 24 to 92 transition. The total distance between the RT and the LIR is at most 8 cm depending on the resolved signals being probed.

The velocity of the beam also needs to be considered for optimization of the signal size. The models developed in the last chapter can be used (model B was used) to get precise predictions for the signal size. The distances shown before the LIR in figure 6.1 were used, and all distances after the LIR were assumed to be the same as the previous experiment since the n = 94 state has a much longer lifetime that can accommodate traveling long distances. Table 6.1 shows the velocities that were considered, and at each velocity the total capture cross section, and the fractional capture into n = 24 from a 7F target (taken from CTMC). Also shown is the predicted largest resolved signal size as a fraction of the total CXRT. In predicting the resolved signal size it was assumed that only ¼ of the non-autoionizing capture was by ground state ions, as appears to be the case. It was found that the n = 24 to 92 transition is maximized at 150 keV. At higher velocities the excitation probability decreases due to a shorter transit time through the 1.5 μm laser, and at lower velocities the radiative decay makes the signals smaller.

Table 6.1: Comparison of the predicted resolved signal sizes the n = 24 to 92 transition for varying beam energies. The second and third columns give the predicted total capture cross section and fractional capture into the n = 24 state from CTMC. The fourth column is the largest predicted resolved RESIS signal size as a fraction of the total CXRT.

Beam Energy	Total Capture cross section (cm^2)	Fractional Capture into n = 24	Peak Resolved Signal Size/CXRT (ppm)
60 keV	7.1×10^{-12}	6.4%	38
90 keV	7.1×10^{-12}	6.9%	44
120 keV	6.8×10^{-12}	6.8%	62
150 keV	6.6×10^{-12}	5.9%	67
240 keV	5.7×10^{-12}	3.9%	46
480 keV	1.9×10^{-12}	2.6%	20
600 keV	1.1×10^{-12}	2.9%	20
900 keV	3.3×10^{-13}	2.4%	13

Figure 6.2 shows the predicted signal versus the stage angle for the n = 24 to 92 transition at 150 keV. The transit width through the laser was used to determine the width of the lines. Since the n state is much lower the separation in L states is much larger, and therefore higher L states are completely resolved. The signal size in figure 6.2 is a fraction of the CXRT in parts per million. The predicted signal sizes include the factor of four reduction due to the superposition of signals from A1 metastable Rydberg levels and ground state Rydberg levels, but the spectrum shown does not include the pattern of signals from the A1 metastable levels which should be similar in size.

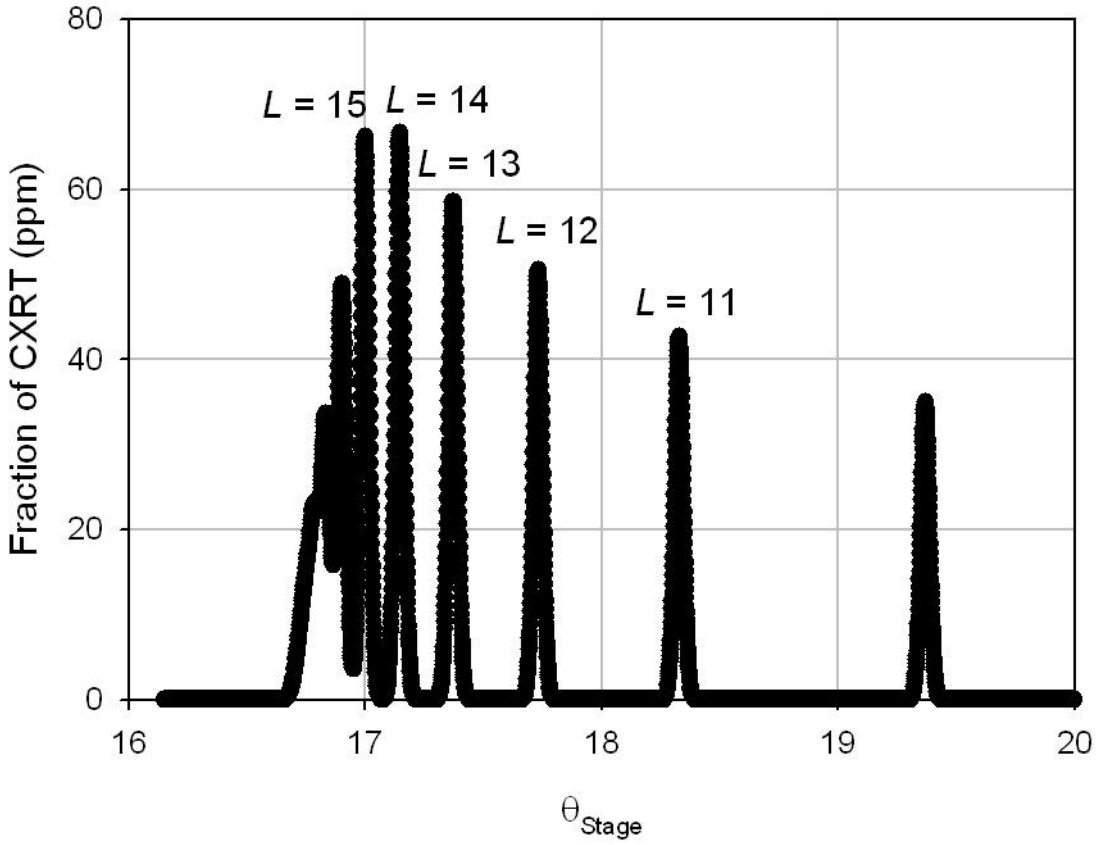

Figure 6.2: Predicted signal size for the U^{6+} at 150 keV n = 24 to 92 transition. The horizontal axis is the stage angle, and the vertical axis is the signal size compared to the total CXRT for a 7*F* target in parts per million. This prediction was made using model B described in chapter 5. It includes the factor of four reduction in signal size due to the superposition of signals from the A1 metastable Rydberg levels, but does not illustrate the complex spectrum, of similar size, expected from those levels.

Table 6.2 is a comparison between the predictions made for the U^{6+} at 150 keV n = 53 to 93 transition and the U^{6+} at 150 keV n = 24 to 92 transition. The predictions from model B were used for each transition for the most accurate comparison. It was shown in chapter 5 that the resolved signal sizes are smaller than predicted for the n = 53 to 93 transition, likely due to only ¼ of the CXRT measured being into the ground state, and the other ¾ into "stable" A1 metastable states. A factor of 0.25 was used to account for this discrepancy for both transitions. In table 6.2 the three largest fully resolved signals were used for comparison. The average

predicted peak size for the n = 24 to 92 transition is about 18 times the average peak size for the n = 53 to 93 transition, 64 ppm to 3.6 ppm respectively.

Table 6.2: Comparison of the predicted resolved signal sizes for U^{6+} at 150keV for the n = 53 to 93 transition and the n = 24 to 92 at 240 keV transition.

Transition	Peak	S_L/CXRT (ppm)
U^{6+} 150 keV n = 53-93	L = 10	4.8
	L = 9	3.5
	L = 8	2.5
U^{6+} 150 keV n = 24-92	L = 15	66
	L = 14	67
	L = 13	59

The contribution to the n = 24 to 92 signal of the C3 state needs to be considered. In the last chapter it was predicted that the C3 resolved signals would only be 14% the size of the ground state resolved signals. The same analysis can be done in for the shorter beamline apparatus. The lower L states in the n = 24 population causes a much greater overall autoionization rate (goes as $1/L^8$), which compensates for the shorter autoionization time before the LIR. In fact, only 5.9% of the C3 state n = 24 population is predicted to survive to the LIR based on autoionization alone. This is down by a factor of 3 from the n = 53 population in the current beamline experiment. This would mean that the C3 resolved signals would be about 5% of the ground state resolved signals. For this reason it was assumed their contribution is negligible.

How would these larger signals affect the signal to noise? Moving from the 10F to 7F target would reduce f_{Cap} by about a factor of 2.8, but exciting n = 24 would increase f_S by a factor of 18. Assuming that the beam energy remains at 150 keV, the autoionizing metastable fraction would remain at 0.95. Because the autoionizing Rydberg levels formed from the 7F target would have lower values of n, and therefore higher rates of autoionization, it is estimated that f_B would be significantly reduced, to f_B = 0.00042, giving the parameter values

of $I_0 \approx 5nA = 5\times10^9 s^{-1}$, $f_{Cap} \approx 0.018$, $f_M \approx 0.95$, $f_S \approx 64 ppm$, and $f_B \approx 0.00042$.

Substituting these values into Eq. 6.3 gives a signal to noise in 660 s of data collection of 20, a net increase of a factor of 24 over the n = 53 to 93 transition. Even reducing the data collection time by a factor of 4 to 165 seconds per point would still yield a S/σ of 12 on a resolved signal. Of course, it would still be expected that the RESIS spectrum would be complex, consisting of a superposition of signals from the J = 1 "stable" metastable Rydberg levels and normal Rydberg levels bound to the ground state. And, it is also possible that metastable autoionization would no longer be the dominant source of background and noise, since the primary U^{6+} beam would be much larger without the discrimination of the 15 degree magnet, and controlling the background would require a high degree of resolution between the primary beam and the energy tagged signal beam. Still, it appears that this single change could make the experiment succeed, using the existing ECR ion source.

The second possible approach would be to use a different ion source that could possibly provide a U^{6+} beam with lower metastable content. One possibility would be the Electron Beam Ion Source (EBIS), which is reputed to have a low metastable fraction compared to ECR sources. While this is commonly asserted in circles of ion source experts, we know of no measurements that actually confirm this. This is partly due to the difficulty of measuring the metastable content of ion beams.. Reducing the metastable fraction of the ion beam would have two immediate beneficial effects. First, since a larger fraction of the beam would represent stable Rydberg levels that would contribute to the RESIS signals, the size of the signals relative to the total capture beam would increase, even at a constant value of f_S. Second, fewer metastable levels would reduce the size of the background, making the measurement of the RESIS signals much less time-consuming. An added plus would be if the reduced metastable fraction also applied to

the "stable" metastables bound to the excited $J = 1$ level. This could increase the size of f_S by up to a factor of four, and also reduce the complexity of the RESIS signal's spectrum.

To examine the effect on the RESIS signal to noise, and determine the range of acceptable reductions in total beam intensity, equation 6.3 can be evaluated using four sets of parameter values as a function of the metastable fraction f_M.

a) the $n = 53$ to 93 conditions:

$I_0 \approx 5nA = 5\times10^9\, s^{-1}$, $f_{Cap} \approx 0.05$, $f_S \approx 3.6\, ppm$, and $f_B \approx 0.0014$

b) the $n = 53$ to 93 conditions with $f_S = \dfrac{4 f_S}{1+3 f_M}$

c) the $n = 24$ to 92 conditions:

$I_0 \approx 5nA = 5\times10^9\, s^{-1}$, $f_{Cap} = 0.018$, $f_S \approx 64\, ppm$, and $f_B \approx 0.00042$

d) the $n = 24$ to 92 conditions with $f_S = \dfrac{4 f_S}{1+3 f_M}$

Conditions b) and d) assume that as f_M decreases the factor of 4 decrease in RESIS signal size gradually goes away. Figure 6.3 shows each of these four parameter cases plotted versus f_M.

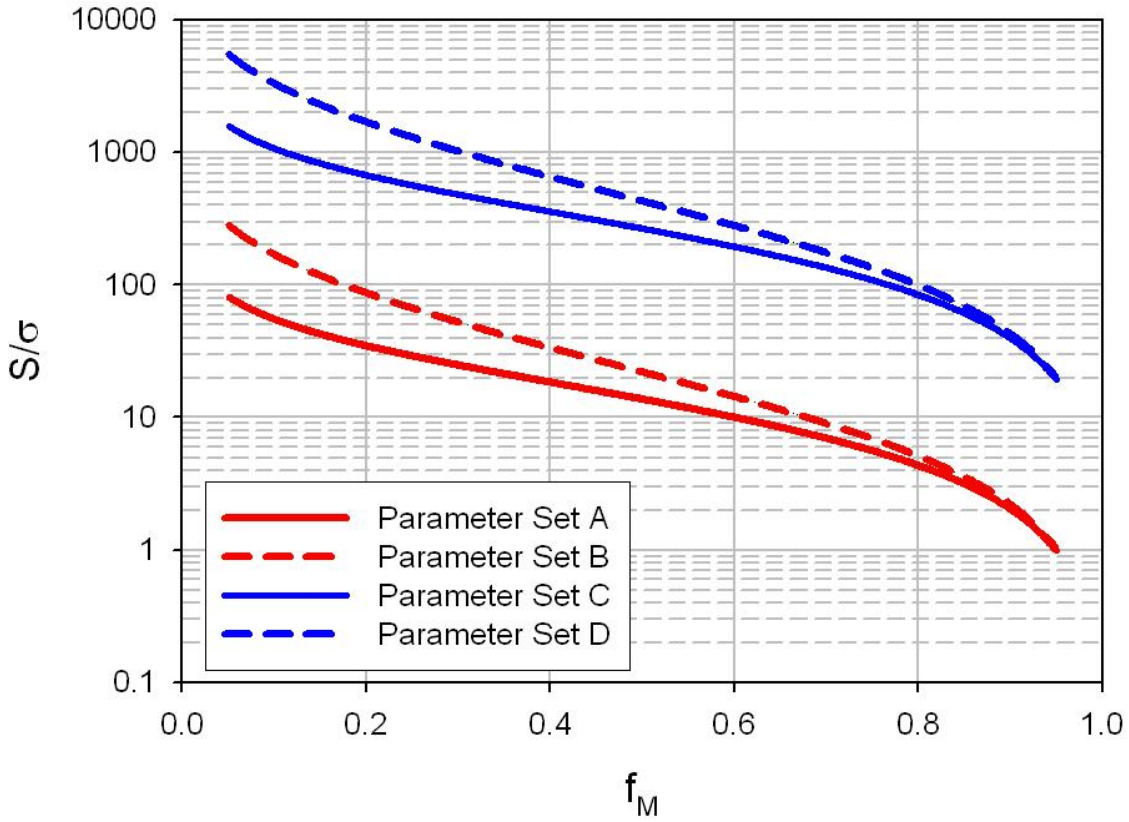

Figure 6.3: Predicted signal to noise versus f_M for the four parameter sets described in the text. The red lines are the n = 53 to 93 transition, and the blue lines are the n = 24 to 92 transition. The solid lines are a constant f_S, and the dotted lines are when f_S increases with decreasing f_M. The data collection time used was 660 seconds, and the initial U^{6+} beam was assumed to be 5 nA.

Note in figure 6.3 that at f_M = 0.95, the n = 53 to 93 S/σ is near 1.0 as before, and the n = 24 to 92 S/σ is near 20. As f_M decreases, the S/σ for both signals increases. The n = 53 to 93 S/σ reaches 35 at f_M = 0.20 or 88 if the J = 1 fraction also decreases. The n = 24 to 92 S/σ reaches 681 at f_M = 0.2 or 1702 if the reduced J = 1 fraction is included. The square of these factors would represent the acceptable decreases in the product of beam intensity (I_0) and data collection time (T). For example, in the most favorable case at f_M = 0.20 the beam current could be reduced by a factor of $(1702)^2 = 2.9 \times 10^6$ and still have a S/σ of about 1 in 660 seconds. In other words the beam current of 5 fA for 230 s, instead of 5 nA for 660 s. This means that a

substantial fraction of overall beam intensity could be sacrificed with a different ion source, if it meant fewer metastable states were present.

Overall, either redesigning the experiment to look at lower *n* states, or decreasing the metastable population from the ion source could improve the signal to noise in the U^{6+} RESIS experiment. If both of these were achieved, then the signal to noise could be improved by very large amounts.

References

[1] S. L. Woods, and S. R. Lundeen, *Phys. Rev. A* **85**, 042505 (2012) and references therein.

[2] S. Woods, C. Smith, J. Keele and S. R. Lundeen, *Phys. Rev. A* **87**, 022511 (2013).

[3] E. L. Snow, M. A. Gearba, R. A. Komara, S. R. Lundeen and W. G. Sturrus, *Phys. Rev. A* **74**, 049905 (2006).

[4] E. L. Snow and S. R. Lundeen, *Phys. Rev. A* **77**, 052501 (2008).

[5] M. E. Hanni, J. A. Keele, W. G. Sturrus, S. R. Lundeen, *Phys. Rev. A* **78**, 062510 (2008).

[6] S. R. Lundeen and C. W. Fehrenbach, *Phys. Rev. A* **75**, 032523 (2007).

[7] M. E. Hanni, Ph.D. dissertation, Colorado State University, 2010.

[8] M. E. Hanni, Julie A. Keele, S. R. Lundeen, and C. W. Fehrenbach, *Phys. Rev. A* **82**, 022512 (2010).

[9] J. A. Keele, S. R. Lundeen and C. W. Fehrenbach, *Phys. Rev. A* **83**, 062509 (2011).

[10] J. A. Keele, C. S. Smith, S. R. Lundeen and C. W. Fehrenbach, *Phys. Rev. A* **85**, 064502 (2012).

[11] D. S. Fisher, Ph.D. dissertation, Colorado State University, 2000.

[12] Beam Imaging Solutions Inc. (2015). Available: http://www.beamimaging.com/BOS.html

[13] J. A. Keele, Ph.D. dissertation, Colorado State University, 2013.

[14] J. J. Sakurai, *Modern Quantum Mechanics*, edited by S. F. Tuan (Addison-Wesly Publishing Company, Inc., Menlo Park, CA, 1994).

[15] A. R. Edmonds, *Angular Momentum in Quantum Mechanics*, (Princeton University Press, Princeton, NJ, 1974).

[16] J. A. Keele (private communication).

[17] M. Aramowitz and I. A. Stegun, *Handbook of Mathematical Functions with Formulas, Graphs, and Mathematical Tables, 9th printing* (Dover Publications, Inc., New York, 1972).

[18] U. I. Safronova and M. S. Safronova, *Phys. Rev. A* **84**, 052515 (2011).

[19] U. I. Safronova and M. S. Safronova (private communication).

[20] H. A. Bethe and E. E. Salpeter, *Quantum Mechanics of One- and Two-Electron Atoms*, (Dover Publications, Inc., Mineola, New York, 2008).

[21] A. Brazuk, D. Dijkkamp, A. G. Drentje, F. J. de Heer, and H. Winter, *J. Phys. B: At. Mol. Phys.* **17**, 2489-2505 (1984).

[22] E. P. Benis, M. Zamkov, P. Richard, and T. J. M. Zouros, *Nuc. Instr. and Meth. In Phys. Res. B.* **205**, 517-521 (2003).

[23] A. P. Hickman, R. E. Olson, and J. Pascale, in *Rydberg states of atoms and molecules*, Edited by R. F. Stebbings and F. B. Dunning (Cambridge University Press, New York, 1983), Chap. 6, p. 187.

[24] D. S. Fisher, C. W. Fehrenbach, S.R. Lundeen, E. A. Hessels, and B.D. DePaola, *Phys. Rev. A* **56**, 4656 (1997).

[25] S. R. Lundeen, R. A. Komara, C. W. Fehrenbach, and B. D. DePaola, *Phys. Rev. A* **64**, 052714 (2001).

[26] E.S. Chang. *Phys. Rev. A* **31**, 495 (1985).

[27] M. A. Gearba, R. A. Komara, S. R. Lundeen, C. W. Fehrenbach, and B. D. De Paola, *Phys. Rev. A* **71**, 013424 (2005).

[28] C. R. Quick and H. C. Bryant, *J. Opt. Soc. Am. B* **7**, 708 (1990).

[29] G. B. Arfken and H. J. Weber, *Mathematical Methods for Physicists,* (Elsevier Academic Pres, London, United Kingdom, 2005).

[30] J. T. Verdeyen, *Laser Electronics*, (Prentice Hall, Inc., Upper Saddle River, New Jersey, 1981).

[31] Rio Redfern Integrated Optics Inc. (2015). Available: http://www.rio-inc.com/_products/orion-laser-source.html [2015, April].

[32] IPG Photonics Co. (2015). Available: http://www.ipgphotonics.com/products_15micron_amp_linear.htm [2015,April].

Appendix A: Metastable Content of Ion Beams

The method detailed in section 4.5 of this text was used to measure the metastable fractions of multiple ions. Table A.1 shows the experimental parameters used for each ion. Table A.2 shows the values measured for each ion. These measured values were then used to calculate the values in table A.3.

Table A.1: Experimental details for each ion.

	U^{6+}	Kr^{6+}	U^{5+}	Pb^{4+}	Th^{4+}	Th^{3+}
Page Number	CSS6-151	CSS10-53	CSS9-85	CSS6-82	CSS10-10	CSS10-28
Beam Energy	150 keV	150 keV	125 keV	72 keV	100 keV	75 keV
Transition	*n* = 53 to 93	*n* = 53 to 105	*n* = 45 to 85	*n* = 38 to 79	*n* = 37 to 73	*n* = 28 to 66
V_S (1":2")	-8 kV	-5 kV	-7 kV	-5 kV	-6.5 kV	-4 kV
$V_{10"}$	7 kV	5 kV	5 kV	4 kV	5 kV	3 kV

Table A.2: Data measured showing the measured parameters needed to learn about the metastable concentration of our ion beams for various ions.

	U^{6+}	Kr^{6+}	U^{5+}	Pb^{4+}	Th^{4+}	Th^{3+}
B (mV at 1300)	70	154	237	211	201	65
S_{HL} (mV at 1300)	3.9	110	52	90	187	73
RP (mV at 1300)	2,688	8,340	10,427	4,050	11,598	3,333
CXRT (mV at 1300)	3,768	65,699	36,517	31,089	115,439	100,025
RPP (mV at 1300)	55	141	347	488	249	112
ΔB (mV at 1300)	31	47	121	82	80	32
K_{PI}	45%	31%	51%	39%	40%	49%

Table A.3: Experimentally calculated values from the measured values in table A.2 using the method detailed in section 4.5.

	U^{6+}	Kr^{6+}	U^{5+}	Pb^{4+}	Th^{4+}	Th^{3+}
Time to Detector from Capture (μS)	5.76	3.42	6.29	7.33	6.94	8.07
M_S (mV at 1300)	246	910	1,361	1,779	1,245	457
M_{15° (mV at 1300)	2,934	9,250	11,788	5,829	12,843	3,790
$Beam_{15^\circ}$ (mV at 1300)	6,702	74,949	48,305	36,918	128,282	103,815
$f_{Decayed}$	92%	90%	88%	69%	90%	88%
$f_{M,\ 15^\circ}$	44%	12%	24%	16%	10%	3.7%
ε_{SI}	28%	17%	17%	12%	16%	14%
$M_S/Beam_{15^\circ}$	3.7%	1.2%	2.8%	4.8%	1.0%	0.4%
$S_{HL}/Beam_{15^\circ}$	0.06%	0.15%	0.10%	0.24%	0.15%	0.07%
$B/Beam_{15^\circ}$	1.04%	0.21%	0.49%	0.57%	0.16%	0.06%